Self-Assembled metallomacrocycles that function as sensors and molecular devices

By

Ahmed Zubi

Supervisor Dr. Jim Thomas

A Thesis Submitted for the Degree of Doctor of Philosophy

June 2013

Department of Chemistry
University of Sheffield
Sheffield
S3 7HF

Abstract

This thesis describes the synthesis of macrocyclic trinuclear ruthenium(II) “bowls” that incorporated 9-methyladenine, 9-benzyl-9H-purin-6-amine, 9-ethyladenine and 9-(4-methoxybenzyl)-9H-purin-6-amine as ligands with good yields and high purities. Their binding to a variety of anion guests was investigated through nuclear magnetic resonance as well as electrochemical studies. These macrocycles possess extremely interesting binding affinity: ^{1}H-NMR investigations revealed selectivity in the macrocycles-host binding, particularly with medium sized halide anions, namely chloride and bromide, being most strongly bound. Generally, electrochemistry-based titrations showed good agreement with the NMR host-guest titrations results, with potential shifts being dependent on binding affinities -although there are some specific differences in the results with fluoride and iodide. In the case of nuclear magnetic resonance we found that the fluoride ion is too small in size to be suitable for the macrocycle cavity to bind strongly, whilst in the case of electrochemistry titrations larges shifts are seen after addition of fluoride due to the high charge density of this ion.

It was found that more complex oxo-anions also bound to the host and affected the Ru^{II} based oxidations. However, in general, the binding affinities for these more complex anions were lower than the highest values for halide guests. Again electrochemical potential shifts generally correlated with binding affinity. Studies also revealed that the electrochemical response to addition of anion guest was complex, as the guest induced shifts of the three Ru^{II} oxidations of the bowls were not always the same. This observation indicates that individual guests preferentially

stabilize specific oxidation states of the bowl. Due to this phenomenon, the macrocycles can function as novel “ion-switched electron transfer gates.”

Acknowledgements

As my time in Sheffield University draws to a close I would like to take this opportunity to thank the many people that have helped, supported and encouraged me throughout my Ph.D. My apologies for those I have omitted, but you are not forgotten.

In the first place I would like to record my gratitude to my wonderful supervisor, Jim Thomas for his supervision, advice and guidance from the very early stages of this research.

I would also like to thank the technical staff within the department. A special thanks goes to Dr Brian Taylor and Susan Bradshaw in the NMR service, Harry Adams for the X-ray crystallography, Simon Thorpe and Sharon Spey in Mass Spectrometry, Peter Farran and Nick Smith in stores and Elaine Fisher as Secretary of the Department.

Thanks to the Thomas group, both past and present: Hanan, Adel, Ina, Mike, Paul, Hiwa and Tom and for creating such a great friendships at the office. A special thanks to Ashley Wragg for help. A big list of mentions for various other people from the last few years, in no particular order: Abdu, Katie, Almahdi, Hend and faithful friend Khalid Ageel.

I am grateful for financial support from the higher education ministry in Libya.

And extra big thanks goes to Professor Christopher Hunter and Dr Simon Turega for their help.

As I find no words to express my thanks to my parents who gave me life, love, and everything to be the person who I am. I thank my children, brothers and sisters, and all relatives for their love, support, prayers and for waiting, waiting, and waiting for me all these years.

A very special thanks to my loving wife for all the things she has done for me. She is always there for me when I need her support and help. She always has a great smile. I am grateful for you. Thank you for your kindness and generosity. It is very much appreciated.

Abbreviations Used in Text

CH_3CN	Acetonitrile
[9]aneS3	1, 4, 7- trithiacyclononane
bipy	4, 4’-bipyridine
bpy	2, 2’-bipyridine
Cp	Cyclopentadiene
CV	Cyclic Voltammogram
DMSO	Dimethylsulfoxide
Eq	Equivalent
Et	Ethyl
ET	Electron Transfer
en	Ethylenediamine
FAB-MS	Fast Atom Bombardment Mass Spectrometry
HOMO	Highest Occupied Molecular Orbital
IVCT	Inter Valence Charge Transfer
LC	Ligand Centred
LMCT	Ligand-to-Metal Charge Transfer
LUMO	Lowest Unoccupied Molecular Orbital
Me	Methyl
MLCT	Metal-to-Ligand Charge Transfer
MMCT	Metal-to-Metal Charge Transfer
MS	Mass spectrometry
NMR	Nuclear Magnetic Resonance
OTTLE	Optically Transparent Thin-Layer Electrode
Ph	Phenyl
PF_6^-	Hexafluorophosphate
UV-Vis	Ultraviolet/Visible
UV-Vis-NIR	Ultraviolet/Visible/Near Infra Red

Table of Contents

Table of Figures

Table of Tables

Chapter 1

1. Introduction

Supramolecular chemistry is defined as the chemistry of the non-covalent bond.[1] The development of this area of chemistry has been tremendous within the last quarter of a century. This expansion is mainly due to the growing knowledge regarding synthetic and characterisation methods for complex structures.[2-3] Researchers in supramolecular chemistry examine weaker and reversible noncovalent interactions, such as hydrogen bonding, metal coordination hydrophobic forces, van der waals forces, π interactions, and electrostatic effects. Crucial areas that have been researched by supramolecular chemistry involve molecular folding, molecular self-assembly, molecular recognition, and host-guest chemistry. Expansion into these areas is mainly due to the growing knowledge concerning synthetic and characterization methods for complex construction. This research has been inspired by the structure and function of assemblies observed in nature such as the hydrogen bonded structure of DNA, the ability of enzyme receptor sites to act on one molecule with absolute selectivity, and the control by metalloproteins such as haemoglobin over a metal coordination environment. True to its inspiration, supramolecular chemistry is a highly interdisciplinary field encompassing chemistry (selective and recognition transformation), biology (translocation of drugs across membranes), and materials science (construction of macroscopic assemblies and devices on the molecular level).[4] It may be loosely divided into two categories: host-guest chemistry (also known as molecular recognition) and self assembly.

1.1 Host-Guest Chemistry

Host-Guest chemistry in its simplest sense can be considered to involve a molecule (a ‘host’) binding another molecule (a ‘guest’) to produce a host-guest complex or supermolecule. The host is quite often a large molecule or aggregate for example an enzyme or synthetic cyclic compound holding a sizeable, central cavity or hole. The host is also the molecular species possessing convergent binding sites (e.g. Lewis basic donor atoms etc.). The guest may be a simple inorganic anion, a monoatomic cation, a simple inorganic, or a more complex molecule such as a hormone. Guests possess contrasting binding sites (e.g. Lewis acidic metal cation, a spherical hydrogen bond acceptor halide anion). The related field of crystal engineering is concerned is with study of intermolecular interaction in the solid state, the construction of new solids and architectures, and the improvement of functional materials.

The synthetic design of an effective host or receptor complex requires a number of criteria to be met. These involve: -

1-the host should be macrocylic and contain a large cavity in which the number of interactions with the bond guest can be maximized.

Macrocycles are very useful in supramolecular chemistry as they provide whole cavities that can completely surround guest molecules and may be chemically modified to fine-tune their properties. Cyclodextrins, calixarenes, cucurbiturils and crown ethers are readily synthesized in good quantities and they are therefore convenient for use supramolecular systems.

2- The Van der Waals surfaces and electrostatic potential surfaces of the host and guest should be complementary.

3- The host should be relatively rigid so that the loss of conformational entropy on binding a guest is minimised.

The synthesis of such macrocyclic structures is not straightforward; the use of high dilution is one way to accomplish the synthesis of macrocyclic structures, but yields can be low and chromatographic separation of linear and cyclic oligomers difficult. One alternative is template directed synthesis.[5] This approach is effective when there are strong interactions between the template and the precursor. But templating is not so successful for the construction of hosts for neutral guests where the interactions between template and precursor are orders of magnitude weaker.

1.1.1 Self-Assembly

Current research has seized on self-assembly as a promising approach to the generation of compounds with enormous molecular sized cavities. Self-assembly is one of the core concepts of supramolecular chemistry and has been defined as the spontaneous formation of higher-ordered structures from molecular construction blocks. Research into biological systems led to this hypothesis being put forward.[6]As understanding on the complex architectures found within living cells became deeper, the idea that such assemblies were built up by the convergent assembly of smaller building blocks was increasingly accepted. In order to provide a general framework for discussion and research, Lindsey.[7] Created a wide-ranging classification scheme for self-assembly processes. Encompassing self-assembly processes in biology and chemistry, this definitive scheme is divided into seven broad, overlapping classes.

1.1.1.1 Class 1. Strict Self-Assembly

Strict self-assembly concerns all processes where components assemble reversibly and the resulting structure is the most stable structure available to that system under those conditions. One example of such a system is the Tobacco Mosaic Virus (TMV)[8-9] whose particles consist of a helical strand of DNA embedded in a right-handed helix composed of identical protein subunits. TMV particles will dissociate into their component parts by changes in pH, temperature or even pressure. However, once the correct conditions are attained again, protein subunits and RNA spontaneously reassemble into virus particles that are indistinguishable from the original TMV.

1.1.1.2 Class 2. Irreversible Self-Assembly

This class is the converse situation of 2.1. Steps towards the final assembly are irreversible; consequently the building blocks must assemble into the final correct structure with no margin for error. This type of process is currently attracting much attention in synthetic organic chemistry.[9-10]

1.1.1.3 Class 3. Precursor Modification Followed by Self-Assembly

These processes involve the synthesis of precursors that are subsequently modified. A biological example is collagen synthesis. Collagens are fibrous proteins that form the major component of skin and bone. They are the most abundant mammalian protein and are found in long, extracellular polymeric structures called fibrils. In turn, these fibrils are often aggregated into larger cables known as fibers that are big enough to be viewed under light microscopes[11].

Assembly of such structures within a cell would be fatal. To prevent such an occurrence a precursor, known as procollagen, is synthesised. Procollagen consists of triple helical polypeptide strands capped at their terminal ends by amino acid chains, called propeptides, that prevent aggregation of procollagen molecules. Once synthesised, procollagen is secreted out of the cell, where proteolytic enzymes remove the propeptides. The resulting collagen molecules are several orders of magnitude less soluble than their precursors and self-assembly of fibrils is rapidly initiated.[11]

1.1.1.4 Class 4. Self-Assembly with Post-Modification

In this case the self-assembly process precedes the final modifications that lead to the targeted architecture. Using this powerful methodology, self-assembled structures can be irreversibly locked into position. Within supramolecular chemistry, this strategy has been most commonly employed in the elegant syntheses of catenanes, rotaxanes, knots, and other interlocked species.[12]

1.1.1.5 Class 5. Assisted Self-Assembly

Here external factors, that are not part of the final assembly, mediate the self-assembly process. This concept was developed as the function of molecular chaperones became apparent.[13] Chaperones help in folding of nascent polypeptide chains by preventing aggregation of peptide sequences and modulate refolding of denatured proteins. Chaperones do not affect the thermodynamics of folding - the ratio of folded and unfolded polypeptides is left unchanged – but they do influence the kinetics of the process. It is thought that this is accomplished by stabilising intermediates along the folding pathway, thus decreasing activation-energy barriers.

1.1.1.6 Class 6. Directed Self-Assembly

In Lindsey’s original definition this class includes processes where a template participates as a structural element in the self-assembly process, but does not appear in the final assembled architecture. An example from biology is the scaffolding protein directed assembly of viral capsids. External and internal scaffolding protein frameworks direct the construction of the protein coat that houses the viral DNA. Packaging of DNA is then accompanied by withdrawal of the internal scaffolding, and the final virion is produced after removal of the external scaffold.[14]

An example from chemistry is the use of vesicles, liquids and foams to direct biomimetic mineralisation and polymerisation. Such templates, whose existence may only be transitory, have been used to template the assembly of structurally complex, three-dimensional architectures.[15]

Subsequently, within supramolecular chemistry, the term directed self-assembly has become more generally understood to include any templated process that brings together molecular components, even if the directing moiety is part of the final structure.[16]

1.1.1.7 Class 7. Self-assembly with Intermittent Processing

This final class incorporates elements from all the proceeding classes. It includes all processes where there are sequential phases of self-assembly and irreversible modification. Such complex processes are still the exclusive domain of biology.

1.1.2 Metal-Ion Templated Self-Assembly

Self-assembled complexes are discrete, structurally well defined species composed of at least two molecular units connected by non-covalent interactions. The use of non-covalent interactions to generate macrocyclic structures is particularly advantageous since the cyclisation process is under thermodynamic control and the entropicallyunfavorablepolymerisation is avoided.

The construction of almost any entity that contains a transition metal requires an assessment of the angles between the binding sites of each donor and acceptor subunit. Based on the value of this angle, the subunits can be classed in two types: linear subunits have an angle of 180°C, and angular subunits have other, smaller angles.[17] When these building blocks are combined the structure of the resulting species will depend solely on the symmetry and the number of binding sites within each subunit. Therefore, the symmetry of the resulting assembly will depend solely on the symmetry of each building block. Thus monocyclic entities can be built by combining subunits with a symmetry axis not higher than twofold, whilst the construction of polycyclic frameworks require at least one subunit to possess a symmetry axis higher than twofold.[18]

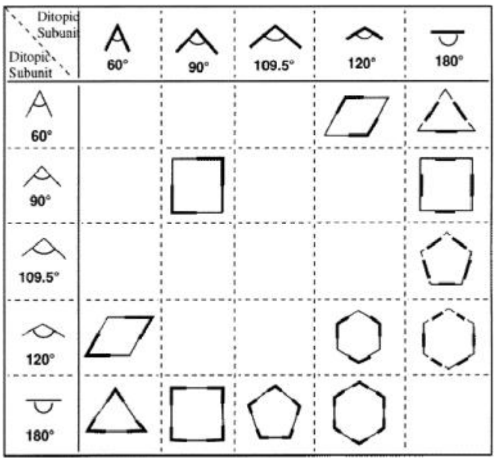

Figure 1.1 Molecular library of cyclic molecular polygons.[16]

The design of three-dimensional polyhedra is more complex since it requires the interaction of many more subunits and at least one subunit needs more than two binding sites. However, a similar molecular library of cyclic molecular polyhedra may be constructed.[17]

It is important to note that this approach only accounts for the angles between the binding sites within each free subunit and extrapolates them into the final product. It can therefore be assumed that the value of the directing angle within each subunit does not change significantly upon its incorporation into the self-assembled structure. In reality, distortions of several degrees may occur, but in most cases they can be neglected, as weak coordination bonding to the transition metal is likely to prevent the formation of highly distorted structures.

The strategy of receptor site self-assembly is one that has only been exploited in synthetic chemistry in recent years. A range of other interactions can be used for the association of two or more compounds in the formation of new recognition sites. For example, Rebek has illustrated that complementary lactam subunits situated on a concave framework can dimerize to form spherical structures - Figure 1.2.[19]

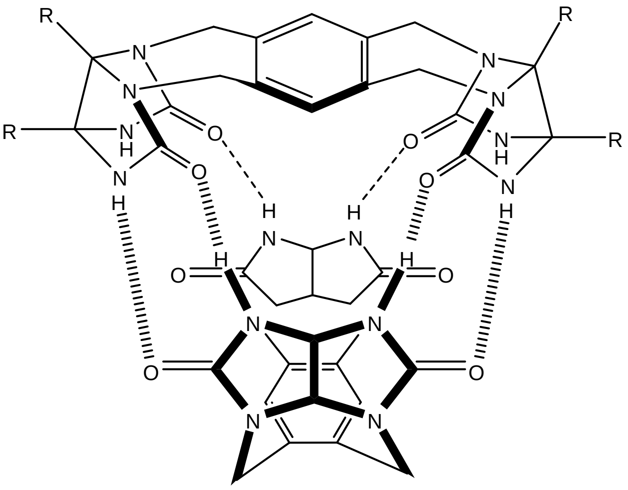

Figure 1.2 Rebek's self-assembled ball structure.

These self-assembly cavities bind small organic guests in nonpolar solvents.[20] The complementarity between thymine and adenine bases has been used by Gokel[20] in the arrangement of two hydrogen-bonded base pair units connected by crown ethers. The resulting box structures are capable of coordinating alkyl bis-ammonium ions inside the self-assembled bis-crown ether cavity - Figure 1.3.

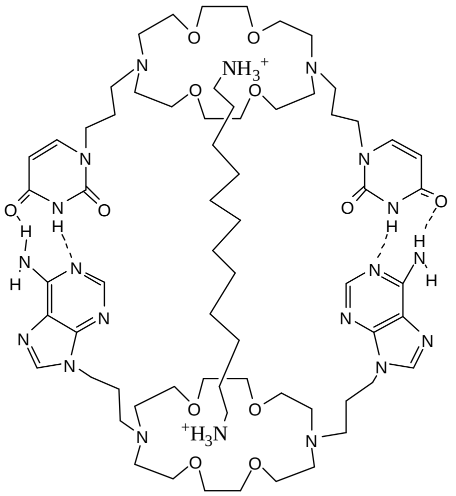

Figure 1.3 Gokel's self-assembling host.

These two examples represent systems where hydrogen bonding is used as the primary interaction to generate the recognition position.

1.2 Intramolecular Assembly of Recognition Sites by a single Metal Ion

The ability of a metal ion to organize a flexible ligand around its coordination sphere has led to the design of several intramolecularly organized recognition sites. This concept is exemplified in Figure 1.9 where coordination of one part a molecule to a metal center results in the allosteric organization of a second distant binding site. For example, the flexible bis(aminomethyl)pyridine derivative – Figure 1.4, developed by Scrimin, is organized by Cu^{2+} binding to the tridentate binding site. This leads to promoted complexation of second Cu^{2+} ion at the distal amine site.

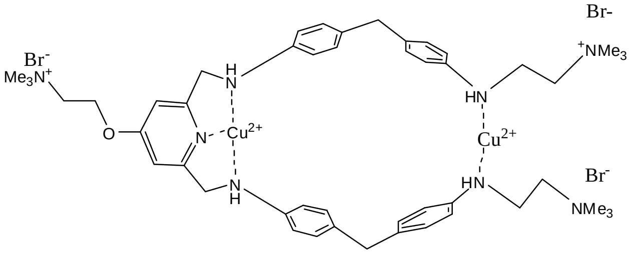

Figure 1.4 Scrimin's self-assembling host bis(aminomethyl)pyridine derivative.

The resulting bis Cu^{2+}complex displays selective catalysis of the hydrolysis of β-amino acid esters due to the cooperative effect of the metal ions, a process which is inhibited by α-amino acids.[21] In a reverse of this strategy, Shinkai has used oligoethercomplexation of alkali metals to organize multiple binding interactions for a nucleotide substrate Figure 1.5.[22]

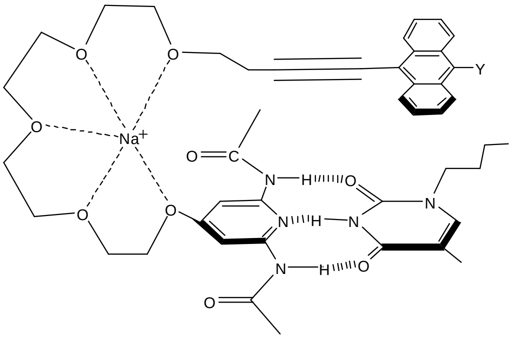

Figure 1.5 Shinkai's self-assembling host.

Anthracene and (diacylamino)-pyridine units were sited at opposite ends of oligo(ethyleneoxy) chain. Addition of Na^+ ions located the two termini to bind in a cooperative manner with an alkyl thymine derivative by simultaneous hydrogen bonding and π-stacking interaction a significant increase in the association constant was seen between the salt free (1000 M^{-1}) and sodium containing (7000 M^{-1}) solutions.

In a strategy that exploits tripodal coordination to a transition metal, Scrimin has developed a metal template transacylase mimic. The key ligand[23] was based on tren derivatives [tris(aminoethyl)amine] functionalized with three m-hydroxyphenyl groups. Addition of Zn(II) ions leads to tripodal coordination and organization of the three hydroxyl groups in region above the metal center. In this position it can interact with the p-nitrophenyl ester of 4-pyridinecarboxylic acid, which is simultaneously coordinated to the open site on the Zn(II). One of the three phenol groups was illustrated to be more acidic than the others and thus more easily deprotonated to form the nucleophilic phenoxide illustrated in Figure 1.6.

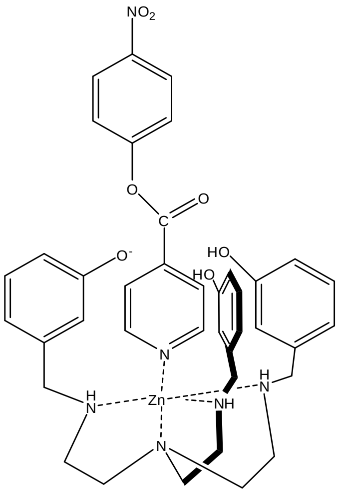

Figure 1.6 Shows Complex of nucleophilic phenoxide with zinc.

Large rate acceleration were seen for the transacylation reaction only in the presence of templating Zn(II) and unfunctionalized hydroxyl groups.

1.3 Self-Assembly of Binuclear Macrocycles

The earliest example of a cyclic self-assembled host molecule was reported by Maverick and co-workers.[24-25] Mixing a $Cu(NH_3)_4^{2+}$ complex and a bis (β–diketone) ligand in a aqueous solution led to the formation of the macrocycle shown in Figure 1.7.

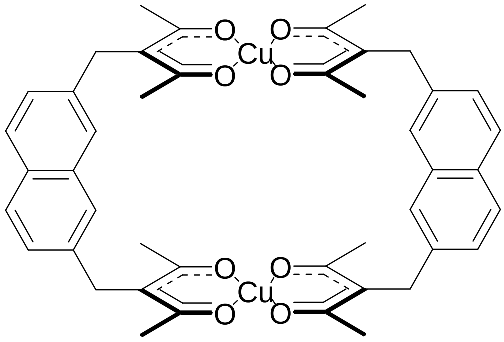

Figure 1.7 The first example of a cyclic self-assembled host.

Binding studies revealed that this macrocycle is a host for pyrazine, pyridine, quinuclidine, and diazabicyclo[2,2,2]octane (DABCO).[24] In chloroform and with other guests also present, DABCO was selectively bound inside the macrocyclic host with K = 220 M^{-1}. X-ray studies of the inclusion complex established the internal coordination of DABCO. These investigations were among the early observations of the intermolecular coordination of bifunctional Lewis bases to binuclear transition–metal-based hosts.[24]

Fujita et al. have assembled several water-soluble binuclear macrocycles.[26-27] Mixing a dipyridyl ligand with an aqueous solution of $[(en)Pd(NO_3)_2]$ leads to the formation of the assembly shown in Figure 1.8.

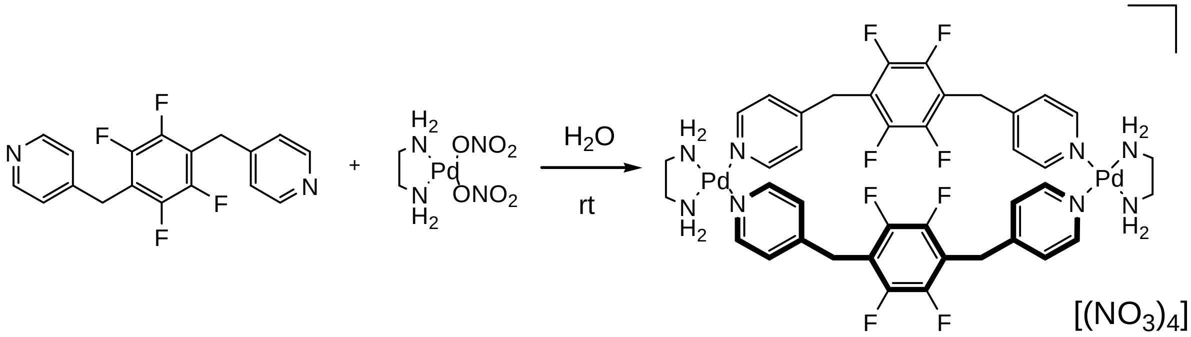

Figure 1.8 Scheme of Self-assembly of Fujita's binuclear macrocycle.

The presence of an electron-deficient perfluoronated phenylene subunit allows the complex to recognize electron-rich compounds, such as naphthalene, in aqueous media.[26-27]

This work was extended by using a slightly different subunit, 4-bis(4-pyridylmethyl)benzene, to assemble a corresponding palladium-based bimetallic species.[28-30] Furthermore, it was shown using dilution studies of this macrocycle in D_2O by ^1H NMR spectroscopy that the monomeric palladium system was in equilibrium with a catenane Figure 1.9.

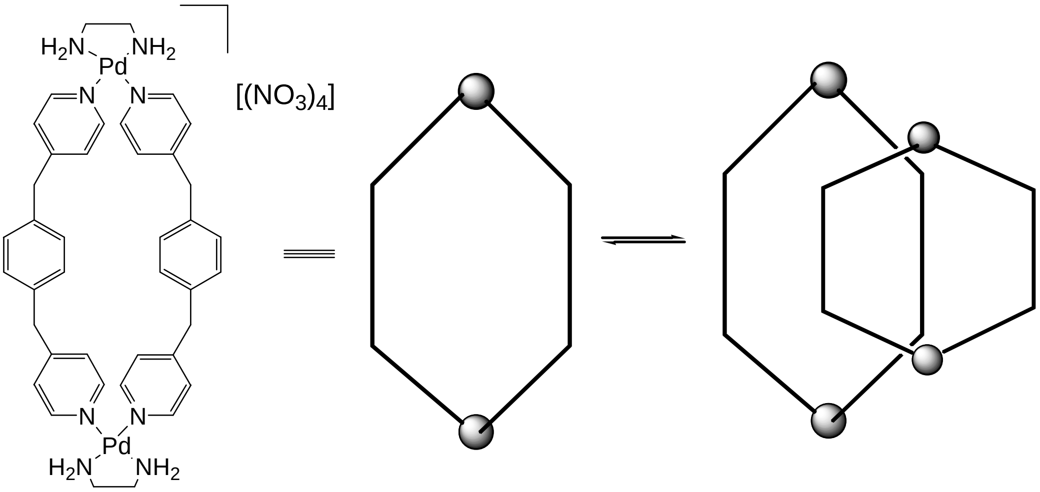

Figure 1.9 Fujita’s binuclear macrocycle in equilibrium with catenane.

This equilibrium favoured the single ring assembly at low concentrations (<2 mM), but at high concentrations (>50 mM), the interpenetrating in Figure 1.9 was the dominant species. Formation of the catenane is due to the benzene unit of one macrocycle behaving as a guest molecule for the other macrocycle. The process is driven by π-π interactions.

By changing to platinum, which forms stronger bonds with pyridine donors, Fujita et al. were able to exclusively form the monocyclic structure at room temperature. On heating to 100°C in water in the presence of $NaNO_3$ however, the formation of the catenane was observed due to the increased thermal lability of the Pt-pyridine bond.[28-29]

The binuclear systems discussed above are all homodimetallic systems, but there are two examples of mixed-metal systems, the first of which was reported by Hupp and co-workers.[31-32] While attempting to synthesise a molecular square using a flexible ligand system, bis(pyridyl)ethane, they isolated the compound in Figure 1.10.

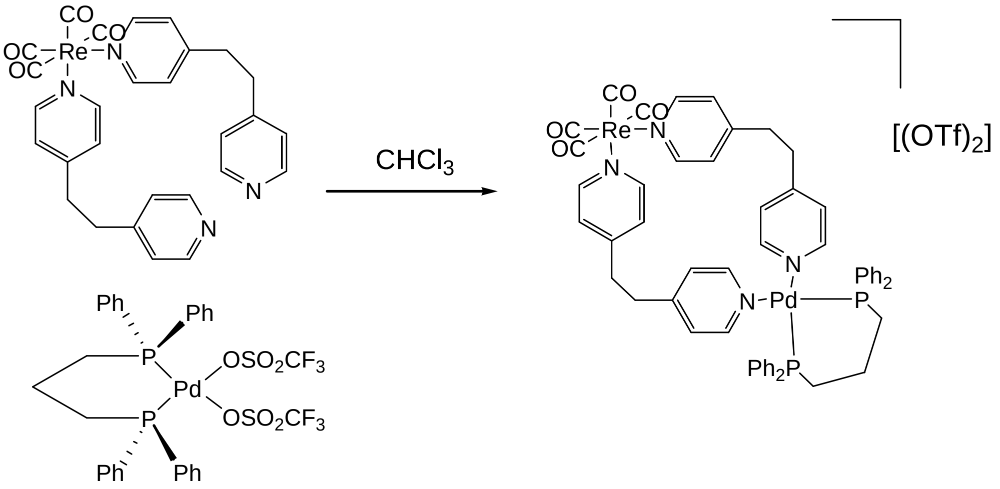

Figure 1.10 Hupp*et al*'s mixed valence systems.

Surprisingly, they found that the luminescence in this system was completely quenched.[31]

1.4 Self-Assembly of Triangles and Squares

Relatively few examples of trinuclear molecules have been reported in the literature. At first glance it would appear to be a simple synthetic challenge. It may be from a design point that a cyclic combination of three linear building blocks with three corners which possess a 60° directing angle would result in the formation of a molecular triangle. One explanation for the rarity of such structures maybe the size of the directing angle which is uncommon in both transition metals and organic ligand linking subunits.

Loeb and co-workers reported such an example where they assembled complementary molecular building blocks with specific angular requirements.[33] Using 4,7-phenanthroline as a 60° corner that favours bridging metal complexes over forming chelate complexes and reacting it with the linear phenyl-bridged bis-palladium complex, formed the self-assembled triangle shown in Figure 1.11.

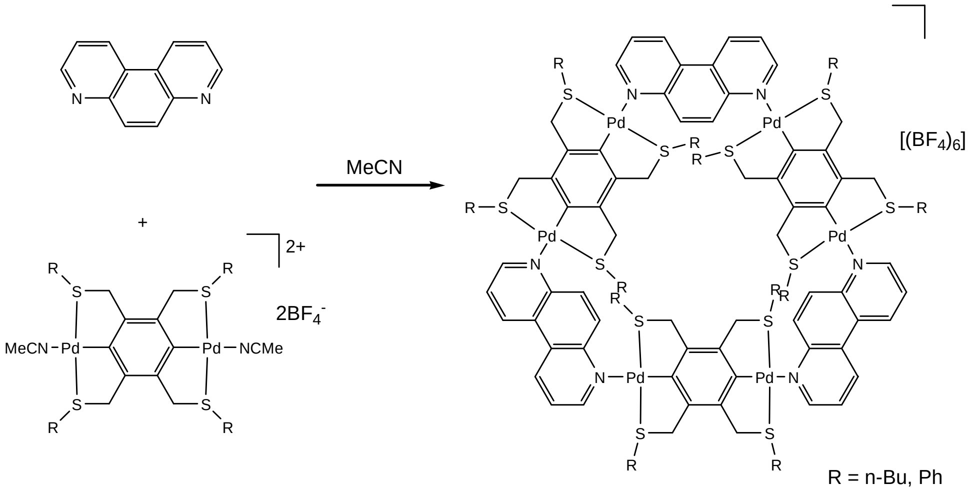

Figure 1.11 Scheme of Self-assembly of Loeb's molecular triangle.

Using variable temperature NMR, Loeb and co-workers were able to provide additional evidence for the cyclic nature of this triangle in solution, showing dynamic behaviour of the compound.[33]

Self-assembly of molecular triangles using less rigid building blocks was observed by Fujita and co-workers.[34-35] Reaction of $[(en)Pd(NO_3)_2]$ with 1 equivalent of a series of bis-heteroaryls in water led to the formation of molecular squares and molecular triangles (see Figure 1.12).

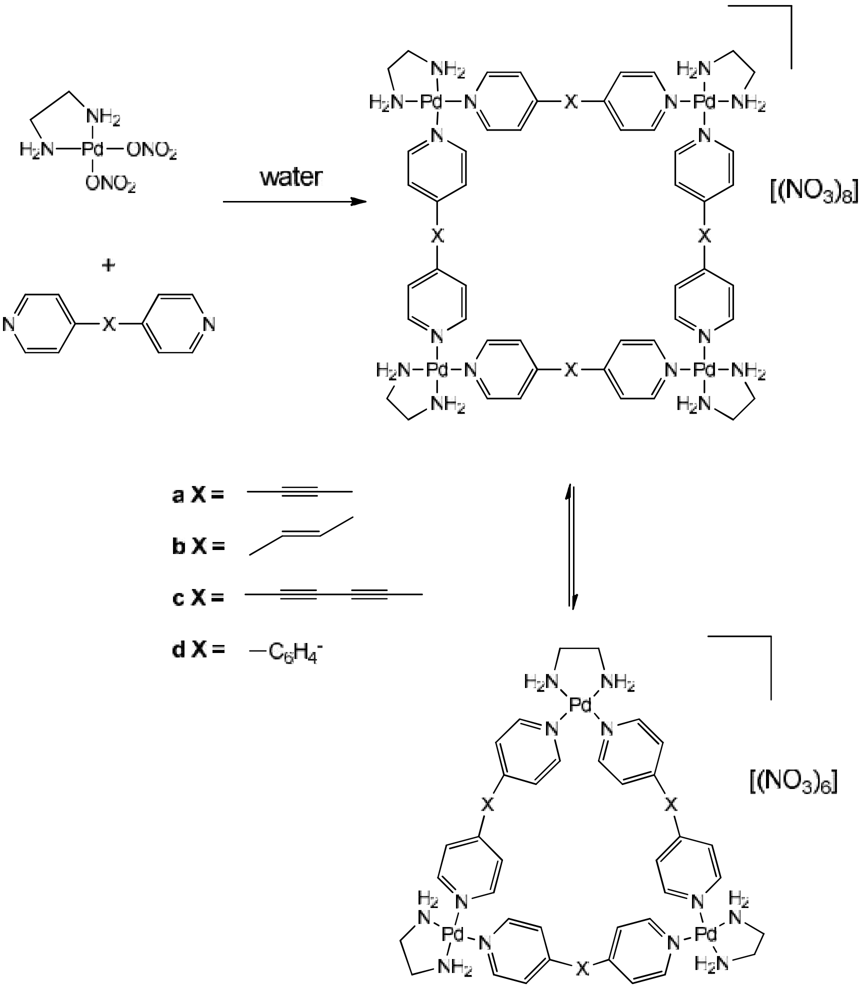

Figure 1.12 Scheme of Self-assembly of Fujita’s molecular squares and molecular triangles.

NMR confirmed the cyclic structure of both products since no signals were observed for the existence of polymeric compounds with uncoordinated end groups. Also, the two products were in equilibrium with one another, with the major product being the molecular square (see Figure 1.12). This was supported by the observation of concentration-dependant effects on the equilibrium. At higher concentrations the ratio shifted in favour of the less strained molecular square (see Figure 1.12). From a thermodynamic perspective, molecular squares are less strained and thus more stable in terms of enthalpy, while entropy favours the triangle since it is assembled from fewer components.[34-35]

In principle, the directional-bonding approach should involve exclusively rigid linkers, which are suppose to undergo only minor distortion upon metal-coordination within the metallacycle. Thus, the orientations of their two coordinate vectors can be guessed quite precisely from a model structure. However, in some cases, even an educated guess may be difficult, for number of reason:

A The linker might have more than two binding sites, and thus, its geometry depends on which sites are used in construction of the metallacycle.

In general, a rigid linker is defined as a molecule that does not bend significantly, typically for the presence of extended conjugation. However, even rigid linkers can have one or more degree of torsional freedom, i.e., free rotation about single bonds.A typically example is 2,2′-bipyrazine (2,2-bpz, Figure 1.13): depending on the mutual orientation of the two six-membered rings and on which N atom (1,1′ and/or 4,4′) are involved in the coordination, different combinations of coordinate vectors (and thus geometries) are possible. Finally, if the linker itself is not rigid, e.g. It comprises some aliphatic fragments between the two binding sites, then any guess about its geometry within the metallocycle will be very tentative at best.[36]

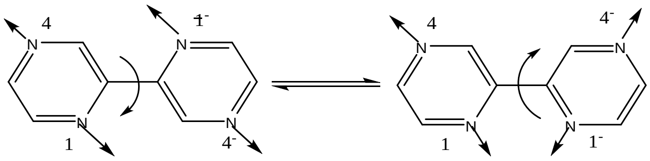

Figure 1.13 2,2′-bpz

The self-assembly of molecular squares is much more widespread and numerous examples are reported in the literature.[37] This requires the interaction of four bidentate 90° angular units with four linear bridges. Square planar transition metal complexes are ideally suited for such assemblies.

The solution structure of this square was confirmed by NMR and mass spectroscopy Figure 1.14. This molecular square also showed the unique ability for molecular recognition of neutral aromatic guests such as benzene and naphthalene.[38]

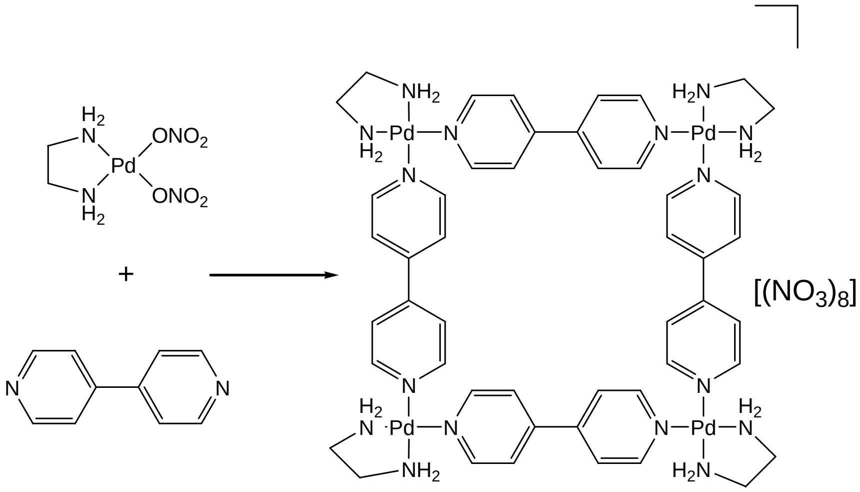

Figure1.14 Fujita's self-assembled square.

1.5 Cp*Rh Complexes of DNA/RNA Nucleobases

Fish and co-workers[31,39]investigated the reaction of 9-methyladenine with [Cp*Rh(H_2O)$_3$][OTf]$_2$ in D_2O at pD 7.2 (pD = pH + 0.4). ^{1}H NMR spectroscopy provided evidence for the formation of a new complex with dramatic shifts for H2 and H8 in comparison to those of free 9-methyladenine at 8.83 and 7.67 ppm, respectively. They found that these dramatic ^{1}H NMR chemical shifts for H2 and H8 were a characteristic feature for Cp*Rh cyclic trimer structures with 9-substituted adenine derivatives, which was verified by X-ray crystallography of the Cp*Rh-9-methyladenine cyclic trimer (see Figure 1.15).

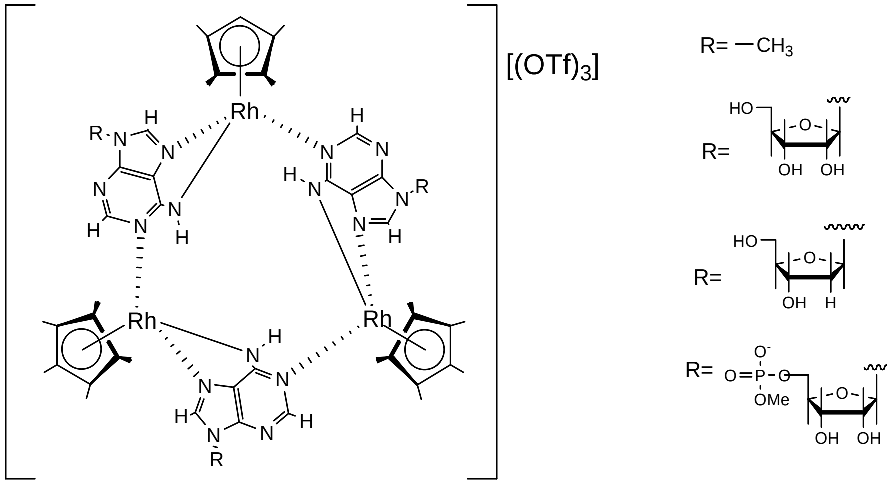

Figure 1.15 Fish's Cp*Rh cyclic trimer structures with 9-substituted adenine derivatives.

The single-crystal X-ray structure of an enantiomer of 9-Me adenine macrocycle was shown to have a triangular dome like supramolecular structure, with three Cp* groups stretching out from the top of the dome, three methyl groups pointing to the bottom. Three adenine planes form the surrounding shell and three Rh atoms are embedded in the top of the dome.[31,39] The structures of all these macrocycles are similar to that of the parent structure except that the three Me groups are replaced by three ribose, deoxyribose, or three Me-5'-ribose monophosphate ester units, respectively.

The shape, the cavity size and the aqueous stability of these Cp*Rh-nucleobase/nucleoside/nucleotide cyclic trimers prompted Fish, *et al*. to utilise them as hosts to recognise biologically relevant molecules in aqueous media. At a physiological pH of 7.37 they were the first reported examples of bioorganometallic hosts, being able to recognize aromatic amino acids L-tryptophan and L-phenylalanine in aqueous media at pH 7. A variety of guest aromatic and aliphatic amino acids, substituted aromatic carboxylic acids, and aliphatic carboxylic acids, were studied by ^{1}H NMR spectroscopy for their interactions with the host complexes. The aromatic groups interact by a classical π-π mechanism, while the aliphatic guests engage in classical hydrophobic interactions.[30-31,39]

1.5.1 Trinuclear metal complexes.

Related non-macrocyclic, but electrochemically active triangles have been reported. For example, Habinet and co-workers studied trinuclear mixed valence of type (I) which are synthesised by oxidation of [{Cp*(dppe)Fe(CO)$_3$}1,3,5-C$_6$H$_3$)] (dppe = η^2-bis(diphenylphosphino)ethane]) with [(C$_5$H$_5$)$_2$Fe][PF$_6$].

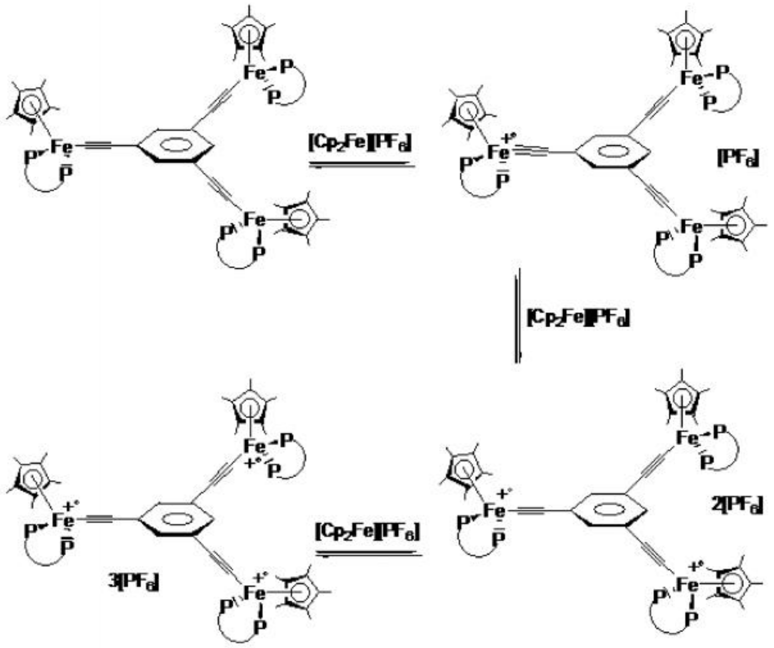

Figure 1.16 $[\{Cp^*(dppe)Fe(CC-)\}_3(1,3,5-C_6H_3)]^{n+}$ (n=0,1, 2, 3) trinuclear iron complexes.

Cyclic voltammetric analysis of complex $[\{Cp^*(dppe)Fe(CO)\}_3(1,3,5-C_6H_3)]$ displays three one electron reversible oxidation waves. The bis(ethnyl)benzene organic moiety acts as a connector between the organoiron building blocks to convey electronic interactions from one metal centre to the other through continuous overlap between the d orbitals of the metal centres and the π orbitals of the polyethylbenzene ligands.[40-41]Analysis of the NIR spectra showed a IVCT band for the weakly coupled mixed valence system $[\{Cp^*(dppe)Fe(CO)\}_3(1,3,5-C_6H_3)]^+$. In the case of the druidical trinuclear mixed valence $[\{Cp^*(dppe)Fe(CO)\}_3(1,3,5-C_6H_3)]^{2+}$. Two distinct IVCT bands were observed and attributed to the two possible independent ways to transfer an electron in the singlet and triplet states of such a mixed valence compound.[40-41]

1.5.2 Lahiri and co-workers complexes

Ruthenium (II) triangles have also been synthesized. For example, Lahiri and co-workers[42] have synthesised, via reactions of $[Ru^{II}(bpy)_2(EtOH)_2]^{2+}$ (bpy = 2,2'-bypyridine) and $[Ru^{II}(phen)_2(EtOH)_2]^{2+}$ (phen = 1,10'-phenanthroline) with the trisodium salt of 1,3,5-triazine-2,4,6 trithiol (Na_3L), the triruthenium complexes A and B (see Figure1.17). In CH_3CN, the complexes A^{3+} and B^{3+} exhibit three reversible one-electron redox processes corresponding to successive Ru(II)/Ru(III) couples.[42] The remarked three responses are assigned as stepwise electron-transfer processes involving the metal centres, $Ru^{II}Ru^{II}Ru^{III}/Ru^{II}Ru^{II}Ru^{II}$(couple I); $Ru^{II}Ru^{III}Ru^{III}/Ru^{II}Ru^{II}Ru^{III}$(couple II); $Ru^{III}Ru^{III}Ru^{III}/Ru^{II}Ru^{III}Ru^{III}$(couple III).[42-43]

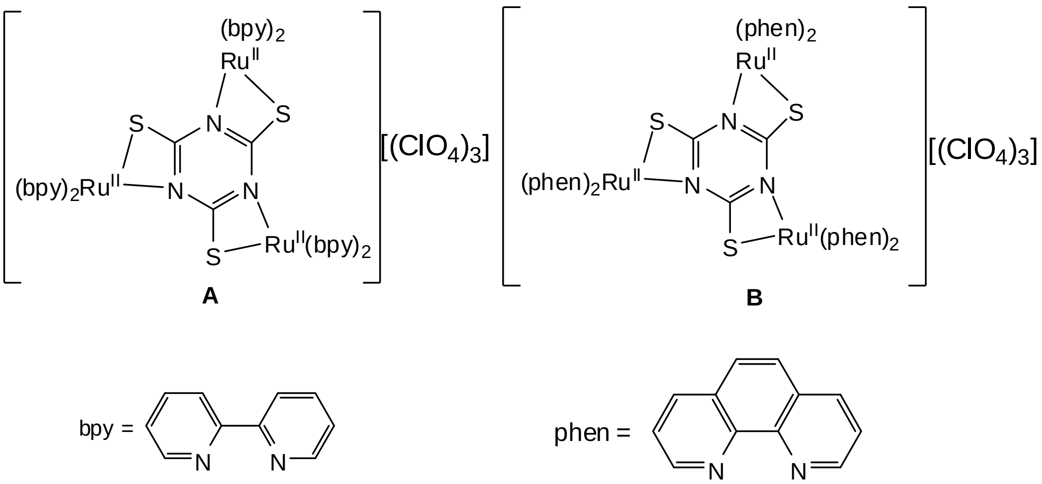

Figure 1.17 Lahiri’ trinuclear ruthenium complexes.

Spectroelectrochemical studies on the bipyridine derivative $\mathbf{A}^{n+}$ (n = 3-6) shows there is electronic interaction between the Ru(II) and Ru(III) sites in the mixed valence species $\mathbf{A}^{4+}$ and $\mathbf{A}^{5+}$. This is apparent from the broad, relatively weak intervalence charge transfer IVCT transitions in the near-IR region which are present for these two oxidation states, but absent for the two isovalent states[42] The width of these transitions is consistent with class II mixed valence states.[44] The electronic coupling constant, V^{ab}, for the two mixed valence states are essentially the same because of the fact that the bridging pathway (between two N atoms of the triazine unit via a metal-substituted linkage) is the same in each case.[42]

1.6 Thermodynamic rules of Host-Guest interaction:

There is an equilibrium between the unbound state, in which of the host and guest are separate from each other, and the bound host- guest complex.

$$H + G \rightleftharpoons HG$$

In this component H= host, G= guest, HG= host- guest complex.[45]

1.6.1 Association and Dissociation constants

$$Ka = \frac{[HG]eq}{[H]\mathrm{eq}[G]\mathrm{eq}}$$

The association constant, K_a for a host-guest interaction is found by multiplying the concentration of the guest and host concentration divided by the product of the concentration of the individual Host and Guest molecules at the point of equilibrium of the system (equilibrium state of the system).

The state of equilibrium between the Host-Guest complex and free molecules also be defined or identified by the dissociation constant, K_d.

$$Kd = \frac{[H]eq[G]eq}{[HG]eq} = \frac{1}{Ka}$$

Gibbs free energy depends on the value of Ka

The resulting change in free energy is related to the equilibrium constant.

$$\Delta G = RT\ln K_a$$

Therefore by knowing value of the association constant, we can solve for the Gibbs free energy of the reaction and because:

$$\Delta G = \Delta H - T\Delta S$$

The Gibbs Free energy can be used to obtain Enthalpy, ΔH, and Entropy, ΔS.

1.7 Nuclear Magnetic Resonance:

NMR is one of the best spectral methods in analytical chemistry. Which is particularly effective in studying host-guest complexes. The binding activity between two molecules generates a significant change in the electronic environment for both molecules, which leads to a change in the signals in resonance spectrum of molecules. [46] Prior NMR investigations have given profitable information about the binding of several guests to hosts. [47-54]

It is worth mentioning that one of the important factors that should not be overlooked when analyzing the host-guest interaction is the time it takes to acquire the data compared with the time for the binding event. In many cases, the binding events are much faster than the time-scale of data acquirement; therefore, in this case the output data is an averaged signal for particular molecules and the complexes.[42,46]

1.8 Electrochemical Sensing

Electrochemical sensing involves the use of electrochemically active host structures that are able to selectively bind or interact with a guest species, resulting in an alteration of the electrochemical properties of the host.[55] The design of a sensor is simple as shown in Figure 1.18 below:

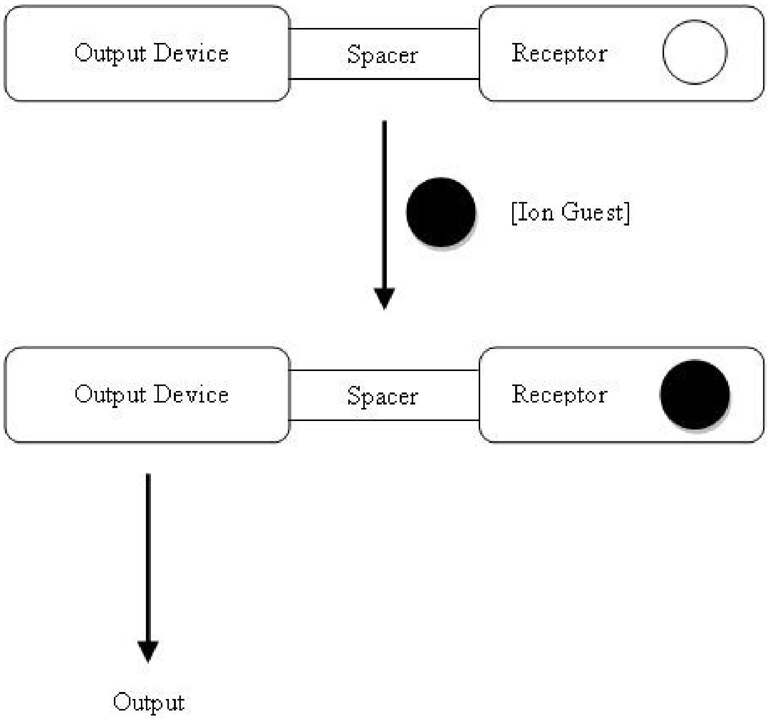

Figure 1.18 Show simple design of sensor.

The receptor is a site on the host complex that is able to bind a specific molecule/ion. In the case of macrocyclic complexes the central cavity is the site where guests bind. The binding of the guest triggers a response in the output device. This allows the binding to be detected. For example, the oxidation potentials of a particular host will be known. If this host is able to selectively bind to a guest it may result in an alteration of the oxidation whether it is an anodic or cathodic shift in the cyclic voltammogram.

The ferrocene and cobaltocenium groups have been extensively used as effective signaling devices in macrocyclic sensors.[56] They are amongst the most effective signaling devices due their production of clear oxidation/reduction potentials. Beer and co-workers have carried out extensive research into the field of electrochemical sensing using these units. For example, in 2005 this group described work on ditopic redox-active polyferrocenylzinc(II) dithiocarbamate macrocyclic receptors.[57] These complexes were found to be excellent hosts that could bind and sense the host anions benzoate and isonicotinate and neutral molecule 4-picoline. Different binding constants were observed for the different hosts interacting with the guest species. All of the receptors were shown to sense binding of isonicotinate and benzoate anions via large cathodic shifts in the respective cyclic voltammograms. This was possible due to the presence of the redox active ferrocene moiety acting as a reporter device on the hosts. The oxidation potentials of the ferrocene units significantly cathodically shifted upon the binding of the anions.

1. 9 Self-assembled electrochemical sensors

Very few self-assembled electrochemical sensors have been reported. In fact, the following section reviews virtually all the work in this area.

Beer, *et al*. (2001) investigated the self-assembly of Cu^{II-}based metalomacrocycle from ditopic dithiocarbamate ligand.[58] Cyclic voltammetry (CV) investigation of these redox active systems indicated that macrocycles **5** and **6** (see Figure 1. 19 **)** function constructively as very specific sensors for anions as guests. The addition of five mole equivalents of Cl^- to acetonitrile solution of **5** produced small shifts.

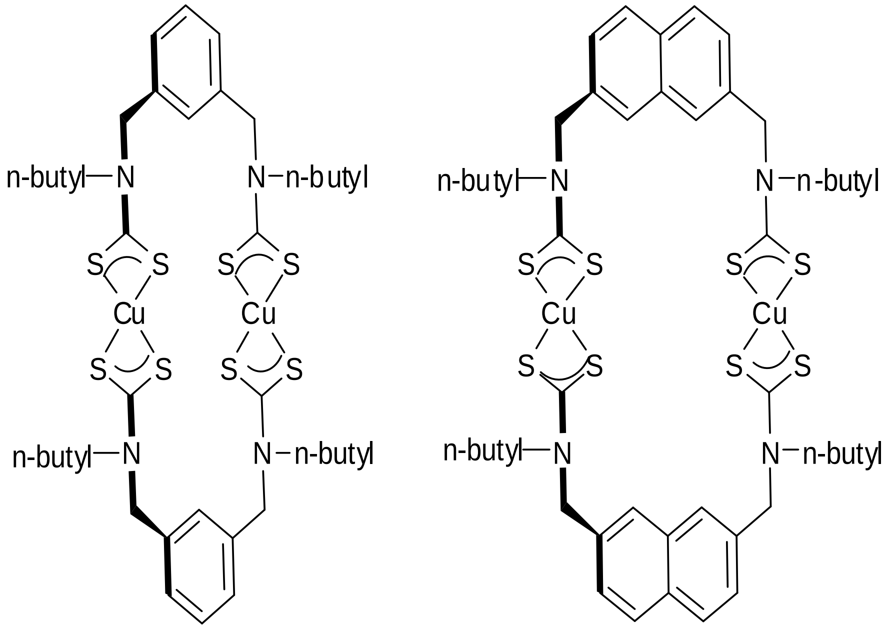

5 **6**

Figure 1. 19 Beer's self-assembly of Cu^{II}–based metalomacrocycle.

However, a noticeable cathodic shift (20 mV) in the $Cu^{II/III}$ oxidation redox pair of the macrocycle was not found on addition of other guests. For macrocycle 6 (see Figure 1. 19), the greatest redox response results from guests that have a tetrahedral shape, dihydrogenphosphate and perrherate;both $H_2PO_4^-$ and ReO_4^- produced a 85 mV oxidation shift in the Cu^{II}/Cu^{III} redox couple of the macrocycle. From these findings, it was concluded that high anion selectivity is enforced by the size of thiocarbamatecopper(II) host. In a later study, the same strategy was used to isolate new metallocrypt and-based sensors. Cryptand compounds were also obtained from dithiocarbamate ligands. In this case octahedral metal ions (Co^{III}, Ni^{IV}, Fe^{III}) were employed to direct assembly.[59] Macrocycles containing polyether were created to complex group I metal cations. CV investigations illustrated that the addition of alkali metal cations to MeCN:DCM(1:1) solutions of these macrocycles show significant anodic shifts in the macrocycle metal-based oxidation importantly, the ratio of metal cation:cryptand cavity size and the extent of anodic shift coincide. The ion Cs^+ produces the greatest electrochemical shifts (45 mV), while Li^+ results in no change in the redox chemistry of cryptand **7 (**see Figure 1.20).

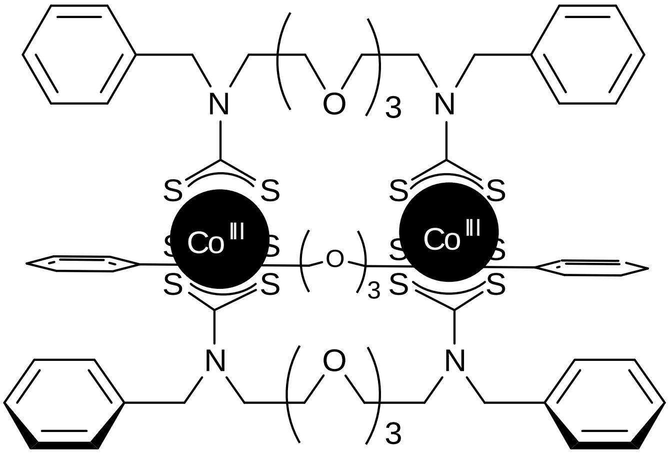

7

Figure 1.20 macrocycles containing polyether.

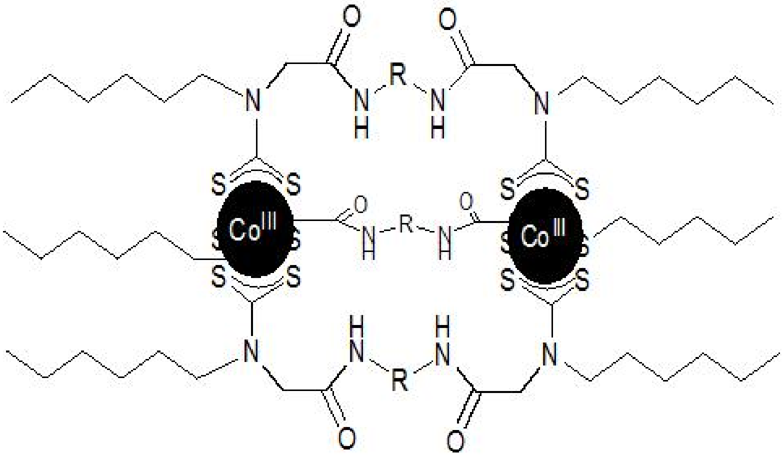

8

Figure 1.21 Macrocycle of cryptand containing amide group

A series of cryptands containing amide hydrogen bond donors such as **8** (see Figure 1.21), were created for anion sensing. Once again, structure specific effects were observed. For example the addition of 10 mole equivalents of $H_2PO_4^-$ to DCM solutions of **8** (see Figure 1.21), resulted in a large cathodic shift of the macrocycle $Co^{IV, III}$ based oxidation couple by $E_{1/2}$ = 125 mV. On the other hand, the addition of Cl^- only caused a 15 mV shift.

The Severin Group have also synthesized electrochemical sensors based on their originally reported self-assembled metallomacrocycles. This first macrocycle binds to Li^+ with huge affinity. Notably, chloroform solution of macrocycle **9** (see Figure 1.22) can quantitatively extract Li^+ from aqueous solutions, in excess of other alkali metal ions.

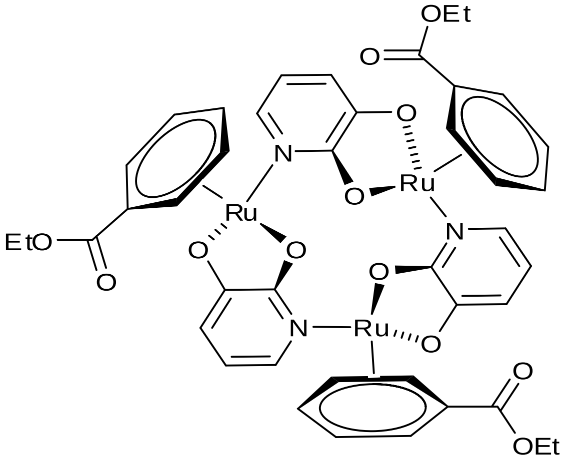

9

Figure 1. 22 Severin's self-assembly of Ru^{II}–based metalomacrocycle

This macrocycle is a kinetic labile thermodynamic product. However, very high sweep rate CV investigations on 9 (see Figure 1.23) in MeCN:DCM (1:1) solvent mixture illustrate that it exhibits three oxidation peaks at 0.683, 0.963 and 1.150 V (against Ag/AgCl), respectively.

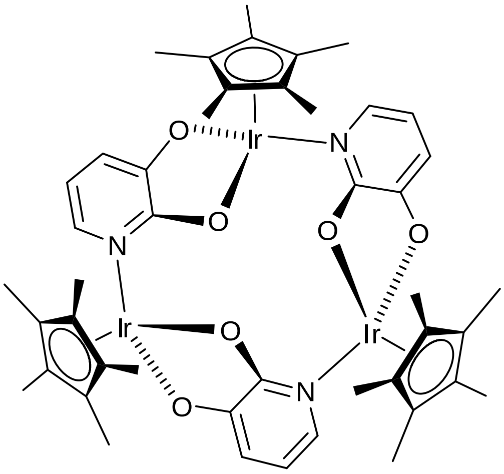

10

Figure 1. 23 self-assembled of Ir with 3-hydroxy-2-pyridone ligands

In the presence of Li^+ the first oxidation peak illustrates a huge anodic shift of over 350 mV.[60] Interestingly binding affinities are dependent on the nature of the metal centre used to template these macrocycles. For example, macrocycle **10** (see Figure 1.22) was self-assembled from the base-catalysed reaction between 3-hydroxy-2-pyridone ligands and $[\{Cp^*IrCl_2\}_2]$. In contrast to **9** macrocycle **10** binds Li^+ with low affinity, it was concluded that this was because the binding site of macrocycle **10** is very rigid and sterically shielded.[61]

By exploitation a ditopic ferrocene based ligand the Duan and Meng groups formed the Ni_4Fc_4 heterometallic macrocycle (Figure 1.24) in good yields through Ni^{II} ion enforced self-assembly.

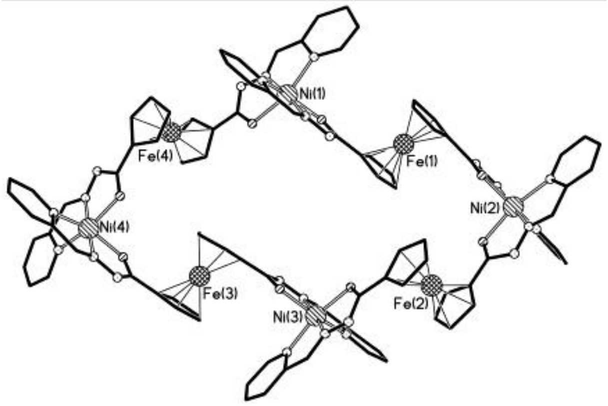

Figure 1. 24 Duan and Meng self-assembly of Ni_4Fc_4 heterometallic macrocycle

It was found that although the ferrocene-base Fe$^{III/II}$ oxidation couple of the macrocycle was unperturbed by the addition of the majority metal ions tested; it is very sensitive to Mg^{2+} ions. Commonly, metal cations induce anodic shifts in ferrocene-based macrocycle; nevertheless the addition only two mole equivalents of $Mg(NO_3)_2$ to organic solvents of macrocycle yielded a 240 mV cathodic shift in the oxidation potential. This suggests a guest-induced reorganisation of the host's electronic arrangement.[62]

1.8 Aims

The aim of this work is to investigate the host guest chemistry of ruthenium(II) supramolecular metal organic host analogous to the rhodium macrocycle complexes, produced by Fish et al.[52] using the facially coordinating [9]aneS$_3$ ligand in place of η5-pentamethylcyclopentadienyl units (see Figure 1.25). These complexes contain adenine based units as bridging ligands and cationic [Ru^{II}([9]aneS$_3$)]$^{2+}$ fragments as vertices.

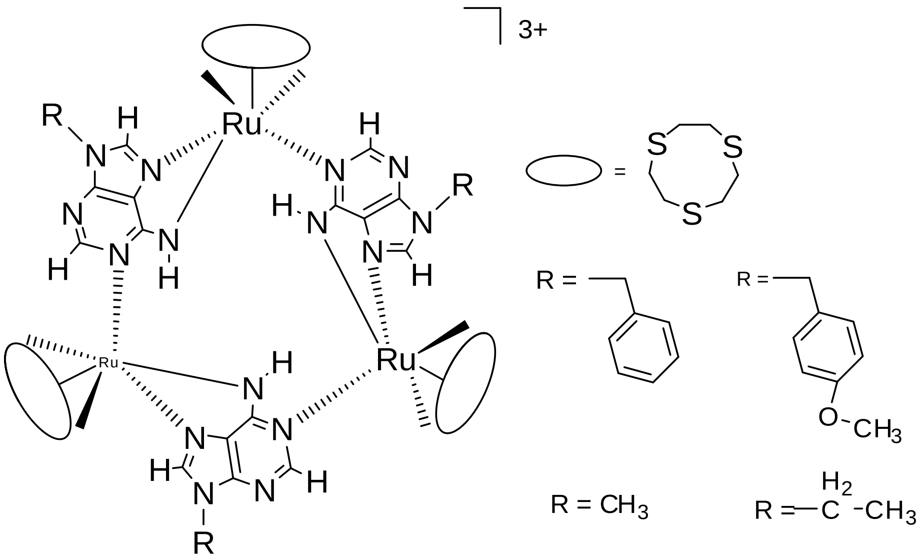

Figure 1.18 scheme of Bowl shaped metallo-macrocyclic complexes containing the [Ru^{II}([9]aneS$_3$)] fragment.

The host guest chemistry of these systems may be of interest as they possess two possible binding sites. At the "base" of the bowl the amine groups of the briging ligands and the thiacrown ligands create a polar site rich in possible hydrogen bond donor sites. On the other face, the adenine aromatic faces create a hydrophobic binding pocket.

Apart from their host-guest chemistry, triangular complexes such as these are appealing targets for the study of redox properties and metal-metal interactions because of their unusual topology. The triangular arrangement of redox centres means two different mixed valence states can be generated. The $[Ru^{II}([9]aneS_3)]^{2+}$ fragment was selected as a synthon for the corner units. Previous work has demonstrated that this moiety possesses suitable electronic and electrochemical properties,[53] and that self-assembly at high temperature allows thermodynamic assembly of species which become “kinetically locked” at room temperature[50] and so avoid kinetic lability. The accessibility of a central cavity, in conjunction with the possibility to exploit the ruthenium(II)/(III) electrochemical couple, provides the basis for a molecular sensor (see Figure 1.26).

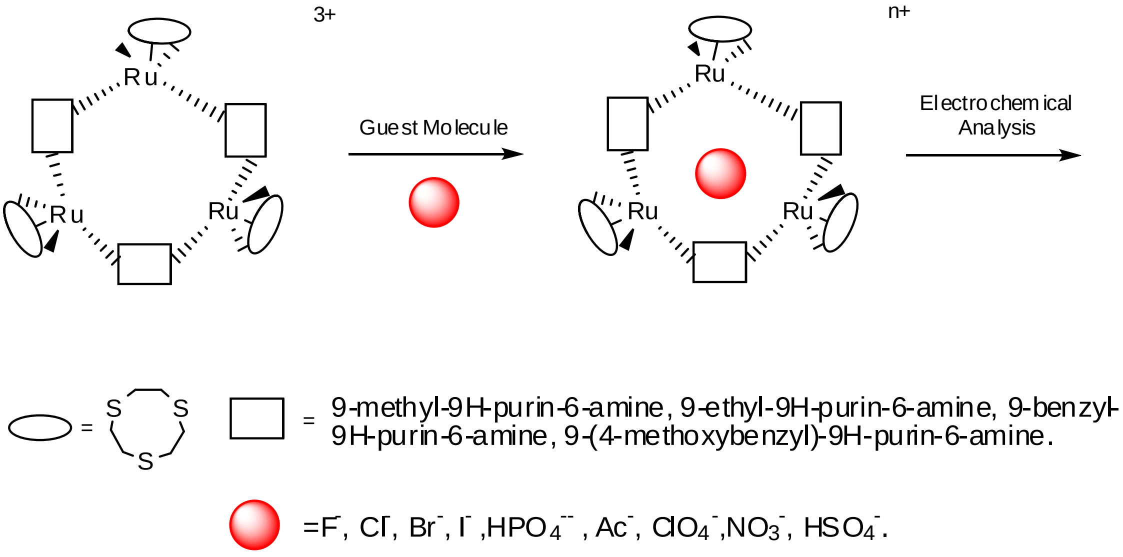

Figure 1.26 Exploitation of the Ru(II)/Ru(III) couple for host-guest chemistry.

CHAPTER 2

2. Synthetic Studies

Initially one previously reported macrocycle was assembled as the host-guest chemistry of this system has yet to be explored. This work was extended to make three new systems. In all cases the bridging ligand was an sterically hindered adenine made by established procedures. The ligand 6-mercaptopurine is commercially available. The syntheses of 9-methyladenine and 9-ethyladenine were through previously reported procedures. These procedures were adapted for the syntheses of the new ligands 9-benzyladenine and 9-methoxyadenine.

2.1 Reaction of [Ru([9]aneS_3)(DMSO)Cl_2] with 9-Methyladenine.

[Ru([9]aneS_3)(DMSO)Cl_2] was reacted with two equivalent of silver trifluorosulfonate in water to produce the [Ru([9]aneS_3)(CF_3SO_3)$_3$]$^{3+}$ metal complex. The silver chloride precipitate is removed by celite filtration and one equivalent of 9-methyladenine, and one equivalent of the hindered amine, 1,2,2,6,6-pentamethylpiperidine (PMP) was added to the reaction mixture to form the complex [Ru([9]aneS_3)(9-methyladenine)]$_3^{3+}$. The compound was isolated as the PF_6 salt on addition of excess NH_4PF_6 and fully characterized. Each nucleobase ligand coordinates to two metal centre via the N(1), N(7) amine groups. The sterically hindered base PMP is a strong Bronstead base but a weak nucleophile. The use of “normal” bases such as NaOH yields intractable black solids. Presumably, such bases react with the thiacrown instead of deprotonating the N5 position. In contrast to the [Cp*Rh^{III}] centre, the [Ru([9]aneS_3)] fragment is not a strong enough Lewis acid to initial deprotonation of amine group.

The product was isolated as a PF_6 salt on addition of excess NH_4PF_6 and characterised. Evidence of trimer formation comes from ^{1}H NMR, mass spectrometry and elemental analysis. A comparison of these data with previous reports confirmed that the expected trinuclear host was synthesized.

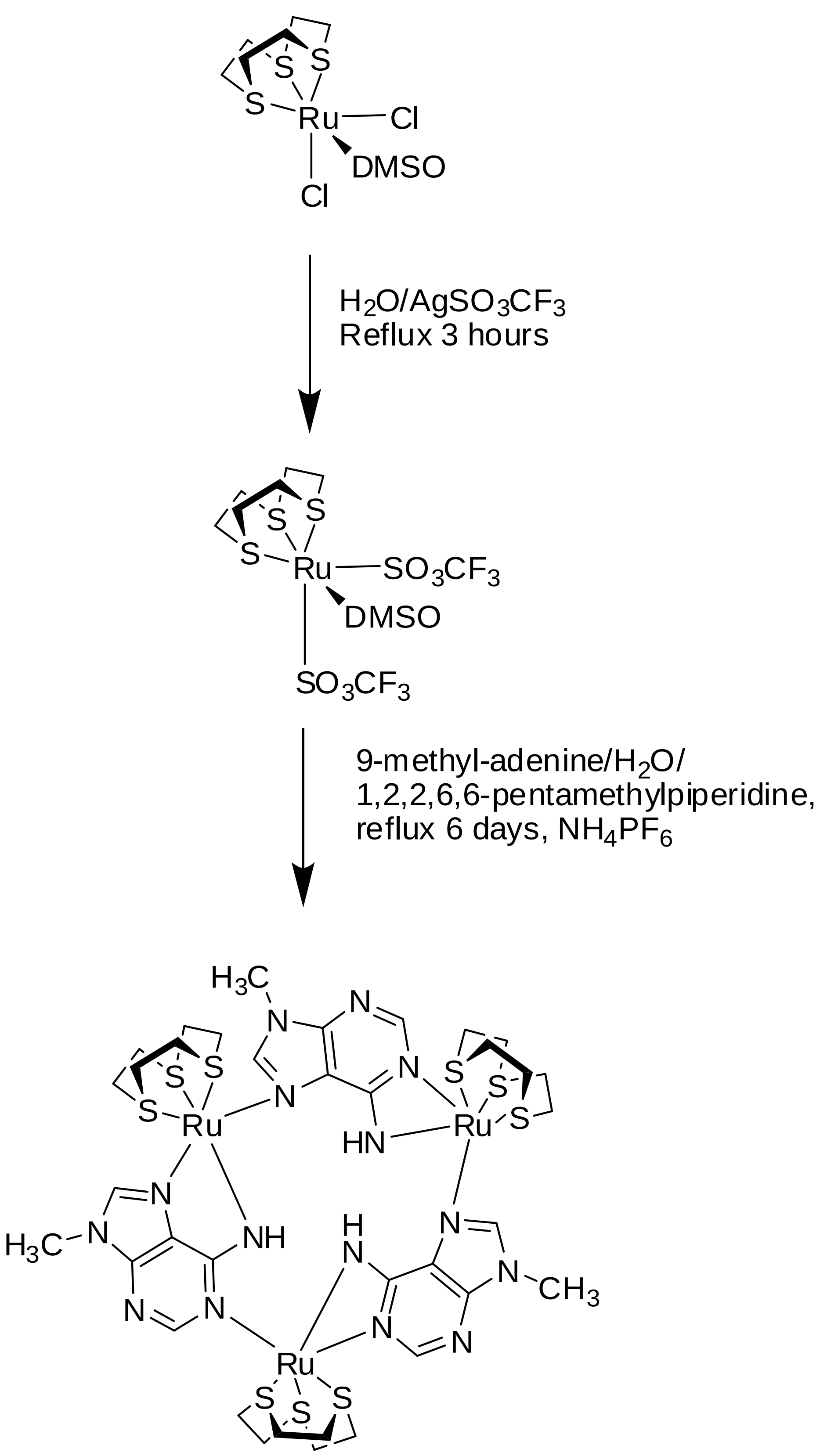

Figure 2.1 scheme of synthesis [Ru([9]aneS_3(9-methyl-adenine)]$_3$[PF_6]$_3$.

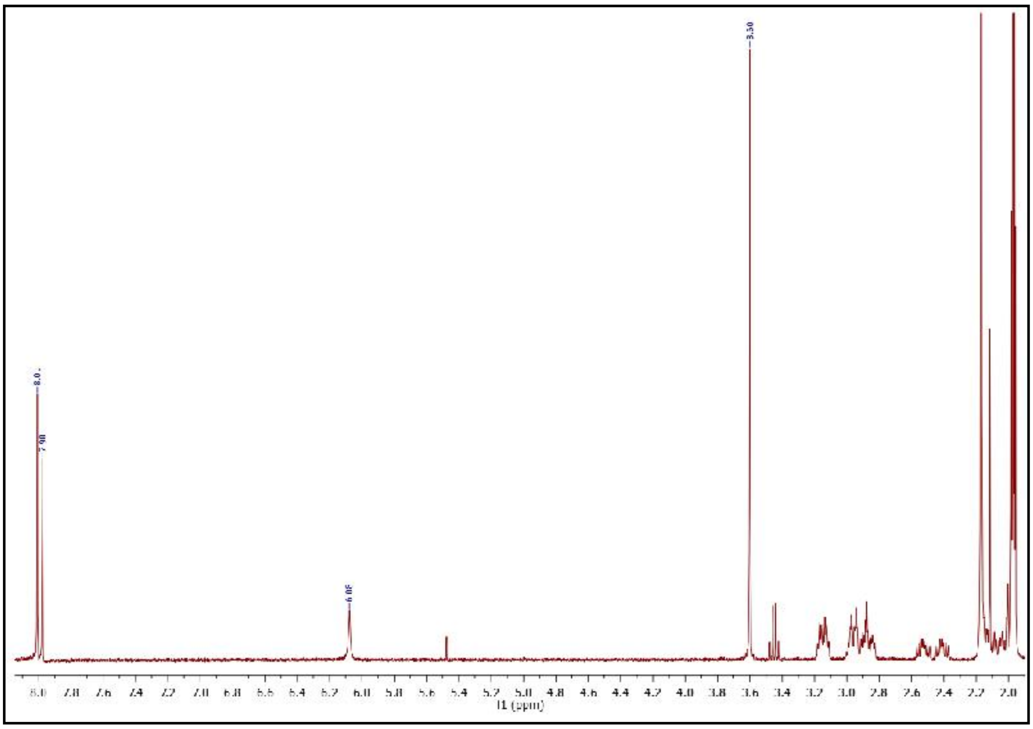

Figure 2.2 ^{1}H NMR of $[Ru([9]aneS_3)(9\text{-methyladenine})]_3^{3+}$ in $CD_3CN\text{-}d_3$.

The numbering scheme employed for 9-methyladenine is shown in Figure 2. 3.

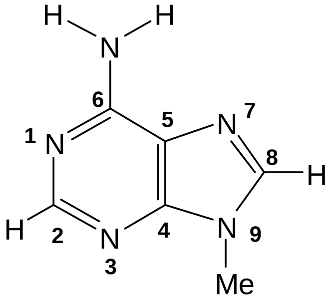

Figure 2.3 Numbering scheme for 9-methyladenine

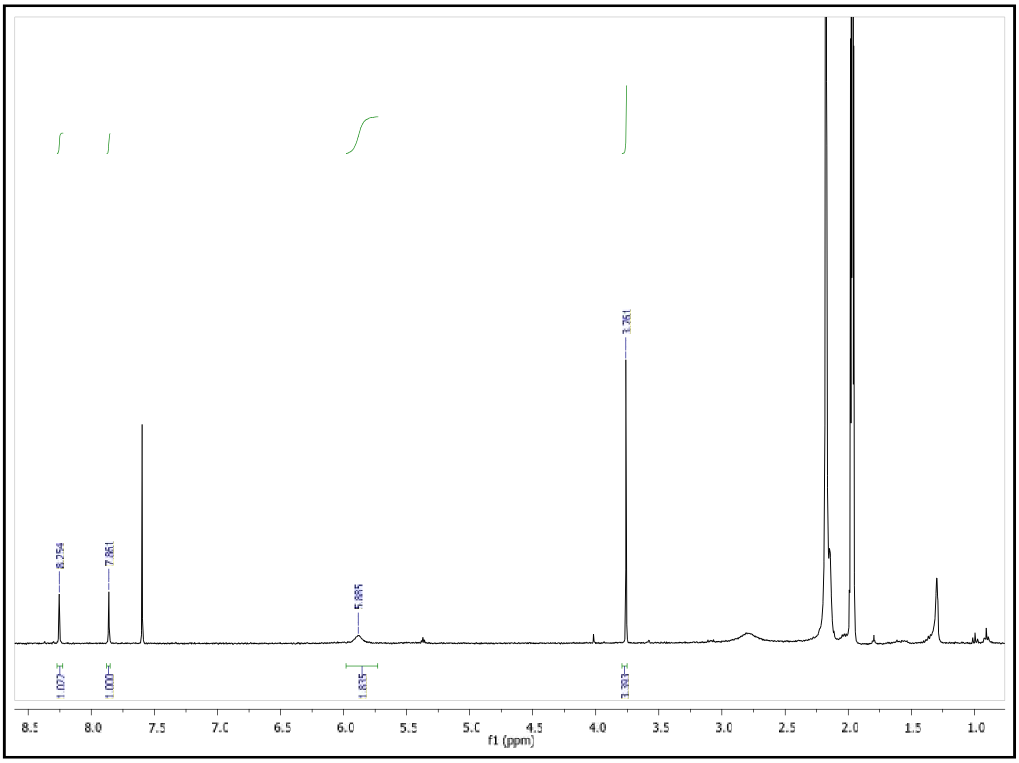

Figure 2.4 ^{1}H NMR of 9-methyladeninein CD_3CN-d_3.

The proton chemical shifts for free 9-methyladenine and complex [Ru([9]aneS_3)(9-methyladenine)]$_3^{3+}$ are given in Table 2.1.

Table 2.1 Proton chemical shift data for unbound 9-methyladenine and complexes [Ru([9]aneS_3)(9-methyladenine)]$_3^{3+}$ in CD_3CN-d_3.

Complex	H2	H8	NH6
9-methyladenine	8.15	8.09	7.21
[Ru([9]aneS_3)(9-methyladenine)]$_3^{3+}$	8.00	7.97	6.07

The complex, [Ru([9]aneS_3)(9-methyladenine)]$_3^{3+}$ shifts for H2 and H8 are observed in comparison to free 9-methyladenine, at 8.15 and 8.09 ppm. The complex displays similar shifts in the signals for H2 and H8. H8 is shifted 0.12 ppm downfield from free 9-methyladenine and H2 is shifted 0.15 ppm upfield in CD_3CN.

The mass spectrum adds support to the structure [Ru([9]aneS_3)(9-methyladenine)]$_3^{3+}$. The complex [Ru([9]aneS_3)(9-methyladenine)]$_3^{3+}$ was analysed as a CF_3SO_3 salt using Electrospray Ionisation Mass Spectrometry (ESI MS). Peaks attributable to [M-2OTf]$^{+/2}$ (m/z 719) and [M – 2OTf – [9]aneS_3]+/2 (m/z 629) were observed. The former and the latter were isotopically resolved and agree very well with the theoretical distribution.

2.2 Reaction of [Ru([9]aneS_3)(DMSO)Cl_2] with 9-ethyladenine.

Using the same procedure used for the previously reported supramolecular compounds, [Ru([9]aneS_3)(DMSO)Cl_2] was reacted with one equivalent of 9-ethyladenine in water to give [Ru([9]aneS_3)(9-ethyladenine)]$_3^{3+}$. Addition of excess NH_4PF_6 precipitated the final product which was characterised using ^{1}H NMR, mass spectrometry and elemental analysis. Again, evidence of trimer formation comes from ^{1}H NMR, mass spectrometry and elemental analysis.

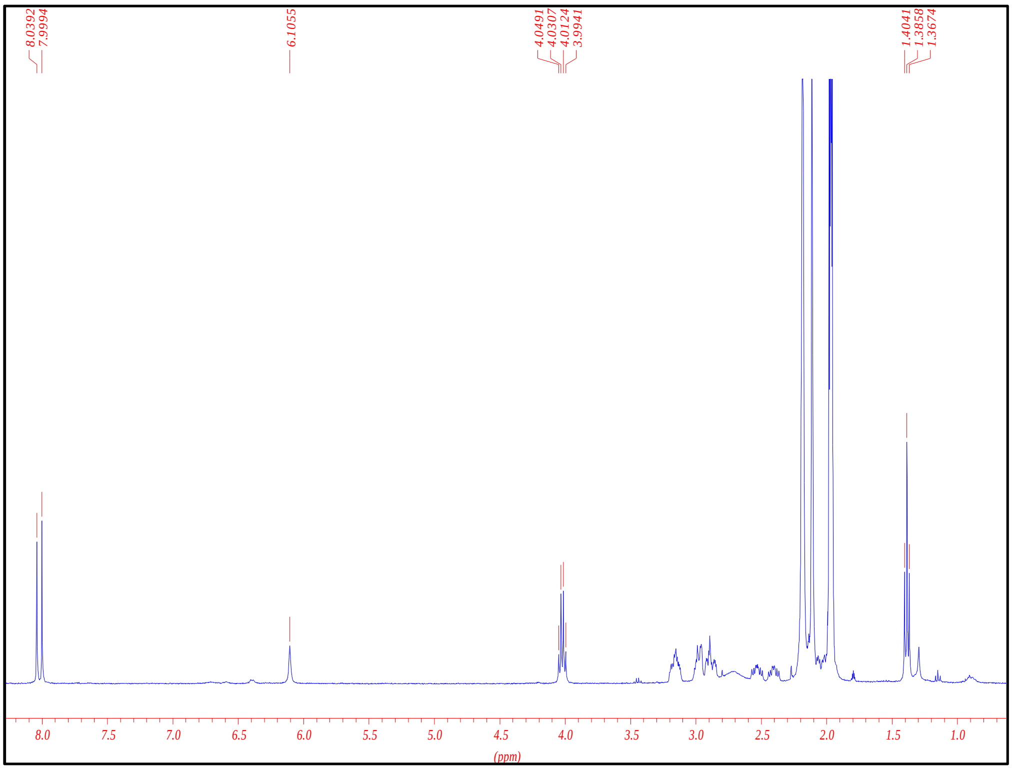

Figure 2. 5 shows the ^{1}H NMR of the macrocycle [Ru([9]aneS_3)(9-ethyladenine)]$_3^{3+}$ in CD_3CN.

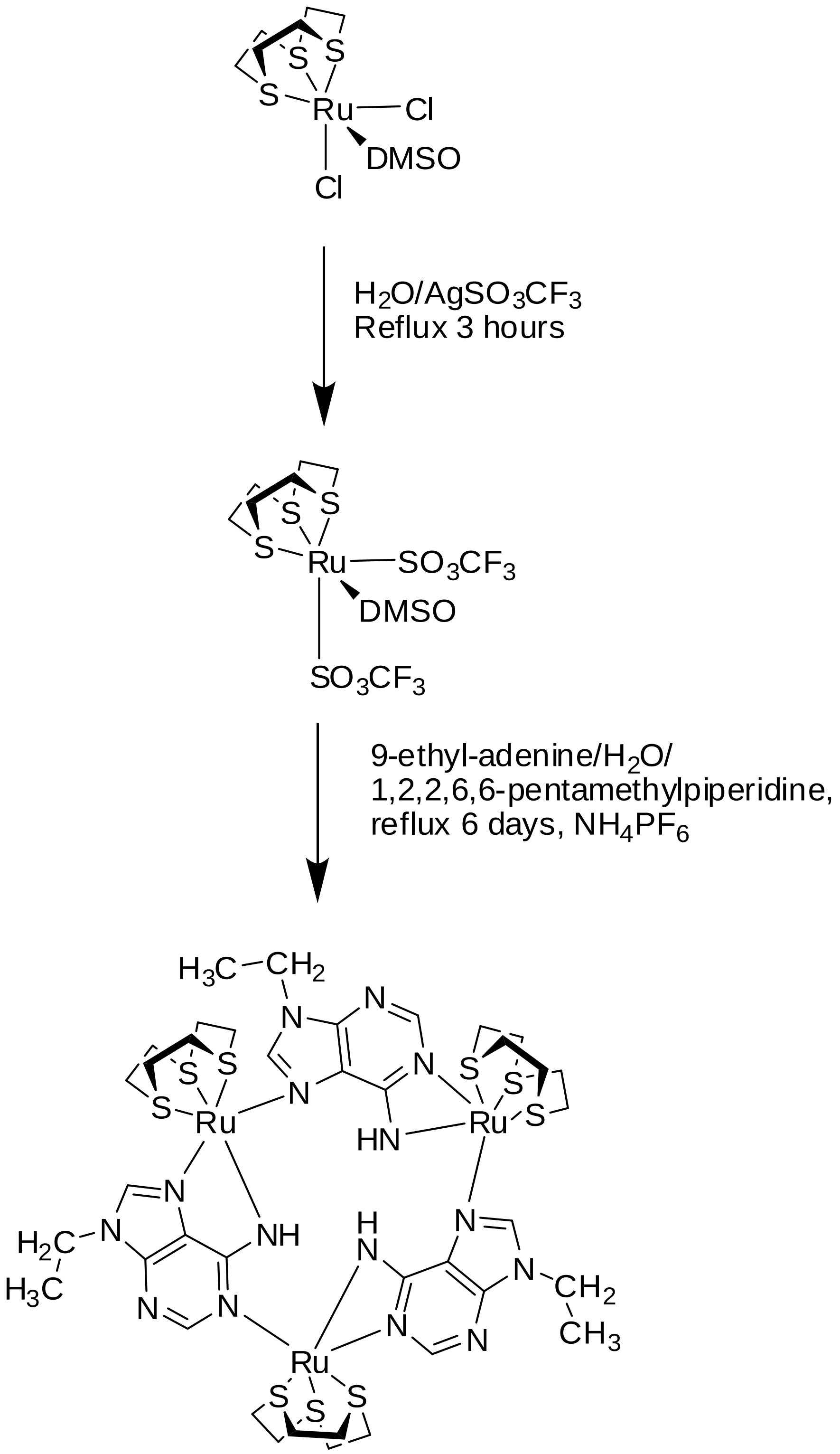

Figure 2.6 scheme of synthesis [Ru([9]aneS_3(9-ethyl-adenine)]$_3$[PF_6]$_3$.

The numbering scheme employed for 9-ethyladenine ligands is shown in Figure 2.7.

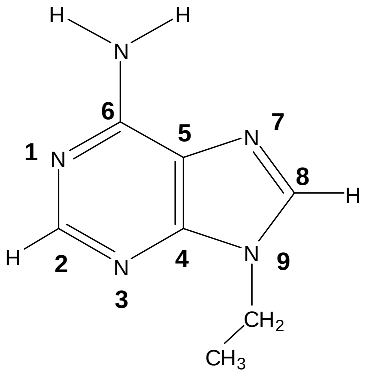

Figure 2.7 Numbering scheme for 9-ethyladenine.

The proton chemical shifts for free 9-ethyladenine and complex[Ru([9]aneS$_3$)(9-ethyladenine)]$_3^{3+}$ are given in Table 2.2.

Table 2.2 Proton chemical shift data for unbound 9-ethyladenine and complexes [Ru([9]aneS3)(9-ethyladenine)]$_3^{3+}$ in CD$_3$CN-d$_3$.

Complex	H2	H8	NH6
9-ethyladenine	8.24	7.92	6.00
[Ru([9]aneS$_3$)(9-ethyladenine)]$_3^{3+}$	8.04	8.00	6.09

Table 2.2 compares the proton chemical shift data for free 9-ethyladenine with complex [Ru([9]aneS$_3$)(9-ethyladenine)]$_3^{3+}$. The complex, [Ru([9]aneS$_3$)(9-ethyladenine)]$_3^{3+}$ shifts for H2 and H8 are observed in comparison to free 9-ethyladenine, at 8.24 and 7.92 ppm. Complex displays similar shifts in the signals for H2 and H8. H8 is shifted .08 ppm downfield from free 9-ethyladenine and H2 is shifted 0.20 ppm upfield in CD$_3$CN.

The mass spectrum adds support to structure [Ru([9]aneS$_3$)(9-ethyladenine)]$_3^{3+}$. Complex [Ru([9]aneS$_3$)(9-ethyladenine)]$_3^{3+}$ was analysed as a CF$_3$SO$_3$ salt using Electrospray Ionisation Mass Spectrometry (ESI MS). Peaks attributable to [M-

2OTf]+/2 (m/z 740.2) were observed. The former and the latter were isotopically resolved and agree very well with the theoretical distribution. See Figure 2.5.

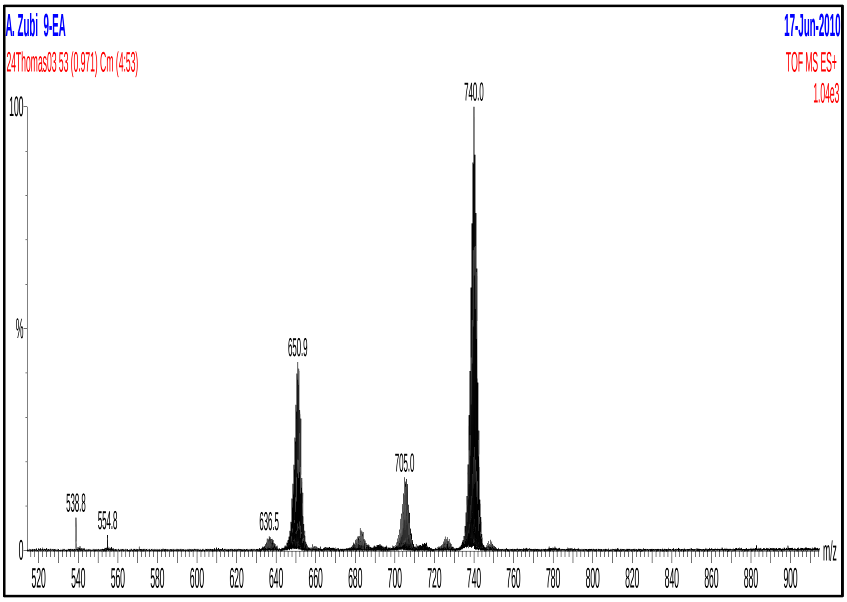

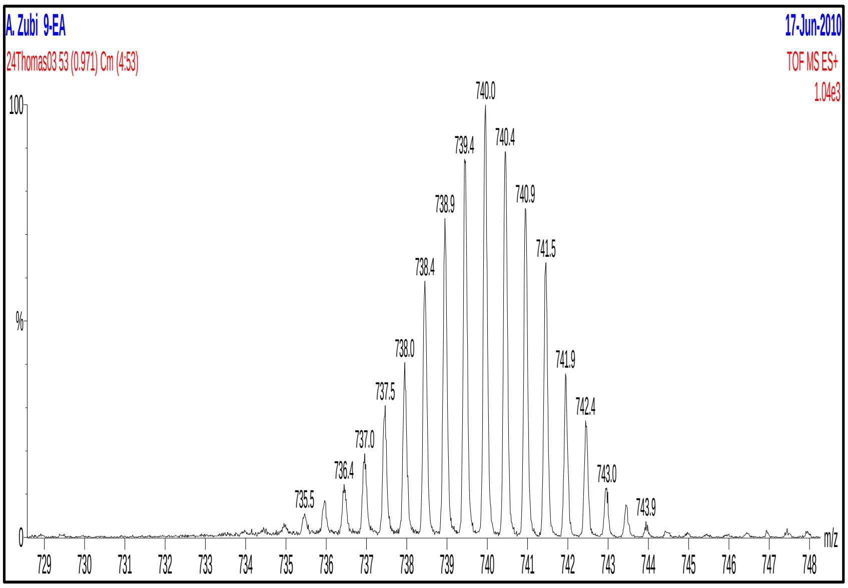

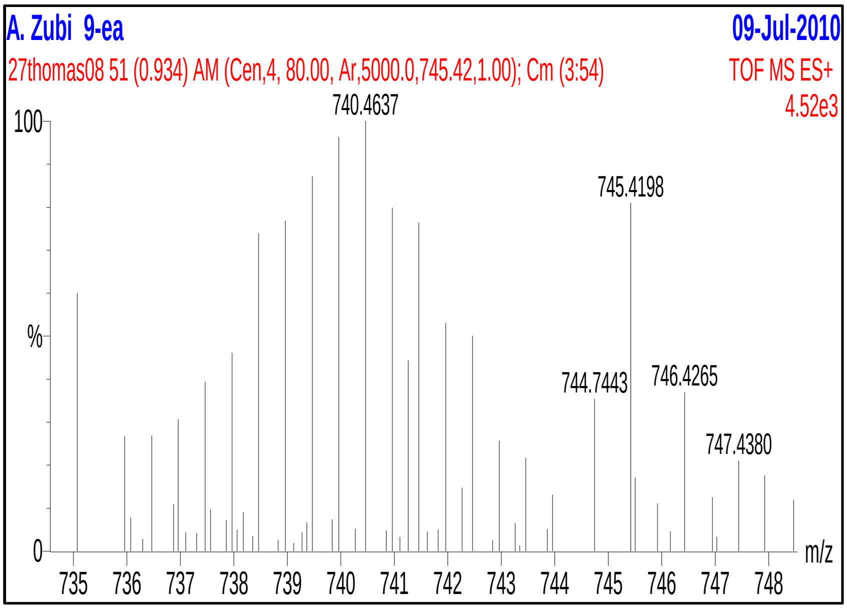

Figure 2.8 Mass of ([M^{++} - (CF$_3$SO$_3$)] (m/z 1479.867)). Mass (740.4637).

2.3 Reaction of [Ru([9]aneS_3)(DMSO)Cl_2] with 9-(4-methoxybenzyl)-purin-6-amine.

Again this macrocycle was isolated using the same procedure that was used for previous supramolecular compounds: [Ru([9]aneS_3)(DMSO)Cl_2] was reacted with one equivalent of 9-(4-methoxybenzyl)-purin-6-amine in water to give $[Ru([9]aneS_3)(9\text{-}(4\text{-methoxybenzyl})\text{-purin-6-amine})]_3^{3+}$. Addition of excess NH_4PF_6 precipitated the final product which was characterized using ^{1}H NMR, mass spectrometry and elemental analysis. Evidence of trimer formation comes from ^{1}H NMR, mass spectrometry and elemental analysis. Figure 2.9 shows the ^{1}H NMR of in CD_3CN.

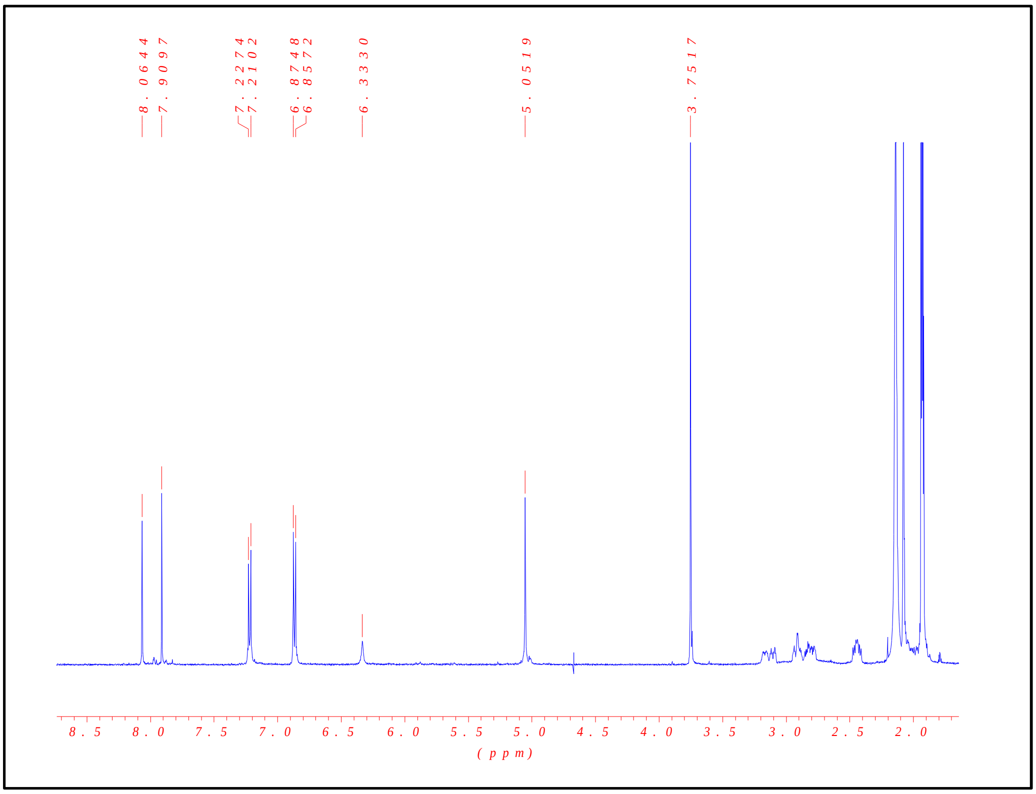

Figure 2. 9 shows the ^{1}H NMR of the macrocycle [Ru([9]aneS_3)(9-(4-methoxybenzyl)- purin-6-amine)]$_3^{3+}$ in CD_3CN.

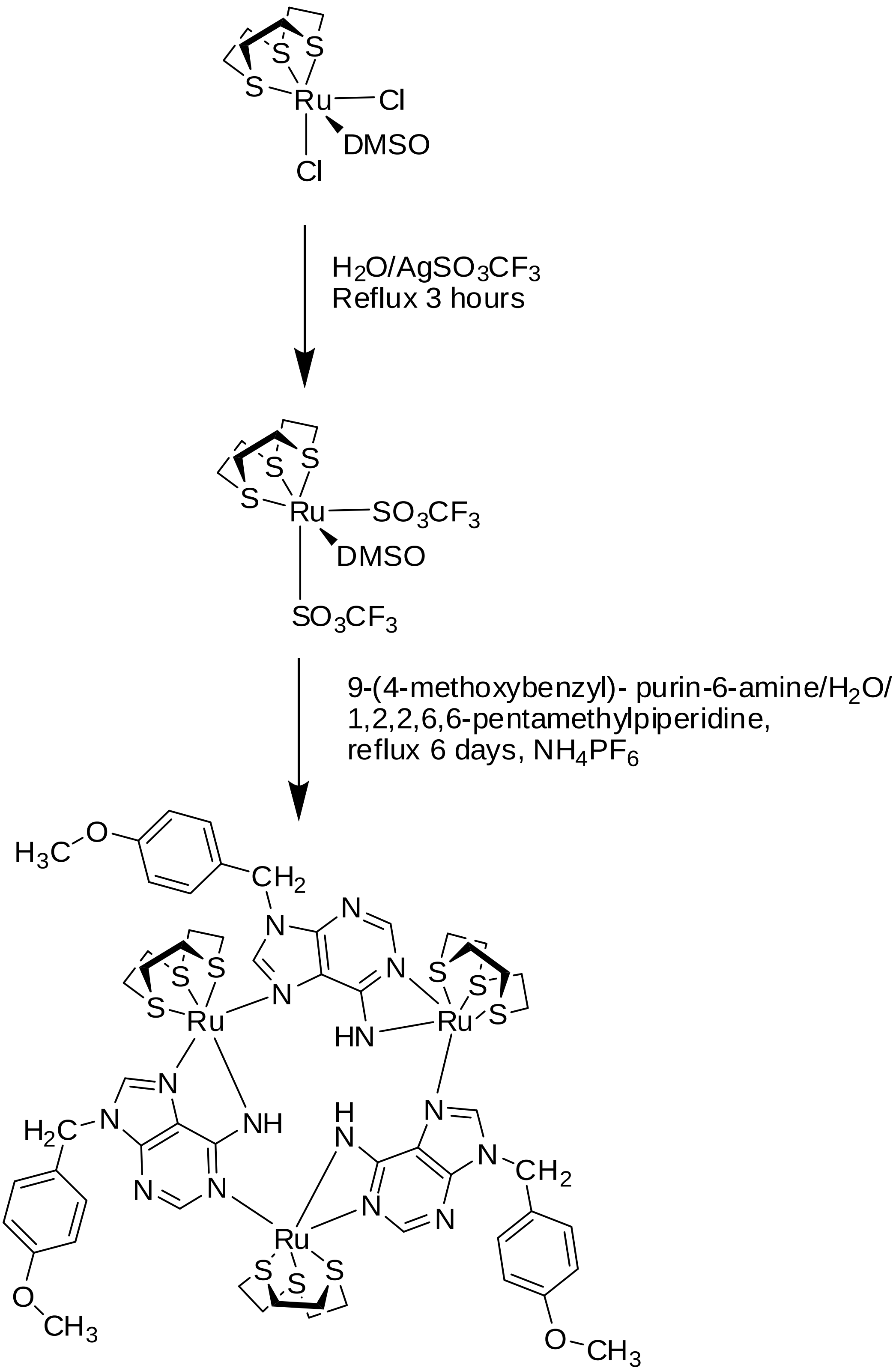

Figure 2.10 scheme of synthesis [Ru([9]aneS_3(9-(4-methoxybenzyl)- purin-6-amine)]$_3$[PF_6]$_3$.

The numbering scheme employed for 9-(4-methoxybenzyl)- purin-6-amine is shown in Figure 2. 11.

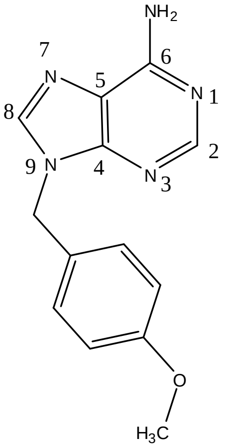

Figure 2.11 Numbering scheme for 9-(4-methoxybenzyl)- purin-6-amine

The proton chemical shifts for free 9-(4-methoxybenzyl)- purin-6-amine and complex [Ru([9]aneS_3)(9-(4-methoxybenzyl)-purin-6-amine)]$_3^{3+}$ are given in Table 2.3.

Table 2.3 Proton chemical shift data for unbound 9-(4-methoxybenzyl)- purin-6-amine and complexes [Ru([9]aneS_3)(9-(4-methoxybenzyl)- purin-6-amine)]$_3^{3+}$

Complex	H2	H8	NH6
[Ru([9]aneS_3)(9-(4-methoxybenzyl)- purin-6-amine)]$_3^{3+}$	8.06	7.94	5.94
9-(4-methoxybenzyl)- purin-6-amine	8.25	7.91	6.33

The complex, [Ru([9]aneS_3)(9-(4-methoxybenzyl)- purin-6-amine)]$_3^{3+}$ shifts for H2 and H8 are observed in comparison to free 9-(4-methoxybenzyl)- purin-6-amine, at 8.25 and 7.94 ppm. H8 is shifted .03 ppm upfield from free 9-(4-methoxybenzyl)-purin-6-amineand H2 is shifted 0.19 ppm upfield in CD_3CN.

The mass spectrum adds support to structure [Ru([9]aneS_3)(9-(4-methoxybenzyl)-purin-6-amine)]$_3^{3+}$. Complex [Ru([9]aneS_3)(9-(4-methoxybenzyl)- purin-6-amine)]$_3^{3+}$ was analysed as a CF_3SO_3 salt using Electrospray Ionisation Mass Spectrometry (ESI MS). Peaks attributable to [M-2OTf]$^{++/2}$ (m/z 878.5) and [M –

2OTf – [9]aneS_3]+/2 (m/z 1905) were observed. The former and the latter were isotopically resolved and agree with the theoretical distribution. See figure 2.12.

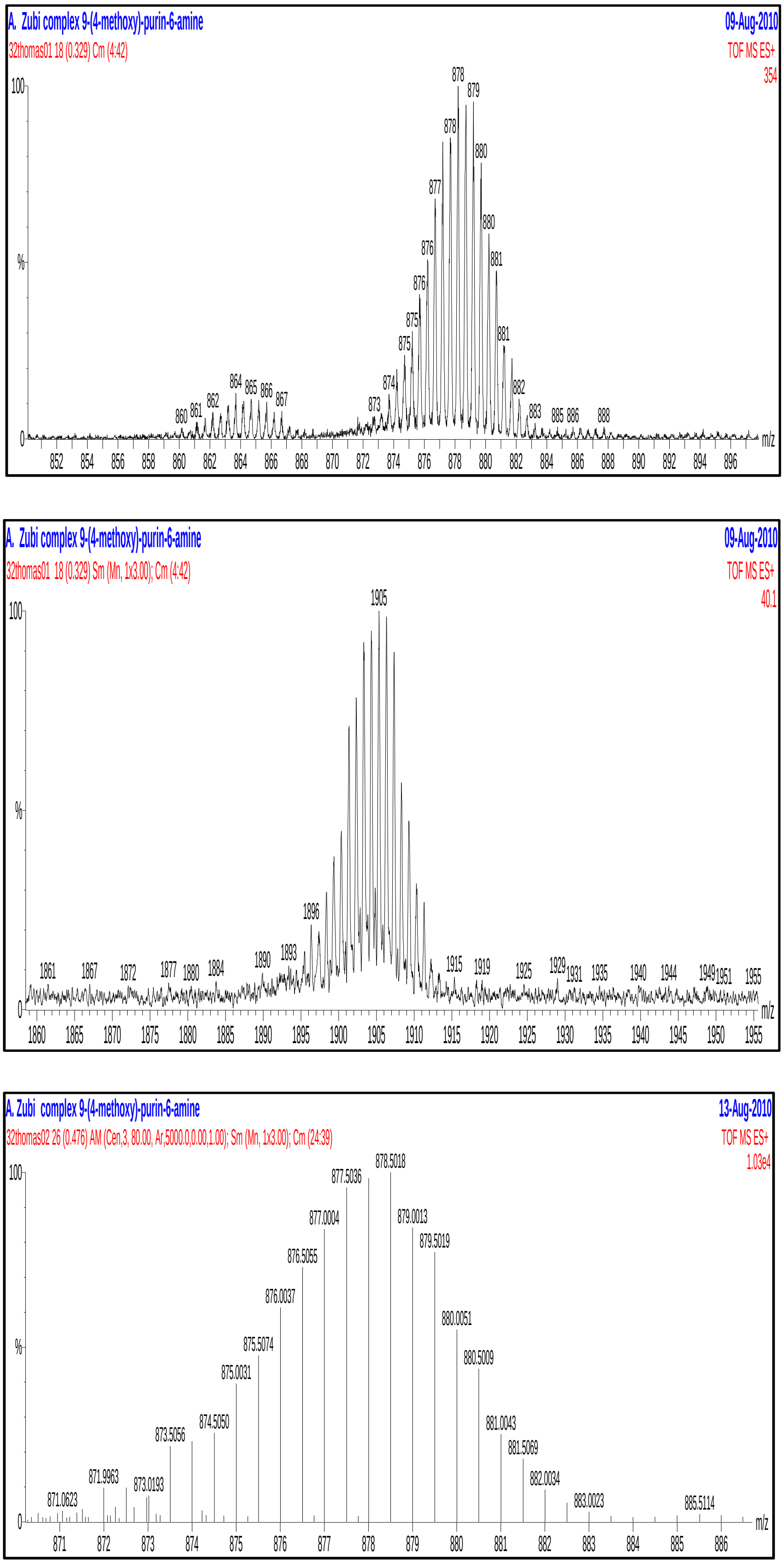

Figure 2.12 Mass of to [M – 2OTf – [9]aneS_3]$^{+/2}$ (m/z 1905) and [M-2OTf]$^{++/2}$ (m/z 878.5) and). Formula: $C_{58}H_{72}N_{15}S_{10}O_6Ru_3F_3/2$. i.e.2+ ion

2.4 Reaction of [Ru([9]aneS_3)(DMSO)Cl_2] with 6-mercaptopurine.

Again this macrocycle was isolated using the same procedure that was used for previous supramolecular compounds: [Ru([9]aneS_3)(DMSO)Cl_2] was reacted with one equivalent of 6-mercaptopurine in water to give [Ru([9]aneS_3)(6-mercaptopurine)]$_4^{4+}$. Addition of excess NH_4PF_6 precipitated the final product which was characterised using ^{1}H NMR, mass spectrometry and elemental analysis. Evidence of trimer formation comes from ^{1}H NMR and mass spectrometry. Figure 2.13 shows the ^{1}H NMR of in DMSO.

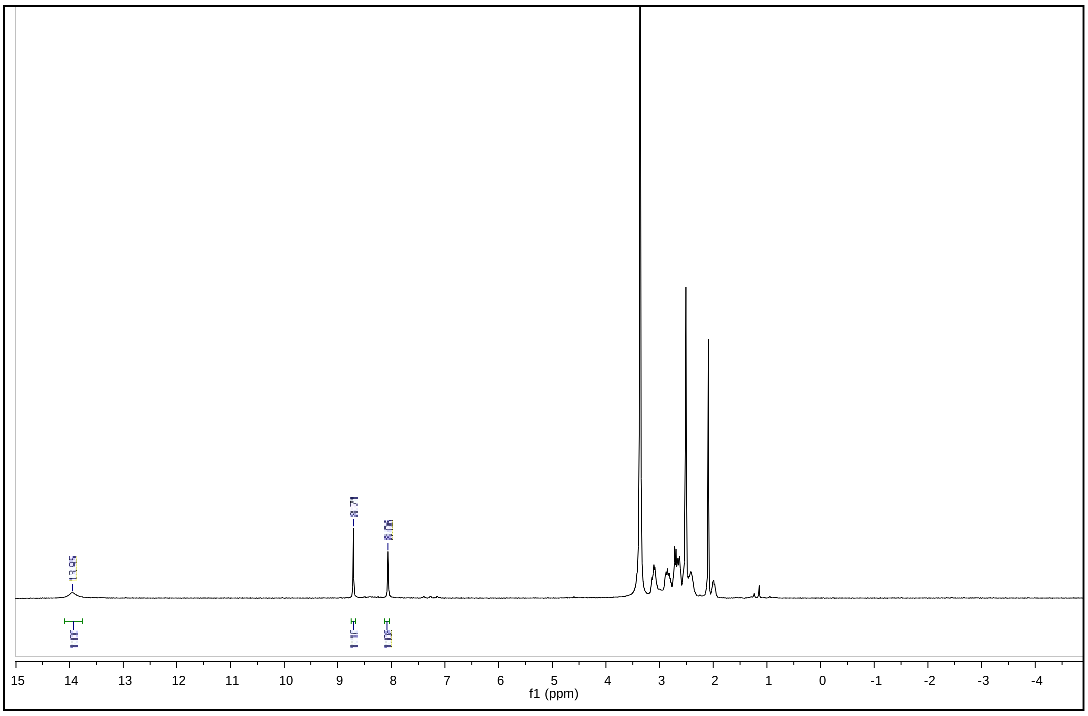

Figure 2.13 ^{1}H NMR of [Ru([9]aneS_3)(6-mercaptopurine)]$_4^{4+}$. DMSOd_6.

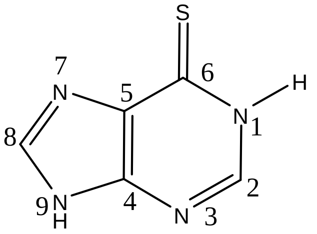

Figure 2.14 Numbering scheme for 6-mercaptopurine.

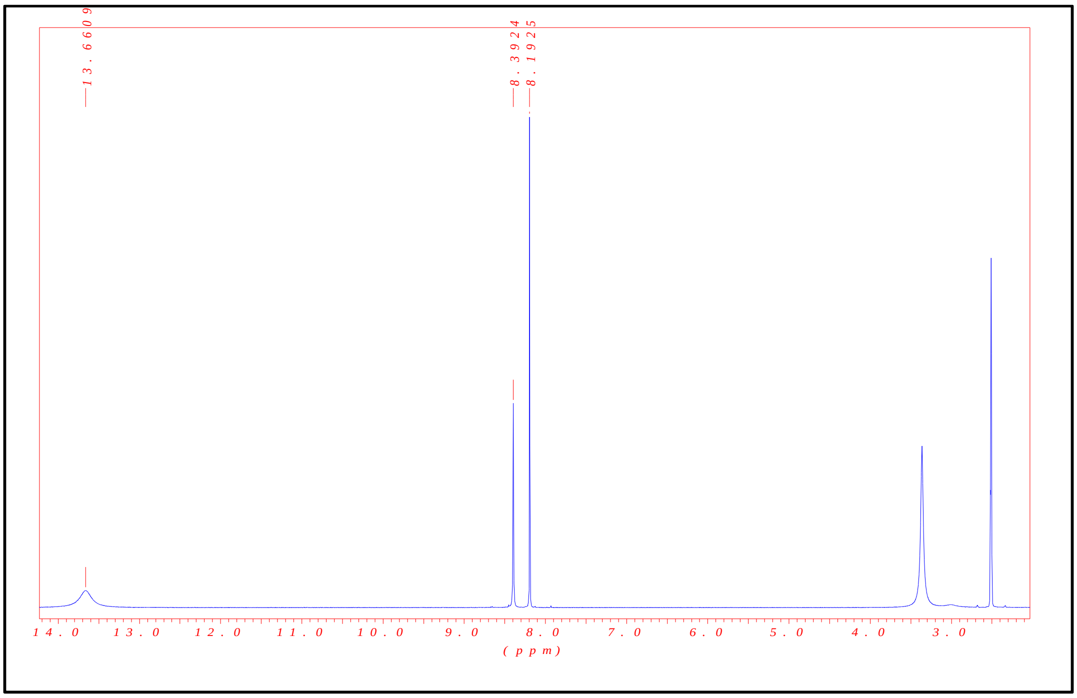

Figure 2.15 shows the ^{1}H NMR of in DMSO for 6-mercaptopurine.

The proton chemical shifts for free 6-mercaptopurine and complex [Ru([9]aneS$_3$)(6-mercaptopurine)]$_4^{3+}$ are given in Table 2.4.

Table 2.4 Proton chemical shift data for unbound 6-mercaptopurine.

Complex	H1,H9	H2	H8
6-mercaptopurine	13.66	8.39	8.19
[Ru([9]aneS$_3$)(6-mercaptopurine)]$_4^{4+}$	13.95	8.70	8.06

The complex, [Ru([9]aneS3)(6-mercaptopurine)]$_4^{4+}$ shifts for H1,H9 ,H8 andH2 are observed in comparison to free 6-mercaptopurine, at 13.66 , 8.39 and 8.19 ppm. H1 and H9 are shifted 0.29 ppm lowfield from free 6-mercaptopurine, H2 is shifted 0.31 ppm lowfield and H8 is shifted 0.13 ppm upfield in DMSO. A comparison of intergrates for 5^{4+} the free ligand confirms the deprotonation of H1 of mercaptopurine in the complex.

The mass spectrum adds support to structure [Ru([9]aneS$_3$)(6-mercaptopurine)]$_4^{4+}$.

Complex [Ru([9]aneS$_3$)(6-mercaptopurine)]$_4^{4+}$ was analysed as a CF$_3$SO$_3$ and PF$_6$ salt using Electrospray Ionisation Mass Spectrometry (ESI MS). Peaks attributable to MS (FAB): M/z (%)=1010.8 (90) [M^{++}- 2CF$_3$SO$_3$] were observed. The former and the latter were isotopically resolved and agree very well with the theoretical distribution. See Figure (2. 16).

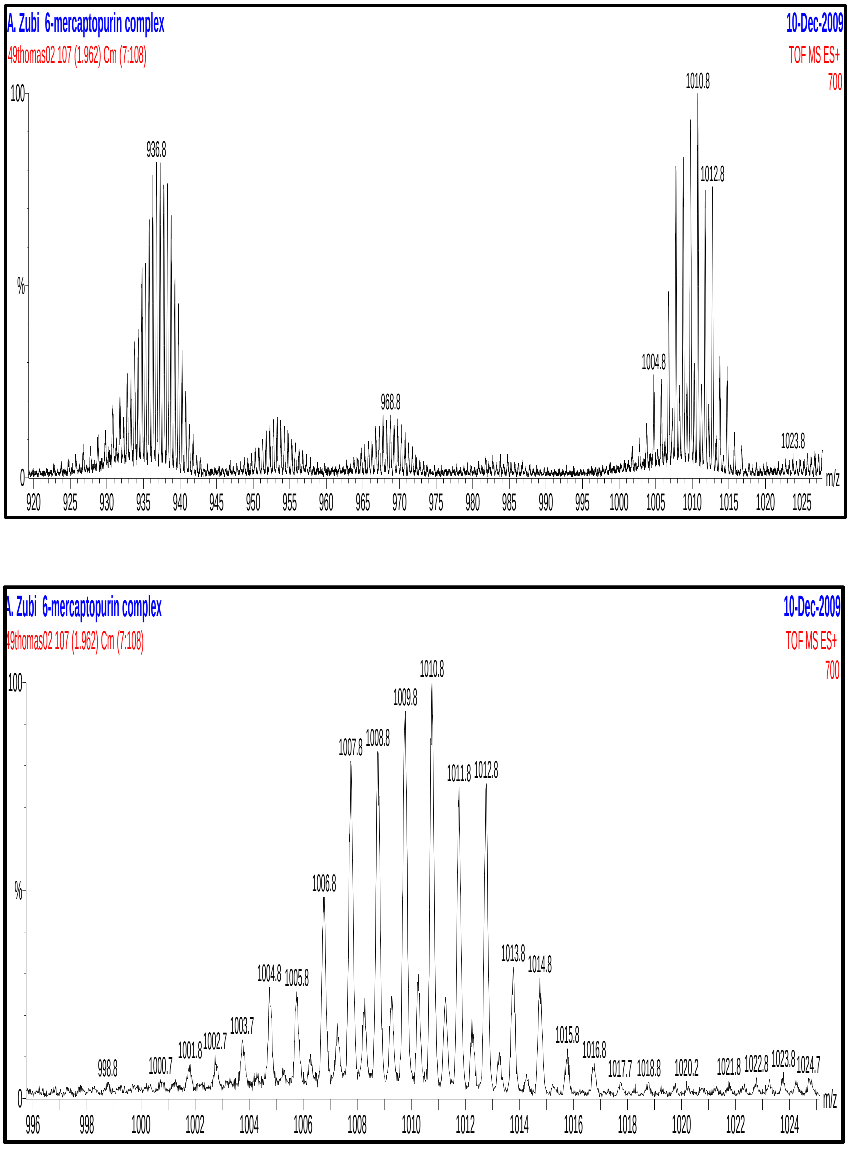

Figure 2.16 Peaks attributable to MS (FAB): M/z (%)=1010.8 (100) [M^{++} - 2CF$_3$SO$_3$] were observed.

2.6 Reaction of [Ru([9]aneS_3)(DMSO)Cl_2] with 9-benzyl-9H-purin-6-amine.

Again this macrocycle was isolated using the same procedure that was used for previous supramolecular compounds: [Ru([9]aneS_3)(DMSO)Cl_2] was reacted with one equivalent of 9-benzyl-9H-purin-6-amine in water to give [Ru([9]aneS_3)(9-benzyl-9H-purin-6-amine))]$_3^{3+}$. Addition of excess NH_4PF_6 precipitated the final product which was characterised using ^{1}H NMR, mass spectrometry and elemental analysis. Evidence of trimer formation comes from ^{1}H NMR and mass spectrometry.

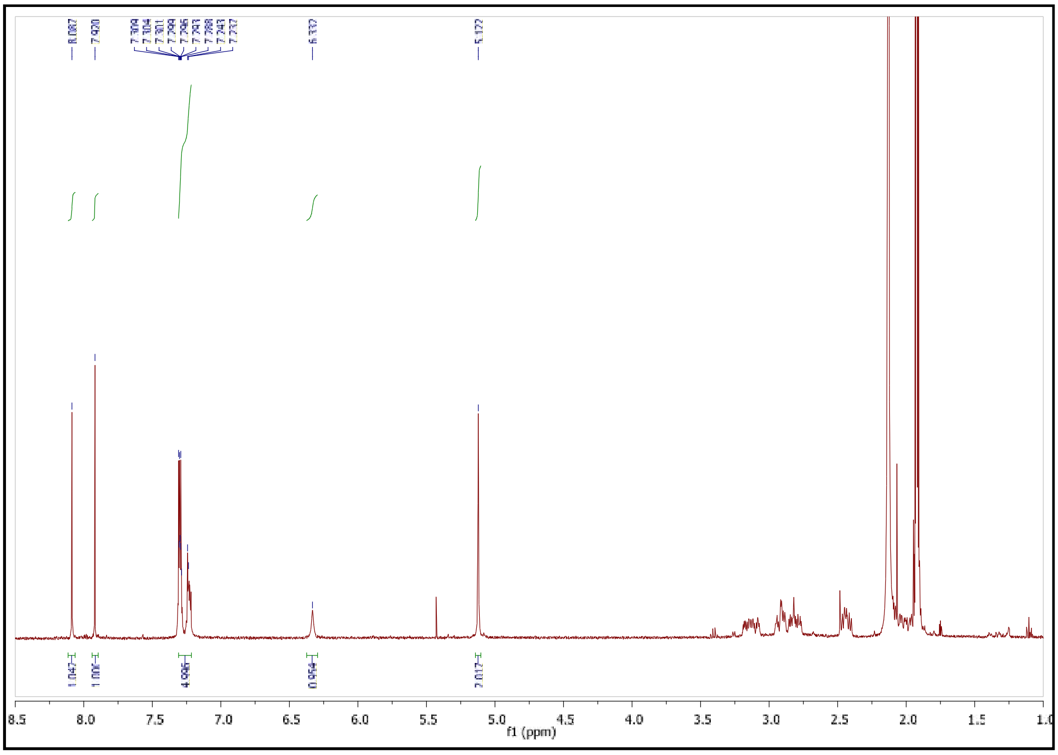

Figure 2.1 ^{1}H NMR of [Ru([9]aneS_3)(9-benzyl-9H-purin-6-amine)]$_3^{3+}$ in CD_3CN.

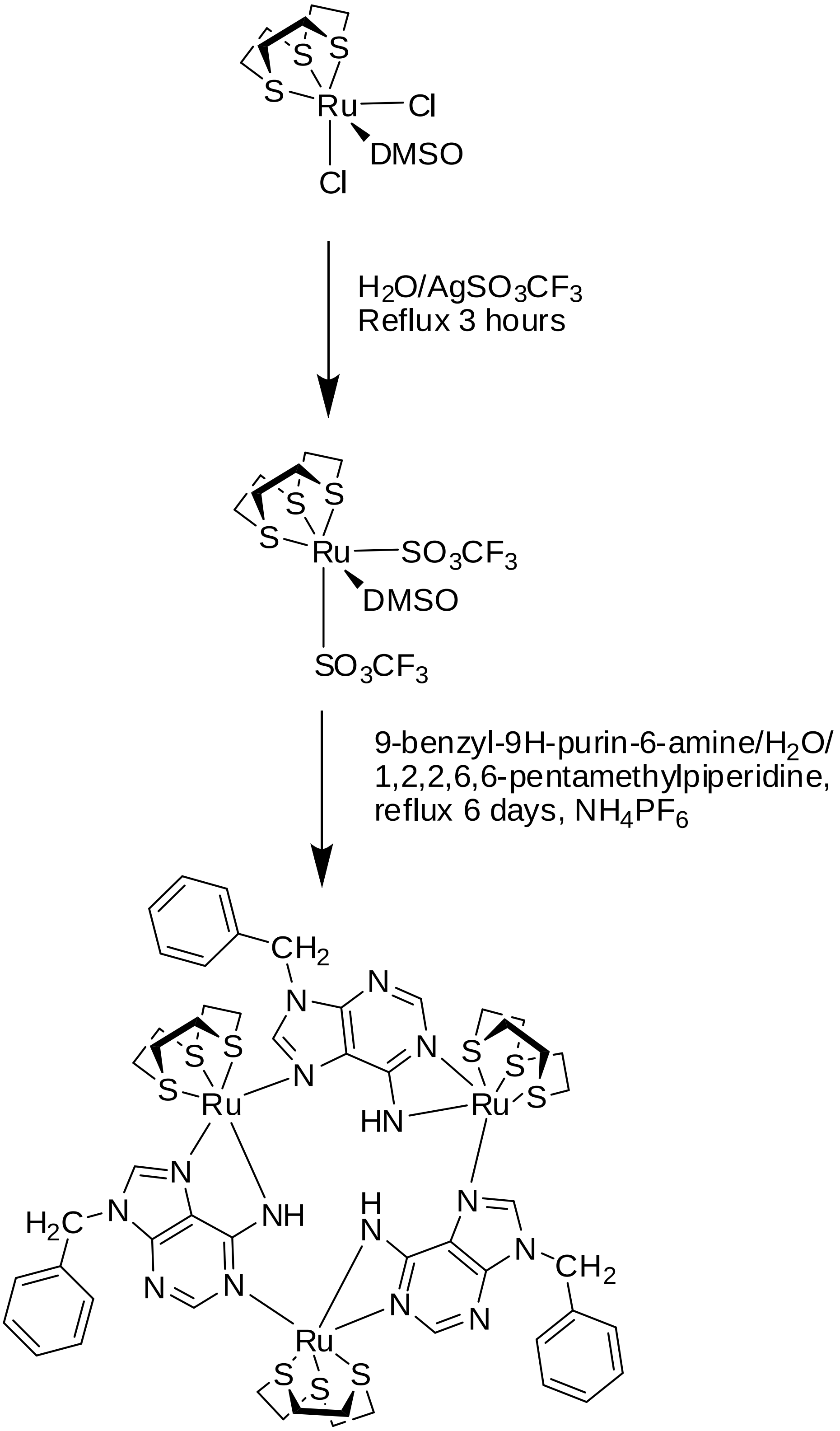

Figure 2.18 scheme of synthesis [Ru([9]aneS_3(9-(9-benzyl-9H-purin-6-amine)]$_3$[PF_6]$_3$.

The numbering scheme employed for 9-benzyl-9H-purin-6-amine is shown in Figure 2.19.

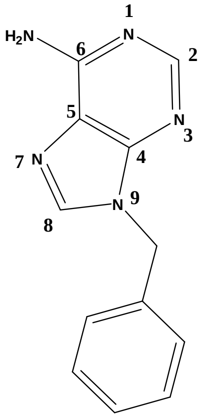

Figure 2.19 Numbering scheme for 9-benzyl-9H-purin-6-amine.

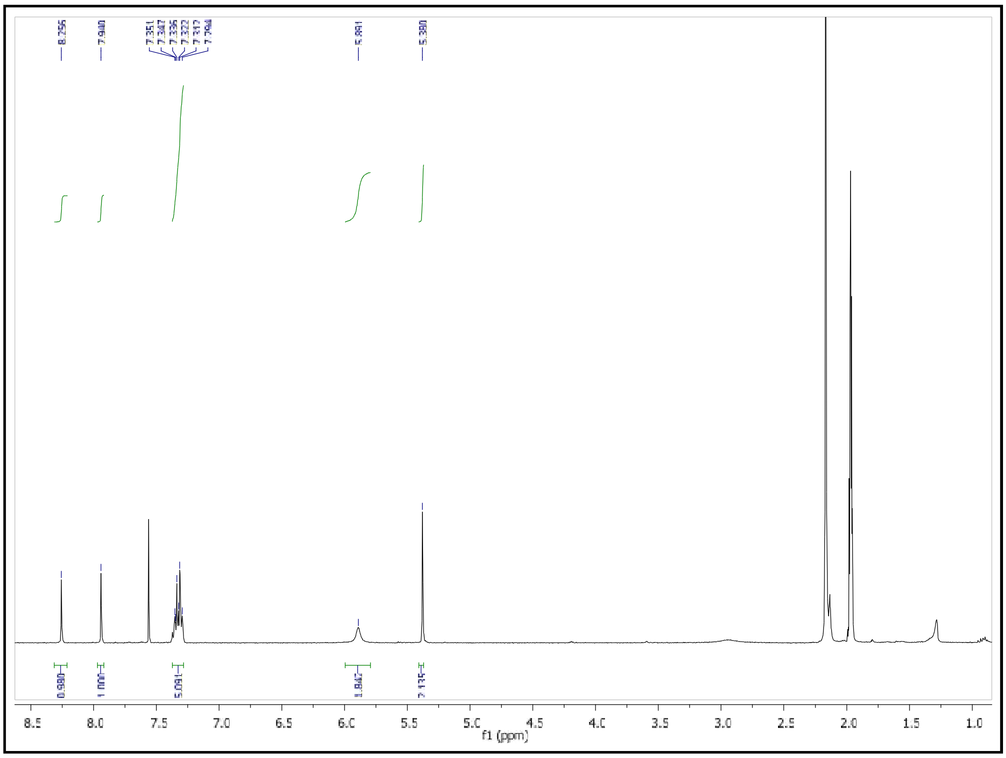

Figure 2.20 Shows the ^{1}H NMR of in CD_3CN for 9-benzyl-9H-purin-6-amine.

The proton chemical shifts for free for 9-benzyl-9H-purin-6-amine and complex [Ru([9]aneS_3)(for 9-benzyl-9H-purin-6-amine)]$_3^{3+}$ are given in table 2.5.

Table 2.5 Proton chemical shift data for 9-benzyl-9H-purin-6-amine unbound and complex [Ru([9]aneS_3)(9-benzyl-9H-purin-6-amine)]$_3^{3+}$ in CD_3CN.

Complex	H2	H8	NH6
9-benzyl-9H-purin-6-amine	8.26	7.94	5.89
[Ru([9]aneS_3)(9-benzyl-9H-purin-6-amine)]$_3^{3+}$	8.09	7.92	6.33

The complex, [Ru([9]aneS_3)(9-benzyl-9H-purin-6-amine)]$_3^{3+}$ shifts for H2 and H8 are observed in comparison to free 9-benzyl-9H-purin-6-amine , at 8.24 and 7.92 ppm. Complex displays similar shifts in the signals for H2 and H8. H8 is shifted .08 ppm downfield from free 9-benzyl-9H-purin-6-amine and H2 is shifted 0.20 ppm upfield in CD_3CN.

The mass spectrum adds support to structure [Ru([9]aneS_3)(9-benzyl-9H-purin-6-amine)]$_3^{3+}$. Complex [Ru([9]aneS_3)(9-benzyl-9H-purin-6-amine)]$_3^{3+}$ was analysed as a CF_3SO_3 salt using Electrospray Ionisation Mass Spectrometry (ESI MS). Peaks attributable to [M-2OTf]+/2 (m/z 833.2) was observed. The former and the latter were isotopically resolved and agree very well with the theoretical distribution. See Figure 2. 21.

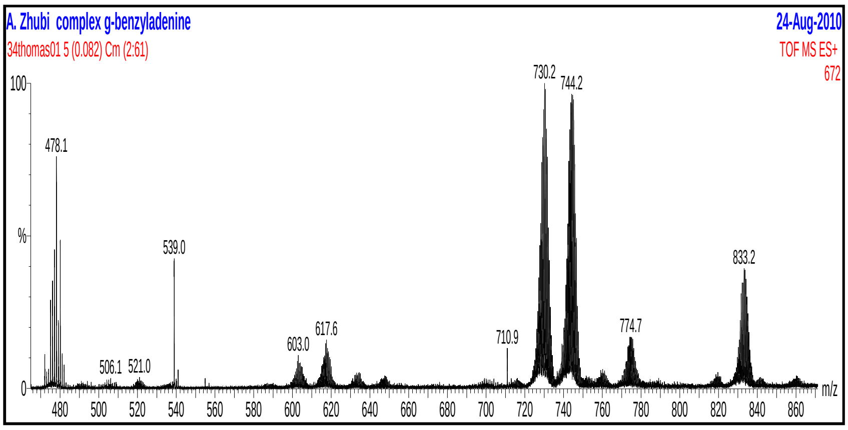

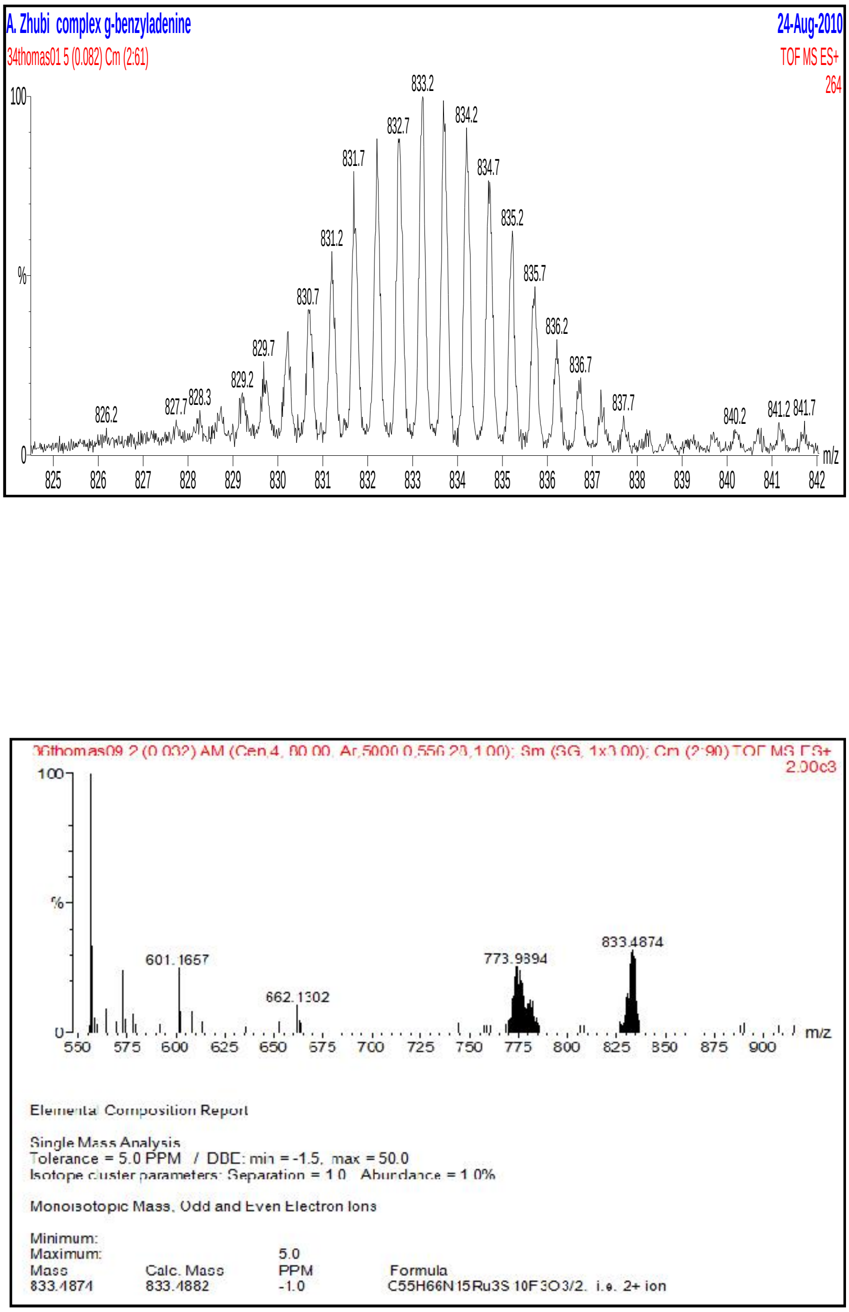

```
Elemental Composition Report

Single Mass Analysis
Tolerance = 5.0 PPM   /  DBE: min = -1.5,  max = 50.0
Isotope cluster parameters: Separation = 1.0   Abundance = 1.0%

Monoisotopic Mass, Odd and Even Electron Ions

Minimum:
Maximum:                            5.0
Mass          Calc. Mass            PPM          Formula
833.4874      833.4882              -1.0         C55H66N15Ru3S10F3O3/2.  i.e. 2+ ion
```

Figure 2. 21 Mass of to [M – 2OTf – [9]aneS3]+/2 (m/z 1905) and $[M\text{-}2OTf]^{++/2}$ (m/ 833.2) and). Formula: $C_{55}H_{66}N_{15}S_{10}O_3Ru_3F_{3/2}$. i.e.2+ ion

2.7 Synthesis and Structural Characterization:

2.7.1 General Method of Macrocycle Synthesis

A brief description of the changes in conditions for the synthesis of macrocycles compared to previous work:

When we used the previous method we found that a lot of our compound was lost during recrystallization, which gave a very poor yield. To improve the yield, three changes to the reaction conditions and workup were used. First, the volume of solution was increased from 25cm^3 to 50 cm^3. This helped to avoid the production of a side product (which appeared to be a oligo/polymeric mixture that dissolves in DMSO). Second, the time of the reaction was increased from four days to six days. Third, the crude product mixture was recrystallized from a new solvent system as this led to the collection of the target compound in high purity and good yield. The combination of these three changes improved the yield as well as the purity. High purity and good yield helped us to investigate the binding between macrocycles and guests. Also a series of electrochemistry experiments have been done to probe the effect guests on macrocycles by SWV technique.

2.7.2 Other Attempted Syntheses

Some initial attempts to obtain larger macrocycles bigger than the triangle reported in this thesis were also investigated. What follows is a brief overview of these attempts. Inspired by related studies on Rh^{III}(Cp*) fragments, the synthesis of macrocyclic squares or bigger macrocycles from ruthenium thiacrown fragments [Ru(9-aneS$_3$)Cl$_2$DMSO]Cl were also investigated using 6-mercaptopurine-9-β-D-ribofuranoside and 6-mercaptopurine as ligands. A series of different attempts, using the same thiacrown fragment and ligands but different temperatures and changing the reaction time were made. Several different solvents were employed, individually or as a mixture (water, ethanol, methanol and acetonitrile). The results from NMR and mass spectrometry showed that the reaction was not success, as NMR revealed a mixture of products and mass spectrometry indicated that this mixture of compounds had small molecular weights.

2.7.3 X-Ray Crystallography Studies

In a number of cases, newly synthesized ligands and self-assembled macrocycles provided x-ray quality crystals. What follows is a brief description of these structures. Unless otherwise stated, the structures described in this section were solved by Harry Adams in the department's X-ray structure determination service. Full details of the structure, including ORTEP diagrams are included in the supplementary data found in the accompanying CD.

2.7.3.1 Ligand 9-(4-methoxybenzyl)-9H-purin-6-amine

This ligand was synthesized by the reaction of adenine with methoxybenzyl chloride in 57% yield.

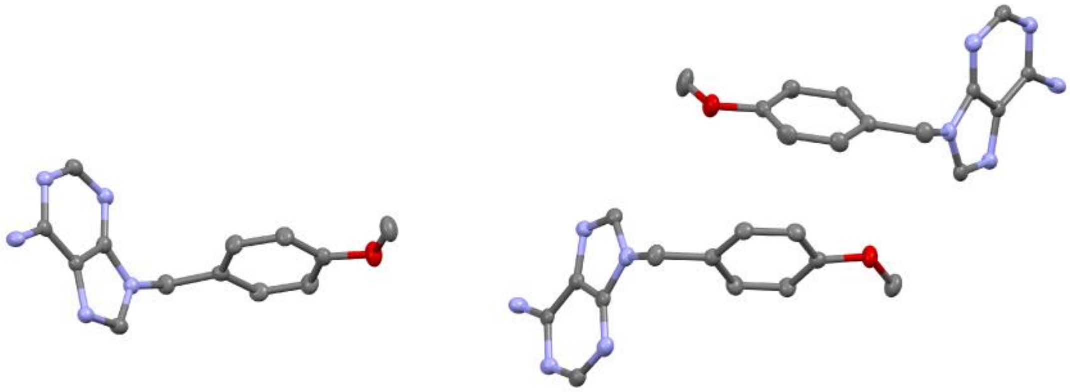

Figure 2.22 Ellipsoid representation of the X-ray crystal structure of 9-(4-methoxybenzyl)-9H-purin-6-amine. Hydrogen atoms omitted for clarity.

Single crystals of 9-(4-methoxybenzyl)-9H-purin-6-amine suitable for X-ray structure analysis were obtained from slow vapour diffusion of mixture acetonitrile and chloroform (1:1) solution. Details of the bond angles and bond lengths are found in the appendix.

As seen from Figure 2.22, the repeat structure is made up of three independent molecules of the ligand, which shows the expected structure with the 4-methoxybenzyl moiety held at an angle to the adenine base by the methylene linker. Figure 2.23 shows how hydrogen-bonding interactions involving dimeric “strands” of adenines lead to the formation of “ribbon” structures.

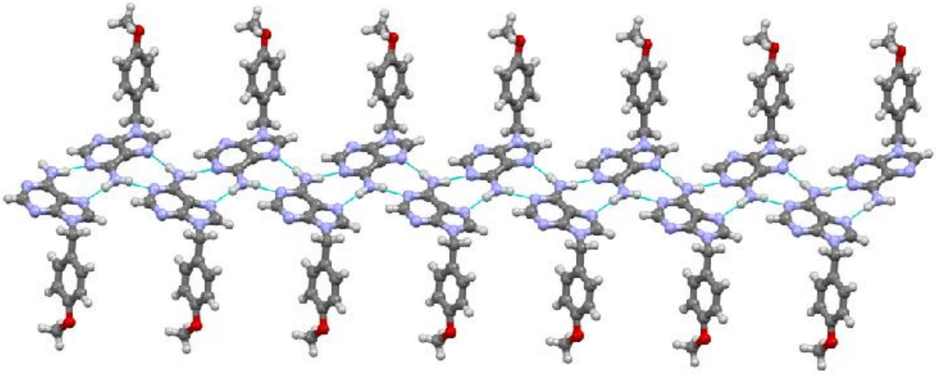

Figure 2.23 Details of the packing of 9-(4-methoxybenzyl)-9H-purin-6-amine showing hydrogen-bonding between individual “strands”.

2.7.3.2 Ligand 9-benzyl-9H-purin-6-amine

This ligand was synthesized by the reaction of adenine with benzyl chloride in 59% yield. Again, single crystals of 9-benzyl-9H-purin-6-amin suitable for X-ray structure analysis were obtained from slow vapour diffusion of mixture acetonitrile and chloroform (1:1). Details of the bond angles and bond lengths are found in the appendix.

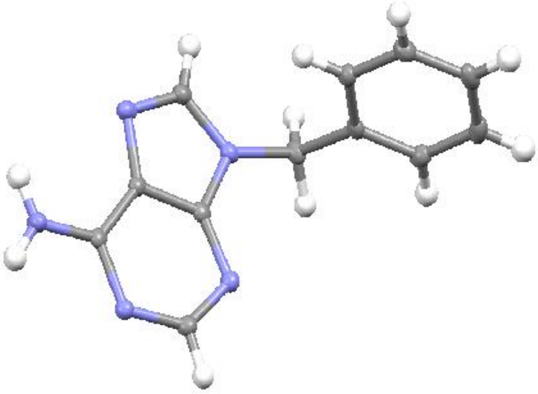

Figure 2.24 Ellipsoid diagram of structure of 9-benzyl-9H-purin-6-amine.

The data also confirms the postulated structure of the ligand. Interestingly, the packing of this ligand is quite different to the methoxybenzyl derivative as it is made of the discrete dimers shown Figure 2.25.

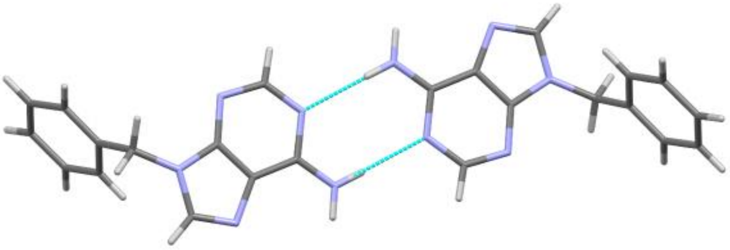

Figure 2.25 Dimer found in the structure of the 9-benzyl-9H-purin-6-amine.

2.7.3.3 [Ru([9]aneS$_3$)(9-methyl-9H-purin-6-amine)]$_3$(PF$_6$)$_3$[1](PF$_6$)$_3$

This supramolecular was synthesized by the reaction of 9-methyl-9H-purin-6-amine with [Ru([9]aneS$_3$)(DMSO)Cl$_2$] in 39% yield. Single crystals of [1](PF$_6$)$_3$ of suitable for an X-ray structure analysis were obtained from slow vapour diffusion in acetonitrile. Details of the bond angles and bond lengths are found in the appendix.

The crystal structure of [**1**](PF$_6$)$_3$ is shown in Figure 2.26, and for the first time this allows us to confirm the detailed structure of the macrocycle.

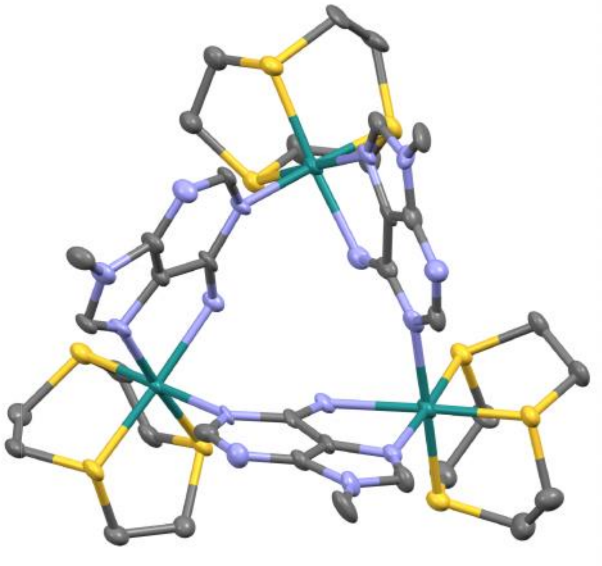

Figure 2. 26 Ellipsoid diagram of the cation in the X-ray crystal structure of the [**1**](PF$_6$)$_3$, hydrogen atoms and counter-ions omitted for clarity.

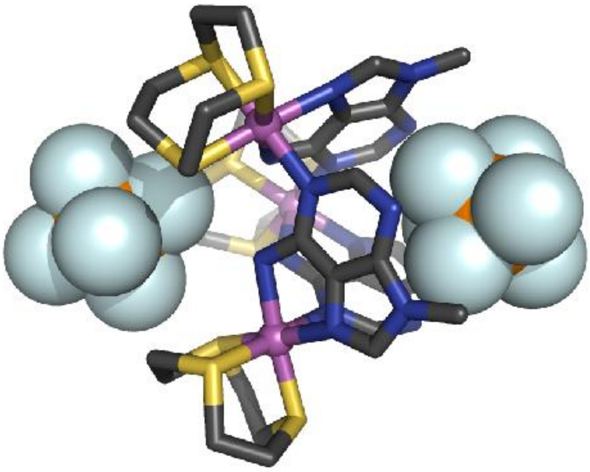

Figure 2.27 Detail from X-ray crystal structure of the [1](PF_6)$_3$ showing the two binding pockets of the macrocyclic host. Hydrogen atoms and counter-ions omitted for clarity.

From the structure, it is clear that the macrocycle shows two possible binding pockets - Figure 2.27. A PF_6^- ion is found sitting at the open face of the bowl making close contacts with hydrogens on the 9-methyl groups of the bridging ligands, while a second is found in in a binding pocket defined by the thiacrown ligands and the three amine hydrogens on the other edge of the 9-methyladenine units. A closer inspection of the structure reveals that the interaction between cationic bowls and anionic guests define extended hexagonal channels that are occupied by further anions – Figure 2.28.

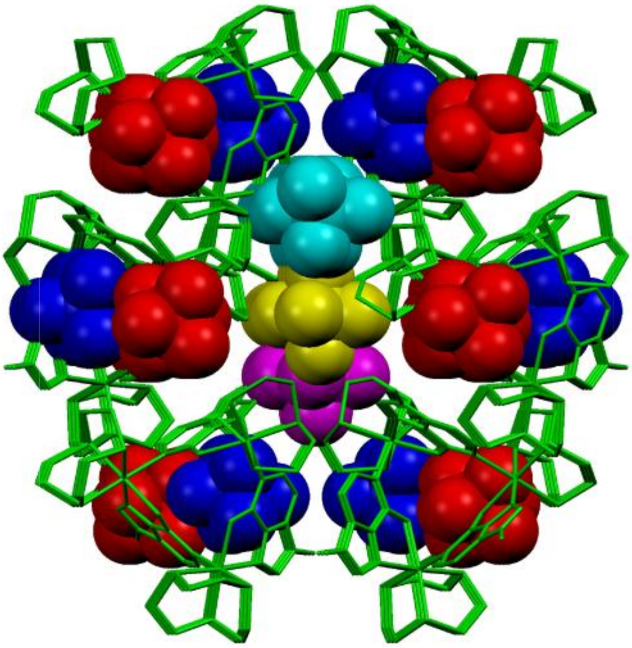

Figure 2.28 Hexagonal channels found in the structure of [1](PF_6)$_3$. Anions of the same colour are symmetry related. Hydrogen atoms and counter-ions omitted for clarity.

2.7.3.4[Ru([9]aneS$_3$)(9-methyl-9H-purin-6-amine)]$_3$(Br)$_3$[1]Br$_3$

This supramolecular was obtained from the change the counter ion of [Ru([9]aneS$_3$)(9-methyl-9H-purin-6-amine)]$_3$(PF$_6$)$_3$ by bromide.

A crystal structure with macrocycle **1**, but a different anion - in this case bromide - was also obtained. The x-ray quality crystals of [**1**](Br)$_3$ were grown from nitromethane/diethylether and details of the structure are shown in Figure 2.29. Details of the bond angles and bond lengths are found in the appendix.

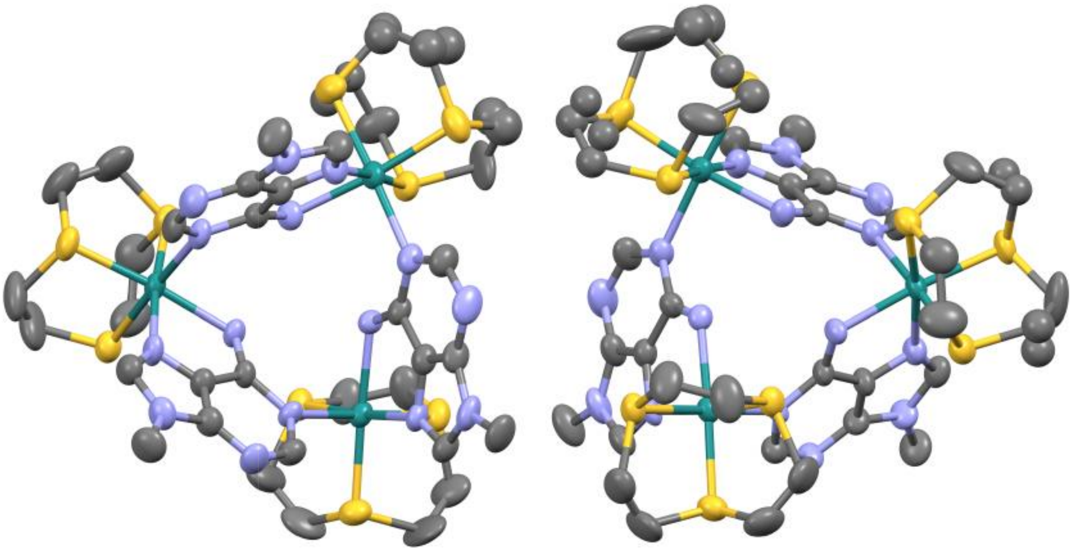

Figure 2.29 Ellipsoid view of the two independent cations in the structure of [1](Br)$_3$. Hydrogen atoms and counter-ions omitted for clarity.

In this structure, only one of the macrocycle two possible binding pockets is occupied. On one face of the macrocycle, a bromide counter-ion sits on top of a binding pocket defined by the thiacrown ligands and the three amine hydrogens on the other edge of the 9-methyl-9H-purin-6-amine units. The other open face of the macrocycle, defined by the 9-methyl-9H-purin-6-amine bridging ligands, forms an unoccupied capsule like space through interleaved close contacts with the same face of a neighboring macrocycle – Figure 2.30. These dimeric capsules pack together to define linear strands and the other bromide anions are located on the outside of the dimer structures forming close contact with a number of thiacrown residues.

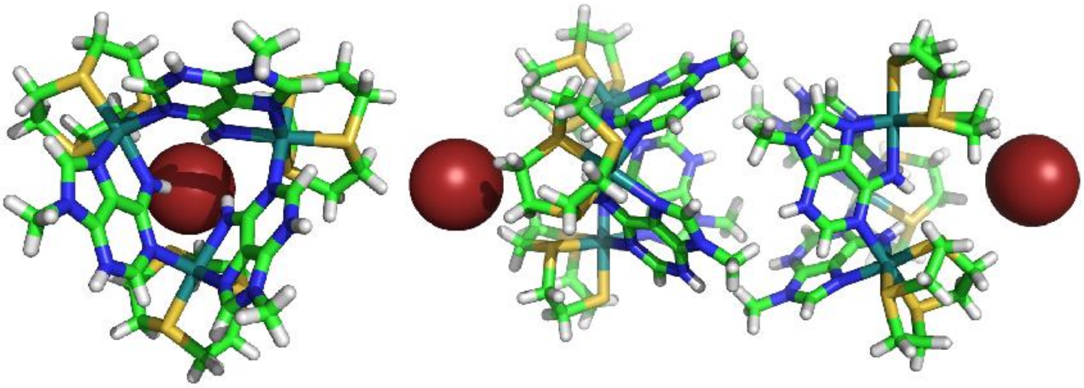

Figure 2.30 Detail from the structure of [1]Br_3 showing the interaction between bromide and hydrogens of thiacrown and bridging ligands (left). Interleaving of two of these units that creates a dimeric “capsule” structure (right).

2.7.3.5 [Ru([9]aneS_3)(9-benzyl-9H-purin-6-amine)]$_3$(CF_3SO_3)$_3$

This supramolecular was synthesized by the reaction of 9-benzyl-9H-purin-6-amine with [Ru([9]aneS_3)(DMSO)Cl_2] in 65% yield.

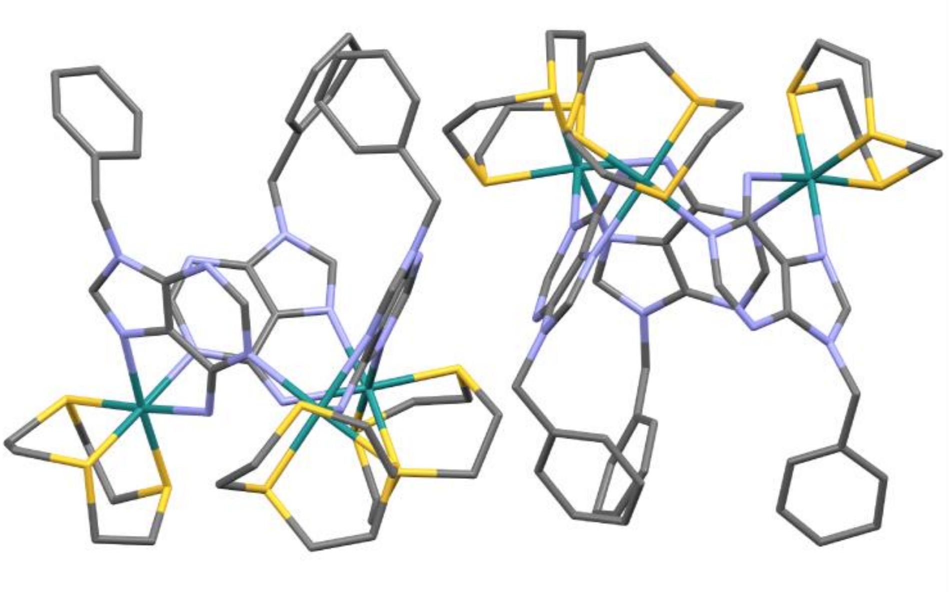

Figure 2.31 Stick representation of the independent macrocyclic cations in the structure of [3](CF_3SO_3)$_3$. Hydrogen atoms and counter-ions omitted for clarity.

Small X-ray quality crystals of macrocycle **3** were grown via slow vapour of acetonitrile solution of the complex. Since these crystals were poorly diffracting, the structure described in this section was solved by the national X-ray structure determination service in Southampton University. Details of the bond angles and bond lengths are found in the appendix.

The crystal confirms the connectivity and overall geometry of the macrocycle. The crystal structure - Figure 2.31- shows that all metal centres possess octahedral geometries with the 9-benzyl-9H-purin-6-amine bridging ligand binding in both mono and bidentate fashion, whilst as expected the 1,4,7- trithiacyclononane is a tridentate ligand. Interestingly, the benzyl units of the bridging ligands extend over the aromatic faces of the adenine moieties to create a well-defined, potentially interesting, binding site for hydrophobic/aromatic guest molecules.

The packing of this structure shows that the triflate counter ions lie away from the complex in channels between rows of cations – Figure 2.32. Presumably -because they are larger in size then bromide of hexafluorophosphate ions - they cannot sit in the relatively small binding pocket of the host.

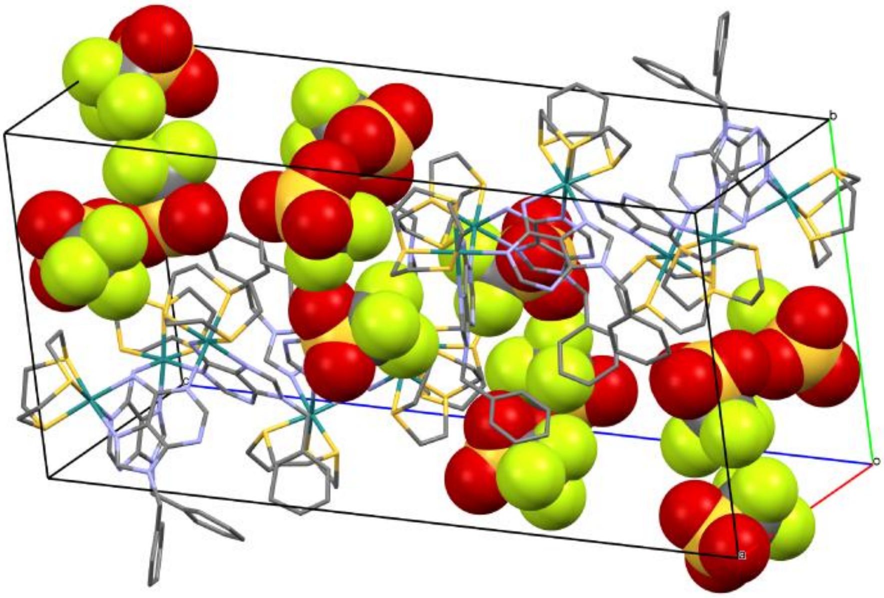

Figure 2.32 Detail from structure of the [3](CF_3SO_3)$_3$ showing triflate ions located in channels away from the macrocycle binding sites.

2.7.3.6 Conclusions

A previously reported and four new self-assembled trinuclear Ru^{II} macrocycles have been synthesized by an improved synthetic method. In two cases, newly synthesized adenine derivatives have been used as the bridging ligands. Crystal structures of the new ligands are reported. In both cases non-covalent interactions, such as pi-pi interactions and hydrogen bonding are observed in the long-range packing of the structures. The structures of the prototype macrocycle **1** with two different anions, bromide and hexafluorophosphate, have also been solved. These studies confirm that the macrocycles are hosts for anions, with potentially two binding sites. Furthermore, it is clear that the long-range order of these structures is highly dependent on the nature of the anionic guest. The structure of a second host, **3**, with triflate anions has also been solved. In this case the triflate anion does not sit in either binding pocket. These studies demonstrate that the macrocycles are hosts for anions and suggest that the “hydrogen bonding” pocket of these hosts is favoured for these interactions.

Chapter3

3. NMR titrations with halide guests

3.1 Titration accuracy and solution concentrations

The interaction of the macrocyclic hosts with a range of halide anions were investigated through ^{1}H NMR spectroscopy. NMR based determinations of K_a are usually only reliable for association constants $<10^4$ M^{-1}; this is a generalisation and requires some detailing. Results obtained for K_a measurements drastically depend on the concentrations and chemical shifts (or other observable NMR changes) being accurately measured and analysed. Chemical shift differences need to be particularly large between free and bound guest; bigger shifts give better results. For ^{1}H-based titrations of host-guest interaction it is preferable for $\Delta\sigma_{max} \geq 0.5$. The perfect situation is when the monitored proton is proximal to an isotropic moiety in the produced complex (for example a carbonyl or aromatic ring). However, meaningful results can even be obtained on a $\Delta\sigma_{max}$ of 0.1 ppm. For a typical spectrometer (400 MHz ^{1}H frequency) observing a sharp singlet (line width 0.2 Hz), chemical shifts can be measured with an accuracy of 0.005 ppm.[63]

Ideally titrations require a series of solutions that can represent the full binding curve between guest and host. In the 1960s Person, Weber, and Deranleau identified the fundamentals of this approach in a series of papers describing the theory of binding measurements. These early papers discussed graphical study of spectroscopic data, but their conclusions are completely general.[63]Later on, Wilcox discussed this issue from a clearer perspective and extended this analysis to NMR curve fitting.[63-64] The big problem with measuring small K_a from $\Delta\sigma_{max}$ values (<10 M^{-1}) is that there will be a huge error associated with the extrapolation to $\Delta\sigma_{max}$. An additional problem when estimating large K_a values ($>10^5$ M^{-1}) is that there is no real curvature in the $\Delta\sigma$ versus $[H]_0/[G]_0$ plot as reagent concentrations change. The guest is effectively entirely complexed by any available amount of host and the graph rises linearly with increasing [H]. This process continues until $\Delta\sigma$ max is reached at the 1:1

stoichiometry. In order to observe curvature in the $\Delta\sigma$ versus $[H]_0/[G]_0$ plot, the solutions should be sufficiently diluted (usually mmol range). However, NMR is a potentially sensitive technique, and experiments are quite often accurate in this mmol range.[63]

3.2 Anion Binding

Anions play a significant role in catalysis and medicine. Additionally, pollutant anions have been linked to the contamination of rivers through the use of phosphate containing fertilizers[65-66] and carcinogenic compounds (metabolites of nitrate).[66] Anions arising from the reprocessing of nuclear fuel (which can discharge into the seas) are also a serious environmental concern. Consequently, anion sensors have a range of possible applications. However, the design of anion hosts as receptors are especially challenging, for a number of reasons. For example, anions are larger than isoelectronic cations and subsequently have a lower charge to radius ratio – Table 3.1.

Table 3.1 A comparison of the radii (r) of isoelectronic anions in octahedral environments.

Anion	r [0A]	Cation	r [^{0}A]
F^-	1.19	Na^+	1.16
Cl^-	1.67	K^+	1.52
Br^-	1.82	Rb^+	1.66
I^-	2.06	Cs^+	1.81

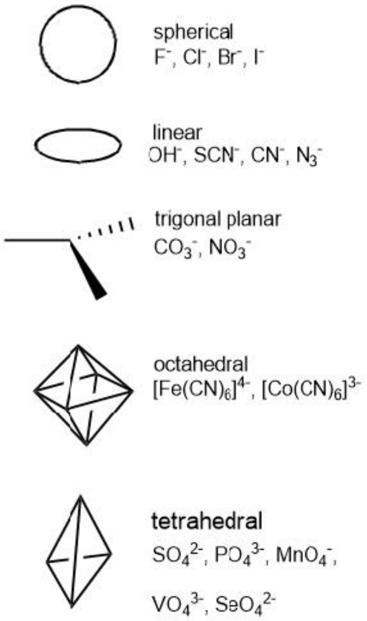

Figure 3.1 The structural diversity of anions.

Compared to cations, anions also have an extensive range of geometries Figure 3.1. And thus, detailed design may be required to produce receptors of complementary size to their anionic guest. Solvent effects also play an important role in dominating binding strength and selectivity for anions. Electrostatic interactions are usually important in anion solvation, and hydroxylic solvents in particular can make strong hydrogen bonds with anions. A potential anion receptor must therefore efficiently contend with the solvent surroundings in which the anion-recognition incident takes place. The neutral receptor that binds anions through ion-dipole interactions may only complex anions in nonprotic organic solvents. Charged receptors generally prefer to bind strongly solvated (hydrate) anions in protic solvent environments.[66-67]

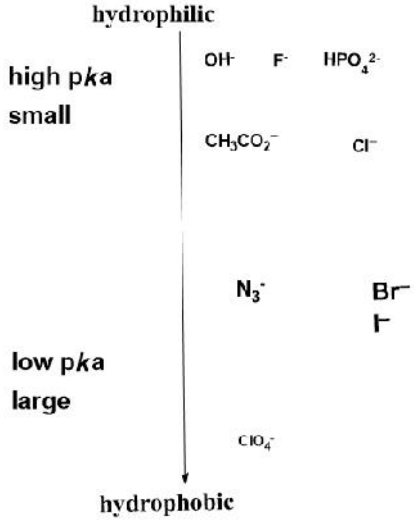

Figure 3.2 Scheme of trends in hydro philicity and hydro phobicity for series of anions.

Hydrophobicity can affect the selectivity of a receptor, the Hofmeister series[66] (Figure 3.2), used in numerous studies on the effect of salts on the solubility of proteins, orders anions by their hydrophobicity (and determined degree of aqueous solvation). This series reflects a general trend: hydrophobic anions generally bind more strongly in hydrophobic binding sites.

3.3 Anion Binding studies

The anion binding properties of [Ru([9]aneS_3)(9-methyl-9H-purin-6-amine)$]_3$ $(PF_6)_3$ (1), [Ru([9]aneS_3)(9-ethyl-9H-purin-6-amine)$]_3(PF_6)_3$ (2), [Ru([9]aneS_3)(9-benzyl-9H-purin-6-amine)$]_3(PF_6)_3$ (3), and [Ru([9]aneS_3)(9-(4-methoxybenzyl)-9H-purin-6-amine)$]_3(PF_6)_3$ (4) were investigated using ^{1}H NMR spectroscopic analysis through the addition of TBAX salts (X= Cl^-, Br^-, I^-, F^-, ClO_4^-, NO_3^-, CH_3COO^-, HSO_4^-, $H_2PO_4^-$).

3.4 ^{1}H NMR Titrations

To measure the strength of anion binding of macrocycles, ^{1}H spectroscopic titration experiment were undertaken in CD_3CN. Spectroscopy samples of the four macrocycles were prepared, to which guest of tetrabutylammonium (TBA) salts were added. The chemical shifts of peaks due to bridging ligand's NH protons of the host were monitored. Anion binding events were quick on the NMR spectroscopic, thereby permitting the calculation of association constants with data fitting to 1:1 stoichiometric binding models- a binding ratio confirmed by Job plots. A range of anions was tested as the macrocycles' hydrogen-bonding cavity is expected to be capable of selectivity binding anions of complementary size and shape within the anion recognition site. For macrocycles **1**, **2**, **3** and **4** the addition of anions as guests caused considerable downfield shift of amide N*H* resonance. The values of K_a were calculated using an Excel program supplied by Prof C. A. Hunter, FRS.

3.5 Halide titrations

3.5.1 Titration of [Ru([9]aneS$_3$)(9-methyl-9H-purin-6-amine)]$_3$ (PF$_6$)$_3$(1)

3.5.1.1 Titration of macrocycle 1 with chloride guest

Our initial study was based on the most common halide: chloride anion. Upon addition of even small amounts of Cl^- significant downfield shifts of –N*H* protons ($\Delta\sigma$max = 1.54) were observed, indicating the chloride binds within the macrocycle**1**cavity. There was also significant splitting of the thiacrown protons: some of protons downfield shift and some protons upfield shift.

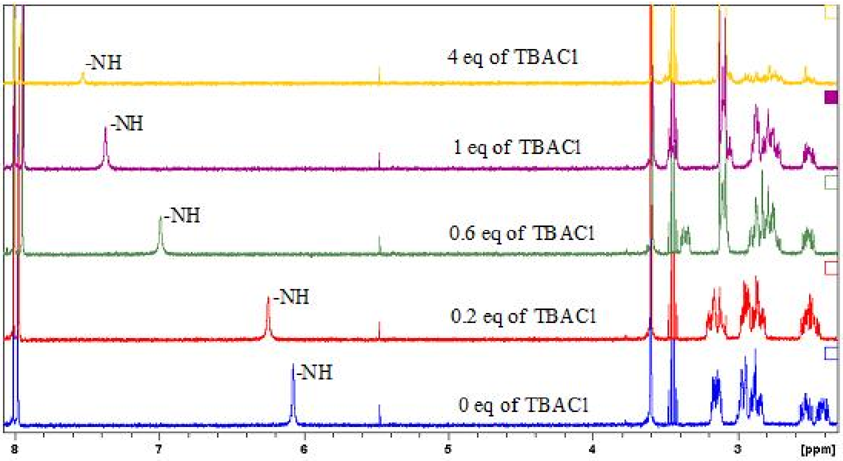

Figure 3.3 ^{1}H NMR (400 MHz) spectra of macrocycle **1** upon addition of equivalents of TBACl. In response, Solvent CD_3CN; temperature: 293 K; [1] =1.5×10^{-6}mol dm^{-3}.

As can be seen from Figure 3.4, there is downfield shifting of the thiacrown protons (labelled a and f), which are indicative of hydrogen binding between the chloride ion and these protons. At the same time upfield shifts of the thiacrown protons labelled b, c and d are also observed, although no appreciable shifts in e protons occur. As will be seen later, these same splitting patterns are also observed on addition of chloride ion to macrocycles **2** and **3**. These changes are consistent with the macrocycle becoming more rigid on addition of the guest: binding into this pocket prevents the previously observed fluxional processes involving the ethylenic groups of the thiacrown. Again as will be seen, these changes are slightly different for each guest almost amounting to a “fingerprint” for each guest anion.

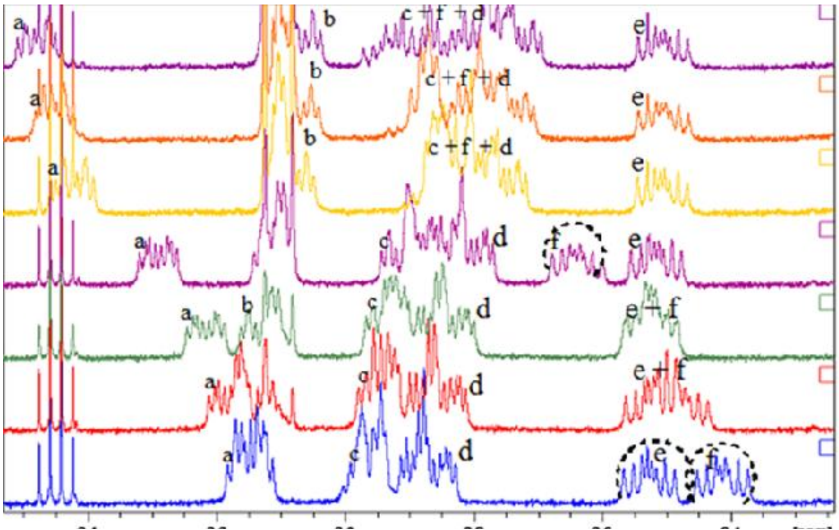

Figure 3.4 ^{1}H NMR (400 MHz) spectra of macrocycl **1** upon addition of equivalents of TBACl. In response, Solvent CD_3CN; temperature: 293 K; [1] =1.5×10^{-6}mol dm^{-3}

It seems likely that the observed behaviour is due to the unique combination of individual guest electronegativities and distance between individual ions and hydrogen atoms of thiacrown.

The shifts in N*H* signal have been used to construct binding curves and Job plots for the interaction between the guest and host below. The Job plots confirm a 1:1 interaction and thus a binding affinity can be estimated from model fits to the obtained binding curve.

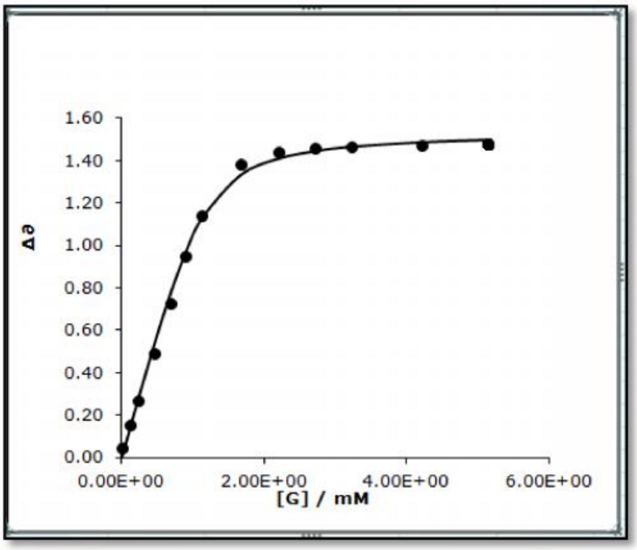

Figure 3.5 Binding curve obtained through analysis of the ^{1}H NMR titration data with chloride, monitoring the N*H* proton (H6) shift. Association constants were determined by using Excel to fit the ^{1}H NMR titration data, The line represents the fit to the model. K_a[[M^{-1}]= 1.56×10^5.

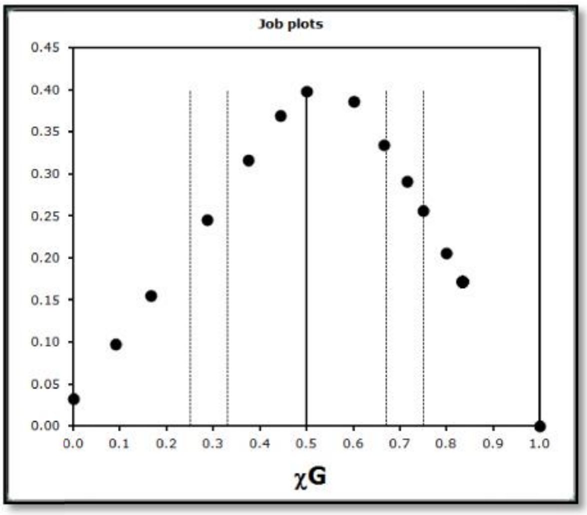

Figure 3.6 Job-plot analysis revealed a 1:1 binding mode for chloride.

3.5.1.2 Titration of macrocycle 1 with Fluoride

Following the promising results with chloride, host-guest chemistry with all the other common halide anions was investigated.

Upon addition of a few titres of F$^-$ to macrocycle **1** very large downfield shifts of the N*H* protons (Δσ$_{max}$ = 3.651) were observed. These are the largest shifts observed for any of the guests that were investigated. However, in contrast to the chloride study, binding between fluoride and macrocycle **1** appears to be relatively weak, as these changes did not appear to reach saturation and unfortunately, macrocycle **1** precipitated after addition of 3.5 equivalents of fluoride.

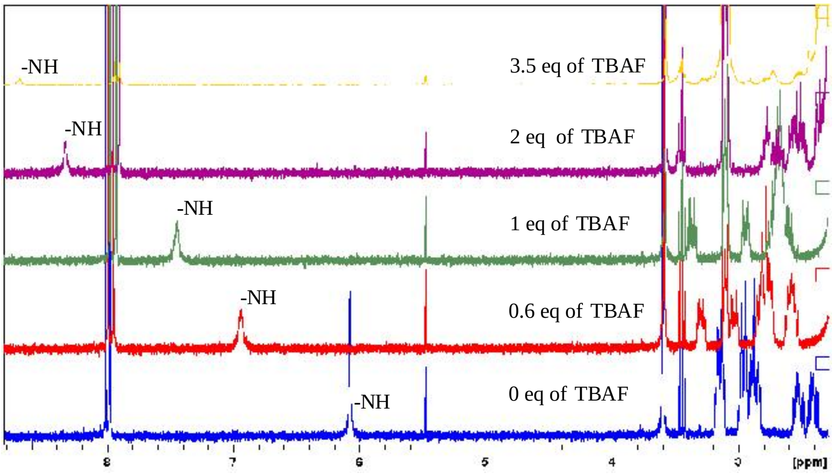

Figure 3.7 ^{1}H NMR (400 MHz) spectra of macrocycle **1** upon addition of equivalents of TBAF. In response, Solvent CD$_3$CN; temperature: 293 K; [1] =1.5×10^{-6}mol dm^{-3}.

In fact this problem is common for all macrocycles with fluoride, making studies of fluoride binding with these macrocycles very difficult relative to the results obtained with chloride. Nevertheless, fits to this data indicate that the affinity between fluoride ion and macrocycle **1** is relatively weak, suggesting that fluoride does not complement the size of the cavities of the macrocycle. However, significant splitting of the thiacrown protons is again observed with some of protons downfield shifting and some protons of upfield shifting.

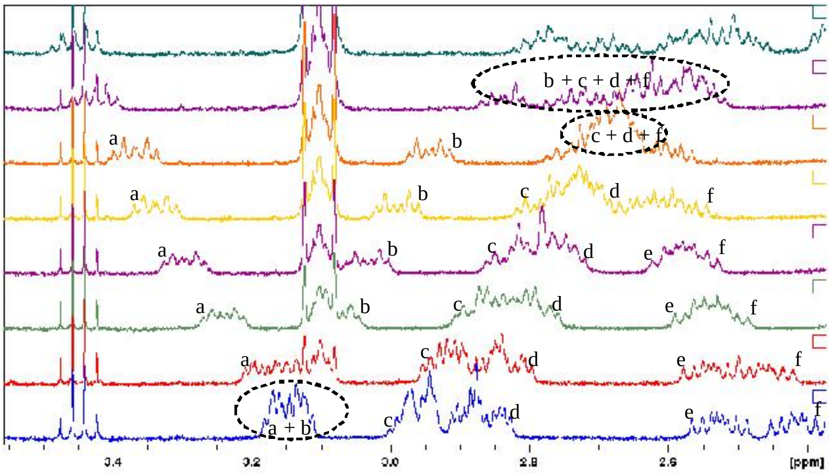

Figure 3.8 ^{1}H NMR (400 MHz) spectra of macrocycle **1** upon addition of equivalents of TBAF. In response, Solvent CD_3CN; temperature: 293 K; [1] $=1.5\times10^{-6}$mol dm^{-3}.

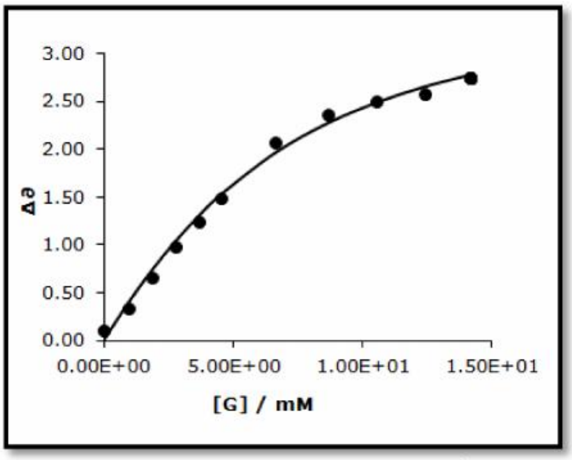

Figure 3.9 Binding curve obtained through analysis of the ^{1}H NMR titration data (with fluoride ion), monitoring the NH proton (H6) shift. Association constants were determined by using Excel to fit the ^{1}H NMR titration data, The line represents the fit to the model. K_a= 2.83×10^{2}M^{-1}.

3.5.1.3 Titration of macrocycle 1 with Bromide

The binding between macrocycle **1** and bromide ion is somewhat similar to data obtained for chloride, although N*H* shifts are lower ($\Delta\sigma_{max}$ = 1.01) and again the thiacrown protons gave a new splitting pattern that is different to that for the chloride and fluoride ions. Figure 3.10 ^{1}H NMR (400 MHz) spectra of macrocycle **1** upon addition of equivalents of TBABr. In response, solvent CD_3CN; temperature: 293 Ka; [1]=$1.5x10^{-6}$ mol dm^{-3} shows the splitting pattern in the thiacrown region after bromide addition. The bromide has a slightly lower binding affinity than chloride but is much stronger than fluoride. This probably reflects the fact that the size difference between the chloride and bromide is not big, while the difference in size with fluoride is large.

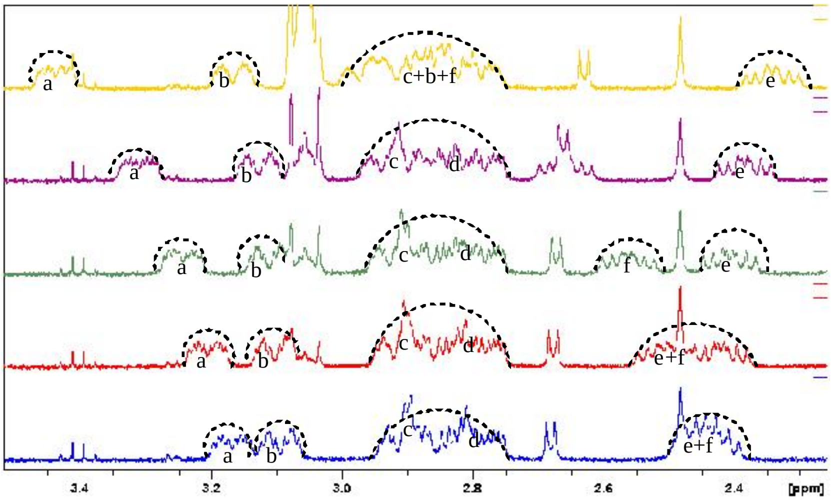

Figure 3.10 ^{1}H NMR (400 MHz) spectra of macrocycle **1** upon addition of equivalents of TBABr. In response, Solvent CD_3CN; temperature: 293 K_a; [1] =1.5×10^{-6}mol dm^{-3}.

3.5.1.4 Titration of macrocycle 1 with Iodide

The data shows that binding between macrocycle **1** and iodide produces similar effects, although shift in the NH are lower ($\Delta\sigma$ = 0.524) than those for the other halides. The calculated binding affinity between macrocycle **1** and iodide is weaker than bromide and chloride but stronger than fluoride, again this is probably due to ion size, but in this case iodide is too large for the binding pocket. Iodide also has own splittings in the thiacrown region, Figure 3.11 shows this splitting pattern.

The interaction of macrocycle **1** with all the halides investigated is summarised in Table 1 and the shifts in the N*H* proton are compared in Figure 1.11. It is clear from this data that medium size halide ions are preferentially bound by the macrocycle.

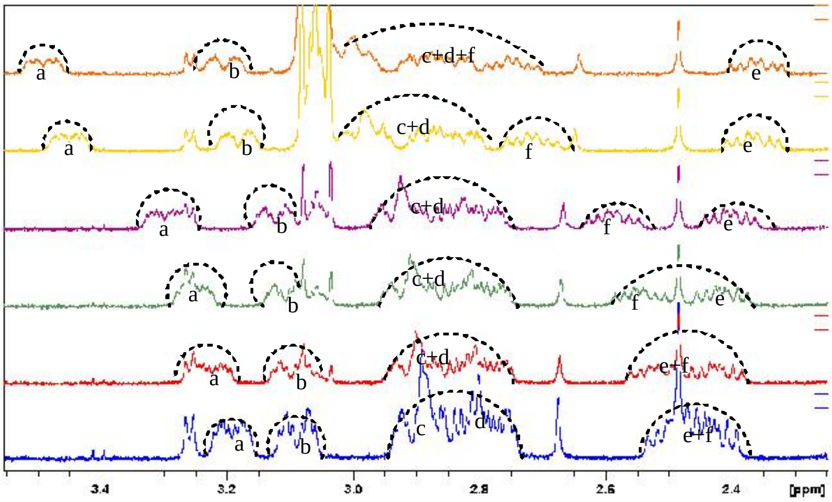

Figure 3.11 ^{1}H NMR (400 MHz) spectra of receptor **1** upon addition of equivalents of TBAI. In response, Solvent CD$_3$CN; temperature: 293 K; [1] $=1.5\times10^{-6}$mol dm^{-3}.

Notably, although fluoride produces large shifts in the host macrocycle signals (presumably due to its highly polarising nature) its binding is the weakest of the halides, probably as it is too small to fit into the host binding pocket.

Table 3.2 shifts in NH resonance ($\Delta\delta$) and 1:1 anion association constants (Ka) of macrocycles **1** and halides Table arranged in binding affinity rank order.[a]

Ion	$K_a[M^{-1}]$	$\Delta\delta$[ppm]
Cl^-	$1.6\times10^5\pm4\%$	1.42
Br^-	$3.9\times10^4\pm3\%$	1.01
I^-	$2.1\times10^3\pm1\%$	0.52
F^-	$2.8\times10^2\pm4\%$	3.65

Anions added as TBA salts. Shifts are for 5 equiv. of anions added. Association constants are calculated by Excel program, with errors of experimental data fitting to the calculated binding isotherms 10%. Solvent: CD$_3$CN, concentration of macrocycles: 1.5×10^{-6} mm, T = 293 K, peaks monitored: amine N*H* of macrocycle **1**.

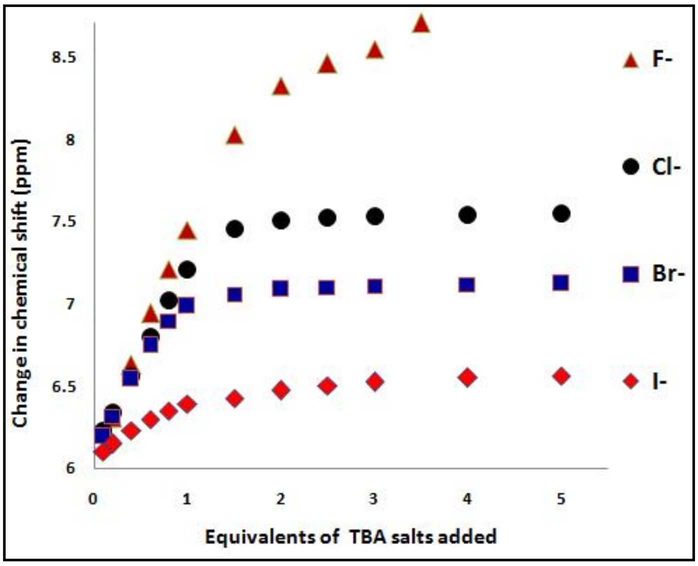

3.12 Plots of the average chemical shift of the amine NH resonances macrocycle **1** versus equivalents of TBA salts(Cl$^-$ ●, Br$^-$ ■, F$^-$ ▲ and I$^-$ ♦) added (solvent: CD_3CN, concentration of macrocycle 1: 1.5 mM, T = 293 K).

3.5.2 Titrations [Ru([9]aneS$_3$)(9-ethyl-9H-purin-6-amine)]$_3$(PF$_6$)$_3$ (2)

After the initial investigation involving macrocycle **1**, the host guest chemistry of the three other macrocycles were investigated. Although titrations of macrocycles **1** and **2** with halides are very similar, this does not preclude the existence of some differences. For example, macrocycle **2** continues to be soluble even after addition of guest halide concentrations that caused host **1** to precipitate.

3.5.2.1 Titration of macrocycle 2 with fluoride

An example of differences between **1** and **2** is provided by titration studies involving macrocycle **2** and fluoride. Fluoride ion caused macrocycle **2** to precipitate after addition 4.5 mole equivalents of TBAF whereas macrocycle **1** precipitated after addition 3.5 mole equivalents of TBAF. Furthermore, judging from NMR shifts, it also appears that hydrogen bonding between this guest and macrocycle **2** is stronger than that observed for macrocycle **1** leading to a higher estimated K_a than that shown for macrocycle **1**.

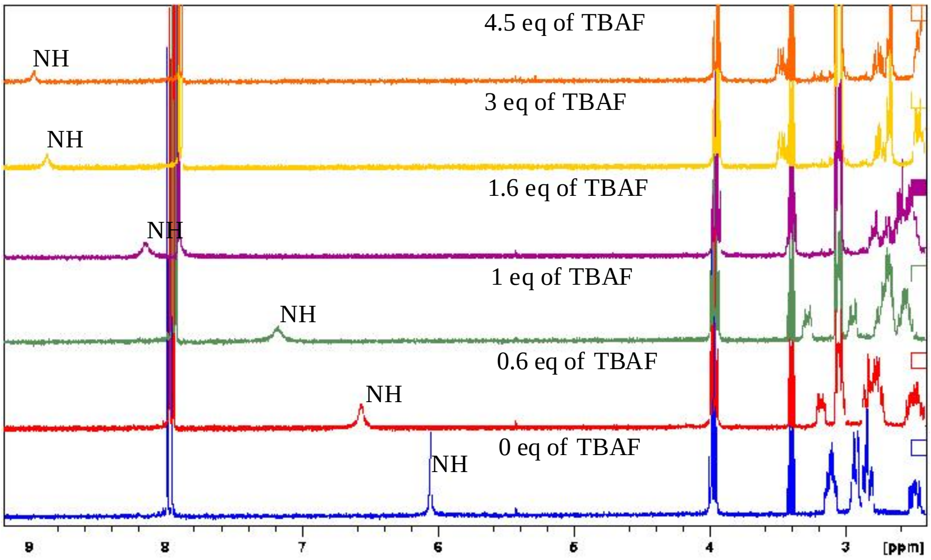

Figure 3.13 ^1H NMR (400 MHz) spectra of macrocycle **2** upon addition of equivalents of TBAF. In response, Solvent CD_3CN; temperature: 293 K_a; [1] $=1.5\times10^{-6}$mol dm^{-3}.

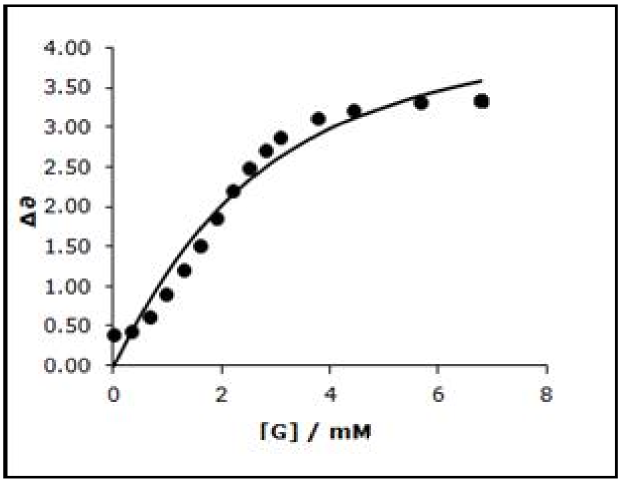

Figure 3.14 Binding curve obtained through analysis of the ^1H NMR titration data for fluoride binding, monitoring the N*H* proton (H6) shift. Association constants were determined by using Excel to fit the ^1H NMR titration data. The line represents the fit to the model. $K_a = 6.69\times10^2\ M^{-1}$.

Experiments on all the halides are summarised in Table 3.3 and Figure below. Generally speaking binding affinities obtained using this host is slightly lower than those obtained for **1**.

Table 3.3 shifts in N*H* resonance (Δδ) and 1:1 anion association constants (K_a) of macrocycles **2**.

Ion	K_a[M^{-1}]	Δδ[ppm]
Cl^-	$2.8\times10^4\pm1\%$	1.46
Br^-	$3.3\times10^4\pm3\%$	1.10
I^-	$1.5\times10^3\pm8\%$	0.55
F^-	$6.7\times10^2\pm1\%$	5.04

[a] Anions added as TBA salts. Shifts are for 5 equiv. of anions added. Association constants are calculated by Excel program, with errors of experimental data fitting to the calculated binding isotherms 10%. Solvent: CD_3CN, concentration of macrocycles: 1.5×10^{-6} mm, T = 293 K, peaks monitored: amine –N*H* macrocycle **1**.

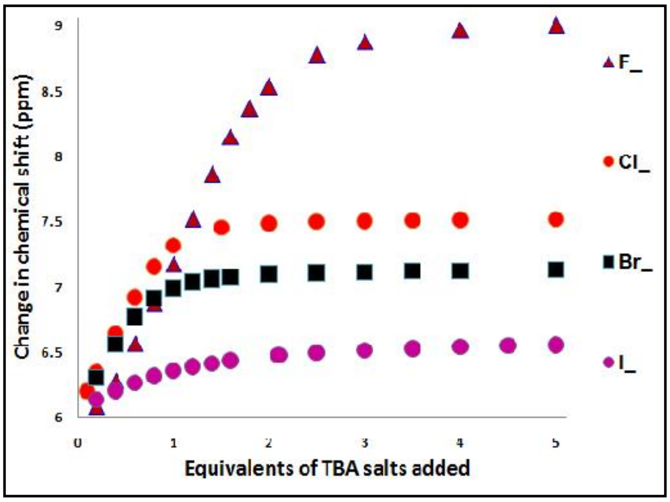

Figure 3.15 Plots of the average chemical shift of the amine N*H* resonances macrocycle **2** versus equivalents of TBA salts (Cl^- ●, Br^- ■, F^- ▲ and I^- ●) added (solvent: CD_3CN, concentration of macrocycle **2** 1: 1.5 mM, T = 293 K).

3.5.3 Titration [Ru([9]ane*S*3)(9-benzyl-9H-purin-6-amine)]$_3$(PF$_6$)$_3$ (3).

Although titrations of macrocycle **3** with halides were quite similar to those for hosts **1** and **2** there were some differences. For example, macrocycle **3** precipitates after addition of 1 molar equivalent of TBAF. Furthermore, there are relatively small upfield shifts in H2 and H8, these contrasts with the behaviour of macrocycle **1**, where these signals shifted to low field. No shifts are observed for the phenyl protons and -CH$_2$ protons. Fits from the fluoride data were still possible although the estimates are probably less accurate.

The relative data for macrocycle **3** binding to halides is summarised in Table 3.3 and **Figure** below. Clearly the binding of this macrocycle to these guests shows a much bigger range of affinities than that of hosts **1** and **2**. Job plots show this binding is (1:1).

Table 3.4 Shifts in NH resonance ($\Delta\delta$) and 1:1 anion association constants (K_a) of macrocycles 3.[a]

Ion	K_a[M^{-1}]	$\Delta\delta$[ppm]
Cl$^-$	$1.6\times10^5\pm5\%$	1.05
Br$^-$	$1.8\times10^5\pm8\%$	0.70
I$^-$	$3.6\times10^3\pm3\%$	0.36
F$^-$	$9.8\pm8\%$	1.65

Anions added as TBA salts. Shifts are for 5 equiv. of anions added. Association constants are calculated by Excel program, with errors of experimental data fitting to the calculated binding isotherms 10%. Solvent: CD$_3$CN, concentration of macrocycles: 1.5×10^{-6} mm, T = 293 K, peaks monitored: amine –N*H* macrocycle **3**.

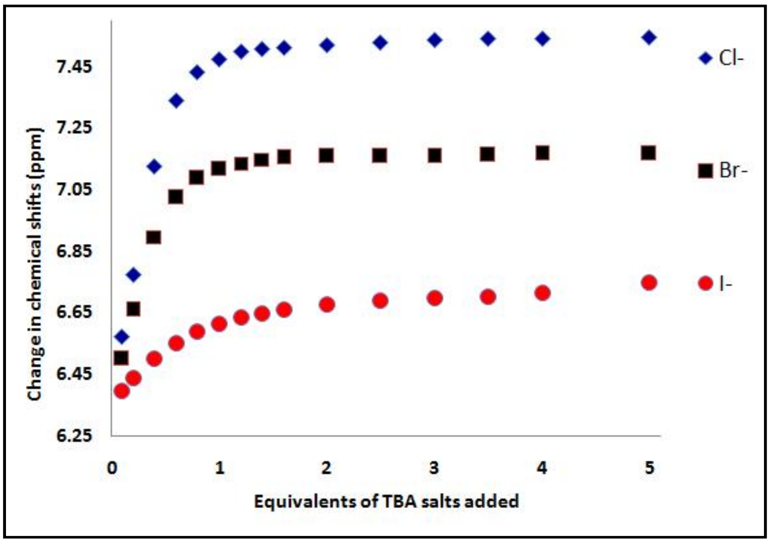

Figure 3.16 Plots of the average chemical shift of the amine NH resonances macrocycle **3** versus equivalents of TBA salts (Cl^- ◆, Br^- ■ and I^- ●) added (solvent: CD_3CN, concentration of macrocycle **3** : 1.5 mM, T = 293 K). Fluoride is not included as it precipitates after addition of around 1 equivalent.

3.5.4 Titration [Ru([9]aneS$_3$)(9-(4-methoxybenzyl)-9H-purin-6-amine)]$_3$(PF$_6$)$_3$ (4)

In terms of solublities this macrocycle is closer to host **3** rather than macrocycles **1** and **2**. For example, macrocycle **4** precipitated after addition of only 1.2 molar equivalents of TBAF. The data collected in these studies is summarized in Table 4 and Figure below. They show that this macrocycle does not have the same range of selectivities/affinities shown by host **3**. Indeed they indicate that macrocycle **4** has the lowest selectivity of all of the **4** macrocycles studied.

Table 3.5 shifts in NH resonance (Δδ) and 1:1 anion association constants (K_a) of macrocycles **4**.

Ion	K_a[M^{-1}]	Δδ[ppm]
Cl^-	$4.1\times10^4 \pm 3\%$	1.01
Br^-	$2.9\times10^4 \pm 4\%$	0.74
I^-	$5.0\times10^3 \pm 3\%$	0.25
F^-	$1.4\times10^2 \pm 5\%$	5.50

[a]Anions added as TBA salts. Shifts are for 5 equiv. of anions added. Association constants were calculated by Excel program, with errors of experimental data fitting

to the calculated binding isotherms 10%. Solvent: CD_3CN, concentration of macrocycles: 1.5×10^{-6} mm, T = 293 K, peaks monitored: amine –N*H* macrocycle **4**.

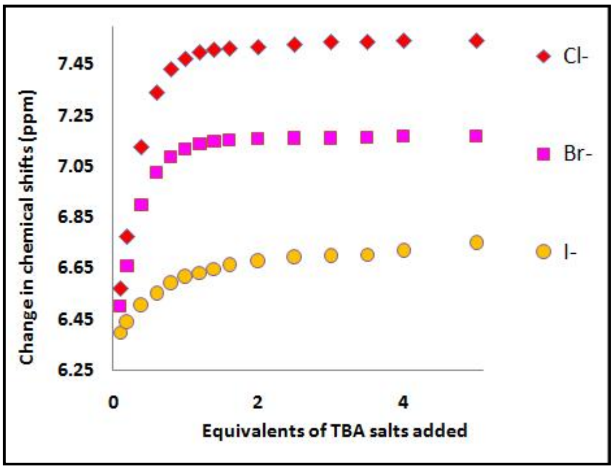

Figure 3.17 Plots of the average chemical shift of the amine NH resonances macrocycle3versus equivalents of TBA salts(Cl^-♦, Br^-■and I^-●) added (solvent: CD_3CN, concentration of macrocycle 3 1: 1.5 mM, T = 293 K). Fluoride is not included as it precipitates after addition of around 1.2 equivalents

3.5.5 Titration macrocycle [1]$(NO_3)_3$ with TBA chloride ion in D_2O

Given the strong binding of the macrocycle with chloride in organic solvent, its interaction in water was also investigated. In these conditions, the host-guest interaction is expected to be greatly attenuated, as water is a highly competitive hydrogen bonding solvent and highly polar.

Upon addition of chloride a slight shift ($\Delta\sigma$ = 0.17) in macrocycle **1** N*H* protons were observed in D_2O titration compared with the shift in CD_3CN titration of $\Delta\sigma$ = 1.54. This suggests binding between macrocycle **1** and chloride ion is attenuated in this solvent. Analysis of the titration data following the N*H* protons gave a greatly reduced association constant (K_a=58.9 M^{-1}). Therefore, macrocycle**1** exhibits a very much lower binding affinity for chloride in aqueous conditions. This is presumably a consequence of the D_2O competing and thus inhibiting hydrogen bonding between N*H* and the anion guest. This suggests that chloride is not bound well in this competitive solvent.

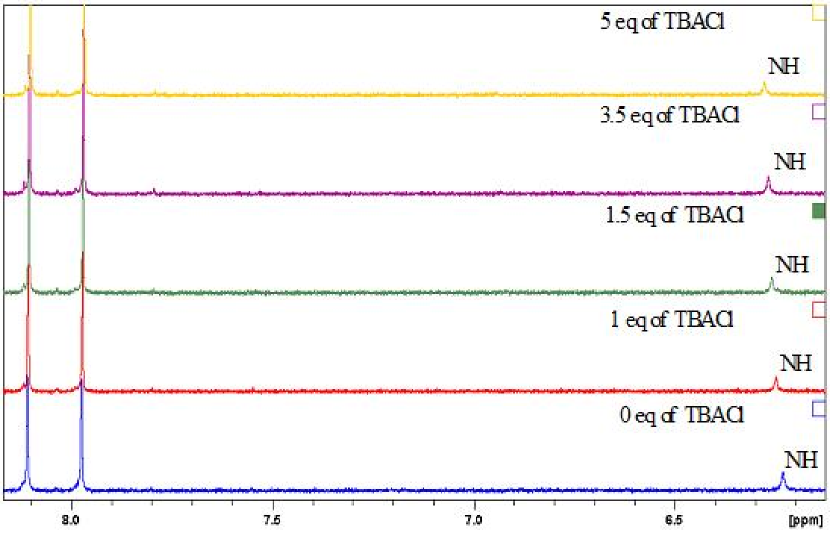

Figure 3.18 ^{1}H NMR (400 MHz) spectra of macrocycle **1** upon addition of equivalents of TBACl In response, Solvent D_2O; temperature: 293 K; [1] =1.5×10^{-6}mol dm^{-3}.

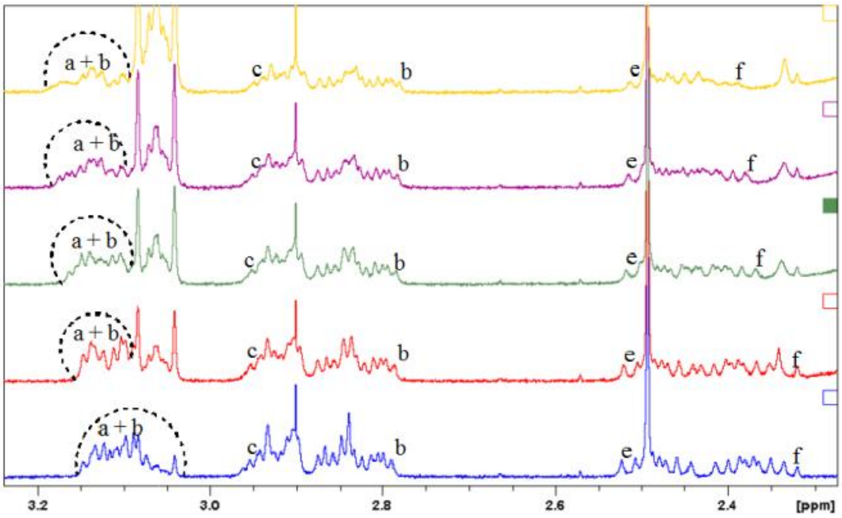

Figure 3.19 ^{1}H NMR (400 MHz) spectra of macrocycle **1** upon addition of equivalents of TBA chloride In response, Solvent D_2O; temperature: 293 K; [1] =1.5×10^{-6}mol dm^{-3}.

In this aqueous titration only small effects on the thiacrown region are observed, compared to the large splitting and shifts observed in the CD_3CN titrations Figure 3.19.

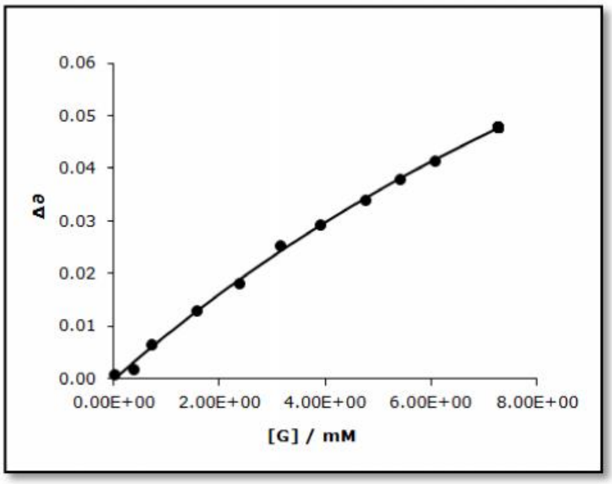

Figure 3.20 Binding curve obtained through analysis of the ^{1}H NMR titration data, monitoring the N*H* proton (H6) shift. Association constants were determined by using Excel to fit the ^{1}H NMR titration data, The line represents the fit to the model K_a= 59 M^{-1}.

3.6 CONCLUSION

Summarising the data for all the titrations: for macrocycles **1** and **2** the addition of chloride and bromide anions caused large downfield shifts ($\Delta\sigma_{max}$>>1) of the N*H* resonance. The same guests produced lower shifts for macrocycles **3** and **4**. A similar trend was observed for iodide generally binding to these anions followed the same trend: $Br^-≈Cl^->>I^->F^-$, which – apart from fluoride - follows the basicity of the anions as expected for simple hydrogen-bond donor-acceptor systems. It is proposed that chloride and bromide bound more strongly than fluoride due to better geometric complementarity between each of the chloride, bromide and macrocycles cavities than fluoride and iodide. Thus, these results indicate that the host cavities of macrocycles **1**, **2**, **3**, and **4** bind chloride and bromide guests best due to a complementary combination of shape, size and basicity.

It is notable that all the macrocycles bind fluoride anion very weakly, despite producing large N*H* shifts. Indeed, the binding of fluoride was found to be more unfavourable than for any of the other halide ions. This is possibly due to the size of the cavities not being complementary to that of the fluoride ion.[68-69] Investigations into the binding between macrocycle **1** and chloride ion in the more competitive solvent water revealed that binding under these circumstances be very weak, therefore it could be argued that hydrogen bonding plays a major role in the binding strength between the ions and the macrocycles.

Chapter 4

4. Oxo titrations

After the investigation of binding to simple spherical halides the interaction of the macrocyclic hosts with more structurally complex oxo anions was explored. In this case the anions investigated could be either tetrahedral or trigonal in shape.

4.1 Titration of [Ru([9]aneS$_3$)(9-methyl-9H-purin-6-amine)]$_3$ (PF$_6$)$_3$ (1)

4.1.1 Titration of macrocycle 1 with acetate ion

Titration with the acetate anion resulted in relatively large downfield shifts of NH protons (Δσ max = 0.948) Figure **4.1**. Furthermore, as in the case of the halide ions, notable splitting of the thiacrown protons occurred with some protons downfield shifted and some protons upfield shifted. However, again, a different splitting pattern is observed in the thiacrown region compared with halide ions.

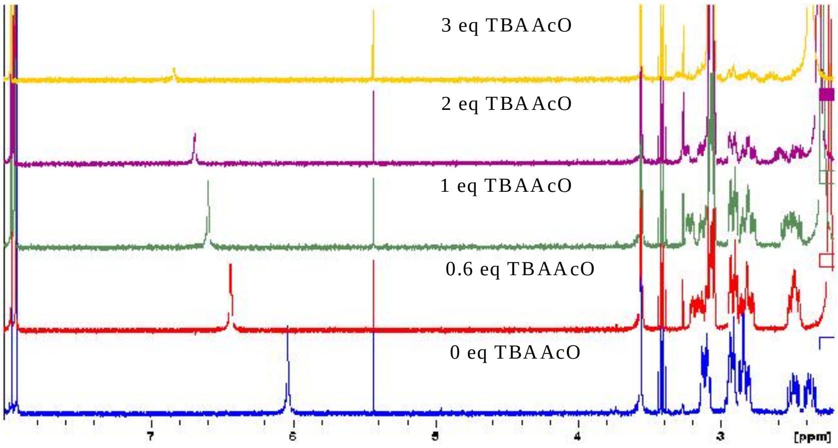

Figure 4.1^{1}H NMR (400 MHz) spectra of macrocycle **1** upon addition of equivalents of TBAOAc. Solvent CD$_3$CN; temperature: 293 K; [1] =1.5×10^{-6} mol dm^{-3}.

There is appreciable downfield shifts of the thiacrown protons labelled a, b and f which are indicative of hydrogen binding between AcO$^-$ and these protons (Figure **4.2**). Upfield shifting of the thiacrown protons labelled e and d and no shifting in the c protons were also observed. All these shifts are very weak in comparison with chloride and bromide guests, but are similar in magnitude to the iodide shifts. Using the N*H* shifts a binding curve for the interaction with acetate was constructed. Since

Job plots clearly indicated 1:1 binding (Figure **4.3**). Model fits to the curve using this binding ratio were carried out leading to an estimated K_a value of $6.34 \times 10^2 M^{-1}$ (Figure **4.4**).

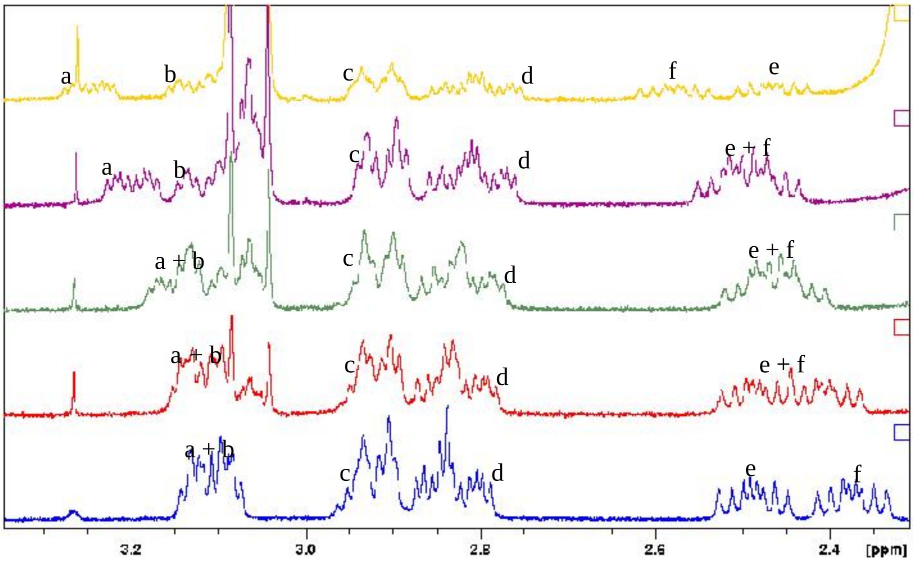

Figure 4.2 ^{1}H NMR (400 MHz) spectra of macrocycle **1** upon addition of equivalents of TBAAcO. Solvent CD_3CN; temperature: 293 K; [1] $=1.5 \times 10^{-6}$ mol dm^{-3}.

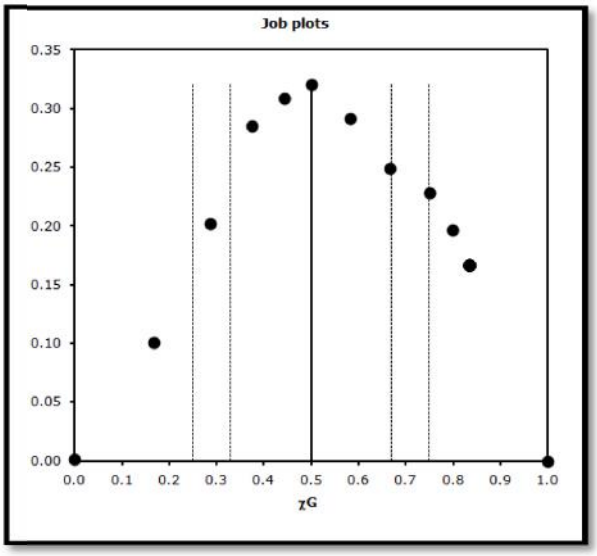

Figure 4.3 A job plot based on the N*H* proton (H6) shifts on addition of acetate clearly indicate a 1:1 binding ratio.

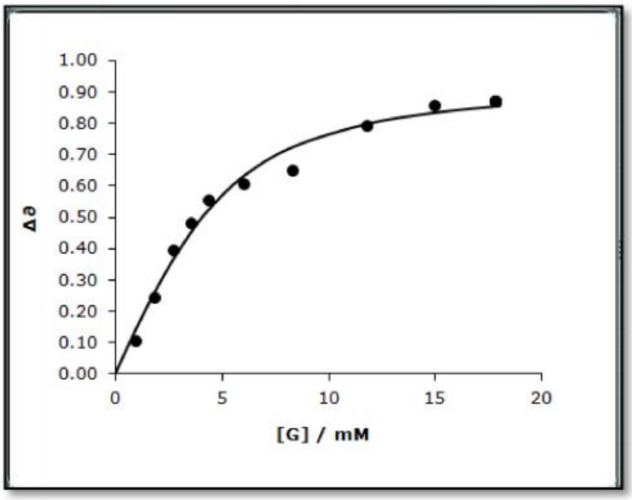

Figure 4.4 Binding curve obtained through analysis of the ^{1}H NMR titration data for addition of acetate guest, monitoring the NH proton (H6) shift. Association constants were determined by fitting the ^{1}H NMR titration data to a 1:1 model. The line represents the line represents the fit to the model. K_a=6.3×10^{2}M^{-1}.

4.1.2 Titration of macrocycle 1 with succinate ion

Upon addition of succinate ion to macrocycle **1**, smaller but clear down field shifts of NH protons (Δσmax = 0.543) occur (Figure 4.5). Furthermore, slight splitting of the thiacrown protons is also observed. However, the host precipitates after addition of more than 1 equivalent of succinate guest.

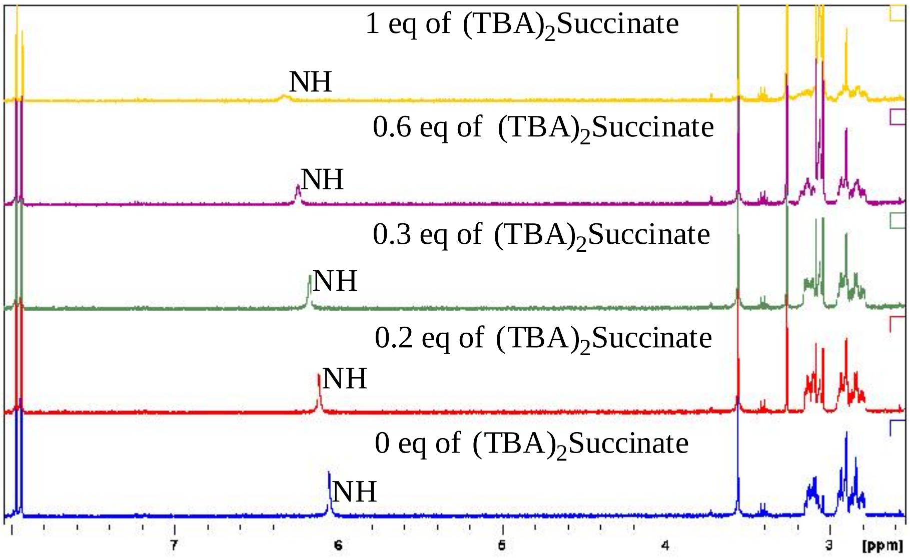

Figure 4.5 ^{1}H NMR (400 MHz) spectra of macrocycle **1** upon addition of equivalents of TBAsuccinate. Solvent CD_3CN; temperature: 293 K; [1] =1.5×10^{-6} mol dm^{-3}.

Figure **4.6** illustrates the relatively small perturbations observed in the thiacrown protons on addition of succinate ion. Slight downfield shift of the thiacrown protons labelled a, b and f are indicative of weak hydrogen binding between succinate ion and these protons. Upfield shifts of the thiacrown protons labelled e and - less so - for d also occur. However, no shifts in the c protons occurred. As mentioned previously, all shifts in thiacrown region in this experiment are very small, suggesting the possibility of a different binding mode, perhaps external to the macrocycle’s cavity for the larger succinate ion.

Binding curves were constructed using the shifts of the macrocycle **1** based on N*H* shown in Figure **4.5**. Unfortunately, due to the poor solubility of the host in the presence of this guest, a meaningful curve for any possible second event could not be constructed. Again, due to poor solubility problems, Job plots for the interaction of host **1** and succinate could not be fully constructed. However it does appear that the first binding event observed in Figure **4.7** is for a 1:1 interaction with the carboxylate units of the succinate guest.

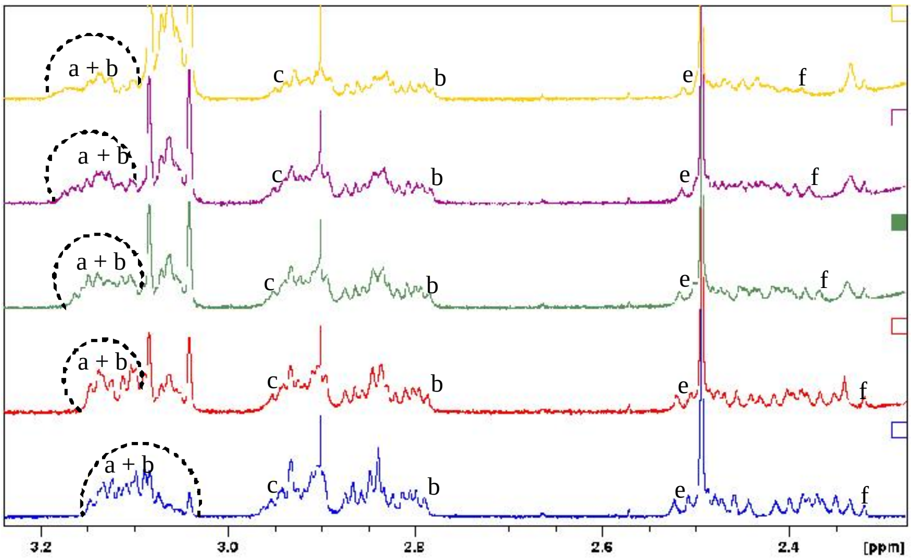

Figure 4.6 ^{1}H NMR (400 MHz) spectra of macrocycle **1** upon addition of equivalents of TBASuccinate. Solvent CD$_3$CN; temperature: 293 K; [1] =1.5×10^{-6} mol dm.

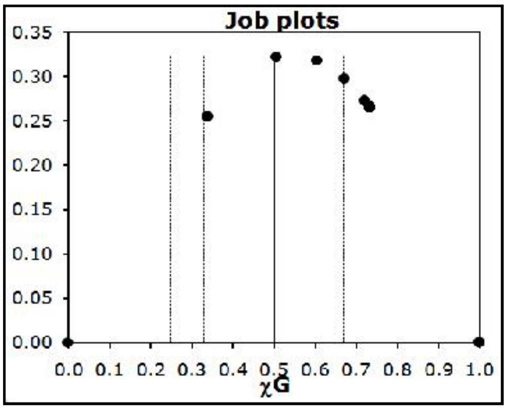

Figure 4.7 A job plot based on the NH proton (H6) shifts on addition of succinate indicate a 1:1 binding ratio.

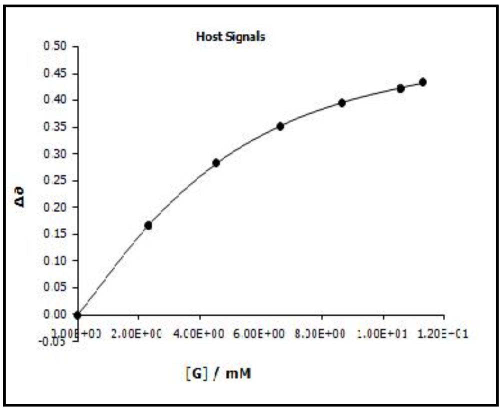

Figure 4.8 Association constants for the 1:1 interaction with succinate were determined by using analysis of the ^{1}H NMR titration data, monitoring the NH proton (H6) gave (K_a= 4.88 X 10^2 M^{-1}).

4.1.3 Titration of macrocycle 1 with dihydrogenphosphate ion

Addition of dihydrogenphosphate ion produces smaller downfield shifts of N*H* protons ($\Delta\sigma$max = 0.27) compared to succinate. However, in this case, the compound precipitated after addition of 2 equivalents of $TBAH_2PO_4$.

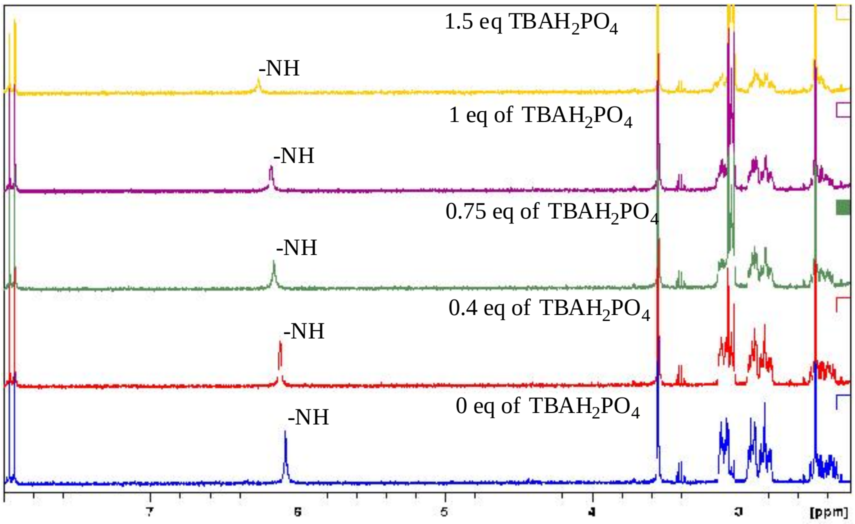

Figure 4.9 ^{1}H NMR (400 MHz) spectra of macrocycle **1** upon addition of equivalents of TBA dihydrogenphosphate. Solvent CD_3CN; temperature: 293 K; [1] $=1.5\times10^{-6}$ mol dm^{-3} TBAH_2PO_4.

Figure **4.10** illustrates the small perturbations observed in thiacrown protons on addition of dihydrogenphosphate ion. Slight downfield shifting of the thiacrown protons labelled a and f occurs. Upfield shifts of the thiacrown protons labelled e and f, to a lesser extent, d occurs. Again, in general all shifts in thiacrown region in this experiment are very small, reflecting the weak interaction between this guest and host **1**. Indeed fits of models to 1:1 binding produced a very low K_a (28 M^{-1}) see Figure **4.11**.

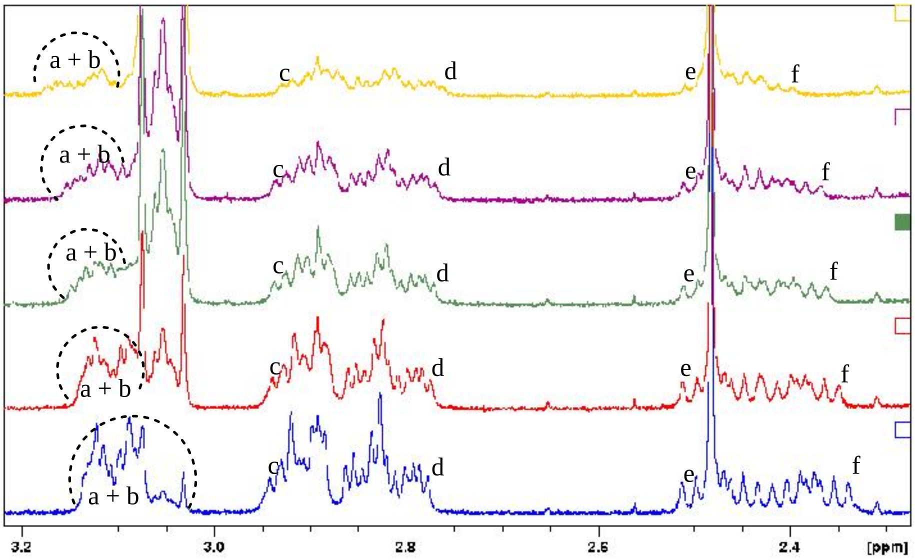

Figure 4.10 ^{1}H NMR (400 MHz) spectra of macrocycle **1** upon addition of equivalents of TBAdihydrogenphosphate. In response, Solvent CD_3CN; temperature: 293 K_a; [1] $=1.5\times10^{-6}$ mol dm^{-3}.

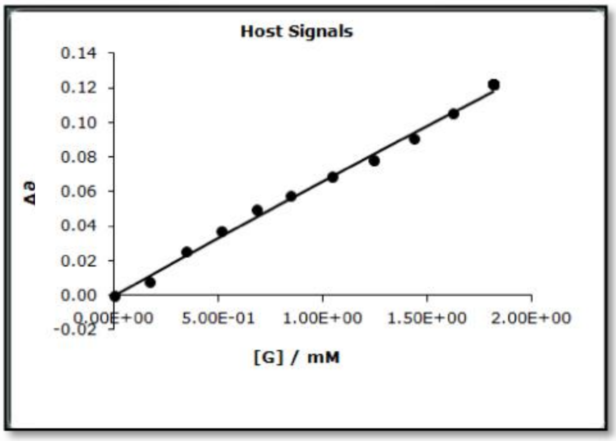

Figure 4.11 Association constants for the interaction with dihydrogenphosphate were determined by analysis of the ^{1}H NMR titration data, monitoring the N*H* proton (H6) gave (K_a= 28 M^{-1}).

4.1.4 Titration of macrocycle 1 with Hydrogensulfate ion (1:1) binding

On addition of this guest only a small downfield shift of N*H* protons (Δσ = 0.222) initially occurs. It is also noticeable that only a very slight splitting of the thiacrown protons is observed on addition of hydrogensulfate ion. This suggests that, like dihydrogenphosphate, any interactions with this anion and the host's binding pocket is weak.

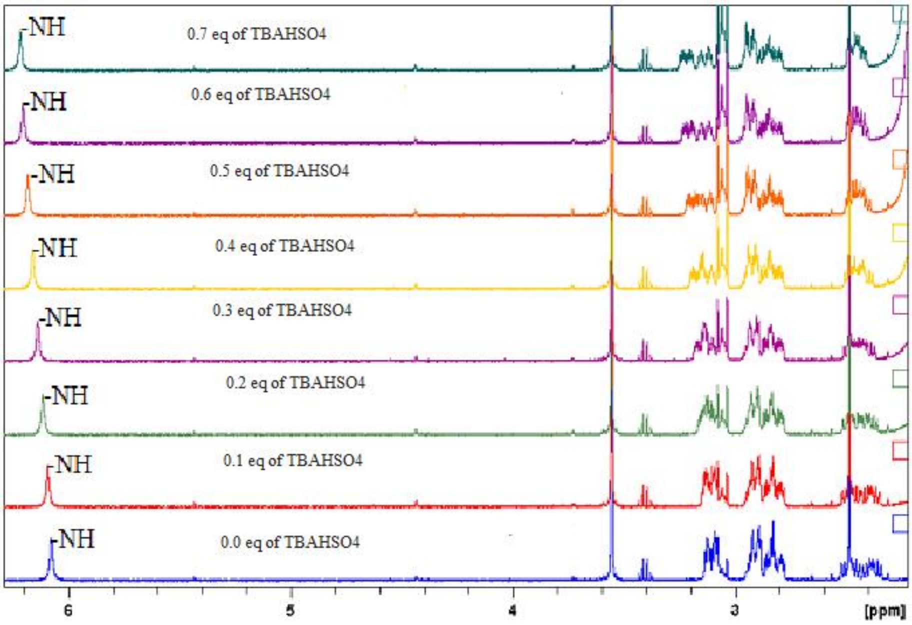

Figure 4.12 ^{1}H NMR (400 MHz) spectra of macrocycle **1** upon addition of equivalents of TBA hydrogensulphate. Solvent CD_3CN; temperature: 293 K; [1] =1.5×10^{-6} mol dm^{-3}.

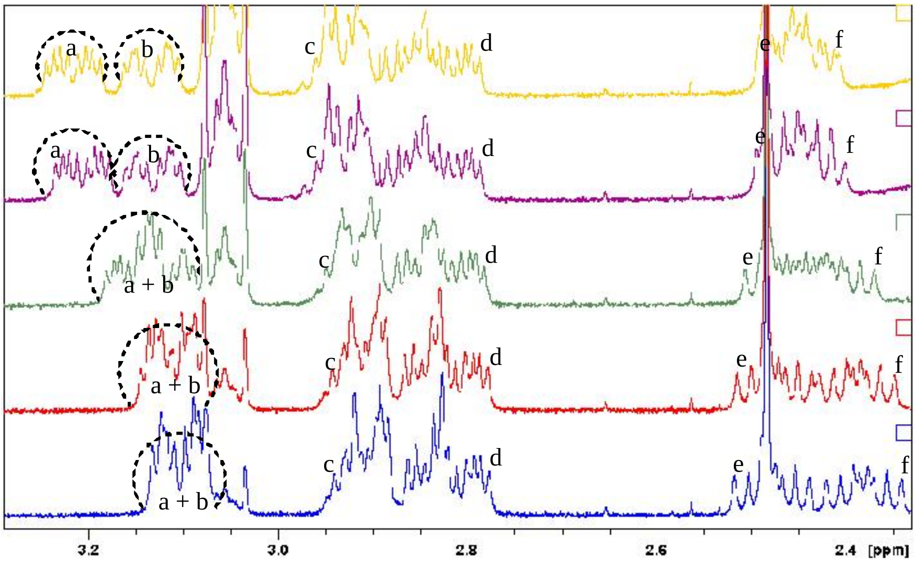

Figure 4.13 ^{1}H NMR (400 MHz) spectra of macrocycle **1** upon addition of equivalents of TBA hydrogensulfate. Solvent CD_3CN; temperature: 293 K; [1] $=1.5\times10^{-6}$ mol dm^{-3}.

Figure **4.13** illustrates the very small perturbation observed in thiacrown protons with hydrogen sulfate ion that indicate the interaction between hydrogen sulfate ion and thiacrown protons are very weak. Slight downfield shifting of the thiacrown protons labelled a, c and f also occurs.

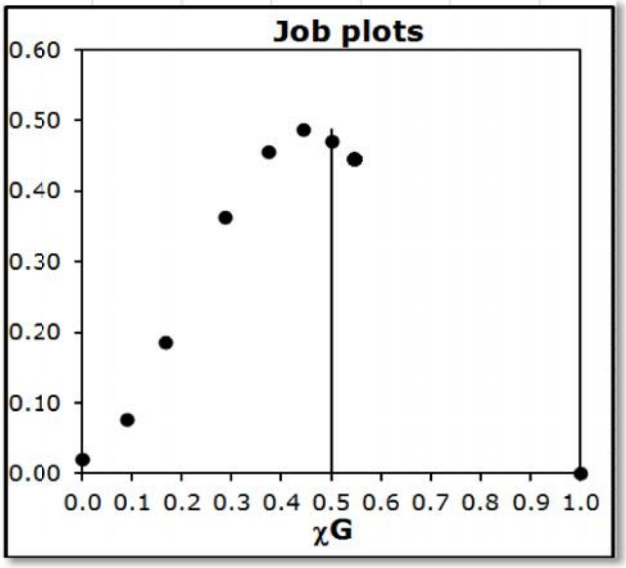

Figure 4.14 Job-plot analysis revealed a 1:1 binding mode for sulfate ion (1:1) binding.

However, somewhat surprisingly, fits of the macrocycle **1** based N*H* shifts to a 1:1 binding model lead to a relatively high K_a value of $5.6\times10^3 M^{-1}$.

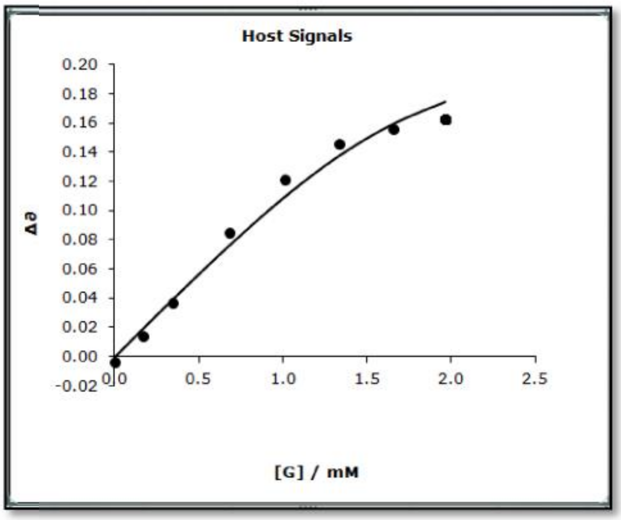

Figure 4.15 Binding curve obtained for addition of hydrogen sulphate through analysis of the ^{1}H NMR titration data, monitoring the N*H* proton (H6) shift. The line represents the fit to the model. K_a=5.6×10^{3}M^{-1}.

4.1.5 Titration of macrocycle1 with hydrogen sulfate ion (1:2) Binding

Further addition of hydrogen sulfate ion over 1:1 ratios produced an unusual and interesting effect. Increasing amounts of the guest caused a sudden and distinctive perturbation in the shifts of the spectra of the macrocycle, suggesting a second binding event. To investigate this effect in more details a second binding titration was performed in CD_3CN. The first set of changes in the spectrum of host **1** ends when ~0.9 eq was added and the N*H* protons shifted from 6.08 ppm to 6.23 ppm. In contrast, the addition of HSO_4^- above this ratio, prompted a sudden upfield shifted in the NH protons to 6.16 ppm (Figure 4.16).

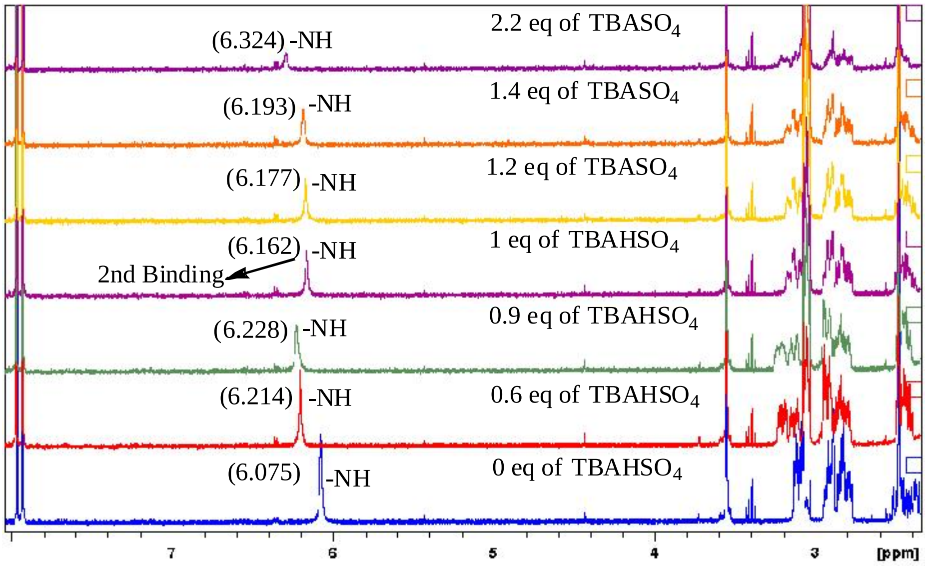

Figure 4.16 ^{1}H NMR (400 MHz) spectra of macrocycle **1** upon addition of equivalents of TBA hydrogensulfate Solvent CD_3CN; temperature: 293 K; [1] =1.5×10^{-6} mol dm^{-3}.

A similar - but clearer - discontinuity was observed in the thiacrown shifts. This is most clearly seen in the proton signals labelled a and b and f in Figure A sudden shift appears at binding ratios above 1 eq of guest, followed by downfield shifting on further additions of guest. The rest of the signals in this region are hardly affected by binding. This second set of changes does not produce a saturation binding curve, suggesting a possible second non-specific binding event.

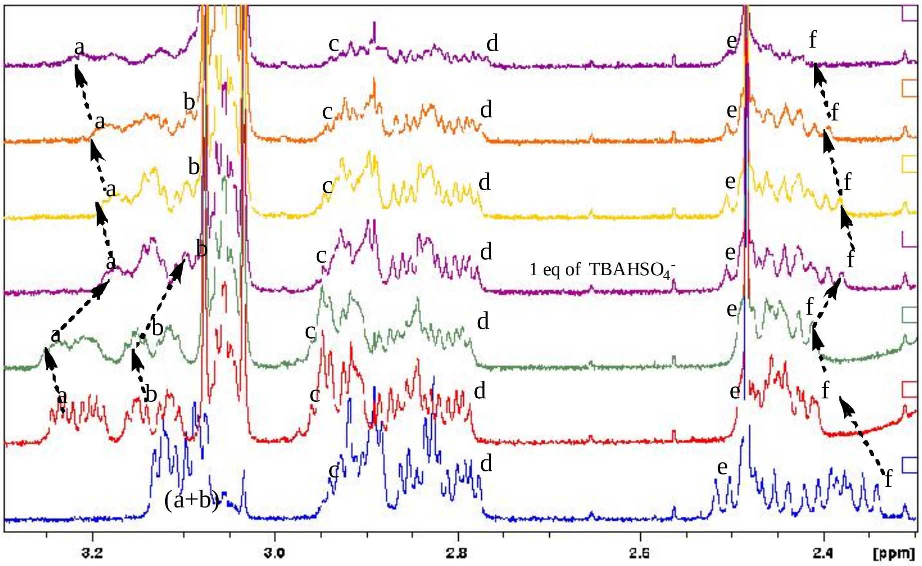

Figure 4.17 ^{1}H NMR (400 MHz) spectra of macrocycle **1** upon addition of second equivalent of TBA hydrogen sulphate. Solvent CD_3CN; temperature: 293 K; [1] =1.5×10^{-6} mol dm^{-3}.

4.1.6 Titration of macrocycle 1 with perchlorate

The perchlorate ion was chosen as a very simple example of a tetrahedral oxo-anion. Upon addition of tetrahedral ClO_4^-, the shifts in N*H* are significantly smaller than those that occurred with acetate ($\Delta\sigma$ max = 0.12). In contrast with the acetate anion-which precipitated after addition of 3 molar equivalents –the macrocycle precipitated after addition 5 molar equivalents of perchlorate guest. All thiacrown shifts were also very small compared to those for chloride and bromide, or even acetate. Very weak downfield shifts of the thiacrown protons labelled a, b, c, d and f and an upfield shift of the thiacrown protons labelled e occurred. These observations all indicate a weaker interaction with perchlorate ion. The reason for this relatively weaker interaction may be due to the shape and size of this guest compared to acetate. The acetate is trigonal and perhaps this guest shape is more complementary to the host binding pocket than the tetrahedral perchlorate.

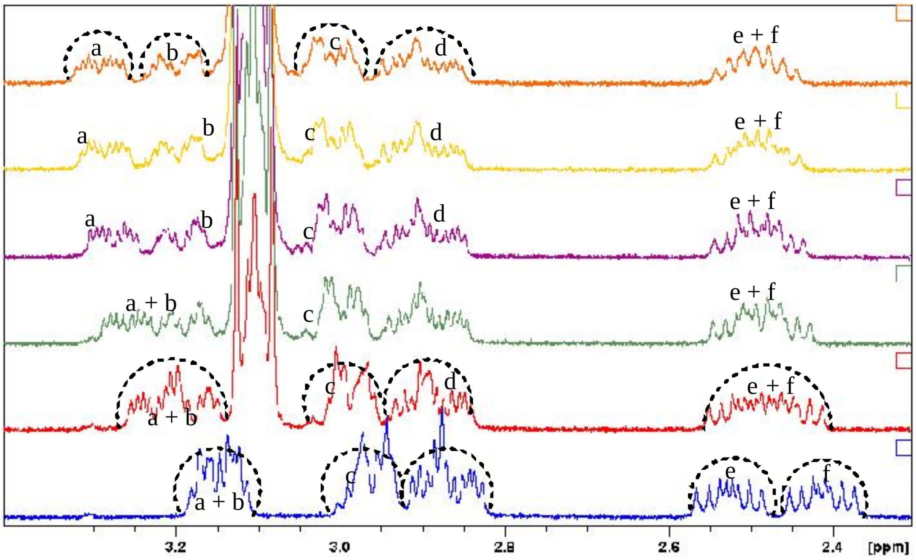

Figure 4.18 ^{1}H NMR (400 MHz) spectra of macrocycle **1** upon addition of equivalents of $TBAClO_4$. Solvent CD_3CN; temperature: 293 K_a; [1] =1.5×10^{-6} mol dm^{-3}.

Job Plots suggest 1:1 binding, therefore association constants were determined by model fitof the ^{1}H NMR titration data, monitoring the N*H* proton (H6) giving a binding affinity estimate of K_a=1.2 x 10^2 M^{-1} around 5 times weaker than the binding to acetate.

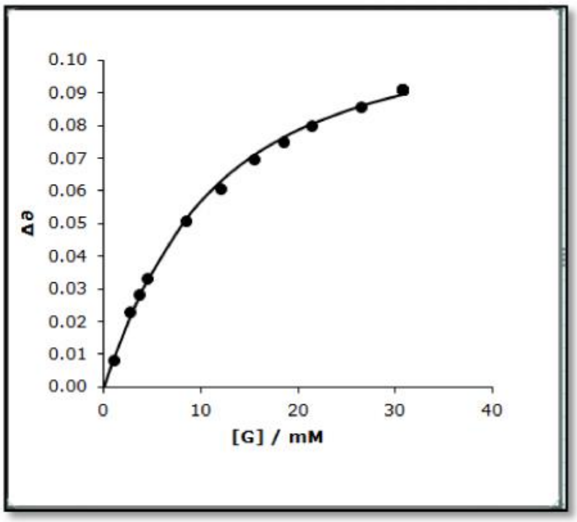

Figure 4.19 Binding curve obtained for addition of perchorate through analysis of the ^{1}H NMR titration data, monitoring the N*H* proton (H6) shift. The line represents the fit to the model. K_a=1.2×10^{2}M^{-1}.

4.1.7 Titration of macrocycle 1 with nitrate ion

Mixing macrocycle **1** with trigonal nitrate ion produced distinctive downfield shifts of N*H* protons ($\Delta\sigma$ = 0.52), which are intermediate to those between acetate and perchlorate guests, again suggesting a relatively weak binding affinity compared to chloride and bromide. However, the shifts are still appreciably larger than those for the tetrahedral perchorate ion suggesting that the shape of the guest is important. Again, downfield shifts of the thiacrown protons labelled a and f are observed indicating hydrogen binding between nitrate ion and the a and f protons. And upfield shifts of the thiacrown proton, labelled e is observed, while there are no shifts for b, c and d protons.

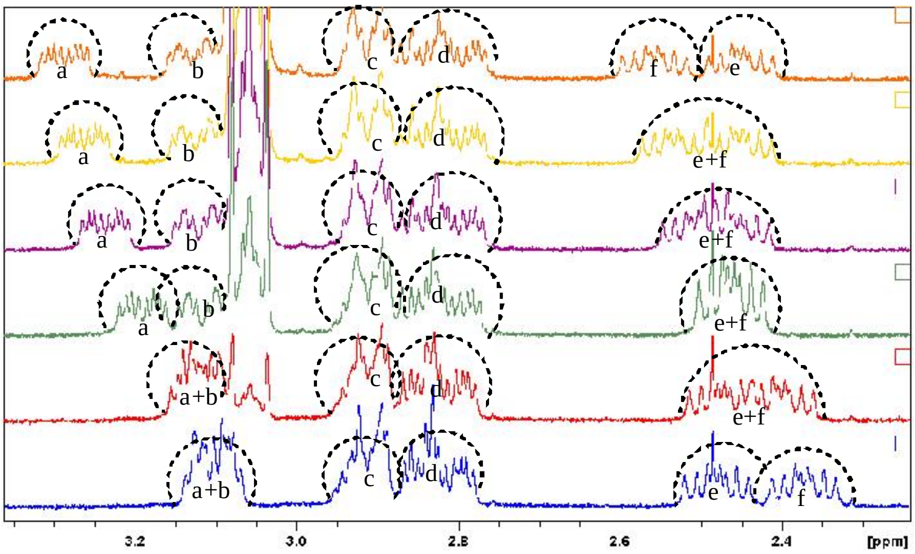

Figure 4.20 ^{1}H NMR (400 MHz) spectra of macrocycle **1** upon addition of equivalents of TBA nitrate Solvent CD$_3$CN; temperature: 293 K; [1] =1.5×10^{-6} mol dm^{-3}.

In this case, there was also some evidence of a second binding event on addition of a second equivalent of guest. However, due to the small shifts observed and problems with solubility it is difficult to obtain binding parameters for this interaction, which judging by the small shifts appears to be quite weak.

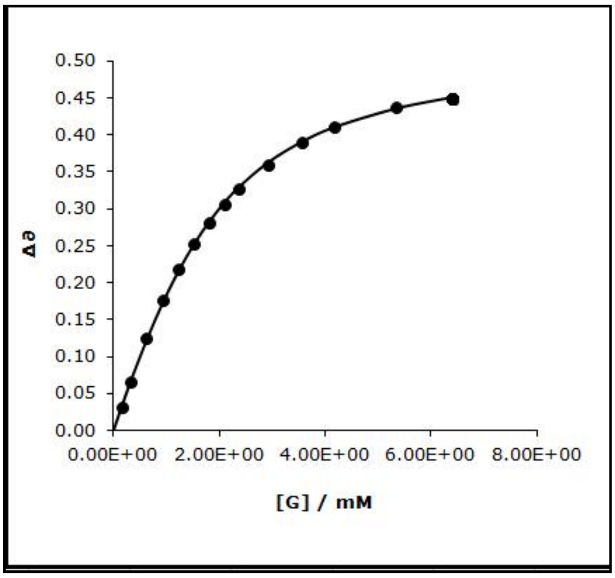

Figure 4.21 Binding curve obtained for addition of nitrate guest through analysis of the ^{1}H NMR titration data, monitoring the N*H* proton (H6) shift. Association constants were determined through fits of the ^{1}H NMR titration data. The line represents the fit to the fit to the model. $K_a=1.19\times10^3 M^{-1}$.

4.1.8 Summary of binding data for macrocycle 1

To aid comparison, the oxo anion binding data for macrocycle **1** are summarized in Table 4.1 while the shifts generated in the N*H* protons are shown in Figure 4.22 and Figure .

Table 4.1 Maximum shifts in NH resonance ($\Delta\delta$) and 1:1 anion association constants (K_a) of macrocycles **1**.[a]

Ion	K_a[M^{-1}]	$\Delta\delta$[ppm]
CH_3COO^-	$6.3\times10^2\pm5\%$	0.95
$(CH_2COO)^{2-}$	$7.7\times10^2\pm7\%$	0.45
NO_3^-	$1.2\times10^3\pm8\%$	0.52
ClO_4^-	$1.2\times10^2\pm2\%$	0.12
$H_2PO_4^-$	$2.8\pm15\%$	0.27
HSO_4^-	$5.6\times10^3\pm7\%$	0.22

[a]Anions added as TBA salts. The two figures below show plots of the chemical shift of the amine N*H* resonances macrocycle **1** versus equivalents of TBA salts. The first figure shows data for anions that can be added in excesses of >5 equivalents. Whilst the data shown in the second figure shows the effect of guests that cause precipitation of the guest at lower binding ratios.

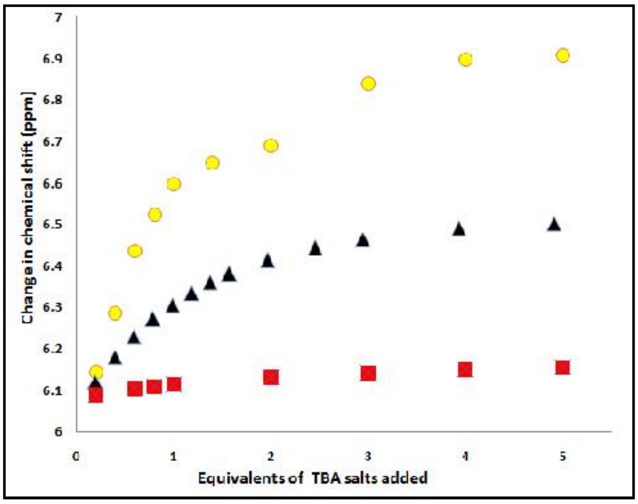

Figure 4.22 Chemical shift of amine N*H* resonances in macrocycle **1** on addition of TBA salts (OAc^-●, NO_3^-▲ andClO_4^-■).

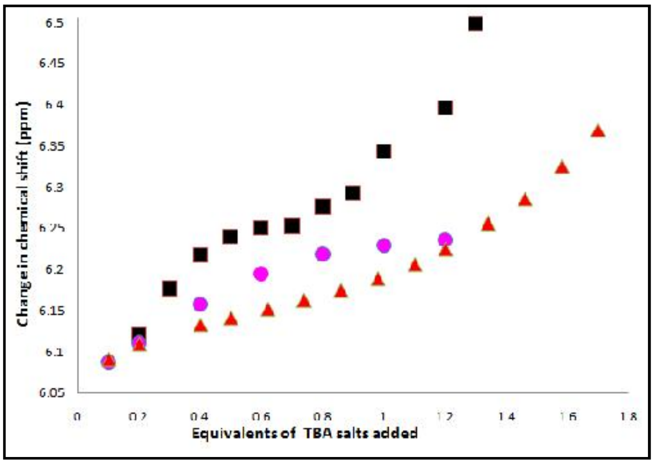

Figure 4.23 Chemical shift of amine N*H* resonances of macrocycle **1** on addition of TBA salts $(CH_2COO)^{2-}$ ■, HSO_4^- ●and $H_2PO_4^-$ ▲).

4.2 Titration of [Ru([9]aneS_3)(9-ethyl-9H-purin-6-amine)]$_3$ $(PF_6)_3$

The host-guest chemistry between the other hosts and the same oxo-anions investigated with host **1** were also explored. Titrations with macrocycle **2** and oxo guests give very similar results to those obtained with macrocycle **1** although the N*H* shifts tended to be larger and macrocycle **2** only precipitated after addition of higher molar equivalents of guests. The results from these experiments are summarized in Table 4.2.

Table 4.2 Maximum shifts in NH resonance (Δδ) and 1:1 anion association constants (K_a) of macrocycles 2.[a]

Ion	$K_a[M^{-1}]$	$\Delta\delta_{max}$[ppm]
AcO^-	$5.2\times10^2\pm4\%$	1.17
NO_3^-	$8.5\times10^2\pm1\%$	0.57
ClO_4^-	$2.1\times10^2\pm1\%$	0.12
$H_2PO_4^-$	$8.1\pm4\%$	0.50
HSO_4^-	$1.6\times10^2\pm3\%$	1.54

[a]Anions added as TBA salts.

As for macrocycle **1**, some of the anionic guest cause host **2** to precipitate relatively rapidly therefore the induced shifts are summarized in two separate figures.

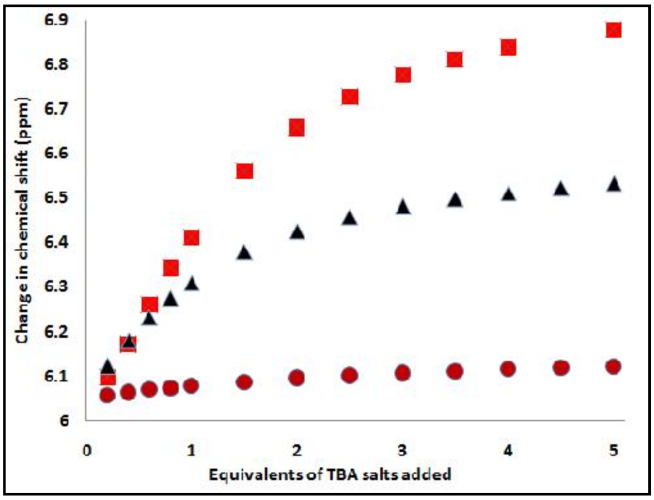

Figure 4.24 Plots of chemical shift of the amine N*H* resonances macrocycle 2 on addition of TBA salts (AcO^- ■, NO_3^- ▲ and ClO_4^- ●) .

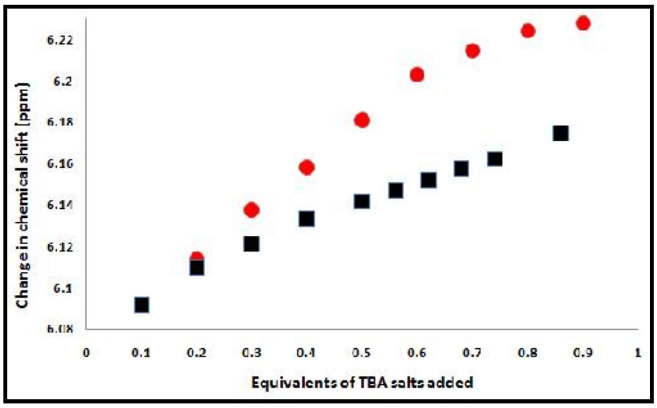

Figure 4.25 Plots of chemical shift of amine N*H* resonances macrocycle **2** versus equivalents of TBA salts (HSO_4^- ● and $H_2PO_4^-$ ■).

4.3 Titration of [Ru([9]aneS_3)(9-benzyl-9H-purin-6-amine)]$_3$(PF_6)$_3$ (3)

Macrocycle **3** also behaves in a similar manner to hosts **1** and **2**, but it precipitates more easily when guests are added, so only titrations with the trigonal guests acetate and nitrate could be fully completed. Interestingly, these experiments indicate that this host binds to these guests with slightly higher affinity than macrocycles **1** and **2**.

Table 4.3 Maximum shifts in NH resonance (Δδ) and 1:1 anion association constants (K_a) of macrocycles 2.[a]

Ion	K_a[M^{-1}]	Δδ[ppm]
AcO^-	$3.1\times10^3\pm2\%$	1.06
NO_3^-	$1.4\times10^3\pm5\%$	0.38

Anions added as TBA salts. Shifts are for 5 equiv. of anions added. [b]Error in the fit Over the data set is estimated at 4%.

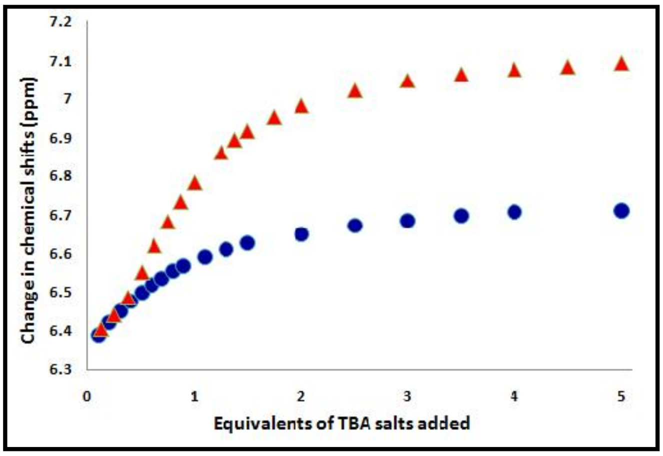

Figure 4.26 Plots of guest induced chemical shifts of the amine N*H* resonances of macrocycle **3** on addition of TBA salts (AcO^- ▲ and NO_3^- ●).

4.4 Titration of [Ru([9]aneS$_3$)(9-(4-methoxybenzyl)-9H-purin-6-amine)]$_3$ (PF$_6$)$_3$ (4)

The solubility of the macrocycle is similar to that of host **3**, rather than **1** and **2**, consequently only the same two guests could be studied. However the association constant values determined for macrocycles **4** with acetate and nitrate ions appear to be slightly lower than those for macrocycle **3**.

Table 4.4 Maximum shifts in NH resonance (Δδ) and 1:1 anion association constants (K_a) of macrocycles **4**.

Ion	K_a[M^{-1}]	Δδ[ppm]
AcO^-	$1.8\times10^3\pm4\%$	0.84
NO_3^-	$1.2\times10^3\pm3\%$	0.42

[a]Anions added as TBA salts.

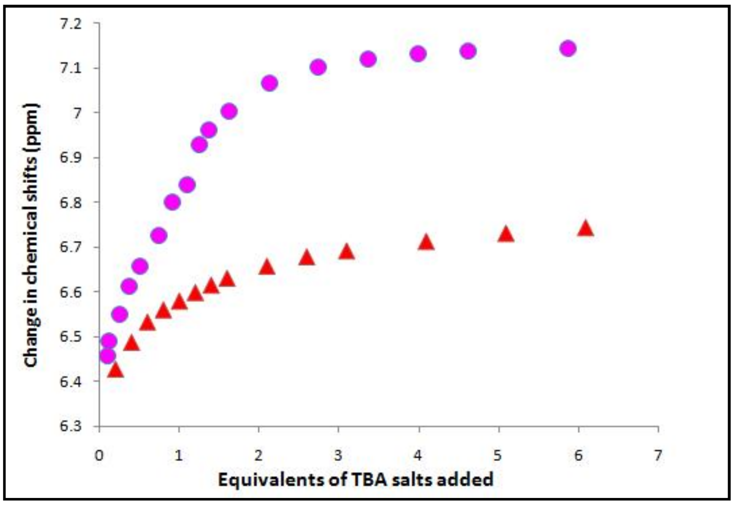

Figure 4.27 Plots of chemical shifts of the amine N*H* resonances of macrocycle **4** on addition of TBA salts (AcO^- ● and NO_3^- ▲).

4.5 Conclusions

Overall the titrations with oxo guests and all the hosts are similar. Although HSO_4^- binds more strongly to host **1**, generally the host cavities seem more suited to acetate, nitrate and perchlorate than other oxo guests; it is also notable that the acetate and nitrate guests do not cause the macrocycle to precipitate so easily. Indeed, other guests precipitated after addition of just a few molar equivalents. In these latter cases the data collected was incomplete, yielding less information on the binding between macrocycles and guests. For example, in the titration between macrocycles and the $H_2PO_4^-$, HSO_4^- and $(CH_2COO)_2^-$ guests, precipitation occurred after the addition of very small amounts of anion to macrocycles **3** and **4**. In both macrocycles **1** and **2** strong interactions were detected with OAc^-, NO_3^- and ClO_4^-in this order: NO_3^- >AcO^->ClO_4^-. In contrast, titrations of NO_3^- and OAc^- with macrocycle **3** and **4** showed the acetate ion binds more strongly than nitrate ion. The results indicate that, generally, triangular shaped guests like NO_3^-, AcO^- are bound more strongly than those of tetrahedral shape (e.g.; ClO_4^-). Taken the halide binding in consideration too, the general observed tendency of anion binding for all the macrocycles is Cl^- >Br^->>I^->AcO->NO_3^->ClO_4^->F^-. This trend broadly follows the basicity of the anions as expected for simple hydrogen bond donor and acceptor systems.[68,70] It is proposed that chloride and bromide bound more strongly than fluoride and oxo guests (which are more basic) due to greater geometric/size complementarity between each of the chloride, bromide and macrocycle cavities compared to the acetate, nitrate and iodide guests. [71-72] In addition, weaker binding is observed with the more basic and larger size nitrate and acetate anions due to unfavourable size complementarity.[73] In sharp contrast to macrocycle **1** and **2**, which exhibit low binding affinities for basic anions (OAc^-, NO_3^-), the macrocycles **3**, and **4** binds OAc^- and NO_3^- anions more strongly, perhaps due to the greater acidity of their N*H* moieties.[74] These investigations reveal that the macrocycles host cavities is of preferable complementary shape, size and electronegativity for halides in particular chloride and bromide, over the non-spherical oxo anions of guests (acetate, succinate, nitrate, hydrogen sulphate, and dihydrogen phosphate).

CHAPTER 5

5.1 Electrochemistry Studies

The electrochemical behavior of the trimetallic complexes described in the previous chapters was investigated by cyclic voltammetry. All electrochemistry was carried out using the same conditions (0.1M [nBu$_4$N][PF$_6$]; 20 °C, Pt working and counter electrodes, Ag$^+$/AgCl reference electrode, Sweep Rate 100 V s^{-1}). If the metal centres of [Ru([9]aneS$_3$)(9-methyladenine)]$_3$$^{3+}$(**1**), [Ru([9]aneS$_3$)(9-ethyladenine)]$_3$$^{3+}$(**2**), [Ru([9]aneS$_3$)(9-benzyl-9H-purin-6-amine)]$_3$$^{3+}$(**3**) and [Ru([9]aneS3)(9-(4-methoxybenzyl)-purin-6-amine)]$_3$$^{3+}$(**4**) are interacting they will not oxidize at the same potential. From simple electrochemical concepts it is expected that oxidation of metal centers in the complexes should occur in three steps. During each step, the potential for each ruthenium (II) oxidation will become greater; electrochemical data for previously reported **1** and new macrocycles **2 – 4** are given in Table 5. 1.

Table 5.1 Electrochemical Data for macrocycles **1**, **2**, **3** and **4** in CH$_3$CN (0.1 M [nBu$_4$N][PF$_6$]; 20 °C, Pt Electrodes, Sweep Rate 0.05 V s-^{1})

Complex	**$E_{1/2}$ $^{(a)}$ (1)/V**	**$E_{1/2}$ $^{(a)}$ (2)/V**	**$K_c$$^{(b)}$**	**$E_{1/2}$ $^{(a)}$ (3)/V**	**$K_c$$^{(b)}$**
1	0.7769	0.9119	1.94x10^2	1.2717	1.25x10^6
2	0.7891	0.9029	0.85x10^2	1.2657	1.41x10^6
3	0.7290	0.8668	2.17x10^2	1.1697	1.36x10^5
4	0.7919	0.9358	2.75x10^2	1.2716	4.92x10^5

(a) vs Ag/AgCl

(b) Kc values were calculated using log Kc = [ΔE1/2/0.059].

(c) Complexes are not fully reversible, therefore only E1 values are quoted.

Previous studies by Nazam Shan of the Thomas group have shown that macrocycle **1** displays three reversible one electron couples. This means at the platinum electrode the trimer undergoes three successive one-electron oxidations to yield species with **4**$^+$, **5**$^+$ and **6**$^+$ charges.

$$[Ru^{II}{}_3]^{3+} \xrightleftharpoons{-\ e^-} [Ru^{II}{}_2Ru^{III}]^{4+} \xrightleftharpoons{-\ e^-} [Ru^{II}Ru^{III}{}_2]^{5+} \xrightleftharpoons{-\ e^-} [Ru^{III}{}_3]^{6+} \qquad 5.1$$

The peak-to-peak separation for the first and second processes, ($\Delta E_{1/2}$(1-2), was found to be 0.135V. These results in a comproportionation constant, K_c, of 1.94x10^2 associated with the following equilibrium.

$$[Ru^{II}{}_3]^{3+} + [Ru^{II}Ru^{III}{}_2]^{5+} \rightleftharpoons 2[Ru^{II}{}_2Ru^{III}]^{4+} \qquad 5.2$$

For the second and third processes, $\Delta E_{1/2}$ (2-3) = 0.360 V. In this case the value of K_c is much higher at 1.25x10^6 and is associated with the following equilibrium.

$$[Ru^{II}{}_2Ru^{III}]^{4+} + 2[Ru^{III}{}_3]^{6+} \rightleftharpoons 2[Ru^{II}Ru^{III}{}_2]^{5+} \qquad 5.3$$

The fact that K_c (5-3) is significantly larger than K_c (5-2) suggests that the **1**$^{5+}$ state displays a stronger intermetallic interaction compared with **1**$^{4+}$. This is in direct contrast to other redox-active triangular complexes containing a tritopic bridging ligand,[75] in which the spacing are approximately constant. This is as would be expected if there is no variation on the pair wise metal-metal interactions across the redox series. The unusual behavior of the macrocycle implies that on moving from **1**$^{4+}$ to **1**$^{5+,}$ there is much greater delocalisation of the positive charges, making the final oxidation more difficult than it would be otherwise. Complex **2** is also characterised by three reversible one-electron couples, but – compared to **1** these are slightly shifted, occurring at +0.789, +0.903 and +1.267 V vs Ag/Cl respectively. Again, ΔE ≤ 100 and │Ipa/Ipc│ = **1**. These values of $E_{1/2}$ closely match those for complex **1** meaning that both complexes **1** and **2** exhibit similar comproportionation constants (see Equation 5.1): the peak to peak separation for the first and second processes for **2** ($\Delta E_{1/2}$ (1-2), is 0.1138 V. This results in a comproportionation constant, Kc, of 0.85 x 10^2. For the second and third processes, $\Delta E_{1/2}$ (5-3) = 0.7763; in this case the value of Kc is much higher at 1.41 x 10^6. These figures indicate that similar levels of electron delocalization are observed within the analogous mixed valence states of both macrocycles.

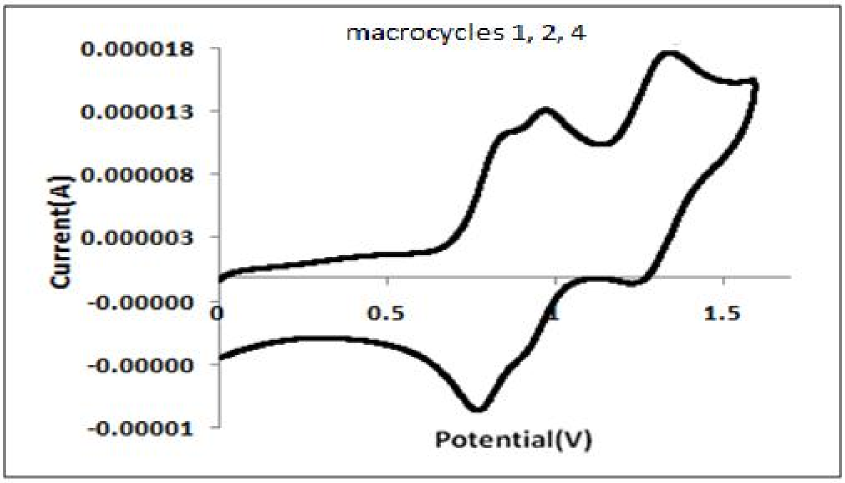

Figure 5.1 Electrochemical CV data for macrocycle **2**. The responses of macrocycle **4** and **1** are very similar.

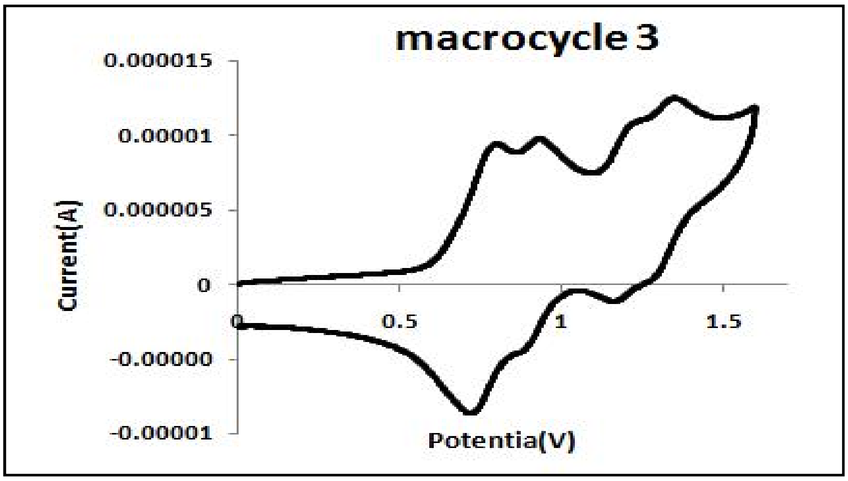

Figure 5.2 Electrochemical CV data for macrocycle **3**.

Although the electrochemical properties of macrocycles **1**, **2** and **4** are very similar, those of **3** are slightly different. Another oxidation process appears in macrocyle **3** after the third metal based oxidation at 1.361 V.This peak is assigned to a ligand-based oxidation (which, in similar conditions, occurs at 1.466 V in the free ligand).

Complexes **3** and **4** produce similar electrochemical results. For complex **4** the difference between the first and second process is $\Delta E_{1/2}(5\text{-}2)$ =0.1439, this leads to a value of K_c very close to that of complex **3**. For the second and third process, $\Delta E_{1/2}(5\text{-}3)$= 0.3358, leading to a value of K_c= 4.92x10^5, again this is similar to **3** and slightly lower than **1** and **2**. These results indicate that, as might be expected, the nature of the bridging ligands affects the electronic delocalization between metal centres. Although this effect is not simple as the two MV states are shifted by contrasting amounts.

5.3 Electrochemistry titrations on newly reported trinuclear hosts

Given the results described in 4.2, the electrochemical response of macrocycles **1 – 4** to guest binding was explored. The support electrolyte used in the experiment was a 0.1 M solution of tetrabutyl ammonium hexafluorophosphate (TBAF) in dry acetonitrile and all cyclic voltammograms were obtained under an atmosphere of dinitrogen. A background cyclic voltammogram of the TBAF solution was initially obtained for all experiments in order to see that the electrodes were clean and working. The mass added to the solution every time was precise and once added formed a host solution with a concentration of 3×10^{-3} M.

The square wave voltammograms of the host was then measured in the 0-1.6 V range and as expected produced the distinctive three peaks. Potentials greater than 1.6 V were not necessary because no oxidation is present above this value. The voltammograms clearly showed the reversible generation of the two mixed valence states at potentials between the three peaks. The guest anions were then titrated into the solution. Initially, the guests tested with macrocycles were structurally relatively simple spherical anions: fluoride, chloride, bromide, and iodide. All of the anions used were present as tetrabutylammonium salts. Solutions of the anions were made up so that they were 25 times more concentrated than the host ensuring that when volumes of guest anion were titrated into the host solution, there would be a minimal change in the volume inside the cell therefore keeping the concentrations of the species in solution relatively constant. Following the first addition of 0.25 equivalents of guest, the concentration of guest in the solution was increased to 0.5 mole equivalents and then raised stepwise to 0.75, 1, 2, 3 and 4 mole equivalents respectively. After each titration, the square wave voltammetry was used to monitor if any electrochemical changes had taken place. The **SWVs** for the progressive increase in anion concentration were plotted on the same axis as one another. This made it very easy to see any shifts upon addition of anion.

5.4 Halide titrations

5.4.1 Titration macrocycle 1 with guests

5.4.1.1 Fluoride guest

On initial inspection of the results, shown in Figure 5.4, it is clear that the F^- anion has a large effect on the oxidations of **1**, producing cathodic shifts. For example, the third peak $E_p(3)$ at 1.27 V is shifted to 1.19 after addition 3 mole equivalents of TBAF. It is also clear that there is a gradual cathodic shift in $E_p(3)$ upon each addition of guest Figure 5.3.

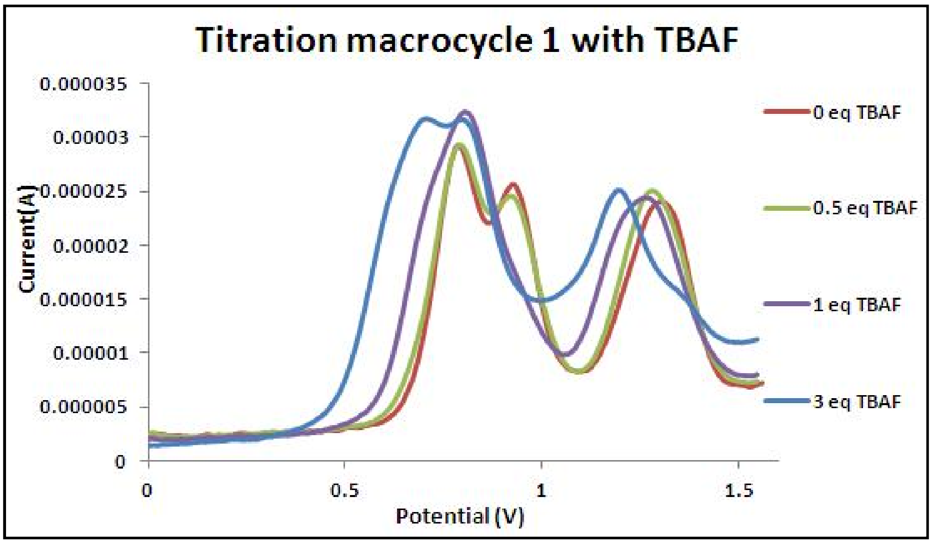

Figure 5.3 SWV of macrocycle **1** upon the addition of aliquots of F.Electrolyte: 0.1 M $TBAPF_6/CH_3CN$ (concentration of macrocycle 1: 0.5 mm. T = 293 K, potential compared to Ag/AgCl reference).

There is also a big shift of 110 mV in $E_p(2)$ after addition of 1 mole equivalent of F^-. The shifts for $E_p(1)$ are more difficult to interpret than those the $E_{1/2}(2)$ and $E_{1/2}(3)$. On addition of 1 mole equivalent of F^- $E_p(1)$ and $E_p(2)$ appear to merge, this may be the result of the high shift for second oxidation compared to the lower shift for first oxidation. After addition of 3 mole equivalents of F^- the first and second oxidation separate again. Clearly, these data show that not all oxidations are affected by the same amount when a guest binds into a site on a host: $E_p(1)$ is relatively less affected by the binding of F$^-$, but $E_p(2)$ and $E_p(3)$ show significant cathodic shifts. This indicates that the two mixed valence state ($Ru^{II}Ru^{III}Ru^{III}$) and ($Ru^{III}Ru^{III}Ru^{III}$) becomes easier to access when the anion is bound.

5.4.1.2 Chloride guest

TBACl is redox active in the potential window used. The SWV curves of TBACl exhibit one cathodic peak, which lies in the potential range between the reversible oxidation peaks $E_p(2)$ and $E_p(3)$ of macrocycle **1**. However, this guest also has a large effect on the electrochemistry of the host – Figure 5.5. The third peak $E_p(3)$ at 1.28 V is shifted to 1.22 V even after addition of 0.25 mole equivalents of TBACl. Addition of more than 1 mole equivalent of Cl$^-$ has little effect on the potential of the macrocycle oxidations, indicating a strong interaction.

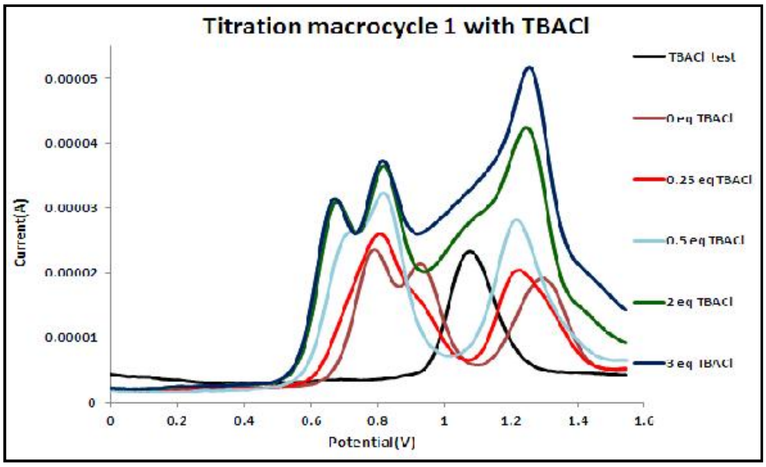

Figure 5.4 SWV of macrocycle **1** upon the addition of aliquots of TBACl. Electrolyte: 0.1 M $TBAPF_6/CH_3CN$ (concentration of macrocycle 1: 0.5 mm. T = 293 K, potential compared to Ag/AgCl reference).

Again $E_p(1)$ is most affected by the binding of Cl$^-$ with the mixed valence states ($Ru^{II}Ru^{II}Ru^{III}$), ($Ru^{II}Ru^{III}Ru^{III}$) becoming stabilized when the anion is bound.

5.4.1.3 Bromide guest

Bromide ion is also redox active. The first cathodic peak of TBABr lies between the potentials for oxidation peaks $E_p(1)$ and $E_p(2)$ of the macrocycle and a second bromide oxidation is observed in the potential between $E_p(2)$ and $E_p(3)$. However, after 0.25 mole equivalent the first anodic peak of TBABr merged into the reversible cathodic peaks $E_p(1)$, $E_p(2)$ of macrocycle **1**. Notably, Figure 6 clearly shows there is no shift in peak $E_p(3)$. Therefore, again, in this titration the mixed valence states ($Ru^{II}Ru^{II}Ru^{III}$), ($Ru^{II}Ru^{III}Ru^{III}$) become stabilized when the anion is bound.

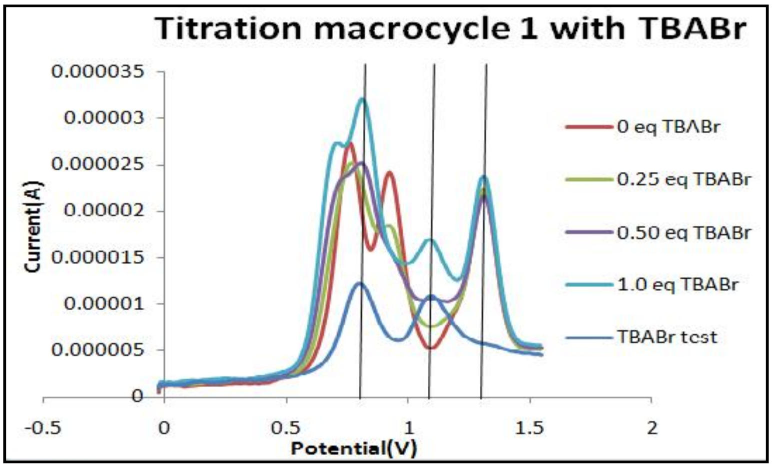

Figure 5.5 SWV of macrocycle **1** upon the addition of aliquots of TBABr. Electrolyte: 0.1 M $TBAPF_6/CH_3CN$ (concentration of macrocycle 1: 0.5 mm. T = 293 K, potential compared to Ag/AgCl reference).

5.4.1.4 Iodide guest

The last halide anion to be investigated using the same conditions and concentrations used for F^- was iodide. Although iodide is redox active, it is clear that, even as the concentration of guest was gradually increased from 0 mole equivalents to 3 molar equivalents see Figure 5.6 virtually no shift in the oxidation potentials of the macrocycle occurs.

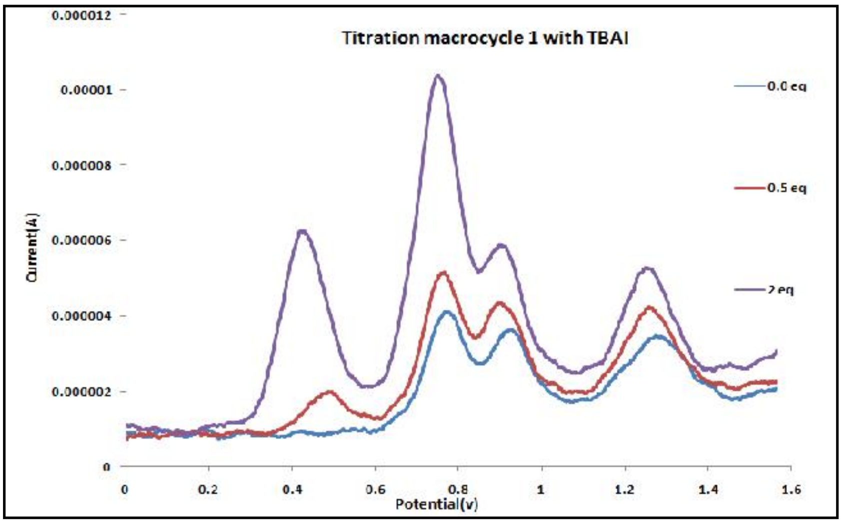

Figure 5.6 SWV of macrocycle **1** upon the addition of aliquots of TBAI. Electrolyte: 0.1 M TBAPF$_6$/CH$_3$CN (concentration of macrocycle 1: 0.5 mm. T = 293 K, potential compared to Ag/AgCl reference).

Table 5.2 below summarizes the maximum changes in electrochemistry for host **1** calls by anion guests:

Table 5.2 shows Maximum shifts in the electrochemistry of macrocycle **1** induced by halide anions.

Ion	**$\Delta E_p(1)$ (mV)**	**$\Delta E_p(2)$ (mV)**	**$\Delta E_p(3)$ (mV)**
F$^-$	-71	-119	-100
Cl$^-$	-120	-101	-78
Br$^-$	-81	-131	-35
I$^-$	-21	-45	-42

5.4.2 Titration of macrocycle 2 with halide guests

The electrochemical response to halide binding of the three newly synthesized macrocycles were also reported and compared to macrocycle **1**. This study began with host **2**.

5.4.2.1 Fluoride guest

Inspection of these results shown in Figure 5.7 reveals that the third peak $E_p(3)$ is shifted by up to 130 mV Figure 5.7.

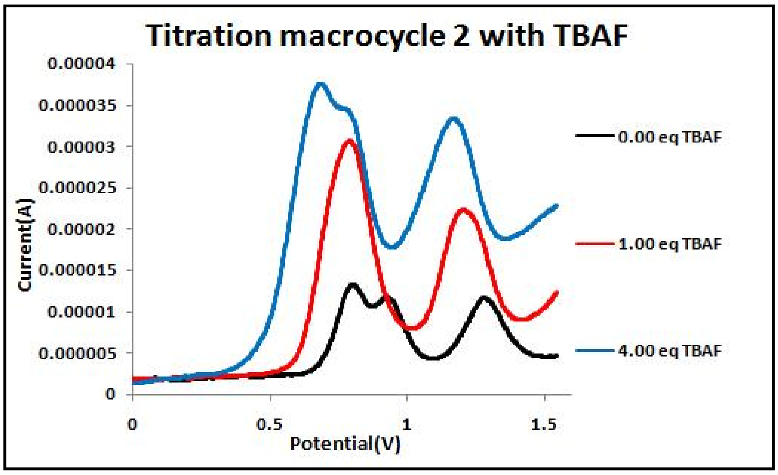

Figure 5.7 SWV of macrocycle **2** upon the addition of aliquots of F^-. Electrolyte: 0.1 M $TBAPF_6/CH_3CN$ (concentration of macrocycle 1: 0.5 mm. T = 293 K, potential compared to Ag/AgCl reference).

A shift of 180 mV occurs in $E_p(2)$ after addition of 3 molar equivalents of F^-. As for host **1**, the shifts present for $E_p(1)$ are more difficult to interpret than those the $E_p(2)$ and $E_p(3)$. On addition of 0.5 mole equivalents of F^- there appears to be one peak for $E_p(1)$ and $E_p(2)$. This is due to the high shift for second oxidation and lower shift for first oxidation, but after addition 3 equivalents of F^- two oxidations are observed again. Clearly the SWV behavior of macrocycle **2** is very similar to that of macrocycle **1**. It is noteworthy that in both cases there are no shifts after addition 3 mole equivalents in both macrocycles.

5.4.2.2 Chloride guest

Again it appears that Cl^- has a strong interaction with the host. In particular, the third peak $E_p(3)$ at 1.35 V is shifted to 1.19 after addition of **2** mole equivalent of TBACl and there is no more shifting after addition of 2 mole equivalents. After addition 0.75 mole of guest the oxidation peaks $E_p(1)$ and$E_p(2)$ of macrocycle **1** and the oxidation peak of the guest cannot be seen separately. After addition 3 moles of Cl^- equivalents the first and second oxidation spread again. A big shift of 130 mV is noticed in $E_p(2)$, and $E_p(1)$ after addition of 3 mole equivalent of Cl^-.

Thus, the titration of macrocycle **2** with TBACl is also very similar with to that of macrocycle **1**. But there is some difference in solubility: macrocycle **1** precipitates after the addition of 3 mole equivalents whilst macrocycle **2** precipitates after the addition of 5 mole equivalents. Although both macrocycles **1** and **2** exhibit large electrochemical shifts, larger perturbations were observed for the latter with chloride ion than for macrocycle **1**: $E_p(1)$, $E_p(2)$ and $E_p(3)$ of macrocycle **2** shift by 130 mV, 120 mV and 140 mV respectively. Compared to shifts of 100 mV, 100 mV and 80 mV for **1**.

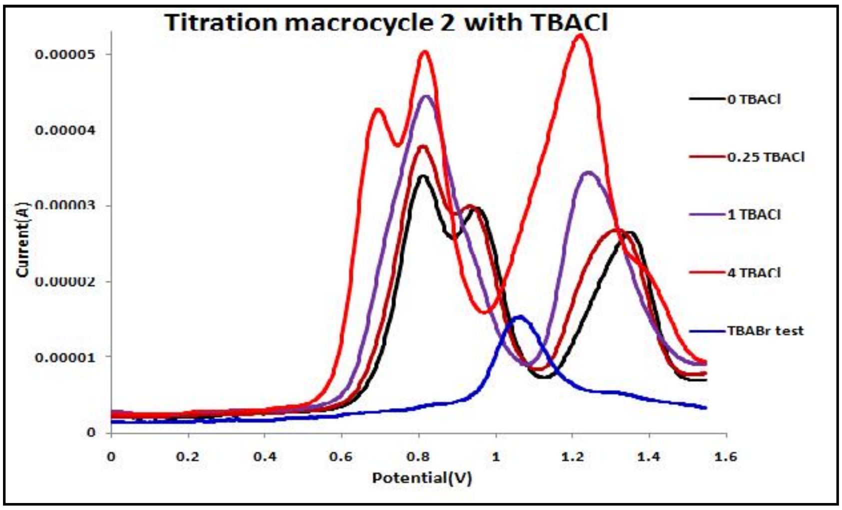

Figure 5.8 SWV of macrocycle **2** upon the addition of aliquots of TBACl. Electrolyte: 0.1 M $TBAPF_6/CH_3CN$ (concentration of macrocycle 1: 0.5 mm. T = 293 K, potential compared to Ag/AgCl reference).

5.4.2.3 Bromide guest

Again, some differences were observed in comparing the titration of macrocycles **1** and **2** with this anion. The biggest difference was that, although no shifts were observed for $E_p(3)$ of macrocycle **1**, measurable shifts were found for $E_p(3)$ of macrocycle **2**.

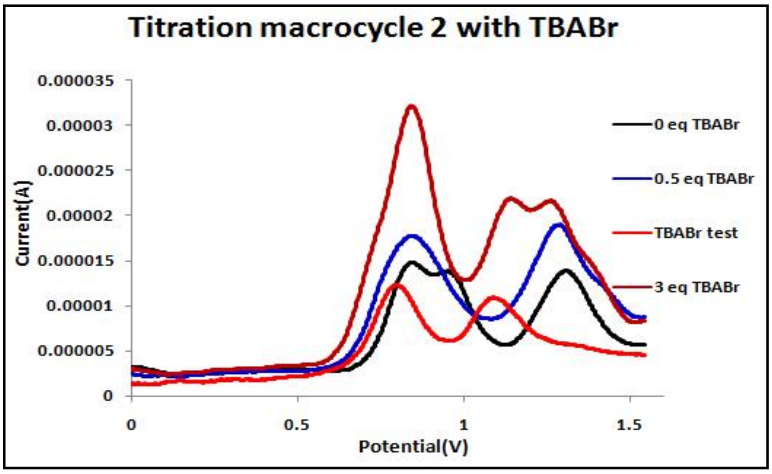

Figure 5.9 SWV of macrocycle **2** upon the addition of aliquots of TBABr. Electrolyte: 0.1 M $TBAPF_6/CH_3CN$ (concentration of macrocycle 1: 0.5 mm. T = 293 K, potential compared to Ag/AgCl reference).

5.4.2.4 Iodide guest

The concentration of guest was gradually increased from 0 mole equivalents to 1 mole equivalents see Figure 5.10. Further addition of anion leads to no shift in potential of new wave.

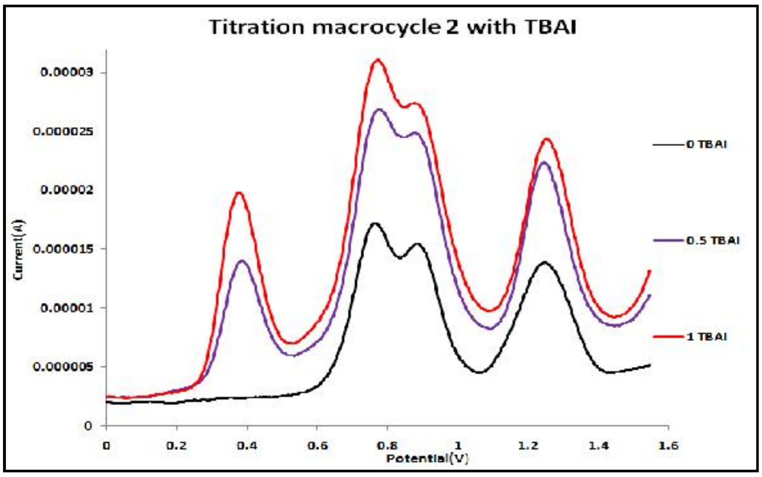

Figure 5.10 SWV of macrocycle **2** upon the addition of aliquots of TBAI. Electrolyte: 0.1 M $TBAPF_6/CH_3CN$ (concentration of macrocycle 1: 0.5 mm. T = 293 K, potential compared to Ag/AgCl reference).

Again, as the table shows, there is no change the values for $E_p(1)$ and $E_p(3)$ during the titration. The values for $E_p(2)$ show very small shift from 0.921 V to 0.912 V. This suggests that both macrocycles **1** and **2** show weak binding to iodide ion. The possible reason for this behavior may be the size of iodide is not being complementary with the cavity macrocycles and the weak negative iodide ion charge, resulting in very weak polarization.

Table 5.3 below summarizes the maximum changes in electrochemistry for host **2** calls by anion guests:

Table 5.3 Maximum shifts in the electrochemistry of macrocycle **2** induced by halide anions.

Ion	**$\Delta E_p(1)$ (mV)**	**$\Delta E_p(2)$ (mV)**	**$\Delta E_p(3)$ (mV)**
F^-	-130	-180	-131
Cl^-	-131	-121	-142
Br^-	merged peak		-40
I^-	-04	-09	-02

5.4.3 Titration of macrocycle 3 with halide guests

5.4.3.1 Fluoride guest

The concentration of guest was gradually increased from 0 mole equivalents to 2 mole equivalents. When the concentration exceeded 2 mole equivalents it was noticed that the product precipitated out of solution. Nevertheless fluoride ion has strong effects on the oxidations of **3** in the 0-1.6 V window.

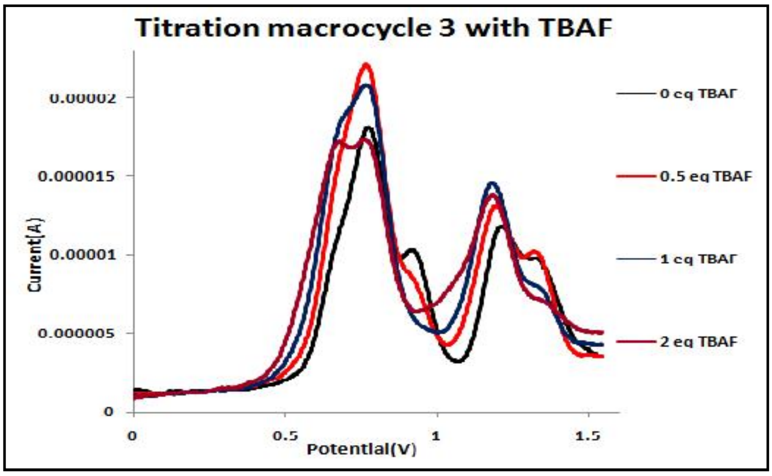

Figure 5.11 SWV of macrocycle **3** upon the addition of aliquots of TBAF. Electrolyte: 0.1 M TBAPF$_6$/CH$_3$CN (concentration of macrocycle 1: 0.5 mm. T = 293 K, potential compared to Ag/AgCl reference).

Again, not all oxidations are affected by the same amount when this guest binds to the host, with E$_p$(3) being relatively less affected by the binding of F$^-$ and with E$_p$(1) and E$_p$(2) showing large shifts, it is seen that obtaining the first and second mixed valence states (Ru^{II}Ru^{II}Ru^{III} ,Ru^{II}Ru^{III}Ru^{III}) becomes easier when the anion is bound.

5.4.3.2 Chloride guest

Again, the chloride ion has a strong effect on oxidations in the window of 0-1.6 V, as it seems that chloride anion is a suitable size for the cavity of the host.

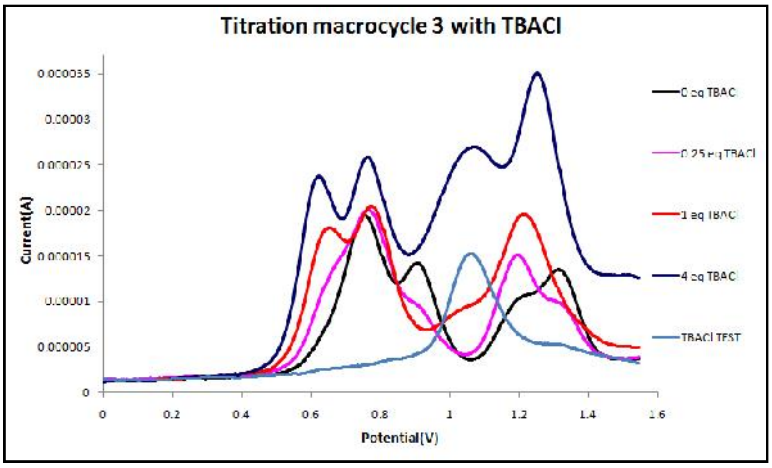

Figure 5.12 SWV of macrocycle **3** upon the addition of aliquots of TBACl. Electrolyte: 0.1 M TBAPF$_6$/CH$_3$CN (concentration of macrocycle 1: 0.5 mm. T = 293 K, potential compared to Ag/AgCl reference).

After addition of 4 mole equivalents of Cl$^-$, E$_p$(1) and E$_p$(2) are shifted by 140 mV and 150 mV (Figure 5. 13). These shifts to lower potential indicate that the host becomes easier to oxidise to the Ru^{II}Ru^{II}Ru^{III}and Ru^{II}Ru^{III}Ru^{III} states. In contrast, E$_p$(3) shows smaller changes

5.4.3.3 Bromide guest

As with chloride the oxidation peak current increase during the titration.

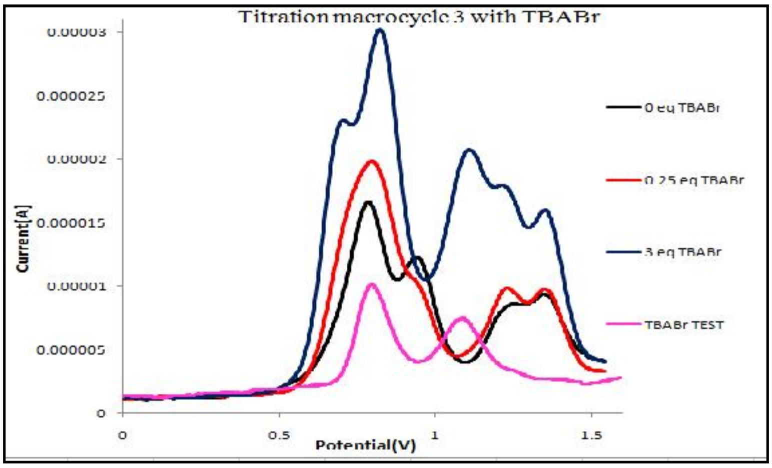

Figure 5.13 SWV of macrocycle **3** upon the addition of aliquots of TBABr. Electrolyte: 0.1 M $TBAPF_6/CH_3CN$ (concentration of macrocycle 1: 0.5 mm. T = 293 K, potential compared to Ag/AgCl reference).

The electrochemical activity of Br^- it self makes the shifts for $E_p(1)$ and $E_p(2)$ more difficult to interpret than that for $E_p(3)$. On addition of 3 mole equivalents of Br^- there appears to be shift of 30 mV.

5.4.3.4 Iodide guest

Again this anion produced no real detectable change in the electrochemistry of this host. Table 5.4 below shows the maximum changes in electrochemistry for host **3** calls by anions guests.

Table 5.4 Maximum shifts in the electrochemistry of macrocycle **3** induced by halide anions.

Ion	**$\Delta E_p(1)$/mV**	**$\Delta E_p(2)$/mV**	**$\Delta E_p(3)$/mV**
F^-	-105	-160	-40
Cl^-	-140	-150	merging peak
Br^-	merging peak		-40

5.4.4 Titration of macrocycle 4 with halide guests

5.4.4.1 Fluoride guest

In this titration, shifts were similar with macrocycles **1**, **2** and **3**. Although, due to this host’s improved solubility up to 7 equivalents of guest can be added before precipitation of the macrocycle occurs.

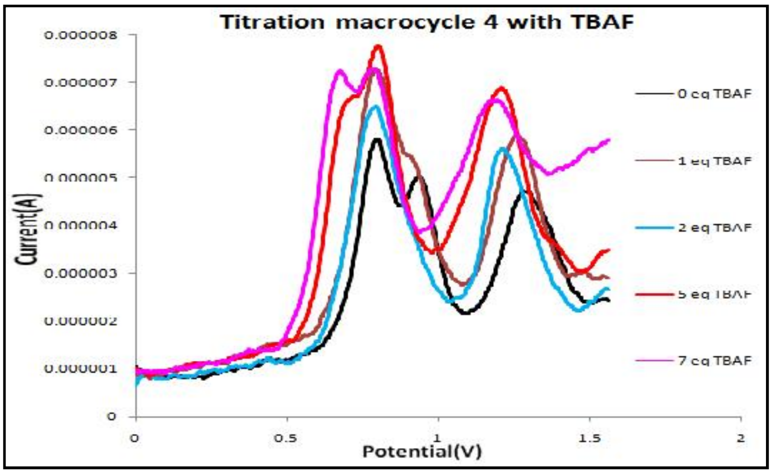

Figure 5.14 SWV of macrocycle **4** upon the addition of aliquots of TBAF. Electrolyte: 0.1 M $TBAPF_6/CH_3CN$ (concentration of macrocycle 1: 0.5 mm. T = 293 K, potential compared to Ag/AgCl reference).

5.4.4.2 Chloride guest

The crucial difference between this titration and previous hostsis that $E_p(1)$ and $E_p(2)$ merge and there is no further shifts in this merged peak after 2 mole equivalents host are added.

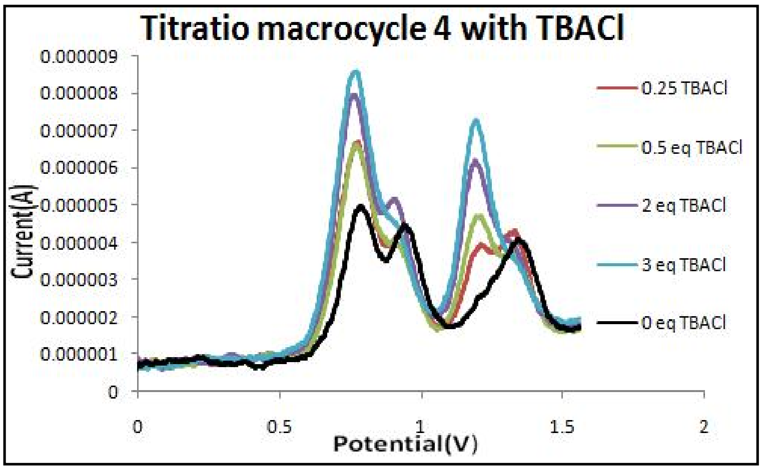

Figure 5.15 SWV of macrocycle **4** upon the addition of aliquots of TBACl. Electrolyte: 0.1 M $TBAPF_6/CH_3CN$ (concentration of macrocycle 1: 0.5 mm. T = 293 K, potential compared to Ag/AgCl reference).

5.4.4.3 Bromide guest

Titrations with TBABr and macrocycle **4** showed less distinctive changes than the same experiments with hosts **1–3**, as in this case the host and guest electrochemical couples merge to produce two relatively poorly defined peaks.

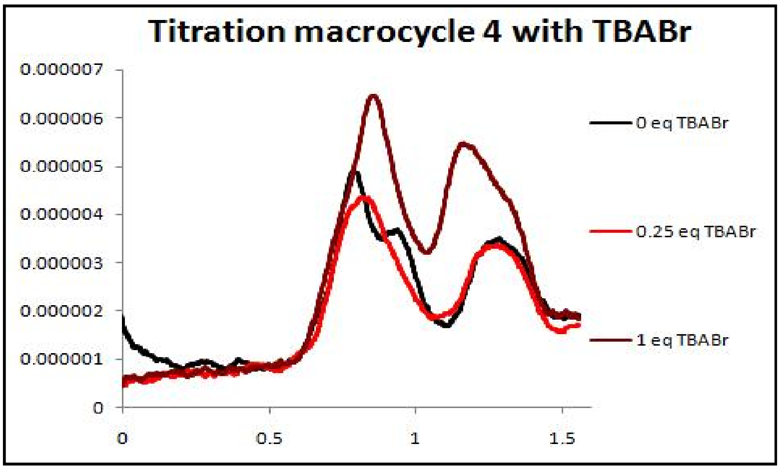

Figure 5.16 SWV of macrocycle **4** upon the addition of aliquots of TBABr. Electrolyte: 0.1 M $TBAPF_6/CH_3CN$ (concentration of macrocycle 1: 0.5 mm. T = 293 K, potential compared to Ag/AgCl reference).

Table 5.5 below shows the maximum changes in electrochemistry for host **4** calls by anion guests:

Table 5.5 Maximum shifts in the electrochemistry of macrocycle **4** induced by halide anions.

Ion	**$\Delta E_p(1)$/mV**	**$\Delta E_p(2)$/mV**	**$\Delta E_p(3)$/mV**
F^-	-120	-149	-110
Cl-	merged peak		merged peak
Br-	merged peak		merged peak

5. 5 Oxo-anion titrations

Since NMR studies showed significant binding interactions with oxo anions, the effect of these guests on the electrochemistry of the macrocycles was also investigated

5.5.1 Titration of macrocycle 1 with the guests

5.5.1.1 Perchlorate guest

ClO_4^- is a relatively large anion whose size may be not be complementary with the cavity of the host. The results of the titration of ClO_4^- against macrocycle **1** are shown in Figure 5.17. The addition of even a large excess of perchlorate ion (6 mole equivalents) to a solution of macrocycle **1** caused no significant changes in the oxidation states.

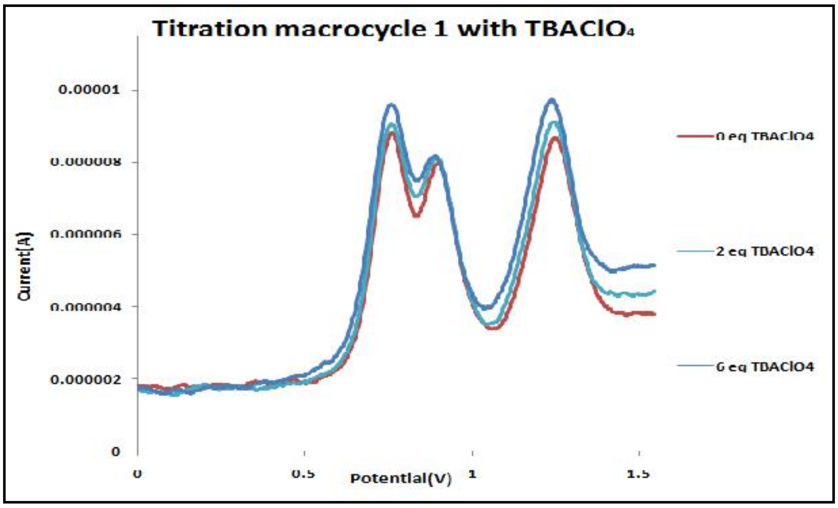

Figure 5.17 SWV of macrocycle **1** upon the addition of aliquots of ClO4-. Electrolyte: 0.1 M $TBAPF_6/CH_3CN$ (concentration of macrocycle 1: 0.5 mm. T = 293 K, potential compared to Ag/AgCl reference).

5. 5.1.2 Nitrate guest

The results of the titration of NO_3^- against macrocycle **1** are shown below in Figure 5.19. Note that addition of 0.25 and 0.5 mole equivalents also induce very small shifts in the SWV and are not shown in these results.

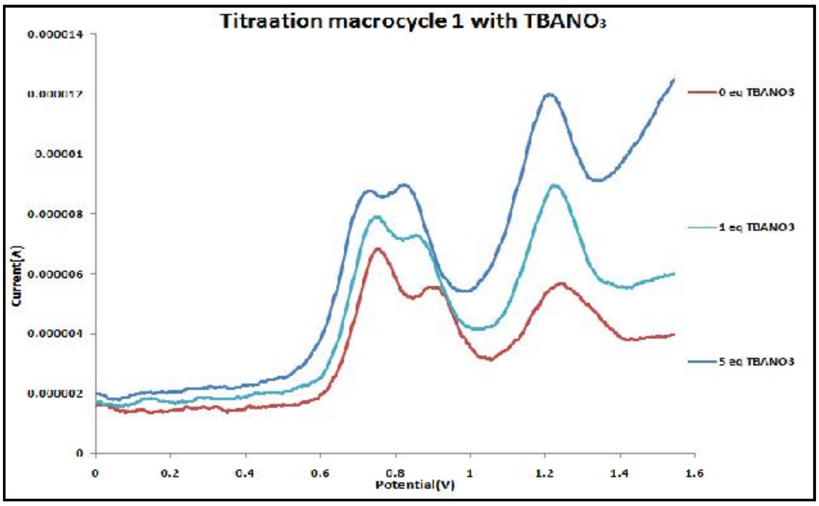

Figure 5.18 SWV of macrocycle **1** upon the addition of aliquots of NO3-. Electrolyte: 0.1 M $TBAPF_6/CH_3CN$ (concentration of macrocycle 1: 0.5 mm. T = 293 K, potential compared to Ag/AgCl reference).

On inspection of these results shown in Figure 5.19. There are small measurable shifts in $E_p(1)$, $E_p(2)$ and $E_p(3)$ upon addition of larger concentration of guest. After addition of 5 mole equivalents of NO_3^-, the three peaks have been shifted by 50 mV,70 mV and 40 mV respectively.

5.3.1.7 Acetate guest

There are in fact very small cathodic shifts induced this guest. The compound precipitated after addition 3 mole equivalents. There are no shifts at $E_p(3)$ after addition 2 mole equivalents of acetate ion, although interestingly these shifts that *are* observed are anodic.

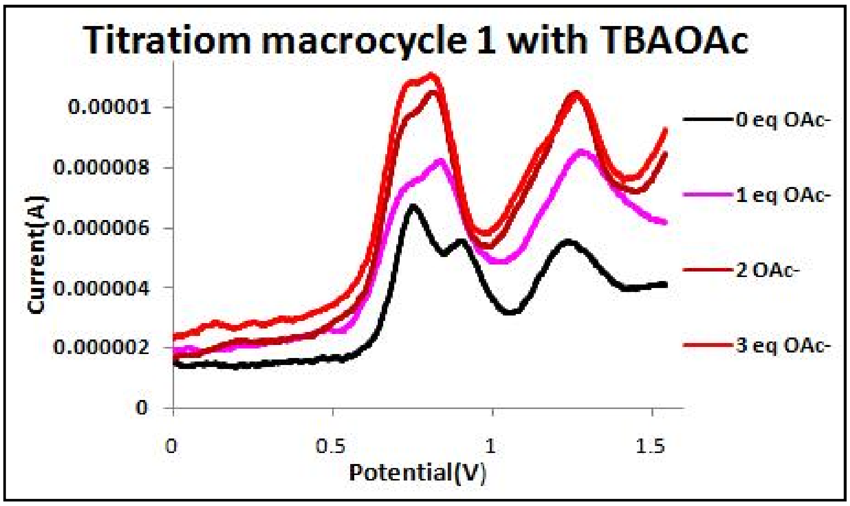

Figure 5.19 SWV of macrocycle **1** upon the addition of aliquots of TBAOAc. Electrolyte: 0.1 M $TBAPF_6/CH_3CN$ (concentration of macrocycle 1: 0.5 mm. T = 293 K, potential compared to Ag/AgCl reference).

Table 5.6 below shows the maximum changes in electrochemistry for host **1** calls by anion guests.

Table 5.6 Maximum shifts in the electrochemistry of macrocycle **1** induced by oxo anions .

Ion	**$\Delta E_p(1)$**	**$\Delta E_p(2)$**	**$\Delta E_p(3)$**
ClO_4^-	-10	-10	-35
NO_3^-	-50	-72	-44
AcO^-	-15	-117	-2

5.3.2 Titration of macrocycle 2 with the guests

5.3.2.1 Perchlorate guest

As for macrocycle **1**, perchlorate ion causes small shifts in the electrochemistry of **2**. The third peak $E_p(3)$ shows a cathodic shift of 80 mV Figure 5. 20. However, there are only small shifts for peaks $E_p(1)$ and $E_p(2)$ of 20 mV and 30 mV respectively. It is noteworthy that $E_p(1)$ and $E_p(2)$ shifts for both macrocycles **1** and **2** were similarly very small. In stark contrast the $E_p(3)$ peaks for macrocycle **2** shifted significantly compared to the $E_p(3)$ peaks of **1**.

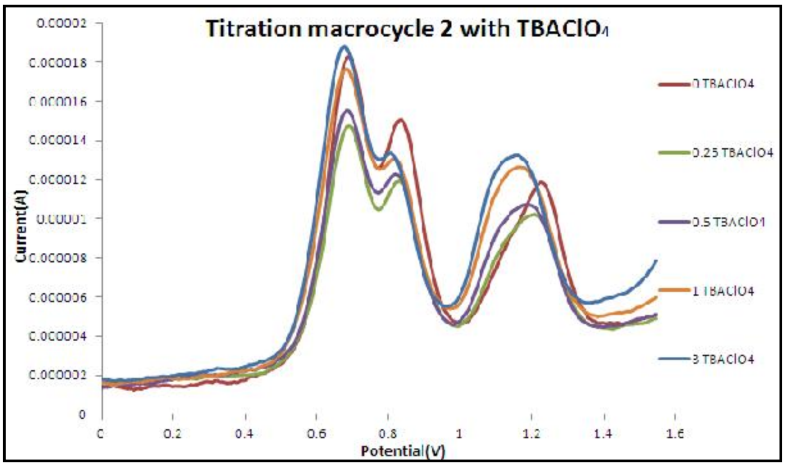

Figure 5.20 SWV of macrocycle **2** upon the addition of aliquots of $TBAClO_4$. Electrolyte: 0.1 M $TBAPF_6/CH_3CN$ (concentration of macrocycle 1: 0.5 mm. T = 293 K, potential compared to Ag/AgCl reference).

5.3.2.6 Acetate guest

The concentration of guest was gradually increased from 0 mole equivalents to 4 mole equivalents - see Figure 5.21. Further addition of anion leads to no further shifts in potential of new wave. The third peak $E_p(3)$ at 1.294 V is shifted to 1.193 V after addition of 4 mole equivalents of TBAOAc Figure 5. 22 clearly show this large shift in peak $E_p(3)$. Also oxidation peaks $E_p(1)$ and $E_p(2)$ of the host merge. This is a result of the high shifting of the second oxidation and low shifting for the first oxidation. Again, this clearly illustrates that not all oxidations are affected by the same amount when a guest binds to the host.

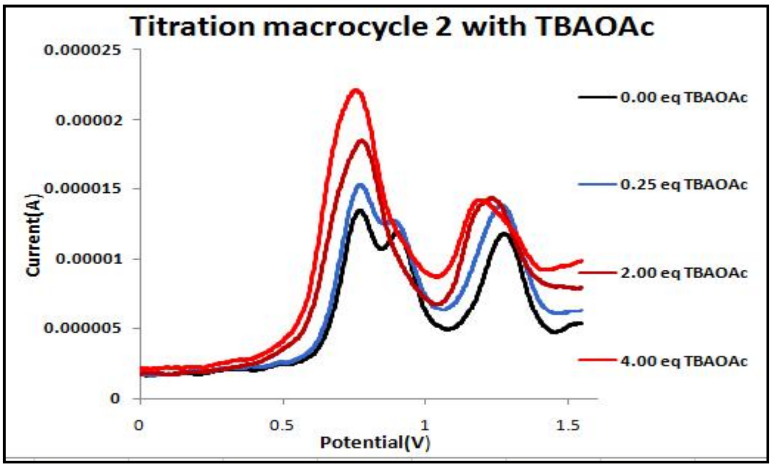

Figure 5. 21 SWV of macrocycle **2** upon the addition of aliquots of TBAOAc. Electrolyte: 0.1 M TBAPF$_6$/CH$_3$CN (concentration of macrocycle 1: 0.5 mm. T = 293 K, potential compared to Ag/AgCl reference).

5.3.3.7 Nitrate guest

The concentration of nitrate was gradually increased from 0 to 3 mole equivalents. Further addition of anion leads to no shifts in potential of new wave. Figure 5.22 clearly shows the peaks E$_p$(1) and E$_p$(2) are shifted more than peak E$_p$(3).

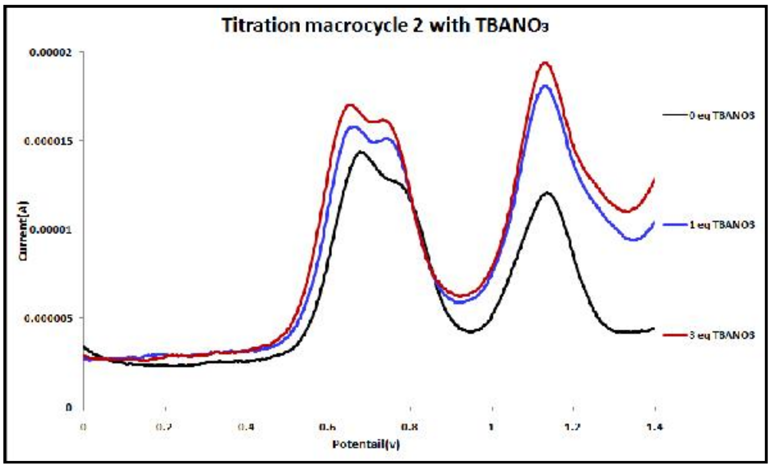

Figure 5.22 SWV of macrocycle **2** upon the addition of aliquots of TBANO$_3$. Electrolyte: 0.1 M TBAPF$_6$/CH$_3$CN (concentration of macrocycle 1: 0.5 mm. T = 293 K, potential compared to Ag/AgCl reference).

Table 5.7 below shows the maximum changes in electrochemistry for host **2** called by anion guests:

Table 5.7 Maximum shifts in the electrochemistry of macrocycle **2** induced by oxo anions.

Ion	**$\Delta E_p(1)$ (mV)**	**$\Delta E_p(2)$ (mV)**	**$\Delta E_p(3)$ (mV)**
ClO_4^-	-21	-31	-82
NO_3^-	merged peak		-101
AcO^-	-43	-57	-10

5.3.2 Titration of macrocycle 3 with oxoguests

5.3.3.1 Perchlorate guest

Again, there are, in fact, very little shifting on addition of this guest. In contrast with macrocycle **2** but similar to macrocycle **1**, there is small shift in $E_p(3)$. The compound precipitated after addition 8 mole equivalents but there are no shifts after addition of 5 mole equivalents.

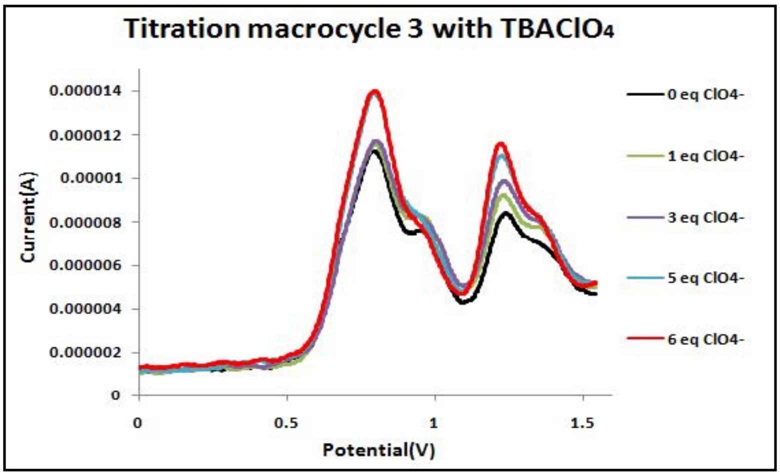

Figure 5.23 SWV of macrocycle **3** upon the addition of aliquots of $TBAClO_4$. Electrolyte: 0.1 M $TBAPF_6/CH_3CN$ (concentration of macrocycle **2**: 0.5 mm. T = 293 K, potential compared to Ag/AgCl reference).

5.3.3.6 Nitrate guest

The nitrate ion has less effect on macrocycle **3** than macrocycle **1**. Not all oxidation are affected by the same amount when the guest binds to the host. Although $E_p(1)$ is relatively unaffected by the binding of nitrate, $E_p(2)$ shows significant shifts, so the second mixed valence state ($Ru^{II}Ru^{III}Ru^{III}$) becomes easier to access when the nitrate ion is bound. The shift present for $E_p(3)$ is more difficult to interpret than those for the $E_p(1)$ and $E_p(2)$.

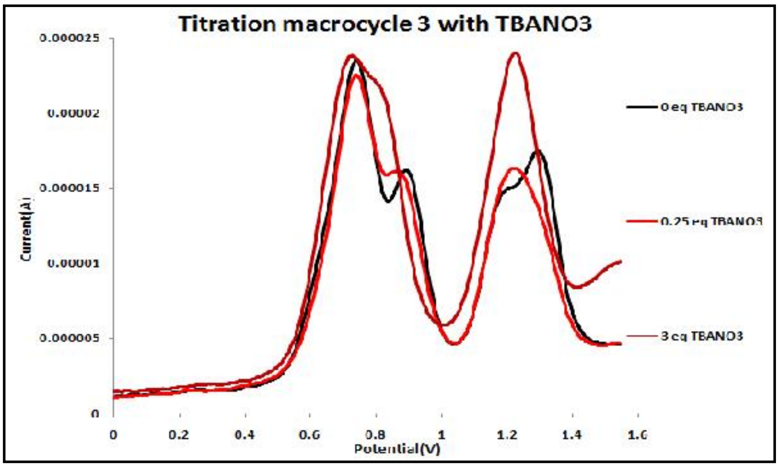

Figure 5.24 SWV of macrocycle **3** upon the addition of aliquots of $TBANO_3$. Electrolyte: 0.1 M $TBAPF_6/CH_3CN$ (concentration of macrocycle **3**: 0.5 mm. T = 293 K, potential compared to Ag/AgCl reference).

5.3.3.7 Acetate guest

There is negligible change in oxidation values for $E_p(1)$ on addition of OAc^-. In contrast $E_p(2)$ shifts were much bigger and this peak merges with the first oxidation peak.

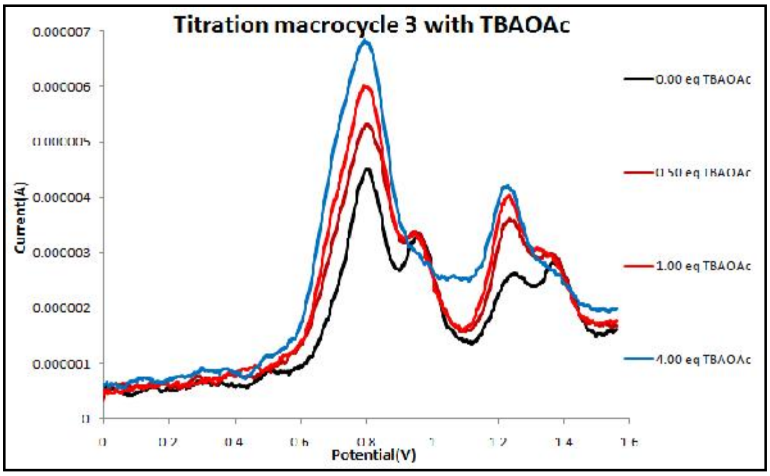

Figure 5.25 SWV of macrocycle **3** upon the addition of aliquots of TBAOAc. Electrolyte: 0.1 M $TBAPF_6/CH_3CN$ (concentration of macrocycle **3**: 0.5 mm. T = 293 K, potential compared to Ag/AgClreference).

Table 5.8 below shows the maximum changes in electrochemistry for host **3** calls by anion guests:

Table 5.8 Maximum shifts in the electrochemistry of macrocycle **3** induced by oxo anions.

Ion	**$\Delta E_p(1)$/mV**	**$\Delta E_p(2)$/mV**	**$\Delta E_p(3)$/mV**
ClO_4^-	merged peak		-13
NO_3^-	merged peak		-16
AcO^-	merged peak		-2

5.3.2 Titration of macrocycle 4 with oxo guests

5.3.4.1 Perchlorate guest

The shifts in macrocycle **4** with $TBAClO_4$ were similar to those in macrocycle **1** and differ sharply from those in macrocycle **2** in $E_p(3)$ shifts.

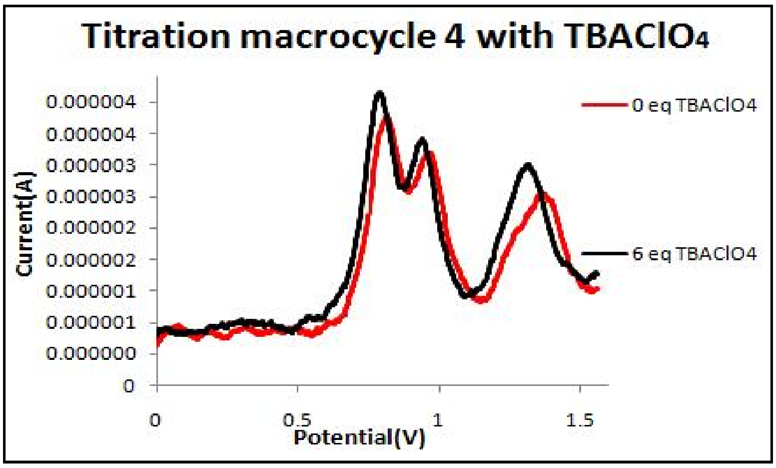

Figure 5.26 SWV of macrocycle **4** upon the addition of aliquots of $TBAClO_4$. Electrolyte: 0.1 M $TBAPF_6/CH_3CN$ (concentration of macrocycle **4**: 0.5 mm. T = 293 K, potential compared to Ag/AgCl reference).

5.3.4.5 Nitrate guest

No significant shifts occurred in the oxidation peaks of macrocycle **4**. This is similar to macrocycle **2**, **3** and in contrast to macrocycle **1**.

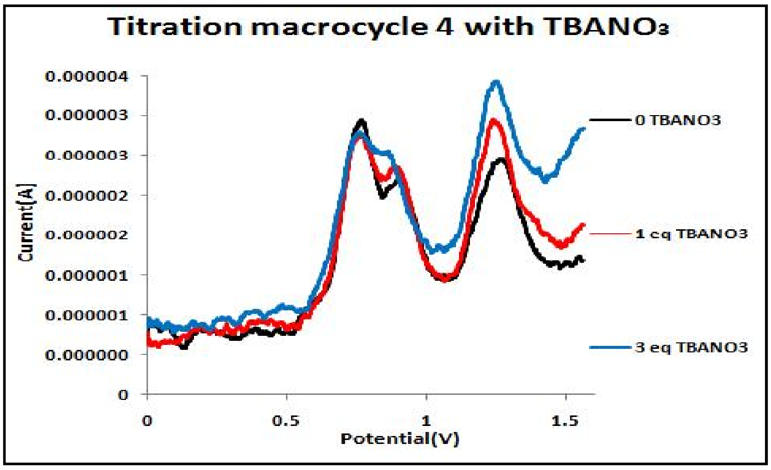

Figure 5.27 SWV of macrocycle **4** upon the addition of aliquots of $TBANO_3$. Electrolyte: 0.1 M $TBAPF_6/CH_3CN$ (concentration of macrocycle **4**: 0.5 mm. T = 293 K, potential compared to Ag/AgCl reference).

5.3.4.6 Acetate guest

The addition of amounts of tetrabutyl ammonium acetate to electrochemical solution of macrocycle **4** led to large shifts of $E_p(3)$ peaks, and a maximum shift (130 mV) was observed after six mole equivalents of acetate ion had been added. There are also significant shifts of $E_p(1)$ and $E_p(2)$ peaks to produce a merged peak.

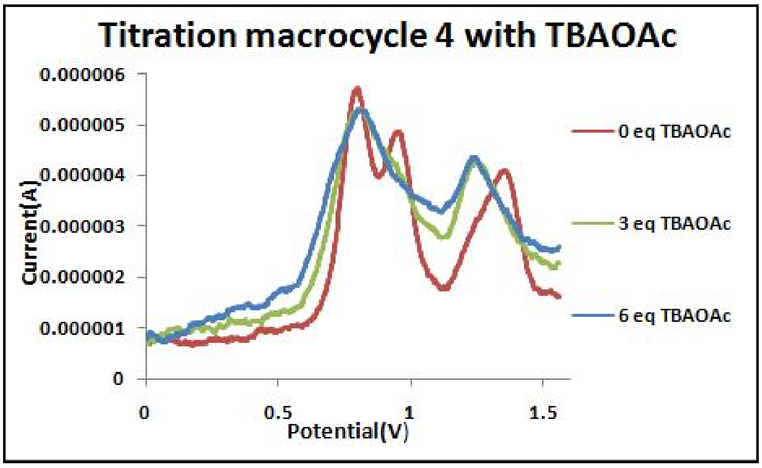

Figure 5.28 SWV of macrocycle **4** upon the addition of aliquots of $TBANO_3$. Electrolyte: 0.1 M $TBAPF_6/CH_3CN$ (concentration of macrocycle **4**: 0.5 mm. T = 293 K, potential compared to Ag/AgCl reference).

Table 5.9 below shows the maximum changes in electrochemistry for host **4** cased by anion guests:

Table 5.9 shows Maximum shifts in the electrochemistry of macrocycle **4** induced by halide anions.

Ion	**$\Delta E_p(1)$/mV**	**$\Delta E_p(2)$/mV**	**$\Delta E_p(3)$/mV**
ClO_4^-	-11	-31	-71
NO_3^-	Merged peak		-18
AcO^-	Merged peak		-130

5.4 Conclusions

The oxo guests have tetrahedral and triangular shapes while halides all have spherical shapes. From these electrochemical titration results, we find that the effect of medium sized halides have on the electrochemistry of the hosts are larger than the oxo ions. The possible reason for this behavior is because the size and shape of these specific halide ions (chloride and bromide) are more suited to the macrocycles' cavities. They also possess higher electronegativity and this must be a factor. Generally, a comparison of all the data reveals that the electrochemical response of the hosts is dependent on the binding affinities, which were measured through NMR titrations and reported in the previous chapter.

5. 6 Spectroelectrochemistry Studies

5.6.1 Spectroelectrochemistry of macrocycle 4.

Macrocycle **1** has been studied by this technique previously by Thomas group.[76] However for the first time macrocycle **4** was examined by UV/Vis/NIR spectroelectrochemistry in acetonitrile using an OTTLE cell thermostated at 273. Unfortunately, due to time constraints studies on the other two macrocycles could not be completed.

The redox interconversions examined for **4** were fully chemically reversible, as shown by the presence of clean isosbestic points during the interconversions in all cases. In the fully reduced state, $\mathbf{4}^{3+}$ the spectrum contain two transitions. They are assigned as a ligand centred π-π* transition at 238 nm and a Ru(d)→L(π*) Metal to Ligand Charge Transfer (MLCT) transition involving the adenine ligands at 287 nm. On oxidation to $\mathbf{4}^{4+}$, this MLCT (whose origin is Ru(II) diminishes in intensity and two new features develop in the low energy part of the spectrum: a relatively weak transition centred at 848 nm and a broad, lower energy transition at ca. 1441 nm Figure 5.30. The transition at 849 nm is assigned to a thiacrown→Ru(III) ligand to metal charge transfer LMCT. In addition, above 998 nm, the spectrum of $\mathbf{4}^{4+}$ is dominated by a broad, low intensity absorption ($\varepsilon \approx 152$ dm^3 mol^{-1} cm^{-1}) and has the characteristic position and appearance of an intervalence charge transfer (IVCT) band Figure 5.29.

Further oxidation to $\mathbf{4}^{5+}$ results in an additional collapse of the Ru(II)→adenine MLCT, accompanied by simultaneous growth of the thiacrown→Ru(III) LMCT band. However, the most notable feature of the $\mathbf{4}^{5+}$ absorption spectrum is an intense structured band in the NIR, displaying a maximum absorbance at 2115 nm ($\varepsilon \approx 340$ dm^3 mol^{-1} cm^{-1}) Figure 5.30.

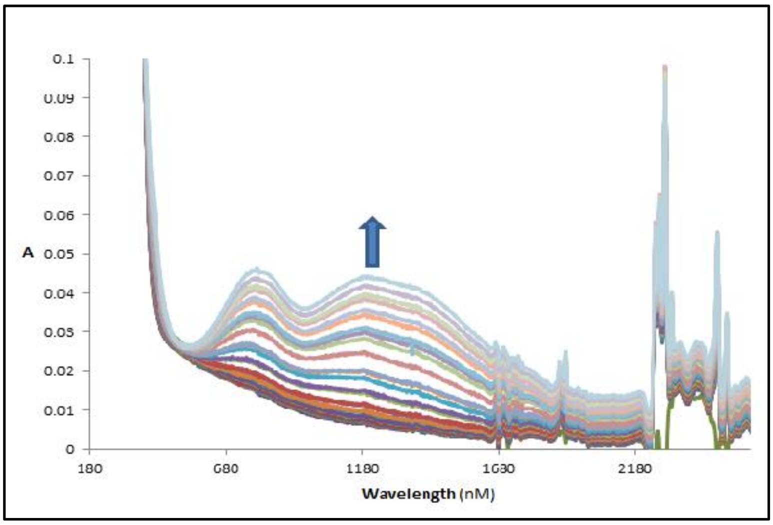

Figure 5.29 Electronic spectra associated with the oxidation of $\mathbf{4}^{3+}$ to $\mathbf{4}^{4+}$.

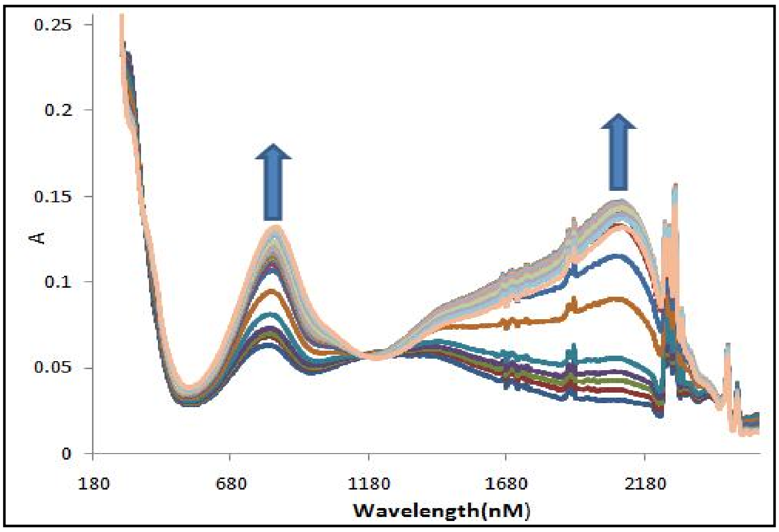

Figure 5.30 Electronic spectra associated with the oxidation of $\mathbf{4}^{4+}$ to $\mathbf{4}^{5+}$.

The final oxidation to give $\mathbf{4}^{6+}$ results in collapse of all NIR bands (which confirms their assignment as IVCT processes) and further growth of the thiacrown→Ru(III) LMCT (see Figure 5.31).

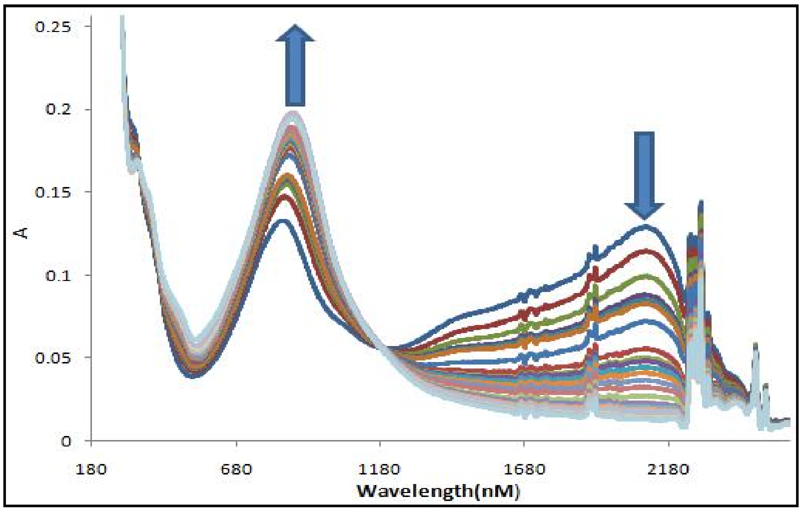

Figure 5.31 Electronic spectra associated with the oxidation of $\mathbf{4}^{5+}$ to $\mathbf{4}^{6+}$.

The energies of the NIR bands observed for the mixed valence [Ru^{II}/Ru^{II}/Ru^{III}], $\mathbf{4}^{4+}$, and [Ru^{II}/Ru^{III}/Ru^{III}], $\mathbf{4}^{5+}$, states are consistent with previous reports of intervalence charge transfer indicating electron transfer between Ru^{II} and Ru^{III} sites.[77-78] However, the differing intensities and structure of these bands imply very different electron transfer properties.

The NIR of $\mathbf{4}^{4+}$ contains a structured, low intensity, extremely broad band that seems to be comprised of several overlapping transitions. Similar structured IVCTs have previously been observed in oligo-nuclear Ru and Os based mixed valence systems[79-81] and arise due to a combination of low symmetry, extensive orbital mixing and spin orbit coupling splitting the $d\pi^5$ states into Kramer doublets, Figure 5. 32.

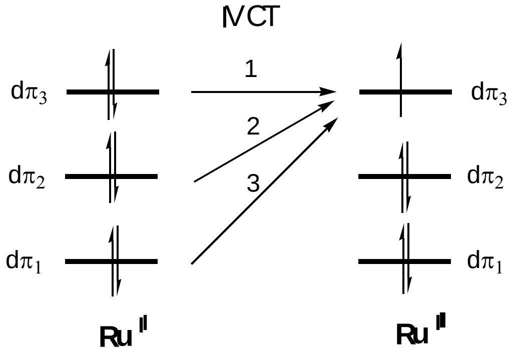

Figure 5.32 Schematic energy level diagram for Ru^{III}(N↔N)Ru^{II}$\mathbf{4}^{4+}$ (↔ denotes the ligand bridge).

There are three IVCT transitions for **4**, the one at lowest energy being IVCT **1**. The relatively low intensity of these transitions, along with the low Kc value of 800, indicates that $\mathbf{4}^{4+}$ is a valence localised structure. In contrast, the NIR band for $\mathbf{4}^{5+}$ is intense and clearly consists of at least three overlapping transitions. The intensity of these transitions and their sharpness suggests that the $\mathbf{4}^{5+}$ state is a valence delocalised system.

Further evidence for these conclusions can be drawn from the application of Hush theory[82] to the lowest energy IVCTs of the $\mathbf{4}^{4+}$ and $\mathbf{4}^{5+}$ states. Assuming Gaussian shaped bands, the low energy shoulder for the IVCT of $\mathbf{4}^{4+}$ can be used to estimate $\Delta\nu_{1/2}$for this transition.[79] In this case, $\Delta\nu_{1/2}$(exptal) ≈3992 cm^{-1},is lower than $\Delta\nu_{1/2}$(calc) = 4353 cm^{-1}. Taken together, the data on $\mathbf{4}^{4+}$ indicates that it is a Robin and Day[43] class III (valence delocalised) system, or perhaps a Class II/III (valence localised/solvent decoupled) system.[79,83]

In contrast, the same calculation carried out on the lowest energy band for $\mathbf{4}^{5+}$ reveals that$\Delta\nu_{1/2}$(exptal) = 1256cm^{-1} is much narrower than $\Delta\nu_{1/2}$(calc) = 3384 cm^{-1}. Given this very narrow bandwidth, the large *Kc*, and the exceptionally high intensity of this IVCT (εmax = 4958 dm^3 mol^{-1} cm^{-1}) it is clear that $\mathbf{4}^{5+}$ is fully valence delocalised, solvent decoupled, class III system. The UV/Vis data for macrocycle **4** are summarised in Table 5.10.

Table 5.10 Summary of UV/Vis data for macrocycle **4**.

macrocycle	λmax (nm)	ε (dm^3 mol^{-1} cm^{-1})	Assignment
$\mathbf{4}^{3+}$	238	25346	π-π*
	287	56205	MLCT
$\mathbf{4}^{4+}$	848	1894	LMCT
	1441	1526	IVCT
$\mathbf{4}^{5+}$	874	3031	LMCT
	2115	3378	IVCT
$\mathbf{4}^{6+}$	889	4559	LMCT

5.6.2 Anion switching of MV states

This unique combination of readily accessible multiple oxidation states and anion-induced electrochemical shifts also means that these macrocyclic hosts can potentially function as an entirely new form of device in which access to a specific MV state is gated by ion recognition. Spectroelectrochemistry was used to investigate this possibility. In these initial studies, fluoride was used as a guest as it is not redox active in the potential window employed.

A MeCN solution of the host**1**$^{3+}$ was first oxidized into the $\mathrm{Ru^{II}{}_2Ru^{III}}$ MV state by holding it at a potential just under that required for oxidation into the $\mathrm{Ru^{II}Ru^{III}{}_2}$ MV state (0.980 V). The formation of **1**$^{4+}$ was confirmed though generation of characteristic absorption spectrum which includes structured intervalence charge transfer (IVCT) bands in the NIR- Figure 5.34. After adding one equivalent of F^- to **1**$^{4+}$, the absorption spectrum initially reverted to that of **1**$^{3+}$, as the diffusion current produced by the guest addition disturbed the electrochemical equilibrium at the electrode. Therefore, the solution was left for >15 minutes, allowing time for the anion guest to diffuse from the top of the OTTLE to the electrode and for a new equilibrium between the electrode and oxidized product to be established.

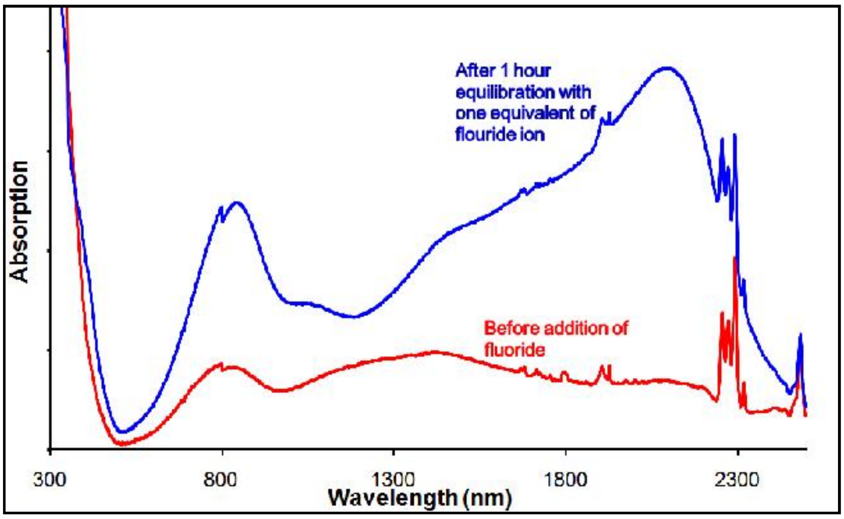

Figure 5.33 shows the effect fluoride on macrocycle **1**, the IVCT bands displayed bathochromic shifting and increase in intensity.

After this period, even though the applied potential had been held constant, it was found that the absorption spectrum had spontaneously changed. Strikingly, the IVCT bands displayed bathochromic shifting and increases in intensity; at higher energy, the thiacrown(S)→Ru^{III} ligand-to-metal charge-transfer centered at ~800 nm also grew in intensity. The finally generated spectrum is characteristic of **1**$^{5+}$. These changes confirm an unprecedented phenomenon: anion-gated switching between MV states *without* a change in potential. This response can also be viewed as the operation of a novel Boolean logic AND gate where the two inputs are a potential difference and the fluoride anion, while the output is the easily detectible optical change induced by the modulation in electronic delocalization.

5.6 Conclusion

Due to its cationic charge and array of hydrogen-bonding sites involving the thiacrown and macrocycles bridging ligands, the structure of hosts is ideally suited to anion binding. Although the well-defined cavity of the host also means that it shows good binding selectivity for specific halide anions, its distinctive binding to halide anions induces anodic shifts in the Ru^{II}-based oxidation potentials of the host, facilitating a new phenomenon: ion-gated switching of MV states.

In future work, since this host is kinetically robust, binding studies in a variety of solvents can be envisaged. The synthesis and host-guest chemistry of derivatives of this prototype structure are also currently underway and these studies will form the basis of future reports.

Chapter 6

6 Experimental Techniques and Synthetic Procedures

6.1 Materials and Equipment

6.1.1 Chemicals

All chemicals were purchased from commercial sources and used as suppliedunless otherwise stated.

6.1.2 Solvents

Solvents were obtained from commercial sources and were used as supplied except in the following cases:- Dry dichloromethane, acetonitrile and chloroform for all the reactions were obtained using the University of Sheffield Grubbs TM dry solvent system.

6.1.3 Reaction Conditions

Reactions were open to the atmosphere when performed unless otherwise stated.

6.1.4 Chromatography

Alumina column chromatography was carried out on Brockmann grade I.All alumina and silica column sizes were approximately 150 x 30 mm unlessotherwise stated.

6.1.5 Nuclear Magnetic Resonance Spectra

Standard ^{1}H NMR spectra were recorded on a Bruker AV400 machine, working in Fourier transform mode. Somespectra were also recorded on a Bruker DRX500 machine. The following abbreviations are used in the annotation of ^{1}H NMR spectra: br – broad, s – singlet, d – doublet, dd – double doublet, td –triple doublet, t – triplet, q – quartet, m – multiplet.

6.1.6 Mass Spectra

FAB mass spectra were recorded on a Kratos MS80 machine in positive ion mode with a*m*-nitrobenzyl alcohol matrix. ES mass spectra were recorded on a Micromass

LCT ES-TOF machine. All spectra were run by Mr. Simon Thorpe, or Ms. Sharon Spey of the University of Sheffield Mass Spectrometry Service.

6.1.7 Electrochemistry Studies

Cyclic Voltammograms were recorded using a Versastat 4 potentiostat using EG & G software. Measurements were made using approximately 2 mmol solutions made up in anhydrous acetonitrile containing 0.1M Bu_4NPF_6 as the support electrolyte. Potentials were measured against a Ag/AgCl reference electrode and ferrocene used as the internal reference. All cyclic voltammagrams were corrected for internal resistance.

6.1.8 X-Ray Diffraction

Structures were solved by Harry Adams in the department's X-ray structure determination service on a Bruker Smart CCD area detector with Oxford Cryosystems low temperature system and complex scattering factors from the SHELXTL program package.

6.1.9 Spectroelectrochemistry

UV/Vis/NIR spectroelectrochemistry measurements were performed in an OTTLE cell mounted in the sample compartment of a Perkin-Elmer Lamba 19 spectrometer, anhydrous acetonitrile was the solvent in every case and all measurements were carried out 273 K.

6.1.10 ^{1}H-NMR Host-Guest Titration Method

Host:guest titrations were implemented using ^{1}H-NMR spectroscopy. A 1.5×10^{-6} M stock solution of the particular macrocycles **1-4** was prepared in deutirum acetonitrile. Guest solutions were prepared in concentration of about 3×10^{-5} M. Standard addition titrations were performed with aliquots of guest solutions ranging from 5μι to 50μι added immediately to stock solution in the NMR tube, and the ^{1}H-NMR spectra measured in order to monitor the changes in chemical shift of the macrocycles N-H protons until such time as the saturation point was attained.

6.2 EXPERIMENTS

6.2.1 1,4,7- Synthesis of Trithiacyclononane [9]aneS_3.[84]

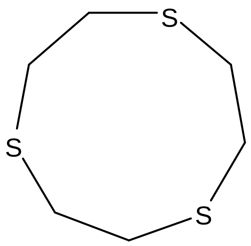

Finely powdered anhydrous cesium carbonate (13.03 g, 40 mmol) was suspended in N,N-dimethylformamide (DMF) (250 mL, from a freshly opened bottle) under a dinitrogen atmosphere. To the vigorously stirred suspension maintained at 100 ^{O}C was added a solution of 2-mercaptoethyl sulfide (5.56 g, 36 mmol) and 1,2-dichloroethane (3.54 g, 36 mmol) in DMF (150 mL) from addition machine at a rate of 3 mL/h. After the addition was complete, stirring was continued at 100 ^{O}C for a further 12 h, after which the solvent was removed in vacuo. The residual white solid was extracted with CH_2C1_2 (3 X 100 mL), and the filtered extract washed with 1.0 M aqueous NaOH (2 X 100 mL) and evaporated to dryness. The resulting sticky solid was washed with water (3 X 50 mL) and dissolved in CH_2CI_2 (100 mL). The solution was dried over $MgSO_4$, and evaporated to dryness. The residue was placed in a sublimation apparatus and heated at 90 ^{O}C under vacuum, whereupon the product crystallized as a white solid on the water-cooled cold finger (0.5 g, 50%); mp 79-80 ^{O}C.

6.2.2 Synthesis 9-methyladenine.[85]

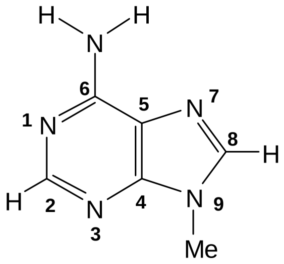

Numbering scheme for 9-methyladenine

Adenine (1.35g, 10 mmol) was dissolved in (40%) tetrabutyl ammonium hydroxide (9 g, 10mmol) solution. This in turn was mixed with a solution comprised of iodomethane (2.86 g, 20 mmol) in dichloromethane (30 mL). After vigorous stirring for 10 minutes, a white solid was filtered and recrystallised from hot ethanol. ^{1}H NMR (CD_3CN, 400 MH): δH = 8.00 (s, 1H), 7.98 (s, 1H), 6.08 (s, 2H), 3.59 (s, 3H) calc Mass (150.0723) found (150.0731)($C_6H_7N_5$).

Preparation of [Ru([9]aneS$_3$)(9-methyladenine)]$_3$[PF$_6$]$_3$. [76]

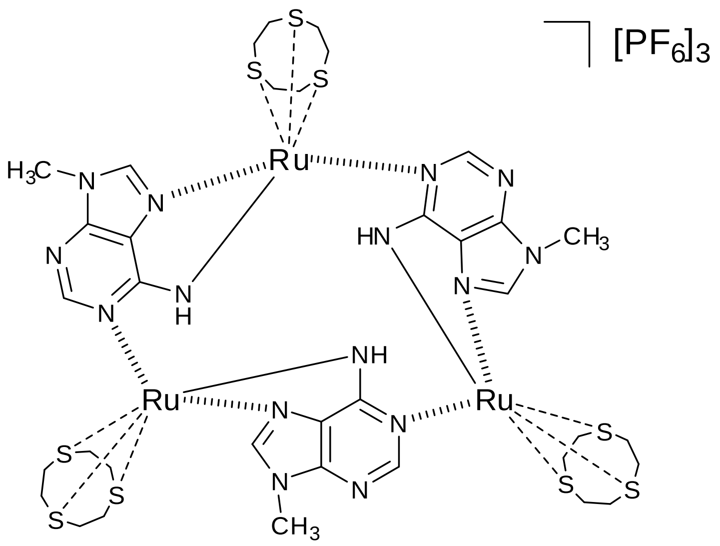

[Ru([9]aneS$_3$)(DMSO)Cl$_2$] (0.215 g, 0.5 mmol) and silver trifluoromethanesulfonate (0.256 g, 1.0 mmol) were heated at reflux for 3 hours in 30 cm^3 of water. After cooling, the silver chloride precipitate was removed by celite filtration. To the filtrate was added 9-methyl-adenine (0.075g, 0.5mmol) and 1, 2, 2, 6, 6 pentamethylpiperidine (0.073g, 0.5mmol) and the resulting solution heated at reflux for 6 days. The solution was allowed to cool and any insoluble material was filtered off. The solution was evaporated to dryness and the remaining solid residue was dissolved in 20 mL of methanol. Any insoluble material was filtered off and then 20 mL diethyl ether was added to the filtrate, the resultant green precipitate was collected by centrifuging. It was dissolved in 10 mL water and addition of ammonium hexafluorophosphate (0.226g, 2.0mmols) precipitated the final product, which was collected by centrifuge and washed by (3 × 10 cm^3) portions of water, ethanol and diethyl ether and then allowed to dry *in vacuo*. Green solid: Yield 0.29 g (35%). UV/VIS (CH$_3$CN): λmax (ε mol^{-1} dm^3 cm^{-1}) = 314nm (15366), 245nm (33729). ^{1}H NMR (DMSO- d$_6$): δH = 8.5 (s, 1H), 7.95 (s, 1H), 6.05 (s, 1H), 3.6 (s, 3H), 3.35 – 1.7 (m, 36H). EA obtained (expected Ru$_3$C$_{36}$H$_{54}$N$_{15}$S$_9$P$_3$F$_{18}$H$_2$O) C – 24.53% (24.08%), H – 3.33% (3.48%), N – 11.2 % (11.7%). MS (FAB): M/z (%) =

1579 (100) [M^+ - PF_6], 1434 (40) [M^+ - $2PF_6$]. MS (ES): M/z (%) 719 (100) [M-2PF6]$^{+/2}$, 629 (100) [M – $2PF_6$ – [9]aneS_3]$^{+/2}$.

6.1.1 9-ethyladenine.[85]

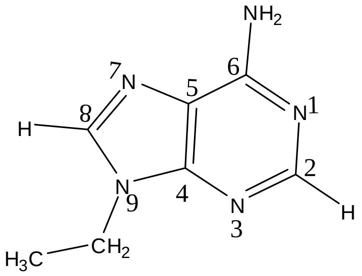

9-Ethyladenine

A mixture of adenine (3.00g, 22.2 mmol), K_2CO_3 (6.14g, 44.4 mmol), and ethyl bromide (3.33 ml) was stirred in DMF (60 ml) for 24 hour under a nitrogen atmosphere. The yellow solution was filtered then concentrated in vacuo. the resulting yellow solid was purified by silica gel flash chromatography (5:95) MeOH/ $CHCl_3$ to yield 9-ethyladenine as a white crystalline solid (1.82g, 50%yield) : mp = 190-193 ^OC. ^1H NMR (CD_3CN, 400 MH): δH = 8.24 (s, 1H), 7.92(s, 1H), 6.00 (s, 2H), 4.219 (dd, J=7, J=15, 2H), 1.47 (s, 3H). Accurate Mass –calc (164.0927) found (164.0923) ($C_7H_9N_5$).

6.1.2 [Ru(9-aneS$_3$)(9-ethyladenine)]$_3$[PF$_6$]$_3$.[76]

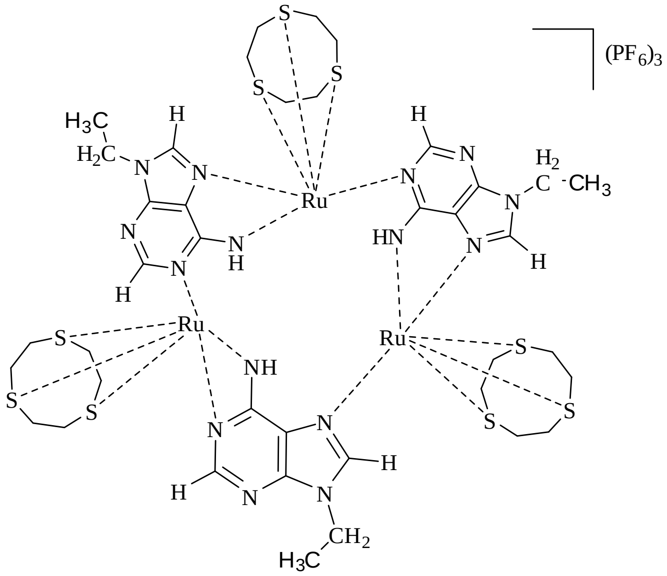

[Ru([9]aneS$_3$)(DMSO)Cl$_2$] (0.215 g, 0.5 mmol) and silver trifluoro methane sulfonate (0.256 g, 1.0 mmol) were heated at reflux for 3 hours in 30 cm^3 of water. After cooling, the silver chloride precipitate was removed by filtration. To the filtrate was added 9-ethyladenine (0.082 g, 0.5mmol) and 1, 2, 2, 6, 6 pentamethyl piperidine (0.073g, 0.5mmol) and the resulting solution heated at reflux for 6 days. The solution was allowed to cool and any insoluble material was filtered off. The solution was evaporated to dryness and the remaining solid residue was dissolved in 20 mL of methanol. Any insoluble material was filtered off and then 20 mL diethylether was added to the filtrate. The resultant green precipitate was collected by centrifuging. It was then dissolved in 10 mL water and addition of ammonium hexafluorophosphate (0.226g, 2.0mmols) precipitated the final product, which was collected by centrifuge and washed by (3 × 10 cm^3) portions of water, ethanol and diethyl ether and then allowed to dry *in vacuo*. Green solid. Yield 0.29 g (35%). ^{1}H NMR (CD$_3$CN, 400 MH): δH = 8.04 (s, 1H), 7.99(s, 1H), 6.1 (s, 1H), 4.04 (dd, J=7, J=15, 2H), 3.19-2.36(m, 12H), 1.40 (s, 3H). 9-ethyladenine obtained (expected) (Ru$_3$C$_{39}$H$_{60}$N$_{15}$S$_9$P$_3$F$_{18}$. CH$_3$CH$_2$OH. 4H$_2$O) C - 26.73%(26.91), H – 3.46%(3.74%), N – 11.04%(11.48%) MS; m/z (%):740.2(100)[M^{+2} -(CF$_3$SO$_3$)$_2$], accurate mass($C_{40}H_{60}N_{15}F_3O_3S_{10}Ru^{3/2}$, i.e. 2^+ion) Accurate Mass - cal. (740.4647) found: (740.4642).

6.1.3 9-(4-methoxybenzyl)- purin-6-amine.[86-87]

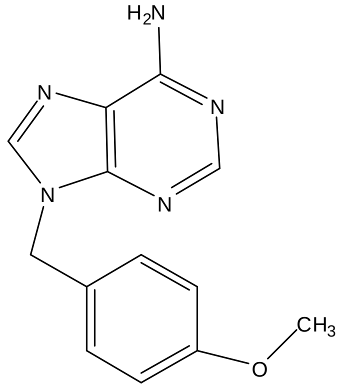

A mixture of adenine (3.00g,22 mmol),K_2CO_3 (6.14g, 44.4 mmol), and (4-methoxybenzylchloride(44.4 mmol, 6.95g) was stirred in DMF (60 ml) for 24 hours under a nitrogen atmosphere the yellow solution was filtered then concentrated *in vacuo*. The resulting yellow solid was purified by silica gel flash chromatography (7.5:92.5) (MeOH/$CHCl_3$). White solid. Yield 5.71 g (57%) ^1H NMR (CD_3CN, 400 MH): δH = 8.24 (s, 1H), 7.94 (s, 1H), 7.28 (d, J = 9, 2H), 6.9 (d, J = 9, 2H), 5.94 (s, 2H), 5.3 (s, 2H), 3.78 (s, 3H). Accurate Mass-calc (256.1198) found (256.1202)($C_{13}H_{14}N_5O$).

6.1.4 [Ru(9-aneS_3)(9-(4-methoxybenzyl)-purin-6-amine)]$_3$[CF_3SO_3]$_3$.[76]

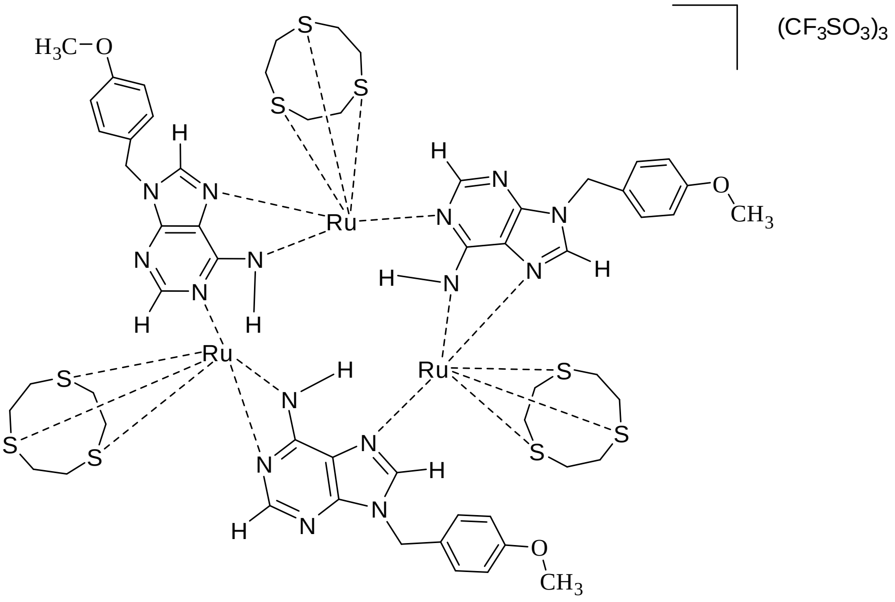

[Ru([9]aneS_3)(DMSO)Cl_2] (0.215 g, 0.5 mmol) and silver trifluoromethanesulfonate (0.256 g, 1.0 mmol) were heated at reflux for 3 hours in 30 cm^3 of water. After cooling, the silver chloride precipitate was removed by celite filtration. To the filtrate was added 9-(4-methoxybenzyl)-purin-6-amine (1.2764 g, 0.5mmol) and 1, 2, 2, 6, 6 pentamethylpiperidine (0.073g, 0.5mmol) and the resulting solution heated at reflux for 6 days. The solution was evaporated to dryness and the remaining solid residue was dissolved in 20 mL of methanol. Any insoluble material was filtered off and then 20 mL diethyl ether was added to the filtrate, the resultant green precipitate was collected by centrifuging. Green solid: Yield 0.72 g (70%). ^{1}H NMR (CD_3CN, 400 MH): δH= 8.11 (s, 1H), 7.95 (s, 1H), 7.25 (d, j=8.81, 2H), 6.9 (d, j=8.56, H=2), 6.38(s, 1H), 5.08(s, 2H), 3.78(s, 3H), 2.43-3.21 (m, 16H). EA obtained (expected) ($Ru_3C_{60}H_{72}N_{15}S_{12}O_{12}F_9.4H_2O$) C-33.82% (33.89%). H- 3.81% (3.79%). N-9.83% (9.88%). MS; m/z (%):1905(100)[M^+ -(CF_3SO_3)], 878.5018 (30) [M^{+2}-(CF_3SO_3)]. Accurate Mass for ($C_{58}H_{72}N_{15}S_{10}O_6Ru_3F3/2$. i.e. 2^+ion) cal. (878.5040) found: (878.5018).

6.1.5 9-benzyl-9H-purin-6-amine.[86-87]

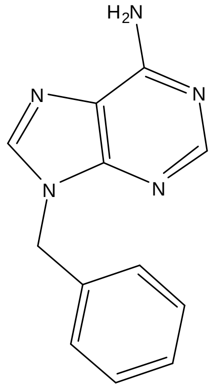

A mixture of adenine (3.00g,22 mmol). K_2CO_3 (6.14g, 44.4 mmol), and benzylchloride (44.4 mmol, 5.595g) was stirred in DMF (60 ml) for 24 hours under a nitrogen atmosphere the yellow solution was filtered then concentrated in vacuo. The resulting yellow solid was purified by silica gel flash chromatography (7.5:92.5) ($MeOH/CHCl_3$). White solid. Yield 5.89 g (59%) ^1H NMR (CD_3CN, 400 MH): δH = 8.256 (s, 1H), 7.9400 (s, 1H), 7.294-7.351 (m, Ar-H), (s, 1H), 5.891 (s, 2H). Accurate mass – calc (226.1093) found (226.1088)($C_{12}H_{12}N_5$).

6.1.6 [Ru(9-aneS$_3$)(9-benzyl-9H-purin-6-amine)-9H-purin-6-amine)]$_3$[CF$_3$SO$_3$]$_3$.[76]

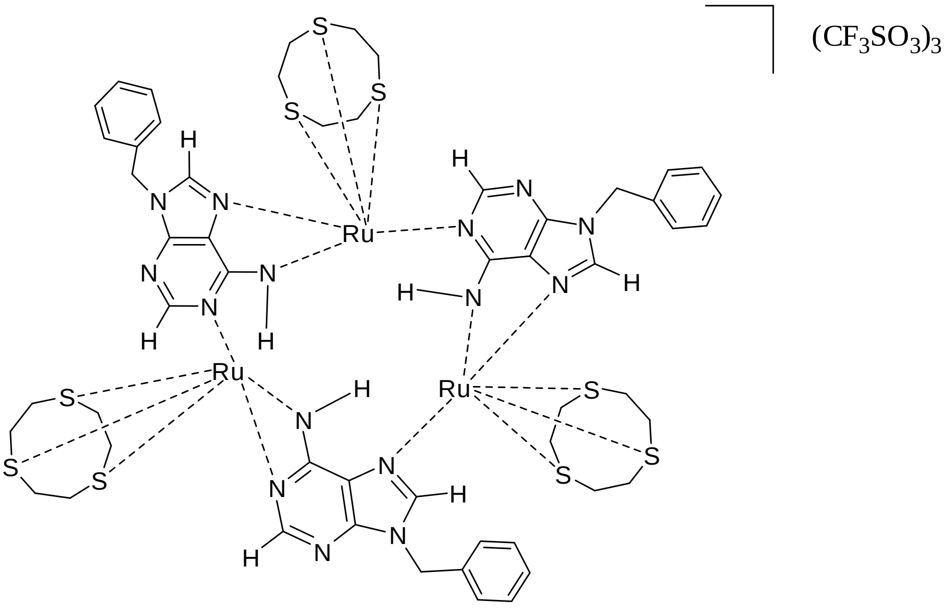

[Ru([9]aneS$_3$)(DMSO)Cl$_2$] (0.215 g, 0.5 mmol) and silver trifluoromethanesulfonate (0.256 g, 1.0 mmol) are heated at reflux for 3 hours in 30 cm^3 of water. After cooling, the silver chloride precipitate was removed by filtration. To the filtrate was added 9-benzyl-9H-purin-6-amine (0.1126 g, 0.5mmol)(dissolved in 20 cm^3 H$_2$0 : EtOH 1:1) and 1, 2, 2, 6, 6 pentamethylpiperidine (0.073g, 0.5mmol) and the resulting solution heated at reflux for 6 days. The solution was evaporated to dryness and the remaining solid residue was dissolved in 20 mL of methanol. Any insoluble material was filtered off and then 20 mL diethyl ether was added to the filtrate, the resultant green precipitate was collected by centrifuging. Green solid, Yield 0.64 g (65%).^{1}H NMR (CD$_3$CN, 400 MH.): δH= 8.087 (s, 1H), 7.92(s, 1H), 7.219-7.304 (m, Ar-H, 6.332(s, 1H), 5.122 (s, 2H), 2.43-3.21 (m, 12H). EA obtained (expected) (C$_{57}$H$_{66}$F$_9$N$_{15}$O$_9$Ru$_3$S$_{12}$, HCF$_3$SO$_3$, 2 CH$_3$OH) C-33.46% (33.08%). H 3.25% (3.47%). N 9.94% (9.64%). MS; m/z(%): 833.2 (100)[M^{++} -(CF$_3$SO$_3$)],833.4874 (50) [M^{+2}-(CF$_3$SO$_3$)]. accurate mass for (C$_{55}$H$_{66}$N$_{15}$Ru$_3$S$_{10}$F$_3$O$_3$/2. i.e. 2$^+$ion) cal. (833.4882) found: (833.4874).

References:

(1) Lehn, J. M. *Pure Appl. Chem.* **1978**, *50*, 871.

(2) Vögtle, F. *Supramolecular Chemistry*; Wiley, Chichester, 1991.

(3) Lehn, J. M. *Supramolecular Chemistry*; VCH, New York, 1995.

(4) Lent, C. S. *Science* **2000**, *288*, 1597.

(5) Anderson, S.; Anderson, H. L.; Sanders, J. K. M. *Acc. Chem. Res.* **1993**, *26*, 469.

(6) Kushner, D. J. *Bacteriol. Rev.* **1969**, *33*, 302.

(7) Lindsey, J. S. *New J. Chem.* **1991**, *15*, 153.

(8) Butler, P. J. G. *Phil. Trans. R. Soc. Lond. B* **1999**, *354*, 537.

(9) Bunce, R. A. *Tetrahedron* **1995**, *51*, 13103.

(10) McCarroll, A. J.; Walton, J. C. *Angew. Chem., Int. Ed.* **2001**, *40*, 2224.

(11) Kucharz, E. J. *The Collagens: Biochemistry and Pathophysiology*; Springer-Verlag, New York, 1992.

(12) Amabilino, D. B.; Stoddart, J. F. *Chem. Rev.* **1995**, *95*, 2725.

(13) Ellis, R. J.; Hemmingsen, S. M. *Trends Biochem. Sci.* **1989**, *14*, 339.

(14) Dokland, T.; McKenna, R.; Ilag, L. L.; Bowman, B. R.; Incardona, N. L.; Fane, B. A.; Rossmann, M. G. *Nature* **1997**, *389*, 308.

(15) Mann, S. *J. Chem. Soc., Dalton Trans.* **1997**, 3953.

(16) McCleskey, S. C.; Metzger, A.; Simmons, C. S.; Anslyn, E. V. *Tetrahedron* **2002**, *58*, 621.

(17) Stang, P. J.; Olenyuk, B. *Acc. Chem. Res.* **1997**, *30*, 502.

(18) Olenyuk, B.; Fechtenkotter, A.; Stang, P. J. *J. Chem. Soc., Dalton Trans.* **1998**, 1707.

(19) Wyler, R.; de Mendoza, J.; Rebek, J. *Angew. Chem., Int. Ed.* **1993**, *32*, 1699.

(20) Kim, M.; Gokel, G. W. *J. Chem. Soc., Chem. Commun.* **1987**, 1686.

(21) Scrimin, P.; Tecilla, P.; Tonellato, U.; Vignaga, N. *J. Chem. Soc., Chem. Commun.* **1991**, 449.

(22) Inouye, M.; Konishi, T.; Isagawa, K. *J. Am. Chem. Soc.* **1993**, *115*, 8091.

(23) Wilcox, C. S.; Hamilton, A. D. *Molecular Design and Bioorganic Catalysis*; Springer, 1996.

(24) Maverick, A. W.; Buckingham, S. C.; Yao, Q.; Bradbury, J. R.; Stanley, G. G. *J. Am. Chem. Soc.* **1986**, *108*, 7430.

(25) Maverick, A. W.; Klavetter, F. L. *Inorg. Chem.* **1984**, *23*, 4129.

(26) Fujita, M.; Nagao, S.; Iida, M.; Ogata, K.; Ogura, K. *J. Am. Chem. Soc.* **1993**, *115*, 1574.

(27) Fujita, M.; Yazaki, J.; Kuramochi, T.; Ogura, K. *Bull. Chem. Soc. Jpn.* **1993**, *66*, 1837.

(28) Fujita, M.; Ibukuro, F.; Hagihara, H.; Ogura, K. *Nature* **1994**, *367*, 720.

(29) Fujita, M. *Acc. Chem. Res.* **1999**, *32*, 53.

(30) Chen, H.; Ogo, S.; Fish, R. H. *J. Am. Chem. Soc.* **1996**, *118*, 4993.

(31) Chen, H.; Maestre, M. F.; Fish, R. H. *J. Am. Chem. Soc.* **1995**, *117,* 3631.

(32) Slone, R. V.; Yoon, D. I.; Calhoun, R. M.; Hupp, J. T. *J. Am. Chem. Soc.* **1995**, *117*, 11813.

(33) Hall, J. R.; Loeb, S. J.; Shimizu, G. K. H.; Yap, G. P. A. *Angew. Chem., Int. Ed.* **1998**, *37*, 121.

(34) Fujita, M.; Yazaki, J.; Ogura, K. *J. Am. Chem. Soc.* **1990**, *112*, 5645.

(35) Fujita, M. *Yuki Gosei Kagaku Kyokaishi* **1996**, *54*, 953.

(36) Zangrando, E.; Casanova, M.; Alessio, E. *Chem. Rev.* **2008**, *108,* 4979.

(37) Leininger, S.; Olenyuk, B.; Stang, P. J. *Chem. Rev.* **2000**, *100*, 853.

(38) Kemmitt, R. D. W.; Mason, S.; Moore, M. R.; Fawcett, J.; Russell, D. R. *J. Chem. Soc., Chem. Commun.* **1990**, 1535.

(39) Smith, D. P.; Baralt, E.; Morales, B.; Olmstead, M. M.; Maestre, M. F.; Fish, R. H. *J. Am. Chem. Soc.* **1992**, *114*, 10647.

(40) Weyland, T.; Costuas, K.; Toupet, L.; Halet, J.-F.; Lapinte, C. *Organometallics* **2000**, *19*, 4228.

(41) Denis, R.; Toupet, L.; Paul, F.; Lapinte, C. *Organometallics* **2000**, *19,* 4240.

(42) Kar, S.; Miller, T. A.; Chakraborty, S.; Sarkar, B.; Pradhan, B.; Sinha, R. K.; Kundu, T.; Ward, M. D.; Kumar, L. G. *Dalton Trans.* **2003**, 2591.

(43) Robin, M. B.; Day, P. *Advan. Inorg. Chem. Radiochem.* **1967**, *10,* 247.

(44) Roche, S.; Thomas, J. A.; Yellowlees, L. J. *Chem. Commun.* **1998**, 1429.

(45) Anslyn, E. V.; Dougherty, D. A. *Modern Physical Organic Chemistry*; University Science Books,U.S., 2006

(46) Hu, J.; Cheng, Y.; Wu, Q.; Zhao, L.; Xu, T. *J. Phys. Chem. B.* **2009**, *113*, 10650.

(47) Li, J.; Piehler, L. T.; Qin, D.; Baker, J. R., Jr.; Tomalia, D. A.; Meier, D. J. *Langmuir* **2000**, *16*, 5613.

(48) Esumi, K.; Kuwabara, K.; Chiba, T.; Kobayashi, F.; Mizutani, H.; Torigoe, K. *Colloids Surf., A* **2002**, *197*, 141.

(49) Esumi, K.; Saika, R.; Miyazaki, M.; Torigoe, K.; Koide, Y. *Colloids Surf., A* **2000**, *166*, 115.

(50) Sidhu, J.; Bloor, D. M.; Couderc-Azouani, S.; Penfold, J.; Holzwarth, J. F.; Wyn-Jones, E. *Langmuir* **2004**, *20*, 9320.

(51) Tam, K. C.; Wyn-Jones, E. *Chem. Soc. Rev.* **2006**, *35*, 693.

(52) Santo, M.; Fox, M. A. *J. Phys. Org. Chem.* **1999**, *12*, 293.

(53) Broeren, M. A. C.; de Waal, B. F. M.; van Genderen, M. H. P.; Sanders, H. M. H. F.; Fytas, G.; Meijer, E. W. *J. Am. Chem. Soc.* **2005**, *127*, 10334.

(54) Boisselier, E.; Ornelas, C.; Pianet, I.; Aranzaes, J. R.; Astruc, D. *Chem. Eur. J.* **2008**, *14*, 5577.

(55) Thomas, J. A. *Dalton Trans.* **2011**, *40*, 12005.

(56) Beer, P. D.; Szemes, F.; Balzani, V.; Sala, C. M.; Drew, M. G. B.; Dent, S. W.; Maestri, M. *J. Am. Chem. Soc.* **1997**, *119*, 11864.

(57) Wong, W. W. H.; Curiel, D.; Lai, S.-W.; Drew, M. G. B.; Beer, P. D. *Dalton Trans.* **2005**, 774.

(58) Beer, P. D.; Berry, N.; Fox, O. D.; Padilla-Tosta, M. E.; Patell, S.; Drew, M. G. B. *Chem. Commun.* **2001**, 199.

(59) Beer, P. D.; Berry, N. G.; Cowley, A. R.; Hayes, E. J.; Oates, E. C.; Wong, W. W. H. *Chem. Commun.* **2003**, 2408.

(60) Piotrowski, H.; Severin, K. *Proc. Natl. Acad. Sci.* **2002**, *99*, 4997.

(61) Lehaire, M.-L.; Scopelliti, R.; Piotrowski, H.; Severin, K. *Angew. Chem., Int. Ed.* **2002**, *41*, 1419.

(62) Li, M.; Cai, P.; Duan, C.; Lu, F.; Xie, J.; Meng, Q. *Inorg. Chem.* **2004**, *43*, 5174.

(63) Fielding, L. *Tetrahedron.* **2000**, *56*, 6151.

(64) Hirose, K. *Journal of inclusion phenomena and macrocyclic chemistry.* **2001**, *39*, 193.

(65) Sessler, J. L.; Barkey, N. M.; Pantos, G. D.; Lynch, V. M. *New J. Chem.* **2007**, *31*, 646.

(66) Beer, P. D.; Gale, P. A. *Angew. Chem., Int. Ed.* **2001**, *40*, 486.

(67) Zhang, Y.; Cremer, P. S. *Curr. Opin. Chem. Biol.* **2006**, *10*, 658.

(68) Gilday, L. C.; White, N. G.; Beer, P. D. *Dalton Trans.* **2012**, *41*, 7092.

(69) Hancock, L. M.; Beer, P. D. *Chem. Eur. J.* **2009**, *15*, 42.

(70) Spence, G. T.; Pitak, M. B.; Beer, P. D. *Chem. Eur. J.* **2012**, *18*, 7100.

(71) Lankshear, M. D.; Beer, P. D. *Acc. Chem. Res.* **2007**, *40*, 657.

(72) Hancock, L. M.; Gilday, L. C.; Carvalho, S.; Costa, P. J.; Felix, V.; Serpell, C. J.; Kilah, N. L.; Beer, P. D. *Chem. Eur. J.* **2010**, *16*, 13082.

(73) White, N. G.; Beer, P. D. *Org. Biomol. Chem.* **2013**, *11*, 1326.

(74) Evans, N. H.; Serpell, C. J.; Christensen, K. E.; Beer, P. D. *Eur. J. Inorg. Chem.* **2012**, *2012*, 939.

(75) Muller, A.; Roy, S. *Coord. Chem. Rev.* **2003**, *245*, 153.

(76) Shan, N.; Ingram, J. D.; Easun, T. L.; Vickers, S. J.; Adams, H.; Ward, M. D.; Thomas, J. A. *Dalton Trans.* **2006**, 2900.

(77) Creutz, C. In *Prog. Inorg. Chem.* 2007, p 1.

(78) Crutchley, R. J. *Adv. Inorg. Chem.* **1994**, *41*, 273.

(79) Demadis, K. D.; Hartshorn, C. M.; Meyer, T. J. *Chem. Rev.* **2001**, *101*, 2655.

(80) Kasack, V.; Kaim, W.; Binder, H.; Jordanov, J.; Roth, E. *Inorg. Chem.* **1995**, *34*, 1924.

(81) Moscherosch, M.; Waldhoer, E.; Binder, H.; Kaim, W.; Fiedler, J. *Inorg. Chem.* **1995**, *34*, 4326.

(82) Hush, N. S. In *Prog. Inorg. Chem.* 2007, p 391.

(83) Brunschwig, B. S.; Creutz, C.; Sutin, N. *Chemical Society Reviews* **2002**, *31*, 168.

(84) Blower, P. J.; Cooper, S. R. *Inorg. Chem.* **1987**, *26*, 2009.

(85) Lambertucci, C.; Antonini, I.; Buccioni, M.; Dal, B. D.; Kachare, D. D.; Volpini, R.; Klotz, K.-N.; Cristalli, G. *Bioorg. Med. Chem.* **2009**, *17*, 2812.

(86) Soltani Rad, M. N.; Khalafi-Nezhad, A.; Behrouz, S.; Asrari, Z.; Behrouz, M.; Amini, Z. *Synthesis* **2009**, *18*, 3067.

(87) Soltani Rad, M. N.; Khalafi-Nezhad, A.; Behrouz, S.; Faghihi, M. A.; Zare, A.; Parhami, A. *Tetrahedron.* **2008**, *64*, 1778.

Appendix

Crystallographic Data

Table 1. Crystal data and structure refinement for 9-benzyl-9H-purin-6-amine (CHP0803P21C).

Identification code	chp0803p21c	
Empirical formula	C12 H11 N5	
Formula weight	225.26	
Temperature	97(2) K	
Wavelength	0.71073 Å	
Crystal system	Monoclinic	
Space group	P2(1)/c	
Unit cell dimensions	a = 11.7666(17) Å	α= 90°.
	b = 12.3383(17) Å	β= 90.336(3)°.
	c = 7.1014(10) Å	γ = 90°.
Volume	1031.0(3) Å^3	
Z	4	
Density (calculated)	1.451 Mg/m^3	
Absorption coefficient	0.094 mm^{-1}	
F(000)	472	
Crystal size	0.30 x 0.10 x 0.10 mm^3	
Theta range for data collection	1.73 to 27.48°.	
Index ranges	-15<=h<=15, -14<=k<=16, -7<=l<=8	
Reflections collected	5712	
Independent reflections	2294 [R(int) = 0.0616]	
Completeness to theta = 27.48°	97.4 %	
Absorption correction	Semi-empirical from equivalents	
Max. and min. transmission	0.9906 and 0.9723	
Refinement method	Full-matrix least-squares on F^2	
Data / restraints / parameters	2294 / 3 / 154	
Goodness-of-fit on F^2	1.071	
Final R indices [I>2sigma(I)]	R1 = 0.0570, wR2 = 0.1439	
R indices (all data)	R1 = 0.0645, wR2 = 0.1512	
Largest diff. peak and hole	0.312 and -0.401 e.Å^{-3}	

Table 2. Atomic coordinates (x 104) and equivalent isotropic displacement parameters (Å2x 103) For 9-benzyl-9H-purin-6-amine (CHP0803P21C). U(eq) is defined as one third of the trace of the orthogonalized Uij tensor.

	x	y	z	U(eq)
N(1)	2147(14)	-23(14)	7060(30)	15(4)
N(2)	1633(14)	-1516(15)	5450(30)	17(4)
N(3)	1590(14)	1373(14)	4840(30)	15(4)
N(4)	707(14)	611(14)	2060(30)	14(4)
N(5)	535(15)	-1218(15)	1460(30)	18(4)
C(1)	4612(18)	218(17)	7520(30)	16(5)
C(2)	5758(18)	466(19)	7500(30)	19(5)
C(3)	6162(18)	1406(19)	8310(30)	20(5)
C(4)	5409(19)	2117(19)	9150(30)	21(5)
C(5)	4254(19)	1877(18)	9150(30)	19(5)
C(6)	3850(17)	927(17)	8360(30)	15(5)
C(7)	2605(17)	649(18)	8570(30)	17(5)
C(8)	2081(17)	-1127(18)	7000(30)	17(5)
C(9)	1376(16)	-589(16)	4410(30)	14(5)
C(10)	867(16)	-425(17)	2630(30)	14(5)
C(11)	1077(17)	1422(17)	3160(30)	16(5)
C(12)	1698(16)	337(17)	5390(30)	14(5)

Table 3. Bond lengths [Å] and angles [°] for 9-benzyl-9H-purin-6-amine CHP0803P21C.

N(1)-C(8)	1.36(3)	C(5)-C(6)-C(7)	118.9(19)
N(1)-C(12)	1.37(3)	C(1)-C(6)-C(7)	121.8(19)
N(1)-C(7)	1.46(3)	N(1)-C(7)-C(6)	114.2(18)
N(2)-C(8)	1.31(3)	N(1)-C(7)-H(7A)	108.7
N(2)-C(9)	1.39(3)	C(6)-C(7)-H(7A)	108.7
N(3)-C(11)	1.34(3)	N(1)-C(7)-H(7B)	108.7
N(3)-C(12)	1.34(3)	C(6)-C(7)-H(7B)	108.7
N(4)-C(11)	1.34(3)	H(7A)-C(7)-H(7B)	107.6
N(4)-C(10)	1.35(3)	N(2)-C(8)-N(1)	114.3(19)
N(5)-C(10)	1.34(3)	N(2)-C(8)-H(8)	122.8
N(5)-H(5A)	0.8800	N(1)-C(8)-H(8)	122.8
N(5)-H(5B)	0.8800	C(12)-C(9)-N(2)	110.6(19)
C(1)-C(2)	1.38(3)	C(12)-C(9)-C(10)	116.4(19)
C(1)-C(6)	1.39(3)	N(2)-C(9)-C(10)	133.0(19)
C(1)-H(1)	0.9500	N(5)-C(10)-N(4)	117.7(19)
C(2)-C(3)	1.38(3)	N(5)-C(10)-C(9)	124.8(19)
C(2)-H(2)	0.9500	N(4)-C(10)-C(9)	117.5(19)
C(3)-C(4)	1.38(3)	N(3)-C(11)-N(4)	129(2)
C(3)-H(3)	0.9500	N(3)-C(11)-H(11)	115.5
C(4)-C(5)	1.39(3)	N(4)-C(11)-H(11)	115.5
C(4)-H(4)	0.9500	N(3)-C(12)-N(1)	126.5(19)
C(5)-C(6)	1.38(3)	N(3)-C(12)-C(9)	128(2)
C(5)-H(5)	0.9500	N(1)-C(12)-C(9)	105.7(18)
C(6)-C(7)	1.51(3)	C(12)-N(1)-C(7)	126.4(18)
C(7)-H(7A)	0.9900	C(8)-N(1)-C(7)	127.5(18)
C(7)-H(7B)	0.9900	C(8)-N(1)-C(12)	106.0(17)
C(8)-H(8)	0.9500	C(11)-H(11)	0.9500
C(9)-C(12)	1.39(3)	C(9)-C(10)	1.41(3)

Symmetry transformations used to generate equivalent atoms:

Table 1. Crystal data and structure refinement for 9-(4-methoxybenzyl)-9H-purin-6-amine (iaj601_0m 0).

Identification code	iaj601_0m

Empirical formula	C13 H13 N5 O	
Formula weight	255.28	
Temperature	150(2) K	
Wavelength	0.71073 Å	
Crystal system	Orthorhombic	
Space group	$P2_12_12_1$	
Unit cell dimensions	a = 8.0824(8) Å	α= 90°.
	b = 16.5719(15) Å	β= 90°.
	c = 27.246(2) Å	γ = 90°.
Volume	3649.4(6) Å^3	
Z	12	
Density (calculated)	1.394 Mg/m^3	
Absorption coefficient	0.095 mm^{-1}	
F(000)	1608	
Crystal size	0.18 x 0.04 x 0.04 mm^3	
Theta range for data collection	1.44 to 27.77°.	
Index ranges	-10<=h<=10, -21<=k<=21, -35<=l<=32	
Reflections collected	27692	
Independent reflections	4758 [R(int) = 0.0659]	
Completeness to theta = 25.00°	99.9 %	
Absorption correction	Semi-empirical from equivalents	
Max. and min. transmission	0.9962 and 0.9831	
Refinement method	Full-matrix least-squares on F^2	
Data / restraints / parameters	4758 / 0 / 517	
Goodness-of-fit on F^2	1.201	
Final R indices [I>2sigma(I)]	R1 = 0.0465, wR2 = 0.1161	
R indices (all data)	R1 = 0.0631, wR2 = 0.1323	
Largest diff. peak and hole	0.288 and -0.299 e.Å^{-3}	

Table 2. Atomic coordinates (x 10^4) and equivalent isotropic displacement parameters (Å^{2}x 10^3) For 9-(4-methoxybenzyl)-9H-purin-6-amine (iaj601_0m). U(eq) is defined as one third of the trace of the orthogonalized U^{ij} tensor.

	x	y	z	U(eq)
N(1)	3283(4)	9078(2)	9099(1)	22(1)
N(2)	4224(3)	10184(2)	9489(1)	22(1)
N(3)	-183(3)	10242(2)	9877(1)	22(1)
N(4)	389(4)	9123(2)	9332(1)	24(1)
N(5)	1771(4)	11160(2)	10137(1)	24(1)
O(1)	2432(3)	8214(2)	6795(1)	33(1)
N(1A)	7338(4)	413(2)	5977(1)	23(1)
N(2A)	6440(4)	1504(2)	5569(1)	22(1)
N(3A)	10260(4)	458(2)	5771(1)	26(1)
N(4A)	10879(4)	1575(2)	5228(1)	24(1)
N(5A)	8915(4)	2464(2)	4931(1)	26(1)
O(1A)	7332(3)	30(1)	8327(1)	30(1)
N(1B)	8270(4)	3099(2)	1189(1)	21(1)
N(2B)	9224(3)	2049(2)	750(1)	22(1)
N(3B)	5393(4)	3092(2)	937(1)	23(1)
N(4B)	4815(3)	2028(2)	354(1)	21(1)
N(5B)	6762(4)	1119(2)	74(1)	25(1)
O(1B)	7251(4)	3014(1)	3531(1)	33(1)

Table 3. Bond lengths [Å] and angles [°] for 9-(4-methoxybenzyl)-9H-purin-6-amine (iaj601_0m).

N(1)-C(8)	1.365(4)
N(1)-C(12)	1.371(4)
N(1)-C(7)	1.464(4)
N(2)-C(8)	1.312(4)
N(2)-C(9)	1.388(4)
N(3)-C(11)	1.340(4)
N(3)-C(10)	1.356(4)
N(4)-C(11)	1.333(4)
N(4)-C(12)	1.348(4)
N(5)-C(10)	1.333(4)
N(1A)-C(8A)	1.364(4)
N(1A)-C(12A)	1.371(4)
N(1A)-C(7A)	1.463(4)
N(2A)-C(8A)	1.315(4)
N(2A)-C(9A)	1.391(4)
N(3A)-C(11A)	1.330(4)
N(3A)-C(12A)	1.343(4)
N(4A)-C(10A)	1.348(4)
N(4A)-C(11A)	1.347(4)
N(1B)-C(7B)	1.454(4)
N(2B)-C(8B)	1.313(4)
N(2B)-C(9B)	1.393(4)
N(3B)-C(11B)	1.326(4)
N(3B)-C(12B)	1.344(4)
N(4B)-C(11B)	1.343(4)
N(4B)-C(10B)	1.362(4)
N(5B)-C(10B)	1.335(4)
C(8)-N(1)-C(12)	105.7(3)
C(8)-N(1)-C(7)	128.2(3)
C(12)-N(1)-C(7)	125.3(3)
C(8)-N(2)-C(9)	103.5(3)
C(11)-N(3)-C(10)	118.7(3)
C(11)-N(4)-C(12)	109.7(3)
N(1)-C(7)-C(4)	115.1(3)
N(2)-C(8)-N(1)	114.4(3)
N(2)-C(9)-C(12)	110.5(3)
N(2)-C(9)-C(10)	132.8(3)
C(12)-C(9)-C(10)	116.5(3)

N(5A)-C(10A)	1.334(4)	N(5)-C(10)-N(3)	118.0(3)
N(1B)-C(12B)	1.373(4)	N(5)-C(10)-C(9)	124.5(3)
N(1B)-C(8B)	1.372(4)	N(3)-C(10)-C(9)	117.5(3)
N(1)-C(8)	1.365(4)	N(4)-C(11)-N(3)	129.8(3)
N(1)-C(12)	1.371(4)	N(4)-C(12)-N(1)	126.2(3)
N(1)-C(7)	1.464(4)	N(4)-C(12)-C(9)	127.8(3)
N(2)-C(8)	1.312(4)	N(1)-C(12)-C(9)	106.0(3)
N(2)-C(9)	1.388(4)	C(8A)-N(1A)-C(12A)	106.4(3)
N(3)-C(11)	1.340(4)	C(8A)-N(1A)-C(7A)	127.4(3)
N(3)-C(10)	1.356(4)	C(12A)-N(1A)-C(7A)	126.1(3)
N(4)-C(11)	1.333(4)	C(8A)-N(2A)-C(9A)	103.9(3)
N(4)-C(12)	1.348(4)	C(11A)-N(3A)-C(12A)	110.1(3)
N(5)-C(10)	1.333(4)	C(10A)-N(4A)-C(11A)	118.8(3)
N(1A)-C(8A)	1.364(4)	N(1A)-C(7A)-C(4A)	113.7(3)
N(1A)-C(12A)	1.371(4)	(2A)-C(8A)-N(1A)	113.7(3)
N(1A)-C(7A)	1.463(4)	N(2A)-C(9A)-C(12A)	110.3(3)
N(2A)-C(8A)	1.315(4)	N(2A)-C(9A)-C(10A)	132.8(3)
N(2A)-C(9A)	1.391(4)	N(5A)-C(10A)-N(4A)	119.1(3)
N(3A)-C(11A)	1.330(4)	N(5A)-C(10A)-C(9A)	123.5(3)
N(3A)-C(12A)	1.343(4)	N(4A)-C(10A)-C(9A)	117.4(3)
N(4A)-C(10A)	1.348(4)	N(3A)-C(11A)-N(4A)	129.5(3)
N(4A)-C(11A)	1.347(4)	N(3A)-C(12A)-N(1A)	127.0(3)
N(5A)-C(10A)	1.334(4)	N(3A)-C(12A)-C(9A)	127.3(3)
N(1B)-C(12B)	1.373(4)	N(1A)-C(12A)-C(9A)	105.7(3)
N(1B)-C(8B)	1.372(4)	C(12B)-N(1B)-C(8B)	105.9(2)
N(1)-C(8)	1.365(4)	C(12B)-N(1B)-C(7B)	125.9(3)
N(1)-C(12)	1.371(4)	C(8B)-N(1B)-C(7B)	128.2(3)
N(1)-C(7)	1.464(4)	C(8B)-N(2B)-C(9B)	104.2(3)
N(2)-C(8)	1.312(4)	C(11B)-N(3B)-C(12B)	110.0(3)
N(2)-C(9)	1.388(4)	C(11B)-N(4B)-C(10B)	118.2(3)
N(3)-C(11)	1.340(4)	N(1B)-C(7B)-C(4B)	114.2(2)
N(5B)-C(10B)-N(4B)	117.8(3)	N(2B)-C(8B)-N(1B)	113.7(3)
N(5B)-C(10B)-C(9B)	124.7(3)	C(12B)-C(9B)-N(2B)	110.0(3)
N(4B)-C(10B)-C(9B)	117.5(3)	N(1B)-C(7B)	1.454(4)
N(3B)-C(11B)-N(4B)	130.0(3)	N(5B)-C(10B)-N(4B)	117.8(3)
N(3B)-C(12B)-N(1B)	126.4(3)	N(5B)-C(10B)-C(9B)	124.7(3)

Symmetry transformations used to generate equivalent atoms:

Summary of crystallographic data for **[1]**[(Br)$_3$].

Table 1. Crystal data and structure refinement for **[1]**[(Br)$_3$].

Identification code	iaj627new	
Empirical formula	C36 H54 Br3 N15 Ru3 S9	
Formula weight	1528.42	
Temperature	150(2) K	
Wavelength	0.71073 Å	
Crystal system	Monoclinic	
Space group	P2(1)/c	
Unit cell dimensions	a = 27.5205(14) Å	α= 90°.
	b = 21.6096(12) Å	β= 119.123(2)°.
	c = 21.7526(12) Å	γ = 90°.
Volume	11301.0(11) Å^3	
Z	8	
Density (calculated)	1.797 Mg/m^3	
Absorption coefficient	3.288 mm^{-1}	
F(000)	6048	
Crystal size	0.43 x 0.32 x 0.32 mm^3	
Theta range for data collection	0.85 to 26.98°.	
Index ranges	-34<=h<=30, -26<=k<=27, -27<=l<=27	
Reflections collected	139458	
Independent reflections	24312 [R(int) = 0.0548]	
Completeness to theta = 26.98°	98.8 %	
Absorption correction	Semi-empirical from equivalents	
Max. and min. transmission	0.4193 and 0.3321	
Refinement method	Full-matrix least-squares on F^2	
Data / restraints / parameters	24312 / 32 / 1187	
Goodness-of-fit on F^2	1.090	
Final R indices [I>2sigma(I)]	R1 = 0.0547, wR2 = 0.1456	
R indices (all data)	R1 = 0.1128, wR2 = 0.1645	
Largest diff. peak and hole	1.198 and -1.846 e.Å^{-3}	

Table 2. Atomic coordinates (x 10^4) and equivalent isotropic displacement parameters (Å^{2}x 103) For [1][$(Br)_3$] (iaj627new). U(eq) is defined as one third of the trace of the orthogonalized Uij tensor.

	x	y	z	U(eq)
Ru(1)	8904(1)	3244(1)	2435(1)	38(1)
Ru(2)	8820(1)	5781(1)	1684(1)	34(1)
Ru(3)	10831(1)	4448(1)	2735(1)	36(1)
Ru(1A)	4188(1)	4349(1)	2220(1)	35(1)
Ru(2A)	6207(1)	5672(1)	3340(1)	32(1)
Ru(3A)	6120(1)	3140(1)	2542(1)	37(1)
Br(1)	7475(1)	3923(1)	9484(1)	73(1)
Br(2)	7495(1)	3785(1)	5505(1)	71(1)
Br(3)	8123(1)	7956(1)	3906(1)	75(1)
Br(4)	6876(1)	6921(1)	6106(1)	79(1)
Br(5)	610(1)	6416(1)	409(1)	117(1)
Br(6)	5604(1)	3751(1)	5459(1)	104(1)
S(1)	8361(1)	3366(1)	1260(1)	43(1)
S(2)	9229(1)	2341(1)	2225(1)	56(1)
S(3)	8202(1)	2693(1)	2447(1)	61(1)
S(4)	7953(1)	5783(1)	712(1)	47(1)
S(5)	8837(1)	6828(1)	1571(1)	54(1)
S(6)	9186(1)	5689(1)	942(1)	46(1)
S(7)	10539(1)	3763(1)	1827(1)	46(1)
S(8)	11092(1)	5099(1)	2123(1)	50(1)
S(9)	11692(1)	4005(1)	3221(1)	49(1)
S(1A)	3322(1)	3919(1)	1714(1)	49(1)
S(2A)	3925(1)	4994(1)	2834(1)	48(1)
S(3A)	4463(1)	3652(1)	3116(1)	44(1)
S(4A)	5821(1)	5568(1)	4058(1)	42(1)
S(5A)	6189(1)	6716(1)	3468(1)	49(1)
S(6A)	7065(1)	5664(1)	4325(1)	44(1)
S(7A)	5777(1)	2237(1)	2718(1)	62(1)
S(8A)	6648(1)	3238(1)	3724(1)	44(1)
S(9A)	6828(1)	2588(1)	2542(1)	60(1)
N(1)	8624(2)	4122(2)	2630(2)	40(1)
N(2)	8289(2)	4597(3)	3372(3)	55(2)
N(3)	8235(2)	5742(3)	3216(3)	48(1)

N(4)	8497(2)	5795(2)	2398(2)	38(1)
N(5)	8784(2)	4801(2)	1846(2)	33(1)
N(6)	9629(2)	5778(2)	2605(2)	35(1)
N(7)	10187(2)	6254(2)	3769(3)	46(1)
N(8)	11119(2)	5777(2)	4391(2)	47(1)
N(9)	11019(2)	5116(2)	3548(2)	42(1)
N(10)	10050(2)	4934(2)	2296(2)	35(1)
N(11)	10586(2)	3884(2)	3350(2)	37(1)
N(12)	10910(2)	3530(2)	4560(2)	48(1)
N(13)	10135(2)	3047(2)	4662(2)	48(1)
N(14)	9475(2)	3169(2)	3542(2)	44(1)
N(15)	9623(2)	3680(2)	2487(2)	39(1)
N(1A)	5407(2)	5675(2)	2403(2)	32(1)
N(2A)	4870(2)	6173(2)	1255(3)	42(1)
N(3A)	3926(2)	5712(2)	602(2)	43(1)
N(4A)	4018(2)	5030(2)	1415(2)	40(1)
N(5A)	4974(2)	4827(2)	2680(2)	33(1)
N(6A)	6412(2)	4022(2)	2377(2)	39(1)
N(7A)	6753(2)	4518(3)	1649(3)	60(2)
N(8A)	6812(2)	5654(3)	1824(2)	47(1)
N(9A)	6542(2)	5692(2)	2634(2)	39(1)
N(10A)	6244(2)	4695(2)	3157(2)	33(1)
N(11A)	4437(2)	3787(2)	1602(2)	36(1)
N(12A)	4126(2)	3441(2)	394(2)	49(1)
N(13A)	4905(2)	2957(2)	306(3)	48(1)
N(14A)	5560(2)	3076(2)	1428(3)	43(1)
N(15A)	5398(2)	3582(2)	2479(2)	37(1)

Summary of crystallographic data for **[1]**[(Br)$_3$].

Table 3. Bond lengths [Å] and angles [°] for [1][(Br)3]. iaj627new.

Ru(1)-N(14)	2.147(5)	Ru(3A)-N(14A)	2.153(5)
Ru(1)-N(15)	2.146(5)	Ru(3A)-N(6A)	2.166(5)
Ru(1)-N(1)	2.167(5)	N(9)-Ru(3)-N(10)	79.98(17)
Ru(1)-S(1)	2.2625(15)	N(10)-Ru(3)-S(8)	88.24(13)
Ru(1)-S(3)	2.2793(18)	S(7)-Ru(3)-S(8)	88.46(6)
Ru(1)-S(2)	2.2812(18)	N(9)-Ru(3)-S(9)	96.92(13)
Ru(2)-N(4)	2.134(5)	N(11)-Ru(3)-S(9)	92.49(12)
Ru(2)-N(6)	2.153(4)	N(10)-Ru(3)-S(9)	175.59(13)
Ru(2)-N(5)	2.157(4)	S(7)-Ru(3)-S(9)	88.76(6)
Ru(2)-S(5)	2.2768(17)	S(8)-Ru(3)-S(9)	88.77(6)
Ru(2)-S(6)	2.2886(16)	N(5A)-Ru(1A)-N(11A)	90.46(17)
Ru(2)-S(4)	2.2909(16)	N(5A)-Ru(1A)-N(4A)	79.80(16)
Ru(3)-N(9)	2.141(5)	N(11A)-Ru(1A)-N(4A)	83.51(18)
Ru(3)-N(11)	2.146(5)	N(5A)-Ru(1A)-S(2A)	88.17(12)
Ru(3)-N(10)	2.153(4)	N(11A)-Ru(1A)-S(2A)	176.46(13)
Ru(3)-S(7)	2.2794(16)	N(4A)-Ru(1A)-S(2A)	93.04(14)
Ru(3)-S(8)	2.2797(18)	N(5A)-Ru(1A)-S(3A)	94.53(12)
Ru(3)-S(9)	2.2809(15)	N(11A)-Ru(1A)-S(3A)	95.04(13)
Ru(1A)-N(5A)	2.154(4)	N(4A)-Ru(1A)-S(3A)	174.12(13)
Ru(1A)-N(11A)	2.155(5)	N(9A)-Ru(2A)-N(1A)	85.44(16)
Ru(1A)-N(4A)	2.157(5)	N(9A)-Ru(2A)-N(10A)	79.21(18)
Ru(1A)-S(2A)	2.2798(17)	N(1A)-Ru(2A)-N(10A)	86.99(16)
Ru(1A)-S(3A)	2.2809(15)	N(9A)-Ru(2A)-S(5A)	96.36(14)
Ru(1A)-S(1A)	2.2825(15)	N(1A)-Ru(2A)-S(5A)	92.26(12)
Ru(2A)-N(9A)	2.142(5)	N(10A)-Ru(2A)-S(5A)	175.55(13)
Ru(2A)-N(1A)	2.151(4)	N(9A)-Ru(2A)-S(4A)	175.17(13)
Ru(2A)-N(10A)	2.160(4)	N(1A)-Ru(2A)-S(4A)	92.65(12)
Ru(2A)-S(5A)	2.2783(17)	N(10A)-Ru(2A)-S(4A)	96.27(12)
Ru(2A)-S(4A)	2.2875(16)	S(5A)-Ru(2A)-S(4A)	88.14(6)
Ru(2A)-S(6A)	2.2904(15)	N(9A)-Ru(2A)-S(6A)	93.62(12)
N(1A)-Ru(2A)-S(6A)	179.03(13)	N(10A)-Ru(2A)-S(6A)	92.60(12)
S(5A)-Ru(2A)-S(6A)	88.08(6)	S(4A)-Ru(2A)-S(6A)	88.27(6)
N(15A)-Ru(3A)-N(14A)	79.80(17)	N(15A)-Ru(3A)-N(6A)	90.27(17)
N(14A)-Ru(3A)-N(6A)	89.43(18)	N(15A)-Ru(3A)-S(8A)	95.35(12)

N(14A)-Ru(3A)-S(8A)	175.11(14)	N(6A)-Ru(3A)-S(8A)	91.17(12)
N(15A)-Ru(3A)-S(7A)	86.88(13)	N(14A)-Ru(3A)-S(7A)	90.33(14)
N(6A)-Ru(3A)-S(7A)	177.14(13)	S(8A)-Ru(3A)-S(7A)	88.83(6)
N(15A)-Ru(3A)-S(9A)	174.03(13)	N(14A)-Ru(3A)-S(9A)	96.32(14)
N(6A)-Ru(3A)-S(9A)	94.25(14)	S(8A)-Ru(3A)-S(9A)	88.47(6)
S(7A)-Ru(3A)-S(9A)	88.61(7)	Ru(2)-N(5)-H(5)	123.5
Ru(3)-N(10)-H(10)	123.4	Ru(1)-N(15)-H(15)	123.3
Ru(1A)-N(5A)-H(5NA)	123.4	C(24A)-N(6A)-Ru(3A)	117.5(4)
C(28A)-N(6A)-Ru(3A)	124.4(4)	C(26A)-N(9A)-Ru(2A)	149.5(5)
Ru(2A)-N(10A)-H(10N)	123.1	C(31A)-N(14A)-Ru(3A)	149.0(4)
C(32A)-N(14A)-Ru(3A)	106.2(4)	C(33A)-N(15A)-Ru(3A)	112.9(4)
Ru(3A)-N(15A)-H(15N)	123.5		

Symmetry transformations used to generate equivalent atoms:

Table 4. Anisotropic displacement parameters (Å2x 10³) for [1][(Br)$_3$]. (iaj627new). The anisotropic
displacement factor exponent takes the form: $-2\pi^2$[h^2 $a^{*2}U^{11}$ + ... + 2 h k a* b* U^{12}]

	U^{11}	U^{22}	U^{33}	U^{23}	U^{13}	U^{12}
Ru(1)	31(1)	46(1)	32(1)	3(1)	11(1)	1(1)
Ru(2)	33(1)	40(1)	31(1)	4(1)	18(1)	6(1)
Ru(3)	26(1)	48(1)	31(1)	-3(1)	13(1)	5(1)
Ru(1A)	27(1)	44(1)	32(1)	2(1)	13(1)	-5(1)
Ru(2A)	31(1)	38(1)	29(1)	-1(1)	16(1)	-4(1)
Ru(3A)	33(1)	40(1)	34(1)	-5(1)	13(1)	0(1)
Br(1)	64(1)	82(1)	70(1)	-6(1)	30(1)	-6(1)
Br(2)	61(1)	83(1)	63(1)	2(1)	25(1)	15(1)
Br(3)	55(1)	107(1)	51(1)	-15(1)	17(1)	7(1)
Br(4)	57(1)	121(1)	54(1)	-25(1)	23(1)	-2(1)
Br(5)	93(1)	146(1)	99(1)	-48(1)	36(1)	12(1)
Br(6)	78(1)	156(1)	72(1)	14(1)	32(1)	-17(1)
S(1)	34(1)	52(1)	36(1)	1(1)	10(1)	4(1)
S(2)	46(1)	50(1)	53(1)	-1(1)	9(1)	8(1)
S(3)	49(1)	80(1)	53(1)	4(1)	24(1)	-15(1)
S(4)	37(1)	62(1)	41(1)	10(1)	18(1)	6(1)
S(5)	61(1)	42(1)	55(1)	6(1)	25(1)	8(1)
S(6)	43(1)	59(1)	41(1)	7(1)	26(1)	6(1)
S(7)	41(1)	59(1)	38(1)	-8(1)	20(1)	3(1)
S(8)	45(1)	59(1)	54(1)	2(1)	30(1)	4(1)
S(9)	32(1)	70(1)	43(1)	2(1)	17(1)	13(1)
S(1A)	29(1)	67(1)	47(1)	-3(1)	17(1)	-12(1)
S(2A)	48(1)	53(1)	50(1)	0(1)	30(1)	-2(1)
S(3A)	42(1)	47(1)	39(1)	6(1)	18(1)	-5(1)
S(4A)	43(1)	52(1)	40(1)	-3(1)	26(1)	-2(1)
S(5A)	53(1)	40(1)	50(1)	-3(1)	22(1)	-5(1)
S(6A)	35(1)	58(1)	37(1)	-5(1)	16(1)	-2(1)
S(7A)	50(1)	44(1)	66(1)	4(1)	8(1)	-8(1)
S(8A)	38(1)	50(1)	36(1)	0(1)	13(1)	1(1)
S(9A)	55(1)	72(1)	51(1)	-8(1)	24(1)	19(1)
N(1)	38(3)	54(3)	31(3)	7(2)	19(2)	8(2)
N(2)	57(4)	80(4)	40(3)	13(3)	34(3)	14(3)

N(3)	38(3)	70(4)	41(3)	4(3)	23(3)	18(3)
N(4)	33(3)	47(3)	42(3)	2(2)	25(2)	8(2)
N(5)	38(3)	33(3)	32(2)	2(2)	21(2)	4(2)
N(6)	35(3)	37(3)	33(3)	-4(2)	17(2)	7(2)
N(7)	47(3)	56(3)	41(3)	-11(2)	26(3)	5(3)
N(8)	40(3)	63(4)	31(3)	-7(2)	13(2)	-6(3)
N(9)	23(3)	57(3)	39(3)	-5(2)	10(2)	4(2)
N(10)	30(3)	45(3)	32(3)	-5(2)	17(2)	5(2)
N(11)	27(3)	53(3)	27(2)	-3(2)	9(2)	6(2)
N(12)	42(3)	62(4)	32(3)	-3(2)	12(2)	5(3)
N(13)	46(3)	68(4)	31(3)	10(2)	19(3)	12(3)
N(14)	42(3)	58(3)	36(3)	5(2)	22(2)	-1(3)
N(15)	37(3)	50(3)	26(2)	0(2)	13(2)	0(2)
N(1A)	31(3)	33(3)	33(2)	3(2)	17(2)	-8(2)
N(2A)	38(3)	46(3)	43(3)	13(2)	20(2)	2(2)
N(3A)	41(3)	51(3)	28(3)	10(2)	9(2)	5(2)
N(4A)	31(3)	48(3)	34(3)	0(2)	10(2)	-2(2)
N(5A)	24(2)	38(3)	26(2)	2(2)	5(2)	-3(2)
N(6A)	37(3)	48(3)	34(3)	-10(2)	18(2)	-4(2)
N(7A)	61(4)	79(4)	53(3)	-18(3)	39(3)	-12(3)
N(8A)	45(3)	71(4)	36(3)	-7(3)	28(3)	-20(3)
N(9A)	30(3)	51(3)	35(3)	2(2)	15(2)	-12(2)
N(10A)	36(3)	40(3)	27(2)	3(2)	18(2)	2(2)
N(11A)	31(3)	42(3)	33(3)	-3(2)	14(2)	-3(2)
N(12A)	43(3)	60(4)	33(3)	-1(2)	10(2)	-4(3)
N(13A)	54(3)	54(3)	33(3)	-6(2)	18(3)	-8(3)
N(14A)	39(3)	49(3)	44(3)	-9(2)	22(2)	-1(2)
N(15A)	35(3)	46(3)	28(2)	-7(2)	13(2)	0(2)

Table 1. Crystal data and structure refinement for [1][$(PF_6)_3$] (iaj602c2).

Identification code	iaj602c2	
Empirical formula	C36 H57 F18 N15 P3 Ru3 S9	
Formula weight	1726.63	
Temperature	150(2) K	
Wavelength	0.71073 Å	
Crystal system	Monoclinic	
Space group	C2	
Unit cell dimensions	a = 27.5079(16) Å	α= 90°.
	b = 16.0629(9) Å	β= 108.033(4)°.
	c = 14.4082(10) Å	γ = 90°.
Volume	6053.6(6) Å^3	
Z	4	
Density (calculated)	1.894 Mg/m^3	
Absorption coefficient	1.230 mm^{-1}	
F(000)	3444	
Crystal size	0.32 x 0.28 x 0.23 mm^3	
Theta range for data collection	1.49 to 27.50°.	
Index ranges	-35<=h<=35, -20<=k<=20, -18<=l<=18	
Reflections collected	62696	
Independent reflections	7169 [R(int) = 0.0963]	
Completeness to theta = 27.50°	99.6 %	
Absorption correction	Semi-empirical from equivalents	
Max. and min. transmission	0.7652 and 0.6944	
Refinement method	Full-matrix least-squares on F^2	
Data / restraints / parameters	7169 / 12 / 791	
Goodness-of-fit on F^2	1.102	
Final R indices [I>2sigma(I)]	R1 = 0.0574, wR2 = 0.1496	
R indices (all data)	R1 = 0.0728, wR2 = 0.1652	
Absolute structure parameter	0(10)	
Largest diff. peak and hole	1.886 and -1.957 e.Å^{-3}	

Table 2. Atomic coordinates (x 10^4) and equivalent isotropic displacement parameters (Å^{2}x 10^3) For [1][(PF_6)$_3$] (iaj602c2). U(eq) is defined as one third of the trace of the orthogonalized U^{ij} tensor.

	x	y	z	U(eq)
Ru(1)	6598(1)	6703(1)	1840(1)	22(1)
Ru(2)	6166(1)	3244(1)	1976(1)	22(1)
Ru(3)	8138(1)	4263(1)	1912(1)	22(1)
S(1)	6460(1)	2153(2)	3023(2)	29(1)
S(2)	5348(1)	2768(2)	1717(2)	28(1)
S(3)	6082(1)	3988(2)	3277(2)	26(1)
S(4)	6130(1)	7167(2)	2806(2)	28(1)
S(5)	7315(1)	6802(2)	3177(2)	26(1)
S(6)	6723(1)	8059(2)	1488(2)	27(1)
S(7)	8146(1)	3468(2)	3250(2)	26(1)
S(8)	8689(1)	3319(2)	1602(2)	26(1)
S(9)	8830(1)	4972(2)	2906(2)	27(1)
N(1)	7594(3)	5214(5)	2045(6)	22(2)
N(2)	7044(3)	6260(5)	942(6)	18(2)
N(3)	7168(4)	6486(6)	-640(7)	27(2)
N(4)	7897(4)	5631(6)	-810(7)	26(2)
N(5)	8085(3)	4981(6)	622(7)	24(2)
N(6)	6937(3)	3604(6)	2064(6)	24(2)
N(7)	7476(3)	3611(6)	995(6)	22(2)
N(8)	7140(3)	2922(6)	-593(7)	29(2)
N(9)	6312(3)	2221(6)	-734(7)	27(2)
N(10)	6248(3)	2606(5)	716(7)	26(2)
N(11)	6432(3)	5412(6)	2023(6)	23(2)
N(12)	5919(3)	4287(6)	1004(6)	24(2)
N(13)	5376(4)	4677(6)	-646(6)	27(2)
N(14)	5400(4)	6198(6)	-900(7)	30(2)
N(15)	5952(3)	6535(5)	580(7)	26(2)

Table 3. Bond lengths [Å] and angles [°] for [1][(PF_6)$_3$] iaj602c2.

Ru(1)-N(15)	2.129(9)	N(12)-Ru(2)-N(6)	86.3(3)
Ru(1)-N(11)	2.158(9)	N(10)-Ru(2)-N(6)	79.6(3)
Ru(1)-N(2)	2.159(8)	N(12)-Ru(2)-S(3)	92.0(3)

Ru(1)-S(6)	2.286(3)	N(10)-Ru(2)-S(3)	176.9(2)
Ru(1)-S(4)	2.295(3)	N(6)-Ru(2)-S(3)	99.0(2)
Ru(1)-S(5)	2.297(3)	N(12)-Ru(2)-S(1)	177.8(2)
Ru(2)-N(12)	2.155(9)	N(10)-Ru(2)-S(1)	94.8(2)
Ru(2)-N(10)	2.157(10)	N(6)-Ru(2)-S(1)	91.5(2)
Ru(2)-N(6)	2.166(9)	S(3)-Ru(2)-S(1)	87.97(10)
Ru(2)-S(3)	2.294(3)	N(12)-Ru(2)-S(2)	93.3(2)
Ru(2)-S(1)	2.291(3)	N(10)-Ru(2)-S(2)	93.3(2)
Ru(2)-S(2)	2.295(3)	N(6)-Ru(2)-S(2)	172.9(3)
Ru(3)-N(5)	2.154(9)	S(3)-Ru(2)-S(2)	88.05(10)
Ru(3)-N(7)	2.162(9)	S(1)-Ru(2)-S(2)	88.91(10)
Ru(3)-N(1)	2.188(8)	N(5)-Ru(3)-N(7)	85.0(3)
Ru(3)-S(8)	2.284(3)	N(5)-Ru(3)-N(1)	80.6(3)
Ru(3)-S(9)	2.297(3)	N(7)-Ru(3)-N(1)	85.5(3)
Ru(3)-S(7)	2.307(3)	N(5)-Ru(3)-S(8)	93.4(3)
N(15)-Ru(1)-N(11)	80.2(3)	N(7)-Ru(3)-S(8)	92.5(2)
N(15)-Ru(1)-N(2)	85.8(3)	N(1)-Ru(3)-S(8)	173.7(2)
N(11)-Ru(1)-N(2)	86.4(3)	N(5)-Ru(3)-S(9)	95.4(2)
N(15)-Ru(1)-S(6)	94.3(2)	N(7)-Ru(3)-S(9)	178.6(2)
N(11)-Ru(1)-S(6)	174.3(2)	N(1)-Ru(3)-S(9)	93.3(2)
N(2)-Ru(1)-S(6)	91.7(2)	S(8)-Ru(3)-S(9)	88.83(10)
N(15)-Ru(1)-S(4)	94.7(3)	N(5)-Ru(3)-S(7)	176.6(2)
N(11)-Ru(1)-S(4)	93.3(2)	N(7)-Ru(3)-S(7)	91.8(2)
N(2)-Ru(1)-S(4)	179.4(2)	N(1)-Ru(3)-S(7)	98.2(2)
S(6)-Ru(1)-S(4)	88.64(10)	S(8)-Ru(3)-S(7)	87.76(10)
N(15)-Ru(1)-S(5)	176.2(3)	S(9)-Ru(3)-S(7)	87.79(10)
N(11)-Ru(1)-S(5)	97.1(2)	C(6)-S(1)-Ru(2)	103.4(4)
N(2)-Ru(1)-S(5)	91.5(2)	C(1)-S(1)-Ru(2)	105.8(4)
S(6)-Ru(1)-S(5)	88.38(10)	C(3)-S(2)-Ru(2)	107.0(4)
S(4)-Ru(1)-S(5)	88.03(10)	C(2)-S(2)-Ru(2)	102.5(4)
N(12)-Ru(2)-N(10)	85.2(3)	C(4)-S(3)-Ru(2)	102.4(4)
Ru(1)-N(15)	2.129(9)	C(5)-S(3)-Ru(2)	106.6(4)
Ru(1)-N(11)	2.158(9)	C(12)-S(4)-Ru(1)	106.1(4)
Ru(1)-N(2)	2.159(8)	C(7)-S(4)-Ru(1)	103.2(4)
Ru(1)-S(6)	2.286(3)	C(8)-S(5)-Ru(1)	105.8(4)
Ru(1)-S(4)	2.295(3)	C(9)-S(5)-Ru(1)	102.7(4)
Ru(1)-S(5)	2.297(3)	C(11)-S(6)-Ru(1)	104.2(4)
Ru(2)-N(12)	2.155(9)	C(10)-S(6)-Ru(1)	107.1(4)

Ru(2)-N(10)	2.157(10)	C(13)-S(7)-Ru(3)	102.3(4)
Ru(2)-N(6)	2.166(9)	C(18)-S(7)-Ru(3)	105.6(4)
Ru(2)-S(3)	2.294(3)	C(14)-S(8)-Ru(3)	108.3(4)
Ru(2)-S(1)	2.291(3)	C(15)-S(8)-Ru(3)	103.1(4)
Ru(2)-S(2)	2.295(3)	C(17)-S(9)-Ru(3)	104.2(4)
Ru(3)-N(5)	2.154(9)	C(16)-S(9)-Ru(3)	106.8(4)
Ru(3)-N(7)	2.162(9)	C(19)-N(1)-Ru(3)	110.0(6)
Ru(3)-N(1)	2.188(8)	Ru(3)-N(1)-H(1A)	109.7
Ru(3)-S(8)	2.284(3)	Ru(3)-N(1)-H(1B)	109.7
Ru(3)-S(9)	2.297(3)	C(20)-N(2)-Ru(1)	117.1(7)
Ru(3)-S(7)	2.307(3)	C(19)-N(2)-Ru(1)	126.2(7)
N(15)-Ru(1)-N(11)	80.2(3)	C(22)-N(5)-Ru(3)	148.9(8)
N(15)-Ru(1)-N(2)	85.8(3)	C(23)-N(5)-Ru(3)	104.7(7)
N(11)-Ru(1)-N(2)	86.4(3)	C(28)-N(6)-Ru(2)	113.3(7)
N(15)-Ru(1)-S(6)	94.3(2)	Ru(2)-N(6)-H(6A)	108.9
N(11)-Ru(1)-S(6)	174.3(2)	Ru(2)-N(6)-H(6B)	108.9
N(2)-Ru(1)-S(6)	91.7(2)	C(24)-N(7)-Ru(3)	118.0(7)
N(15)-Ru(1)-S(4)	94.7(3)	C(28)-N(7)-Ru(3)	123.4(7)
N(11)-Ru(1)-S(4)	93.3(2)	C(26)-N(10)-Ru(2)	149.7(8)
N(2)-Ru(1)-S(4)	179.4(2)	C(27)-N(10)-Ru(2)	105.5(7)
S(6)-Ru(1)-S(4)	88.64(10)	C(29)-N(11)-Ru(1)	112.6(7)
N(15)-Ru(1)-S(5)	176.2(3)	Ru(1)-N(11)-H(11A)	109.1
N(11)-Ru(1)-S(5)	97.1(2)	Ru(1)-N(11)-H(11B)	109.1
N(2)-Ru(1)-S(5)	91.5(2)	C(30)-N(12)-Ru(2)	118.8(7)
S(6)-Ru(1)-S(5)	88.38(10)	N(12)-Ru(2)-N(6)	86.3(3)

Table 4. Anisotropic displacement parameters ($Å^2$x 10^3) for [1][$(PF_6)_3$] iaj602c2. The anisotropic displacement factor exponent takes the form: $-2\pi^2[h^2 a^{*2}U^{11} + ... + 2 h k a^* b^* U^{12}]$

	U^{11}	U^{22}	U^{33}	U^{23}	U^{13}	U^{12}
Ru(1)	27(1)	10(1)	28(1)	-1(1)	6(1)	-1(1)
Ru(2)	25(1)	12(1)	29(1)	0(1)	6(1)	-2(1)
Ru(3)	24(1)	12(1)	27(1)	1(1)	5(1)	0(1)
S(1)	34(1)	16(1)	36(2)	4(1)	10(1)	3(1)
S(2)	29(1)	18(1)	36(2)	-2(1)	8(1)	-5(1)
S(3)	30(1)	16(1)	30(1)	1(1)	7(1)	0(1)
S(4)	34(1)	17(1)	35(2)	-4(1)	12(1)	-4(1)
S(5)	33(1)	14(1)	30(1)	-2(1)	8(1)	-1(1)
S(6)	33(1)	12(1)	34(2)	2(1)	6(1)	0(1)
S(7)	29(1)	17(1)	28(1)	0(1)	5(1)	-1(1)
S(8)	27(1)	16(1)	34(1)	1(1)	8(1)	2(1)
S(9)	28(1)	20(1)	30(1)	-1(1)	4(1)	-4(1)
N(1)	28(4)	9(4)	28(5)	-5(3)	8(4)	-4(3)
N(2)	22(4)	5(3)	27(4)	1(3)	5(3)	4(3)
N(3)	31(5)	23(5)	26(5)	4(4)	10(4)	4(4)
N(4)	37(5)	16(4)	28(5)	-2(4)	13(4)	5(4)
N(5)	22(4)	14(4)	33(5)	0(4)	5(4)	-2(3)
N(6)	31(4)	18(4)	20(4)	4(4)	3(4)	2(4)
N(7)	35(5)	16(4)	18(4)	5(3)	12(4)	2(4)
N(8)	27(4)	25(5)	33(5)	-3(4)	5(4)	-2(4)
N(9)	18(4)	27(5)	30(5)	-6(4)	0(4)	5(3)
N(10)	24(4)	10(4)	37(5)	2(4)	1(4)	1(3)
N(11)	24(4)	18(4)	24(5)	-1(3)	5(4)	-2(3)
N(12)	27(4)	11(4)	32(5)	2(4)	4(4)	-3(3)
N(13)	32(5)	23(5)	20(4)	0(4)	2(4)	-3(4)
N(14)	36(5)	20(5)	34(5)	8(4)	9(4)	-2(4)
N(15)	30(4)	10(4)	34(5)	3(3)	7(4)	-4(3)

Table 1. Crystal data and structure refinement for [3][CF_3SO_3]$_3$ 2012ncs0665.

Identification code	2012ncs0665
Empirical formula	C57 H66.50 F9 N15 O9 Ru3 S12
Formula weight	1964.68

Temperature	100(2) K	
Wavelength	0.71075 Å	
Crystal system	Triclinic	
Space group	P-1	
Unit cell dimensions	a = 16.087(4) Å	α= 82.077(6)°.
	b = 16.940(4) Å	β= 78.560(6)°.
	c = 29.637(7) Å	γ = 73.861(5)°.
Volume	7575(3) Å^3	
Z	4	
Density (calculated)	1.723 Mg/m^3	
Absorption coefficient	1.006 mm^{-1}	
F(000)	3962	
Crystal size	0.08 x 0.07 x 0.01 mm^3	
Theta range for data collection	2.98 to 25.03°.	
Index ranges	-18<=h<=19, -20<=k<=20, -35<=l<=35	
Reflections collected	117730	
Independent reflections	26648 [R(int) = 0.1897]	
Completeness to theta = 25.03°	99.6 %	
Absorption correction	Semi-empirical from equivalents	
Max. and min. transmission	0.9900 and 0.9238	
Refinement method	Full-matrix least-squares on F^2	
Data / restraints / parameters	26648 / 31 / 861	
Goodness-of-fit on F^2	1.017	
Final R indices [I>2sigma(I)]	R1 = 0.1277, wR2 = 0.3266	
R indices (all data)	R1 = 0.2060, wR2 = 0.3724	
Largest diff. peak and hole	1.960 and -1.849 e.Å^{-3}	

Table 2. Atomic coordinates (x 10^4) and equivalent isotropic displacement parameters (Å^{2}x 10^3) For [3][CF_3SO_3]$_3$ 2012ncs0665. U(eq) is defined as one third of the trace of the orthogonalized U^{ij} tensor.

	x	y	z	U(eq)
Ru(1)	934(1)	7849(1)	567(1)	40(1)
Ru(2)	1868(1)	6017(1)	2208(1)	38(1)
Ru(3)	4319(1)	7508(1)	990(1)	40(1)
N(1)	1310(8)	7119(7)	1168(4)	40(3)
N(2)	12(7)	8531(7)	1096(4)	36(3)
N(3)	-798(8)	9231(8)	1664(5)	47(3)
N(4)	-132(7)	8341(7)	2308(4)	33(3)
N(5)	958(7)	7166(7)	2006(4)	38(3)
N(6)	2842(7)	6490(7)	1727(4)	37(3)
N(7)	2217(7)	6728(7)	2645(4)	36(3)
N(8)	2534(7)	7613(7)	3037(4)	35(3)
N(9)	3452(8)	8182(7)	2407(4)	43(3)
N(10)	3670(8)	7523(8)	1694(5)	45(3)
N(11)	3074(8)	7591(8)	789(5)	51(3)
N(12)	3767(8)	8815(7)	951(4)	41(3)
N(13)	3120(8)	10137(8)	897(5)	48(3)
N(14)	1708(8)	10022(8)	710(5)	46(3)
N(15)	1774(8)	8594(8)	655(5)	44(3)
Ru(1A)	5837(1)	9092(1)	2737(1)	43(1)
Ru(2A)	4832(1)	7194(1)	4371(1)	48(1)
Ru(3A)	8302(1)	7501(1)	3926(1)	51(1)
N(1A)	6791(7)	8644(7)	3196(4)	39(3)
N(2A)	6915(8)	8397(8)	2289(5)	50(3)
N(3A)	7978(8)	7501(8)	1890(5)	46(3)
N(4A)	8856(7)	6899(7)	2501(4)	40(3)
N(5A)	8183(8)	7587(7)	3214(4)	42(3)
N(6A)	5211(8)	7952(7)	3767(4)	38(3)
N(7A)	4591(8)	6583(8)	3843(5)	45(3)
N(8A)	4441(8)	5990(8)	3246(5)	45(3)
N(9A)	5134(8)	6838(8)	2628(4)	43(3)
N(10A)	5467(8)	7947(7)	2924(4)	42(3)
N(11A)	6963(8)	7438(8)	4120(5)	50(3)

N(12A)	8460(9)	6225(9)	3929(5)	61(4)
N(13A)	8537(10)	4872(10)	3927(6)	65(4)
N(14A)	6919(10)	4975(9)	4131(6)	66(4)
N(15A)	6153(8)	6396(8)	4249(5)	51(3)

Table 3. Bond lengths [Å] and angles [°] for [3][CF$_3$SO$_3$]$_3$ 2012ncs0665 .

Ru(1)-N(1)	2.116(12)	Ru(3)-S(8)	2.289(4)
Ru(1)-N(2)	2.150(12)	Ru(1A)-N(2A)	2.131(13)
Ru(1)-N(15)	2.160(12)	Ru(1A)-N(10A)	2.154(12)
Ru(1)-S(1)	2.280(4)	Ru(1A)-N(1A)	2.163(12)
Ru(1)-S(2)	2.280(4)	Ru(1A)-S(3A)	2.278(4)
Ru(1)-S(3)	2.287(4)	Ru(1A)-S(1A)	2.281(5)
Ru(2)-N(7)	2.129(12)	Ru(1A)-S(2A)	2.285(4)
Ru(2)-N(6)	2.151(11)	Ru(2A)-N(7A)	2.140(13)
Ru(2)-N(5)	2.175(11)	Ru(2A)-N(6A)	2.144(12)
Ru(2)-S(5)	2.273(4)	Ru(2A)-N(15A)	2.170(13)
Ru(2)-S(6)	2.274(4)	Ru(2A)-S(4A)	2.263(4)
Ru(2)-S(4)	2.277(4)	Ru(2A)-S(6A)	2.283(5)
Ru(3)-N(10)	2.140(13)	Ru(2A)-S(5A)	2.293(5)
Ru(1)-N(1)	2.116(12)	Ru(3A)-N(12A)	2.104(15)
Ru(1)-N(2)	2.150(12)	Ru(3A)-N(5A)	2.137(13)
Ru(1)-N(15)	2.160(12)	Ru(3A)-N(11A)	2.144(12)
Ru(1)-S(1)	2.280(4)	Ru(3A)-S(8A)	2.273(5)
Ru(1)-S(2)	2.280(4)	Ru(3A)-S(7A)	2.280(5)
Ru(1)-S(3)	2.287(4)	Ru(3A)-S(9A)	2.287(5)
Ru(2)-N(7)	2.129(12)	N(1)-Ru(1)-N(2)	79.2(4)
Ru(2)-N(6)	2.151(11)	N(1)-Ru(1)-N(15)	86.9(5)
Ru(2)-N(5)	2.175(11)	N(2)-Ru(1)-N(15)	84.6(5)
Ru(2)-S(5)	2.273(4)	N(1)-Ru(1)-S(1)	94.8(3)
Ru(2)-S(6)	2.274(4)	N(2)-Ru(1)-S(1)	173.9(3)
Ru(2)-S(4)	2.277(4)	N(15)-Ru(1)-S(1)	94.2(4)
Ru(3)-N(10)	2.140(13)	N(1)-Ru(1)-S(2)	91.1(3)
Ru(3)-N(12)	2.140(12)	N(2)-Ru(1)-S(2)	93.3(3)
Ru(3)-N(11)	2.164(13)	N(15)-Ru(1)-S(2)	177.4(4)
Ru(3)-S(7)	2.277(4)	S(1)-Ru(1)-S(2)	87.65(16)
Ru(3)-S(9)	2.279(4)	N(1)-Ru(1)-S(3)	176.4(3)
N(2)-Ru(1)-S(3)	97.3(3)	N(7)-Ru(2)-N(6)	80.0(4)
N(15)-Ru(1)-S(3)	93.3(4)	N(7)-Ru(2)-N(5)	85.5(4)
S(1)-Ru(1)-S(3)	88.74(15)	N(6)-Ru(2)-N(5)	84.9(4)
S(2)-Ru(1)-S(3)	88.51(16)	N(7)-Ru(2)-S(5)	92.8(3)
N(6)-Ru(2)-S(5)	92.2(3)	C(19)-N(1)-Ru(1)	115.3(10)
N(5)-Ru(2)-S(5)	176.8(3)	Ru(1)-N(1)-H(1A)	108.5
N(7)-Ru(2)-S(6)	175.6(3)	Ru(1)-N(1)-H(1B)	108.5

N(6)-Ru(2)-S(6)	95.8(3)	C(21)-N(2)-Ru(1)	145.7(11)
N(5)-Ru(2)-S(6)	93.0(3)	C(20)-N(2)-Ru(1)	106.2(9)
S(5)-Ru(2)-S(6)	88.57(15)	C(19)-N(5)-Ru(2)	122.1(9)
N(7)-Ru(2)-S(4)	95.4(3)	C(23)-N(5)-Ru(2)	116.8(10)
N(6)-Ru(2)-S(4)	175.3(3)	C(31)-N(6)-Ru(2)	112.5(9)
N(5)-Ru(2)-S(4)	93.9(3)	Ru(2)-N(6)-H(6A)	109.1
S(5)-Ru(2)-S(4)	88.93(15)	Ru(2)-N(6)-H(6B)	109.1
S(6)-Ru(2)-S(4)	88.80(15)	H(6A)-N(6)-H(6B)	107.8
N(10)-Ru(3)-N(12)	85.2(5)	C(33)-N(7)-C(32)	101.2(12)
N(10)-Ru(3)-N(11)	88.4(5)	C(33)-N(7)-Ru(2)	150.6(10)
N(12)-Ru(3)-N(11)	79.3(5)	C(32)-N(7)-Ru(2)	107.6(9)
N(10)-Ru(3)-S(7)	95.2(3)	C(35)-N(10)-Ru(3)	118.5(10)
N(12)-Ru(3)-S(7)	173.5(3)	C(31)-N(10)-Ru(3)	124.4(10)
N(11)-Ru(3)-S(7)	94.2(4)	C(43)-N(11)-Ru(3)	114.4(10)
N(11)-Ru(3)-S(9)	176.8(4)	Ru(3)-N(11)-H(11A)	108.7
S(7)-Ru(3)-S(9)	88.69(15)	Ru(3)-N(11)-H(11B)	108.7
N(10)-Ru(3)-S(8)	176.2(4)	C(45)-N(12)-Ru(3)	150.3(11)
N(12)-Ru(3)-S(8)	91.6(4)	C(44)-N(12)-Ru(3)	104.1(9)
N(11)-Ru(3)-S(8)	93.1(4)	C(47)-N(15)-Ru(1)	116.1(9)
S(7)-Ru(3)-S(8)	88.21(15)	N(2A)-Ru(1A)-N(10A)	85.2(5)
S(9)-Ru(3)-S(8)	88.51(15)	N(2A)-Ru(1A)-N(1A)	79.2(5)
C(7)-S(4)-Ru(2)	104.0(5)	N(10A)-Ru(1A)-N(1A)	87.6(5)
C(12)-S(4)-Ru(2)	107.4(6)	N(2A)-Ru(1A)-S(3A)	96.2(4)
C(9)-S(5)-Ru(2)	102.4(6)	N(10A)-Ru(1A)-S(3A)	89.8(3)
C(8)-S(5)-Ru(2)	105.9(6)	N(1A)-Ru(1A)-S(3A)	174.9(3)
C(10)-S(6)-Ru(2)	106.2(6)	N(2A)-Ru(1A)-S(1A)	92.9(4)
C(11)-S(6)-Ru(2)	103.5(6)	N(10A)-Ru(1A)-S(1A)	177.2(4)
C(13)-S(7)-Ru(3)	101.8(6)	C(35)-N(10)-Ru(3)	118.5(10)
C(18)-S(7)-Ru(3)	104.6(6)	N(1A)-Ru(1A)-S(1A)	94.0(3)
C(15)-S(8)-Ru(3)	101.8(6)	S(3A)-Ru(1A)-S(1A)	88.44(17)
C(14)-S(8)-Ru(3)	107.8(6)	N(2A)-Ru(1A)-S(2A)	174.7(4)
C(16)-S(9)-Ru(3)	107.5(6)	N(10A)-Ru(1A)-S(2A)	94.1(3)
N(1A)-Ru(1A)-S(2A)	95.5(3)	C(12A)-S(4A)-Ru(2A)	103.8(9)
S(3A)-Ru(1A)-S(2A)	89.06(16)	C(7A)-S(4A)-Ru(2A)	105.2(7)
S(1A)-Ru(1A)-S(2A)	88.01(16)	C(9A)-S(5A)-Ru(2A)	105.0(8)
N(7A)-Ru(2A)-N(6A)	79.3(5)	C(8A)-S(5A)-Ru(2A)	103.2(7)
N(7A)-Ru(2A)-N(15A)	85.2(5)	C(10A)-S(6A)-Ru(2A)	104.6(9)
N(6A)-Ru(2A)-N(15A)	87.4(5)	C(11A)-S(6A)-Ru(2A)	104.9(7)

N(7A)-Ru(2A)-S(4A)	91.9(3)	C(13A)-S(7A)-Ru(3A)	103.2(8)
N(6A)-Ru(2A)-S(4A)	90.8(3)	C(18A)-S(7A)-Ru(3A)	101.0(8)
N(15A)-Ru(2A)-S(4A)	176.8(4)	C(15A)-S(8A)-Ru(3A)	107.2(7)
N(7A)-Ru(2A)-S(6A)	175.7(4)	C(14A)-S(8A)-Ru(3A)	102.8(6)
N(6A)-Ru(2A)-S(6A)	96.4(3)	C(17A)-S(9A)-Ru(3A)	104.4(8)
N(15A)-Ru(2A)-S(6A)	94.4(4)	C(16A)-S(9A)-Ru(3A)	101.8(6)
S(4A)-Ru(2A)-S(6A)	88.39(17)	C(19A)-N(1A)-Ru(1A)	112.3(10)
N(7A)-Ru(2A)-S(5A)	95.9(4)	Ru(1A)-N(1A)-H(1A1)	109.1
N(6A)-Ru(2A)-S(5A)	175.2(4)	Ru(1A)-N(1A)-H(1A2)	109.1
S(4A)-Ru(2A)-S(5A)	89.20(17)	C(21A)-N(2A)-Ru(1A)	146.9(11)
S(6A)-Ru(2A)-S(5A)	88.42(18)	C(20A)-N(2A)-Ru(1A)	105.6(10)
N(12A)-Ru(3A)-N(5A)	86.6(5)	C(23A)-N(5A)-Ru(3A)	117.6(10)
N(12A)-Ru(3A)-N(11A)	79.4(5)	C(19A)-N(5A)-Ru(3A)	125.9(10)
N(5A)-Ru(3A)-N(11A)	89.7(5)	C(31A)-N(6A)-Ru(2A)	113.8(10)
N(12A)-Ru(3A)-S(8A)	175.5(4)	Ru(2A)-N(6A)-H(6A1)	108.8
N(5A)-Ru(3A)-S(8A)	92.6(3)	Ru(2A)-N(6A)-H(6A2)	108.8
N(11A)-Ru(3A)-S(8A)	96.1(4)	C(33A)-N(7A)-Ru(2A)	150.4(12)
N(12A)-Ru(3A)-S(7A)	92.2(4)	C(32A)-N(7A)-Ru(2A)	105.0(10)
N(5A)-Ru(3A)-S(7A)	178.6(4)	C(34A)-N(10A)-Ru(1A)	122.0(10)
N(11A)-Ru(3A)-S(7A)	89.3(4)	C(31A)-N(10A)-Ru(1A)	121.4(10)
S(8A)-Ru(3A)-S(7A)	88.6(2)	C(43A)-N(11A)-Ru(3A)	112.7(11)
N(12A)-Ru(3A)-S(9A)	96.7(4)	C(44A)-N(12A)-Ru(3A)	110.4(11)
N(5A)-Ru(3A)-S(9A)	91.9(3)	C(45A)-N(12A)-Ru(3A)	153.7(14)
N(11A)-Ru(3A)-S(9A)	175.6(4)	C(46A)-N(15A)-Ru(2A)	117.7(11)
N(15A)-Ru(2A)-S(5A)	92.4(4)	C(43A)-N(15A)-Ru(2A)	121.4(11)
S(8A)-Ru(3A)-S(9A)	87.83(19)	C(21A)-N(2A)-Ru(1A)	146.9(11)
S(7A)-Ru(3A)-S(9A)	88.95(18)	C(20A)-N(2A)-Ru(1A)	105.6(10)
C(5A)-S(3A)-Ru(1A)	103.9(6)	C(23A)-N(5A)-Ru(3A)	117.6(10)
C(4A)-S(3A)-Ru(1A)	105.8(6)	C(19A)-N(5A)-Ru(3A)	125.9(10)